Improved Limit State Definitions for Pressure Vessels by a Scale-bridging Application of Damage Mechanics

Von der Fakultät für Georessourcen und Materialtechnik der
Rheinisch-Westfälischen Technischen Hochschule Aachen

zur Erlangung des akademischen Grades eines
Doktors der Ingenieurwissenschaften
genehmigte Dissertation

vorgelegt von Dipl.-Ing.
Victoria Brinnel
aus Frankfurt am Main

Berichter: Univ.-Prof. Dr.-Ing. Wolfgang Bleck
Univ.-Prof. Dr.-Ing. Markus Feldmann

Tag der mündlichen Prüfung: 26. Juli 2017

Danksagung

Die vorliegende Arbeit entstand während meiner Tätigkeit als wissenschaftliche Mitarbeiterin am Institut für Eisenhüttenkunde der RWTH Aachen University. Mein Dank gilt daher zunächst Prof. Wolfgang Bleck für die Möglichkeit, diese Arbeit unter seiner Betreuung durchzuführen und für die vielfältigen Anregungen und Entwicklungsmöglichkeiten, die er mir in dieser Zeit gegeben hat. Des Weiteren möchte ich mich bei Prof. Markus Feldmann vom Institut für Stahlbau für die Übernahme des Korreferats bedanken. Außerdem vielen Dank an Prof. Daniela Zander für die Übernahme des Prüfungsvorsitzes.

Entscheidend geprägt wurde meine Zeit am IEHK durch meine Arbeitsgruppe, damals Werkstoffmechanik und heute Werkstoff- und Bauteilintegrität. Hier zuallererst ein herzliches Dankeschön an meinen langjährigen Gruppenleiter Sebastian Münstermann für die hervorragende Arbeitsatmosphäre, die kontinuierliche Unterstützung und Herausforderung sowie großartigen Kaffee. Ebenso möchte ich mich bei allen Kollegen der Arbeitsgruppe bedanken, die mich in meiner Zeit begleitet haben: Pawel, Denis, Mick, Mohamed, Jimmy, Bo, Georg, Karl, Michael D., Felix und Niloufar und natürlich auch Marc und Horst. Besonderen Dank auch an meine Bürokollegen, Christian, Michael B., Yidu und Markus, gemeinsam haben wir dem tristen Alltag erfolgreich die Stirn geboten. Außerdem an Andrea und Benedikt, ohne die der Wahnsinn so viel schwerer zu ertragen gewesen wäre - was hätte ich bloß ohne euch gemacht.

Darüber hinaus gilt mein Dank allen Kollegen des IEHK für die vielfältige Unterstützung und die herzliche Atmosphäre. Insbesondere durch die Kollegen und Kolleginnen der mechanischen Werkstatt, der Werkstoffprüfung, der Verwaltung, des Sekretariats und der Metallografie habe ich verlässliche und kompetente Unterstützung erfahren.

Auch über das Institut hinaus möchte ich mich bei meinem Projektpartner Simon Schaffrath bedanken, für echte Teamarbeit, die einfach gut funktioniert und Spaß macht. Ebenso gilt mein Dank den Mitgliedern des projektbegleitenden Ausschusses meines Forschungsprojektes, die den Druckbehälter gebaut haben. Ohne die Unterstützung meiner Bachelor- und Masterarbeiter sowie Hiwis wäre die Arbeit ebenfalls nicht zu bewältigen gewesen, daher vielen Dank an Marius, Florian, Stefanie, Frauke, Alain, Yidu und Yuling sowie an Julius, Markus, Christopher, Felix, Nora, Marcel, Niklas und viele Weitere. Ihr wart klasse!

Bei meinen Freunden und meiner Wahlverwandtschaft möchte ich mich dafür bedanken, dass sie mich immer noch begleiten und ich immer anrufen kann. Von Herzen vielen Dank an meine Familie, die meine Neugier geweckt hat, mir so viel mitgegeben hat und immer für mich da ist. Abschließend ein besonderer Dank an Martin: Für die kritische wissenschaftliche Begleitung (ich weiß, n=1...) und Unterstützung, dafür, dass Du schon so lange an meiner Seite bist, aber vor allem dafür, dass ich mich immer auf Dich verlassen kann - Danke!!!

Abstract

The application of modern high strength low alloy steels (HSLA) in pressure vessel design is currently hindered by the corresponding design standards although it might foster resource-efficient constructions. HSLA steels are penalised by a limited admissible exploitation of their properties which prevents thinner constructions. This limitation is imposed by the design stress definition of the design standards, such as the European code EN 13445. They relate the design stress for high strength steels to the tensile strength, including a high safety factor. This leads to lower design stresses for high strength steels due to their high yield-to-tensile ratio. The admissible design stress is only 46% of the nominal yield strength for a grade P690Q.

The current safety factors are based on experiences with common, low strength steels and do not consider the improved toughness properties of modern HSLA steels. Probabilistic safety concepts, as defined in the Eurocode (EN 1990), are a suitable tool to systematically derive more adequate safety factors for modern steels. However, they require a large number of full-scale burst tests. Since these are very costly, probabilistic safety concepts are not directly applicable in pressure vessel design. A possible solution to this problem is to partially replace burst tests by simulations. Ductile failure can hereby be predicted by the methods of damage mechanics. Yet, these models are mainly applied on the small scale or for the failure prediction in components with defects. The aim of this thesis is to develop a comprehensive modelling concept for the prediction of limit states in pressure vessels by damage mechanics simulations and demonstrate its predictive capabilities in comparison to a burst test.

Such a modelling concept needs to fulfil three main requirements: It needs to be efficient so that it can be applied in a high number of large-scale pressure vessel simulations, it needs to cover all relevant stress states, and it needs to refer to nominal toughness values. The latter is necessary because pressure vessel design is always based on nominal material values.

The modelling concept was developed by joining existing simulation approaches and providing new solutions for the missing links. The failure process in high quality HSLA steels was investigated by stopped experiments to define a suitable limit state. The local onset of softening, homogenised over the typical size of a finite element, was defined to be a suitable limit state. A numerical procedure using cell elements was applied to derive the corresponding limit strains in dependence of the stress state from simulations using Gurson models. This enabled the reference to nominal toughness levels which can be adjusted by an artificial deterioration of the Gurson parameters. This concept was extended to consider Lode angle dependence and adiabatic heating. Additionally, a calibration scheme was defined on the basis of a sensitivity analysis to enable a reliable correlation of Gurson parameters and toughness level. Since the application of strain-based limit criteria may lead to mesh influences in large-scaled simulations with varying mesh sizes, a scaling function for the limit strain criterion was developed and tested.

For comparison, a demonstrator pressure vessel made from the high strength steel grade P690Q was tested in a burst test. The vessel had a length of approximately 3 m, an outer diameter of 1200 mm, a nozzle with an outer diameter of 470 mm and a wall thickness of 50 mm. The simulation models were calibrated on small scale tests performed on samples produced from the identical material. During the burst test the vessel was filled with water through valves in the nozzle top. The burst pressure was 680 bar. The failure initiated at the transition from nozzle to vessel by ductile damage. The pressure vessel withstood three times its design pressure of 226 bar.

The modelling concept was tested within simulations of this burst test. The limit state in the simulation was reached first at a pressure of 653 bar; this is 96% of the burst pressure. The critical locations, at which first cracks appeared in the experiment, were predicted correctly at the transition from nozzle to vessel. The scaling function enabled a mesh-independent limit pressure prediction. The prediction capabilities of the developed concept were therefore successfully demonstrated.

An application of this modelling concept with reference to nominal toughness values could show that the predicted nominal limit pressure was well below a global nonlinear behaviour but much higher than the design pressure. The nominal limit state criterion was applied in a large number of pressure vessel simulations within the accompanying research project. These formed the basis for a subsequent application of probabilistic safety concepts. The computed appropriate design stress level was 63% of the yield strength. Consequently, these results question the current penalisation of high strength steels.

The safe applicability of high strength steels in pressure vessel design could therefore be demonstrated by experiments as well as simulations. The potential for a reduction of the safety factors was revealed by the accompanying probabilistic assessment. The developed modelling concept enables an innovative, scale-bridging failure modelling in large-scaled steel structures with references to nominal toughness requirements. It may be used in future studies to investigate the efficient and safe application of high strength steels in other steel constructions and components as well.

Kurzfassung

Die Anwendung moderner hochfester niedriglegierter Stähle (HSLA, high strength low alloy steels) im Druckbehälterbau wird derzeit durch die jeweiligen Auslegungsnormen behindert, obwohl dadurch ressourceneffizientere Konstruktionen möglich wären. HSLA Stähle werden hierbei durch eine eingeschränkte zulässige Ausnutzung ihrer Eigenschaften benachteiligt, welche dünnere Bauweisen verhindert. Diese Einschränkung resultiert aus der Bemessungsspannungsdefinition der Auslegungsnormen, z.B. der europäischen Richtlinie EN 13445. Diese bestimmt die Bemessungsspannung für hochfeste Stähle in Abhängigkeit der Zugfestigkeit mit einem hohen Sicherheitsfaktor. Dies führt dazu, dass für hochfeste Stähle aufgrund ihres hohen Streckgrenzenverhältnisses niedrigere Auslegungsspannungen zulässig sind. Für einen Stahl der Sorte P690Q beträgt die Auslegungsspannung lediglich 46% der Streckgrenze.

Die derzeit gültigen Sicherheitsfaktoren wurden auf der Basis von Erfahrungswerten mit herkömmlichen, niedrigfesten Stahlsorten festgelegt. Probabilistische Sicherheitskonzepte, wie etwa im Eurocode (EN1990) definiert, sind geeignet, um systematisch passendere Sicherheitsfaktoren zu bestimmen. Allerdings benötigen sie als Datenbasis eine große Anzahl von Berstversuchen. Da diese jedoch sehr kostspielig und aufwendig sind, sind probabilistische Sicherheitskonzepte derzeit nicht direkt auf Druckbehälteranwendungen übertragbar. Ein Lösungsansatz für dieses Problem besteht darin, einen Teil der benötigten Versuche durch Simulationen zu ersetzen. Das duktile Versagen kann hierbei von schädigungsmechanischen Modellen vorhergesagt werden. Jedoch werden solche Modelle derzeit eher für die Simulation von kleinen Laborproben oder für die Versagensvorhersage bereits defektbehafteter Komponenten eingesetzt. Das Ziel dieser Arbeit ist es, ein umfassendes Modellierungskonzept für die Grenzzustandsvorhersage in Druckbehältern auf Basis schädigungsmechanischer Simulationen zu entwickeln.

Ein solches Modellierungskonzept muss drei Hauptanforderungen erfüllen: Es muss effizient in einer großen Zahl von Druckbehältersimulationen eingesetzt werden können, es muss alle relevanten Lastzustände erfassen und es muss sich auf Nennzähigkeitsforderungen beziehen können. Letzteres ist erforderlich, da die Auslegung von Druckbehältern immer auf Basis von Nennmaterialkennwerten erfolgt.

Durch das Zusammenführen bestehender Modellierungskonzepte sowie die Bereitstellung neuartiger Verknüpfungsansätze wurde ein solches Konzept entwickelt. Der Versagensprozess in HSLA Stählen wurde anhand gestoppter Experimente untersucht, um einen geeigneten Grenzzustand zu identifizieren. Als solcher wurde der Beginn lokaler Entfestigung, homogenisiert über die typische Größe finiter Elemente, definiert. Die zugehörigen Grenzdehnungen in Abhängigkeit des Spannungszustands wurden numerisch aus Zellelementen abgeleitet, welche Gurson-Modelle zur Abbildung der mechanischen Antwort enthielten. Die Anwendung von Gurson-Modellen ermöglicht hierbei einen Bezug zu Nennzähigkeitsforderungen, welche durch eine künstliche Verschlechte-

rung der Gurson-Parameter eingestellt werden können. Dieses Konzept wurde um Lodewinkelabhängigkeit und die Berücksichtigung adiabatischer Erwärmung erweitert. Zusätzlich wurde ein Kalibrierungsschema auf Basis einer Sensitivitätsanalyse definiert, um eine zuverlässige Korrelation von Gurson-Parametersätzen und Zähigkeitsniveaus zu ermöglichen. Da die Anwendung dehnungsbasierter Grenzzustandskriterien in großskaligen Simulationen mit variierender Netzgröße problematisch sein kann, wurde eine Skalierungsfunktion entwickelt und getestet, die eine Anpassung des Grenzdehnungskriteriums an die Netzgröße ermöglicht.

Zum experimentellen Abgleich wurde ein Druckbehälter, der aus dem hochfesten Stahl P690Q hergestellt wurde, in einem Berstversuch zerstörend getestet. Der Druckbehälter besaß eine Länge von etwa 3 m, einen Außendurchmesser von 1200 mm, einen eingeschweißten Stutzen mit einem Außendurchmesser von 470 mm und eine Wanddicke von 50 mm. Die schädigungsmechanischen Modelle wurden an Kleinproben kalibriert, die aus identischem Material hergestellt wurden. Während des Berstversuchs wurde der Behälter mit Wasser durch Ventile im Stutzendeckel befüllt. Der Berstdruck betrug 680 bar, das Versagen begann am Übergang von Stutzen zum Behältermantel. Der Druckbehälter konnte damit dem Dreifachen seines Auslegungsdrucks von 226 bar standhalten.

Das entwickelte Modellierungskonzept wurde in Simulationen des Berstversuchs getestet. Der Grenzzustand wurde in der Simulation zuerst bei 653 bar erreicht, dies entspricht 96% des Berstdrucks. Die Orte, an welchen erste Risse im Druckbehälter auftraten, wurden korrekt am Übergang von Stutzen zu Mantel vorhergesagt. Die entwickelte Skalierungsfunktion ermöglichte hierbei eine weitgehend netzunabhängige Vorhersage des Grenzzustands. Die Vorhersagefähigkeit des entwickelten Modellierungskonzeptes konnte daher erfolgreich demonstriert werden.

Die Anwendung des Modellierungskonzeptes unter Bezugnahme auf nominale Zähigkeitsanforderungen konnte zeigen, dass die vorhergesagten nominalen Grenzdrücke unterhalb des globalen nichtlinearen Verhaltens lagen, jedoch deutlich höher als der Auslegungsdruck. Das nominale Grenzdehnungskriterium wurde im begleitenden Forschungsprojekt in einer Vielzahl von Druckbehältersimulationen eingesetzt. Diese bildeten die Datenbasis für den folgenden Einsatz probabilistischer Sicherheitskonzepte. Das berechnete, angemessene Niveau für eine Auslegungsspannung betrug 63% der Streckgrenze. Dies ist ein deutlicher Hinweis, dass die aktuelle Benachteiligung hochfester Stähle nicht gerechtfertigt ist.

Die sichere Anwendbarkeit hochfester Druckbehälterstähle konnte sowohl im Experiment als auch in numerischen Simulationen demonstriert werden. Das Reduktionspotential der Sicherheitsfaktoren wurde durch die probabilistische Analyse aufgezeigt. Das entwickelte Modellierungskonzept ermöglicht eine innovative, skalenübergreifende Versagensmodellierung von großskaligen Strukturen und Komponenten unter Berücksichtigung von Nennmaterialkennwerten. Dieses Konzept kann in zukünftigen Studien zur Untersuchung der effizienten und sicheren Anwendung hochfester Stähle in weiteren Konstruktionen und Komponenten angewendet werden.

Contents

List of Symbols and Abbreviations

Arabic Symbols

A, A_0	Cross section, initial cross section
a, b	Fitting parameters scaling function
c_T^i	Fitting parameters temperature dependance function
$c_{\dot{\varepsilon}}^i$	Fitting parameters strain rate dependance function
c_η, c_θ^s,c_θ^{ax}	Parameters of the BW model
E	Young's modulus, external loads acting on a structure
e_a	Wall thickness
e	Euler's number
F	Force
$\overline{F}$	Force vector
f, f^*	Void volume fraction, effective void volume fraction in Gurson models
f_c	Critical void volume fraction in Gurson models
f_N	Void volume fraction of possible secondary voids
f_u^*, f_F	Void volume fractions at failure
f_0	Initial void volume fraction
$\overline{\overline{D}}$	Damping matrix
D	Damage variable
D_i	Fitting parameters for phenomenological damage models
D_m	Mean diameter
f_d	Design stress
g	Limit state function for structural failure
G_f	Fracture energy
I_i	Invariants of the stress tensor
J_i	Invariants of the stress deviator tensor
K	Stress intensity factor
$\overline{\overline{K}}$	Global stiffness matrix
k_H, k_L	Factor for flow stress extrapolation according Hollomon/Ludwik
k_ω	Shear damage parameter
l	Length
l_e	Element length
L	Characteristic length
L_{ind}	Limit state indicator
m	Parameter of the BW model

$\overline{\overline{M}}$	Mass matrix
n, n_H, n_L	Hardening exponent, according to Hollomon/Ludwik
R	Resistance of a structure, electrical resistance
R_{eH}, R_{eL}	Upper and lower yield point
R_m	Tensile strength
$R_{p0.2}$, $R_{p0.2/T}$	Yield strength, Yield strength at temperature T
q_i	Empirical fitting parameters
s_{ij}	Stress deviator tensor
S_N	Standard deviation of void nucleation law
T	Temperature
t	Time
$\overline{u}$	Displacement vector
U	Electrical potential difference or voltage
z	Weld seam factor

Greek Symbols

α, β	Force ratios on cell element
Δ	Difference/Increment
ε	Strain
$\dot{\varepsilon}$	Strain rate
ε^c	Limit strain
ε^e	Elastic strain
ε_f	Failure strain
ε_i	Initiation strain
ε_L	Lüders strain
ε_N	Characteristic strain of void nucleation law
ε^p	Plastic strain
$\overline{\varepsilon}^p$, $\dot{\overline{\varepsilon}}^p$	Equivalent Plastic strain, Equivalent plastic strain rate
ε_t	True stress
ε_u	Uniform elongation
η	Stress triaxiality
η_0	Parameter of the BW model
$\eta_{1,2}$	Boundary triaxialities
θ, $\overline{\theta}$	Lode angle, normalised Lode angle factor
κ	Void growth acceleration factor
λ	Plastic multiplier
ξ	Stress state variable
ρ	Resistivity
σ	Stress

σ_e	Equivalent stress
σ_h	Hydrostatic stress
σ_t	True strain
σ_y	Yield stress
$\tilde{\sigma}$	Effective stress in CDM
γ_{kl}	Angular displacements of a material point
γ_M	Safety factor
γ	Lode angle dependent function of the BW model
Φ	Yield potential
Ψ	Residuum
ω	Normalised deviatoric shear variable
Ω	Stress triaxility function in NT model
ω_0	Stress state function in NT model

Abbreviations

ASME	American Society of Mechanical Engineers
AV	Energy consumed in Charpy test
bcc	Body centred cubic
bm	Base metal
BW	Bai-Wierzbicki model
CDM	Continuum damage mechanics
CT	Compact tension specimen(s)
CTOD	Crack tip opening displacement
DCPD	Direct current potential drop method
FE, FEM	Finite Elements, Finite Element Method
DBA	Design by analysis
DBF	Design by formulae
DIC	Digital image correlation
fcc	face centred cubic
GTN	Gurson-Tvergaard-Needleman model
HAZ	Heat affected zone
HSLA	High strength low alloy
JC	Johnson-Cook model
LM	Light microscopy
LSL	Limit strain locus
MBW	Modified Bai-Wierzbicki model
NH	Nahshon-Hutchinson model
NRB	Notched round bar(s)
NT	Nielsen-Tvergaard model
PS	Plane strain specimen(s)
RT	Room temperature
SENB	Single edge notched bending sample(s)

SEM	Scanning electron microscopy
SRB	Smooth round bar(s)
UCI	Ultrasonic contact impedance
WP	Wide-plate sample(s)
Y/T	Yield-to-tensile ratio
3D	Three-dimensional

1. Introduction

1.1. Motivation and Background

Global CO_2 emissions need to be reduced drastically to prevent further global warming, as recently acknowledged by 195 countries in the Paris agreement [1]. To achieve this, it is necessary to decrease the global energy consumption. Industry applications are responsible for 27% of the world's gross energy consumption while the construction and operation of buildings contribute 37% [2,3]. A more efficient construction and operation of industrial plants, buildings, and infrastructure is therefore essential. As structural steels are regularly used in these fields, an increased use of high strength steels is thus a key factor for improved resource efficiency. These steels enable a reduction of the material use by thinner constructions (e.g. [4]). Additionally, a cascade of secondary effects can be achieved, such as reduced energy consumption in welding, transportation, and operation. This would lead to significant emission savings. Furthermore, a reduction of welding times also may result in cost savings of up to 60% [5].

Modern structural steels, represented by the high strength low alloy steels (HSLA), are available with yield strengths of up to 1300 MPa for industrial and infrastructure applications. Such high strength steels are regularly used in mobile crane design [6] while their application in structural steelwork and plant design is currently very rare. Only projects with special requirements, e.g. in architecture or hydro power plants [4,5,7], use high strength steels. Hence, the possible advantages are not exploited in the overwhelming majority of constructions. A decisive factor limiting the application of HSLA steels are the technical standards that steel constructions and components are subjected to [7,8].

Technical standards are implemented in order to prevent structural failure and its potentially catastrophic consequences for humans or the environment. In the case of serial products, e.g. trains and airplanes, the safety of each type can be tested and approved. In contrast, most steel constructions, e.g. buildings, bridges, pressure vessels, pipelines, and power plants, are designed individually. Consequently, the design procedures are regulated instead of the products. Only constructions designed according to the technical standards are admissible. Minimum material properties, referred to as nominal properties, have to be guaranteed by the steel producers. The design procedures do not consider the actual material properties but rely only on these nominal properties. Examples for such standards are:

- The Eurocode 3 (EN 1993) for steel constructions. The corresponding nominal material requirements are defined in EN 10025.
- The harmonised European pressure vessel design rules for unfired pressure vessels defined in EN 13445. The corresponding nominal material requirements are defined in EN 10028.

Currently, these standards allow the use of high strength steels in general, but limit the exploitation of their properties due to safety concerns. High strength steels are more expensive than conventional grades. If their properties are not fully exploited, their use becomes uneconomical which hinders their application despite possible advantages.

However, the safety concerns are based on experiences with conventional steels of limited toughness. The current regulations might therefore be not appropriate for modern HSLA steels with excellent toughness. A way to improve this situation and foster the application of high strength steels is investigated in this study. In the following, this will be further discussed and explained on the application example of pressure vessels, but the approach is transferable to other steel constructions.

1.1.1. Current design rules for unfired pressure vessels

Steel components may be subjected to constant, transient and cyclic forces as well as environmental influences such as temperatures or corrosive substances. Each loading type triggers different failure modes in steel materials and has to be considered individually. The focus of this study is on failure by constantly increasing, proportional forces. Such a failure is referred to as instant fracture or forced rupture [9]. Macroscopically, two fracture types are distinguished when considering the instant fracture of a steel component:

- Brittle failure is characterised by almost no apparent deformation of the component. Brittle failure happens spontaneously without warning and results in unstable crack propagation. Consequently, brittle failure has to be strictly avoided for structural safety.
- Ductile failure is characterised by a significant plastic deformation of the sample or the structure. The preceding deformation gives evidence of an upcoming structural failure.

Design procedures for pressure vessels subjected to such static loads are given within EN 13445. They include two central aspects:

- The toughness assessment aims at preventing brittle failure. For a selection of steel grades and thicknesses, it is reduced to fulfilling certain levels of Charpy impact toughness. A full fracture mechanics analysis is required for all other cases.
- The strength assessment aims at preventing ductile failure and defines the required wall thicknesses to ensure this.

The strength assessment distinguishes several admissible procedures:

- Design by formulae (DBF): The required wall thickness is determined by analytical design formulas defined in the standard.
- Design by analysis (DBA): The required wall thickness is determined by a simplified numerical analysis, see [10] for an overview. Alternatively, an analytical investigation of critical stresses can be performed.
- Design by experiment: A burst test is obligatory. The procedure can be applied as an alternative to or in addition to the DBF procedure.

The most common procedure is DBF. EN13445-3 provides the required formulas for typical design elements of pressure vessels. For a cylindrical shell for example the maximum pressure is given in dependence of an admissible design stress f_d, a weld seam factor z, the wall thickness e_a, and the mean diameter D_m (Eq. 1.1).

$$P_{max} = \frac{2 f_d \cdot z \cdot e_a}{D_m} \tag{1.1}$$

The admissible design stress f_d is hereby calculated by applying safety factors to the nominal yield strength at design temperature $R_{p0.2/T}$ and the nominal tensile strength R_m (Eq. 1.2). The actual material values are not considered. The safety factors are defined to be 1.5 for the yield strength and 2.4 for the tensile strength, respectively.

$$f_d = \min \left\{ \frac{R_{p0.2/T}}{1.5}; \frac{R_m}{2.4} \right\} \tag{1.2}$$

EN 13445 allows for an alternative procedure for steel grades and production processes with increased quality. In this case the sulphur content is restricted and is is obligatory that the weld seams undergo full non-destructive testing. Under these circumstances the safety factor on the tensile strength may be reduced to 1.875.

This design stress definition affects the application of HSLA steels. In high strength steels the yield strength is closer to the tensile strength than in low strength steels. This is characterised by the yield-to-tensile ratio (Y/T), which increases with the yield strength. Table 1.1 lists the admissible design stresses, the exploitation of the yield strength by the design stress, and the nominal Y/T-ratio for all steels defined in EN 10028. The latter two are also graphically displayed in Fig. 1.1.

Even for the low strength steel P275N the high safety factor of 2.4 is obligatory, resulting in a yield stress exploitation of 59%. The safety factor of 2.4 has to be applied as well for the stronger steel grades. However, the yield strength exploitation is constantly decreasing with increasing yield strength due to the Y/T-ratio. For the steel grade P690Q only 46.5 % of the yield strength is admissible as design stress. Consequently, a wall thickness reduction due to the increased strength would be possible but is not admissible. If the wall thickness cannot be reduced significantly, using high strength steels cannot be profitable. Therefore, their application is hindered.

Table 1.1.: Design stress and exploitation of nominal mechanical properties according to EN 13445 and EN 10028.

Steel grade	$R_{p0.2}$ [MPa]	R_m [MPa]	Y/T=$R_{p0.2}/R_M$	f_d [MPa]	$f_d/R_{p0.2}$
P275N	275	390	0.71	162.50	59.09%
P355N	355	490	0.72	204.17	57.51%
P355M	355	450	0.79	187.50	52.82%
P355Q	355	490	0.72	204.17	57.51%
P420M	420	500	0.84	208.33	49.60%
P460N	460	570	0.81	237.50	51.63%
P460M	460	530	0.87	220.83	48.01%
P460Q	460	550	0.84	229.17	49.82%
P500Q	500	590	0.85	245.83	49.17%
P690Q	690	770	0.90	320.83	46.50%

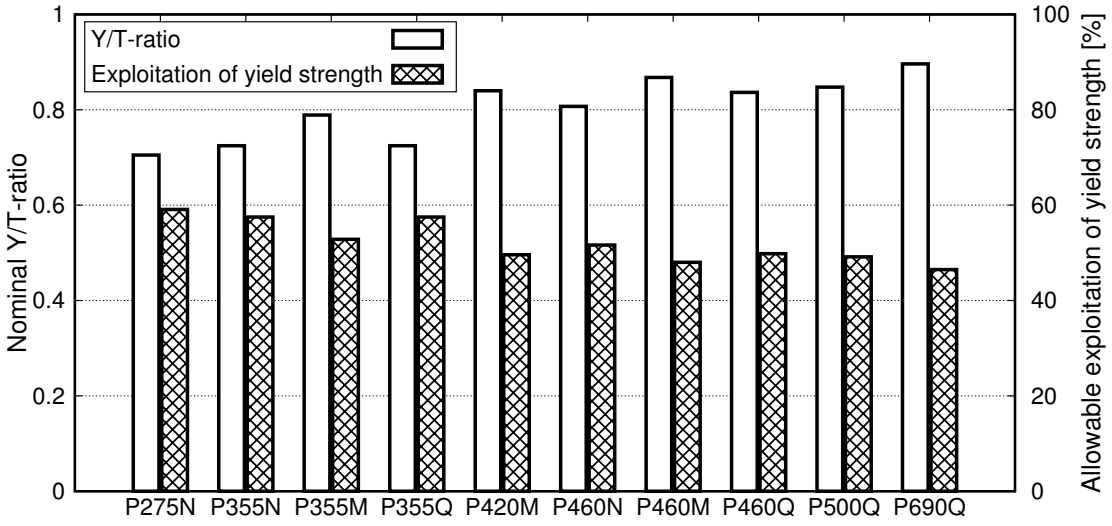

Figure 1.1.: Exploitation of yield strength by design stress and Y/T ratio for all steels classified in EN 10028.

The disproportional penalisation of high strength steels was demonstrated by Diamantoudis and Kermanidis in a study that compared the results of DBF and the DBA procedures for high strength steels [11]. They showed that the DBA procedure allowed a 41% higher pressure compared to DBF for a P355. For a P500Q steel the permissible pressure increased by 70% when using DBA instead of DBF. This demonstrates that with these more advanced procedures a better exploitation of the properties of high strength steels is possible. However, due to the effort and expertise required they are rarely applied.

An alternative to the European design code is the pressure vessel design standard published by the American Society of Mechanical Engineers (ASME) which is regularly applied worldwide. The regulations for unfired pressure vessels are defined in the ASME Boiler and Pressure Vessel Code, Section VIII, Division 1. The allowable stresses are computed using formulas given in Section II, Appendix 1. The definition is similar to Eq. 1.2, but the safety factor on the tensile strength is defined as 3.5. This implies that high strength steels are penalised even more strongly than in the European code. For a grade comparable to P690Q, the SA-517 Grade F, this results in a yield strength exploitation of mere 33%.

For both codes the corresponding regulations were defined based on experiences with common, low strength steels and were simply extrapolated to high strength steels. Within the last 20 years however, the steel quality, especially for low alloy steels, has greatly increased through the use of improved production processes. Due to their fine-grained structure, these steels now reach excellent toughness levels. Yet, the toughness is not considered at all in the strength assessment although an improved toughness not only provides an increased safety with regard to brittle but also with regard to ductile failure. The design rules therefore should be modified to ensure a design procedure more appropriate for the failure behaviour of these modern steel grades. Hence, a systematic assessment of the required safety factors would be beneficial. The Eurocode (EN 1990, Annex D) provides systematic methods for the definitions of safety factors based on probabilistic safety concepts, which are explained in the following section.

1.1.2. Probabilistic safety concepts

Probabilistic safety concepts consider that loads acting on structures as well as their resistances are statistically distributed. These distributions can be assessed with stochastic methods. The limit state function for structural failure g is defined based on a structure's resistance R and the acting loads E (Eq. 1.3). For $g > 0$ the structure is safe while it will fail for $g \leq 0$.

$$g = R - E \tag{1.3}$$

Both variables are statistically distributed. The region, in which failure may occur, is characterised by the overlap of the probability density functions of resistance and acting loads, as schematically displayed in Fig. 1.2a. The probability of failure can be reduced to a desired level by shifting the two distributions apart. This can be achieved by the derivation of statistically based safety factors according to EN 1990. It allows the derivation of statistically based safety factors either by a full probabilistic analysis or through semiprobabilistic methods.

Semiprobabilistic methods are mostly used to enhance normative regulations because it is complicated to assess the statistical distribution of every influencing parameter which would be required for the full probabilistic analysis. These methods compare predictions of a design function to results of full scale experimental tests (Fig. 1.2 b). The experimental failure values are plotted as a function of the design model predictions without safety factors. Ideally, the results would scatter around a line with a slope of 45°, but deviations may occur. The design values always have to be below the experimental failure values for a safe construction. This can be achieved by defining a suitable safety factor γ_M.

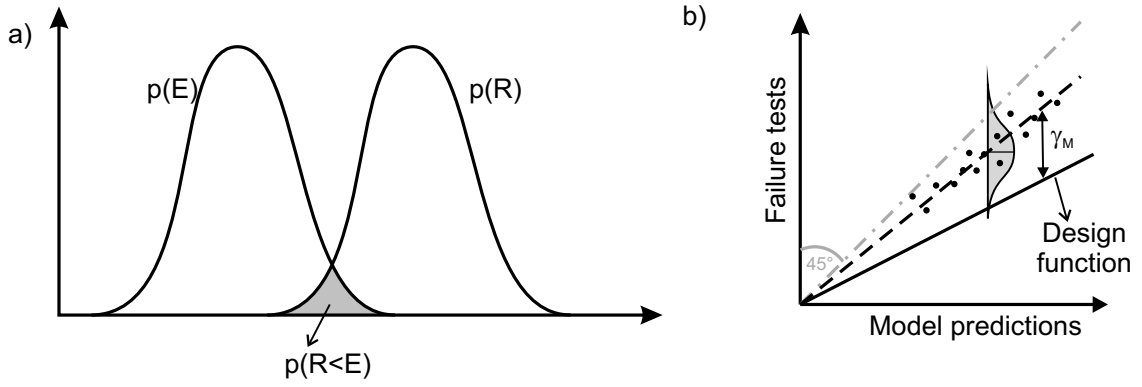

Figure 1.2.: a) Schematic illustration of the stochastic distribution of resistance and load of a structure and the region of failure marked in grey. b) Semi-probabilistic method for the derivation of safety factors based on experimental results. Figures adapted from [12].

The application of probabilistic methods enables a precise definition of the safety factor so that the desired safety level can be achieved. The safety level is selected according to the possible consequences of a failure. EN 1990 defines categories of potentially high, medium and low impacts of a possible failure to human life, economic, social or ecological aspects. A failure probability of 10^{-7} per year is recommended for the highest category of potential impact. This category would be suitable for pressure vessel applications. For building structures, which belong to the medium category, a failure probability of 10^{-4} is accepted within a lifetime of 50 years.

A transfer of probabilistic concepts to pressure vessel design could enable the definition of more adequate safety factors for high strength steels. This would foster the use of these steel grades and make their ecological and economic advantages available to the industry. However, the application of probabilistic methods would require a large number of burst tests. This is economically not feasible because such tests are very expensive and laborious. An alternative approach is pursued within this study and explained in the following.

1.2. Aim of this study

The number of burst tests that is feasible for a probabilistic safety assessment in pressure vessel design is highly limited. One possibility to solve this problem is to partly replace burst tests with numerical simulations. The Finite Element Method (FEM) is a suitable approach to model the mechanical response of constructions to loading. Elastic and plastic deformation can be simulated with excellent accuracy, yet for a burst pressure prediction the material failure has to be included as well.

The safety factors described above are only used within the strength assessment. Therefore, it can be assumed that the relevant failure mode is ductile failure. This failure type can be predicted numerically by using the methods of damage mechanics. Thus, a part of the required experiments could be replaced by numerical simulations using damage mechanics models. Such a procedure could enable an application of probabilistic safety concepts in pressure vessel design.

First studies on such a concept at RWTH Aachen University proved the general feasibility, but the underlying concept of damage mechanics modelling was not sufficient [8, 12]. Several requirements have to be fulfilled to use damage mechanics models reliably for the simulation of pressure vessel failure:

- Efficient application in a large number of component simulations: To replace experimental results by modelling a large number of simulations with varying dimensions, wall thicknesses and constructional elements like nozzles have to be performed. The damage mechanics model has to be efficient to keep the computation time within reasonable bounds.
- Reliable application within different kinds of stress states and loading situations: Although pressure vessels have a simple base geometry, additional elements like nozzles, inlets, and supporting structures may lead to pronounced local cross section transitions. These cause an irregular load distribution and three-dimensional stress states. Moreover, the wall thickness of individual constructions may vary strongly. The damage mechanics model has to characterise ductile failure reliably over the whole range of stress states and possible loading situations.
- Reference to nominal values: Neither the EN nor the ASME codes consider the actual material values for the design of pressure vessels. It is performed strictly on nominal material properties. In general, probabilistic safety concepts are able to consider material scatter, but this deeply interferes with the design philosophy of these codes. An alternative approach is therefore to conduct the numerical burst pressure simulations with nominal failure assumptions. These would presume a material with a low resistance to ductile failure. However,

these assumptions have to be justified and calibrated. The material standard EN 10028 demands a minimum yield strength and a minimum Charpy impact toughness. Consequently, the selected damage mechanics models shall be able to simulate a Charpy impact toughness test to relate to this nominal characteristic.

The aim of this thesis is to develop a comprehensive modelling concept that satisfies all the requirements stated above.

This modelling concept is investigated at the example of the high strength pressure vessel steel P690Q. Currently, the yield strength exploitation of this steel grade is strongly restricted. This is illustrated in Fig. 1.3; in addition, the design stress for the comparable grade of the ASME standard, SA-517 Grade F, is plotted. The developed modelling concept will be tested in comparison to the results of a burst test on a pressure vessel made from P690Q. Finally, failure simulations based on nominal values shall help to answer the question, what level of yield strength exploitation ensures a safe, but efficient application of P690Q (Fig. 1.3). By this, the application of probabilistic safety concepts in pressure vessel design shall be enabled. These can then be used to systematically derive adequate safety factors for modern high strength steels and thereby foster the application of HSLA steels.

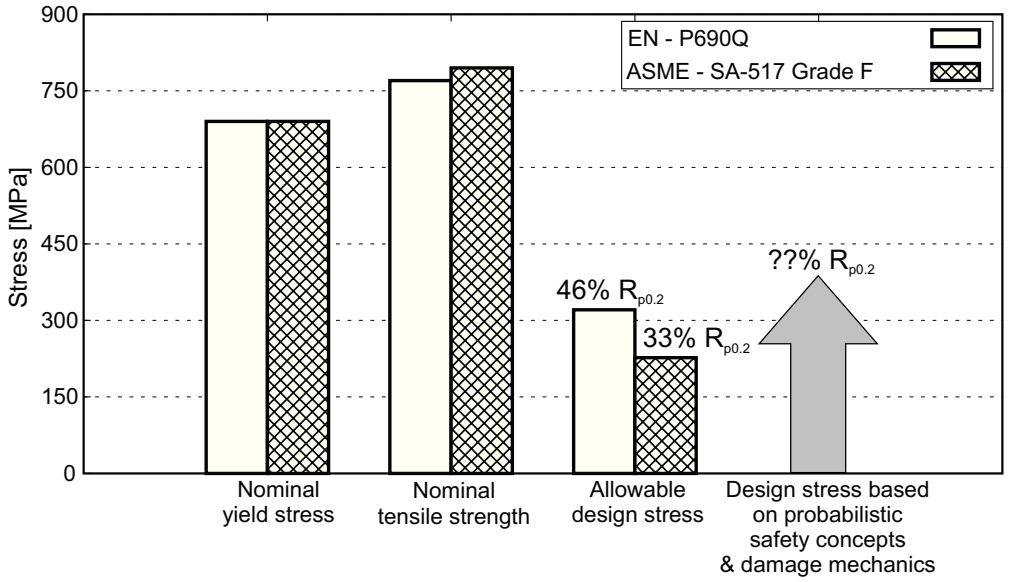

Figure 1.3.: Schematic illustration of the current design stresses and the investigation aim.

2. State of the art

In this study, damage mechanics methods will be used for the description of ductile failure. Thus, this chapter provides an introduction on plasticity and ductile damage as well as their numerical descriptions. The mathematical description of plastic deformation is presented in Section 2.1. The failure behaviour of steels is discussed in Section 2.2 while the damage mechanics models used in this study are presented in Section 2.3 along with a general introduction on damage mechanics modelling. The current state of the art on the prediction of ductile structural failure is summarised in Section 2.4.

2.1. Plastic deformation of steels

2.1.1. Yield behaviour of HSLA steels

The yield behaviour of steels is characterised in a uniaxial tensile test. A smooth round bar or a flat sample is loaded by a constant deformation rate. The force F and the corresponding displacement Δl are measured and subsequently transformed into technical stress and strain by referring to the initial cross section A_0 and the initial measurement length l (Eq. 2.1 - Eq. 2.2) [13]. Typical technical stress-strain diagrams are displayed in Fig. 2.1.

$$\sigma = \frac{F}{A_0} \tag{2.1}$$

$$\varepsilon = \frac{\Delta l}{l} \tag{2.2}$$

During elastic deformation the relation between stress and strain is characterised by Young's modulus E and Hooke's law (Eq. 2.3). The elastic deformation is homogeneously distributed over the complete sample length [13, 14].

$$\sigma = E \cdot \varepsilon \tag{2.3}$$

Continuous and discontinuous yielding can be found in modern steel grades. For continuous yielding, an offset yield point is defined arbitrarily, for example the $R_{p0.2}$-value (Fig. 2.1a). Discontinuous yielding is characterised by the upper yield stress R_{eH}, the lower yield stress R_{eL} and the Lüders strain ε_L (Fig. 2.1b) [13, 15].

The maximum force in the tensile test is reached at the equilibrium point of strain hardening and softening caused by the Poisson effect. This point is characterised by the uniform elongation ε_u and the maximum tensile strength R_m [13, 14]. Subsequently, necking begins. The local stress within the neck is still increasing, but the cross section reduction results in global softening. Technical

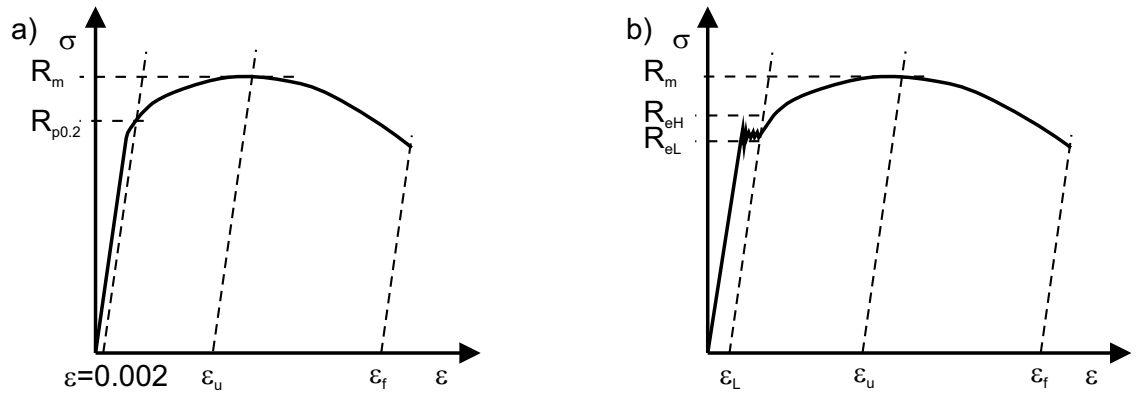

Figure 2.1.: Technical stress-strain diagram with a) continuous yielding and b) discontinuous yielding. The sample breaks at the failure strain ε_f.

strain and stress, which refer to the initial configuration of the sample, are no adequate measures for the local stress and strain state. The true stress σ_t (Eq. 2.4) and the true strain ε_t (Eq. 2.5) refer the force to the current cross section A and the displacement to the current length.

$$\sigma_t = \frac{F}{A} \tag{2.4}$$

$$\varepsilon_t = ln\frac{l+\Delta l}{l} = ln(1+\varepsilon) \tag{2.5}$$

True stress and true strain enable an analytical definition of the uniform elongation given by the Considère criterion (Eq. 2.6) [13]. Under progressed necking, the stress state is no longer uniform so that the definition of true stress has only limited validation. It can be corrected or extrapolated by analytical equations for numerical applications [13].

$$\frac{d\sigma_t}{d\varepsilon_t} = \sigma_t \tag{2.6}$$

The yield stress is also influenced by the temperature and the strain rate $\dot{\varepsilon}$. Two relevant regimes for HSLA steels can be distinguished:

- For moderate temperatures and strain rates of $10^{-4}s^{-1} \leq \dot{\varepsilon} \leq 10^{3}s^{-1}$, the mechanisms of thermally activated flow are relevant. Under these conditions the ability of dislocations to overcome obstacles depends on the temperature and the strain rate. This results in a temperature softening for increasing temperatures and in a strain rate induced hardening [13, 16]. For strain rates larger than $\dot{\varepsilon} \approx 100\mathrm{s}^{-1}$ temperature and strain rate influences interact because the deformation takes place within adiabatic conditions. This means that the heat generated by the deformation of the material cannot dissipate within the given deformation time and therefore induces a local temperature softening [13].
- If the applied strain rates exceed $\dot{\varepsilon} \geq 10^{3}\mathrm{s}^{-1}$, dislocation damping becomes a relevant mechanism. It induces a viscous material behaviour and also an increase of the yield strength. Thermally activated flow and dislocation damping interact for strain rates in the range of $\dot{\varepsilon} \approx 1000/\mathrm{s}$ [16].

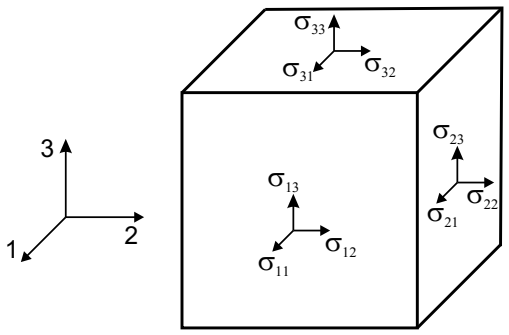

Figure 2.2.: Components of the stress tensor in a volume.

2.1.2. Stress and strain tensor

In the following Einstein notation will be used[1]. The general loading situation of an arbitrary material point is characterised by the stress tensor σ_{ij} [17] (Eq. 2.7).

$$\sigma_{ij} = \begin{bmatrix} \sigma_{11} & \sigma_{12} & \sigma_{13} \\ \sigma_{21} & \sigma_{22} & \sigma_{23} \\ \sigma_{31} & \sigma_{32} & \sigma_{33} \end{bmatrix} \tag{2.7}$$

In classical continuum mechanics moment equilibrium in the material point is assumed so that the stress tensor is symmetric [15]:

$$\sigma_{ij} = \sigma_{ji} \tag{2.8}$$

Consequently, σ_{ij} consists of six independent components. Figure 2.2 shows the components of the stress tensor schematically on a 3D volume. The absolute values of the stress tensor's components depend on the coordinate system. Among all possible coordinate systems the principal stress system is characterised by the fact that the shear stresses vanish. This coordinate system can be found by a determination of the eigenvalues or the principle stresses of the stress tensor[2]:

$$\det(\sigma_{ij} - \sigma\delta_{ij}) = \begin{vmatrix} \sigma_{11} - \sigma & \sigma_{12} & \sigma_{13} \\ \sigma_{21} & \sigma_{22} - \sigma & \sigma_{23} \\ \sigma_{31} & \sigma_{32} & \sigma_{33} - \sigma \end{vmatrix} = 0 \tag{2.9}$$

The resulting cubic equation (Eq. 2.10) contains the three invariants I_i of the stress tensor (Eq. 2.11-2.13). The solutions of this equation are the principal stresses σ_1, σ_2 and σ_3 [17].

$$\sigma^3 - I_1\sigma^2 - I_2\sigma - I_3 = 0 \tag{2.10}$$

$$I_1 = \sigma_{ii} = \sigma_{11} + \sigma_{22} + \sigma_{33} \tag{2.11}$$

$$I_2 = \frac{1}{2}(\sigma_{ij}\sigma_{ij} - \sigma_{ii}\sigma_{jj}) = -(\sigma_{11}\sigma_{22} + \sigma_{22}\sigma_{33} + \sigma_{33}\sigma_{11}) + \sigma_{12}^2 + \sigma_{23}^2 + \sigma_{31}^2 \tag{2.12}$$

[1] Double appearance of an index implies that this term is summarised, e.g. $t_i n_i = \sum_{i=1}^{3} t_i n_i = t_1 n_1 + t_2 n_2 + t_3 n_3$ [17].

[2] δ_{ij} is the Kronecker-Delta defined as: $\delta_{ij} = \begin{cases} 1 & i = j \\ 0 & i \neq j \end{cases}$

$$I_3 = \det[\sigma_{ij}] = \det \begin{vmatrix} \sigma_{11} & \sigma_{12} & \sigma_{13} \\ \sigma_{21} & \sigma_{22} & \sigma_{23} \\ \sigma_{31} & \sigma_{32} & \sigma_{33} \end{vmatrix} \tag{2.13}$$

Plastic deformation in perfect metallic materials can only be induced by a shear deformation of the crystal lattice. Purely hydrostatic stress states, which are equal in all directions and contain no shear components, induce no plasticity in perfect metallic materials without defects. Therefore, the stress tensor is often divided into the hydrostatic stress tensor and the deviatoric stress tensor. The first represents a hydrostatic stress state induced by an average stress σ_h while the latter characterises the deviation from this stress state [17]. The average hydrostatic stress σ_h is defined as:

$$\sigma_h = \frac{1}{3} I_1 = \frac{1}{3}(\sigma_{11} + \sigma_{22} + \sigma_{33}) \tag{2.14}$$

An arbitrary stress tensor σ_{ij} can now be split up introducing the stress deviator tensor s_{ij} [17]:

$$\begin{aligned} \begin{bmatrix} \sigma_{11} & \sigma_{12} & \sigma_{13} \\ \sigma_{21} & \sigma_{22} & \sigma_{23} \\ \sigma_{31} & \sigma_{32} & \sigma_{33} \end{bmatrix} &= \begin{bmatrix} \sigma_h & 0 & 0 \\ 0 & \sigma_h & 0 \\ 0 & 0 & \sigma_h \end{bmatrix} + \begin{bmatrix} \sigma_{11} - \sigma_h & \sigma_{12} & \sigma_{13} \\ \sigma_{21} & \sigma_{22} - \sigma_h & \sigma_{23} \\ \sigma_{31} & \sigma_{32} & \sigma_{33} - \sigma_h \end{bmatrix} \\ \sigma_{ij} &= \frac{1}{3}\sigma_{kk}\delta_{ij} + s_{ij} \end{aligned} \tag{2.15}$$

The invariants of the stress deviator tensor J_i can be defined accordingly [18]:

$$J_1 = s_{ii} = 0 \tag{2.16}$$

$$J_2 = \frac{1}{2} s_{ij} s_{ij} \tag{2.17}$$

$$J_3 = \det(s_{ij}) = \frac{1}{3} s_{ij} s_{jk} s_{ki} \tag{2.18}$$

The counterpart of stress during deformation is strain. The strain tensor ε_{kl} is derived accordingly from the infinitesimal deformations of an arbitrary material cube [17]:

$$\varepsilon_{kl} = \begin{bmatrix} \varepsilon_{11} & \varepsilon_{12} & \varepsilon_{13} \\ \varepsilon_{21} & \varepsilon_{22} & \varepsilon_{23} \\ \varepsilon_{31} & \varepsilon_{32} & \varepsilon_{33} \end{bmatrix} \tag{2.19}$$

Hereby, the components ε_{kk} are the changes in length and the components ε_{kl} can be related to the angular changes γ_{kl} as follows:

$$\varepsilon_{kl} = \frac{1}{2}\gamma_{kl} \tag{2.20}$$

Similar to the stress tensor the strain tensor can be split up in a volumetric and an isochoric part. Principal strains as well as invariants of the strain tensor are defined accordingly [17]. Stress and strain are coupled during elastic deformation by Hooke's law. For a three-dimensional description the elasticity is a fourth order tensor E_{ijkl} with 81 elements out of which 21 are independent [15].

Consequently the general formulation of Hooke's law reads:

$$\sigma_{ij} = E_{ijkl} \cdot \varepsilon_{kl} \tag{2.21}$$

2.1.3. Mathematical description of plasticity

Consider a non-hardening rigid perfectly-plastic material whose constitutive response is schematically shown in Figure 2.3a. The stress only depends on the Young's Modulus E. After the onset of plastification the stress is constant. If the material is unloaded the plastic deformation is preserved. The strain state can therefore be split up in an elastic and plastic part.

$$\varepsilon = \varepsilon^e + \varepsilon^p \tag{2.22}$$

The same is applicable to a hardening material as shown in Fig. 2.3b. Yet, in this case the stress level depends on the previous deformation. Plastic deformation in metals consists of shear deformation in the crystal lattice. The applied stress state determines the amount of slip that takes place in one instance. Hence, under plastic deformation the increment in strain is determined by the stress state, not its absolute value. The history of the stress-strain relation has therefore to be considered to determine the absolute value of plastic strain [19]. Consequently, the description of plastic deformation is formulated in incremental form (Eq. 2.23) or in rate form (Eq. 2.24) [20].

$$\mathrm{d}\varepsilon = d\varepsilon^e + d\varepsilon^p \tag{2.23}$$

$$\dot{\varepsilon} = \dot{\varepsilon}^e + \dot{\varepsilon}^p \tag{2.24}$$

The mathematical description of plastic behaviour consists of three components [20]:

- a yield criterion to assess whether plastic deformation takes place,
- a flow rule to assess the increment of plastic strain,
- a hardening law to assess the current stress level.

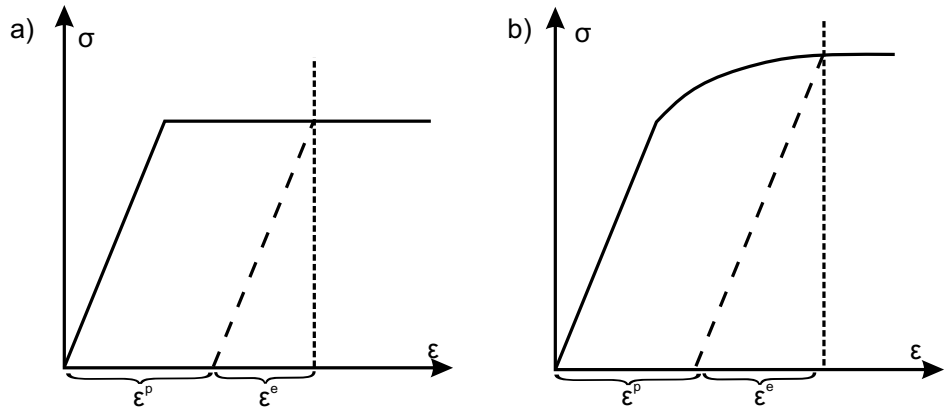

Figure 2.3.: Schematic illustration of the flow behaviour of a) a rigid-perfectly plastic and b) a hardening material.

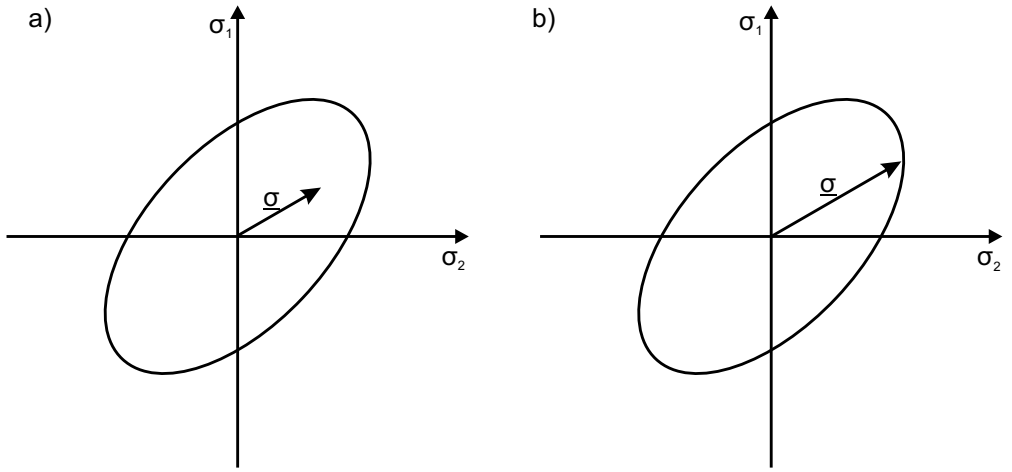

Figure 2.4.: Schematic illustration of a yield surface in a plane stress state a) elastic deformation b) plastic deformation. Figure adapted from [15].

Yield criterion The multiaxial stress state in a component needs to be compared to the result of a uniaxial tensile test to determine whether plastic deformation takes place. Therefore, an equivalent stress σ_e is defined. The essential assumption of a yield criterion is that plastic deformation starts when the equivalent stress is equal to the yield stress [15]. Mathematically, this is usually formulated as a yield potential:

$$\Phi = \sigma_e(\sigma_{ij}) - \sigma_y \leq 0 \tag{2.25}$$

The equivalent stress can also be expressed in dependence of the principal stresses σ_1, σ_2 and σ_3. This enables a graphical representation of the yield criterion in the principal stress space. Fig. 2.4 shows a yield surface and the stress vector for a plane stress state. The yield potential can be displayed as a surface in the principal stress space. The deformation is elastic if the stress vector is within the yield surface. The deformation is plastic if the vector touches the yield surface [15].

The most frequently used yield criterion for ductile metals was formulated by von Mises [21, 22]. His definition of the equivalent stress, which is then used in Eq. 2.25, is based on the second invariant of the stress deviator:

$$\begin{aligned} \sigma_e &= \sqrt{\frac{3}{2} s_{ij} s_{ij}} = \sqrt{3J_2} \\ &= \sqrt{\frac{1}{2}\left[(\sigma_1-\sigma_2)^2+(\sigma_2-\sigma_3)^2+(\sigma_3-\sigma_1)^2\right]} \\ &= \sqrt{\frac{1}{2}\left[(\sigma_{11}-\sigma_{22})^2+(\sigma_{22}-\sigma_{33})^2+(\sigma_{33}-\sigma_{11})^2\right]+3(\sigma_{12}^2+\sigma_{23}^2+\sigma_{31}^2)} \end{aligned} \tag{2.26}$$

This definition of the equivalent stress is also used in combination with other yield potentials or as a simple measure of a stress state. The von Mises yield criterion has proven to be very well applicable to ductile metals [15].

Flow rule The flow rule is used to assess the increment of plastic strain $\dot{\varepsilon}_{ij}^{p}$ which is induced by the current stress state. Flow rules can be derived from thermodynamic or purely mechanical considerations [23]. Detailed derivations are omitted here and can be found in [15,23]. For ductile metals, usually associated flow rules can be applied. They state that the amount of plastic flow is related to the derivation of the yield potential with respect to the stress tensor by a factor $\dot{\lambda}$ (Eq. 2.27). This is based on the principle of maximum dissipation [24].

$$\dot{\varepsilon}_{ij}^{p} = \dot{\lambda} \frac{\partial \Phi}{\partial \sigma_{ij}} \tag{2.27}$$

This implies that in the principal stress space the direction of plastic flow is perpendicular to the yield surface. As a consequence, the yield potential must be convex and differentiable [15].

Hardening law The hardening law accounts for the fact that the yield stress in metals increases during plastic deformation. Consequently, the history of deformation has to be considered. The plastic equivalent strain $\overline{\varepsilon}^{p}$ summarises the effects of the previous plastic deformation. The plastic equivalent strain is defined according to the principle of equivalent work such that the product of equivalent stress and equivalent strain is equal to the product of stress and strain tensor [23]:

$$\sigma_e \dot{\overline{\varepsilon}}^{p} = \sigma_{ij} \dot{\varepsilon}_{ij}^{p} \tag{2.28}$$

By integrating the equivalent plastic strain rate $\dot{\overline{\varepsilon}}^{p}$ the current value of the equivalent plastic strain can be determined:

$$\overline{\varepsilon}^{p} = \int \dot{\overline{\varepsilon}}^{p} dt \tag{2.29}$$

For the von Mises yield criterion this leads to the following definition of the plastic equivalent strain rate [15]:

$$\dot{\overline{\varepsilon}}^{p} = \sqrt{\frac{2}{9}\left[(\dot{\varepsilon}_1^{p} - \dot{\varepsilon}_2^{p})^2 + (\dot{\varepsilon}_1^{p} - \dot{\varepsilon}_3^{p})^2 + (\dot{\varepsilon}_2^{p} - \dot{\varepsilon}_3^{p})^2\right]} \tag{2.30}$$

The yield stress is formulated in dependence of the equivalent plastic strain, the strain rate, and temperature to account for hardening [16]:

$$\sigma_y = f(\overline{\varepsilon}^{p}, \dot{\overline{\varepsilon}}^{p}, T) \tag{2.31}$$

For the use in numerical simulations, the uniaxial flow curve needs to be extrapolated beyond the maximum force. The extrapolation of Hollomon is used frequently and part of the standard DIN ISO 10275 for the assessment of the hardening exponent [13, 16]:

$$\sigma_y(\overline{\varepsilon}^{p}) = k_H (\overline{\varepsilon}^{p})^{n_H} \tag{2.32}$$

The uniform elongation can directly be extracted in this formulation from the hardening exponent n_H while the equation is scaled with a constant k_H. A second, common formulation, which is well suited for steels with discontinuous yielding, is the extrapolation according to Ludwik [13, 16]:

$$\sigma_y(\overline{\varepsilon}^{p}) = \sigma_0 + k_L (\overline{\varepsilon}^{p})^{n_L} \tag{2.33}$$

This formulation considers an additive stress σ_0 in addition to the constant k_L and the hardening factor n_L . A consideration of the dislocation-induced hardening in numerical calculations is possible by using either of the formulations. Additionally, influences of temperature and strain rate need to be considered. This will be further discussed in Section 6.1.1.2.

2.2. Failure behaviour of steels

Structural failure by instant fracture can be caused by two microstructural fracture mechanisms: cleavage and ductile fracture. It is strongly affected by the prevailing stress state. In the following section normalised stress state characteristics are presented along with an introduction of cleavage and ductile fracture. Since the focus of this study is on ductile fracture, its experimental characterisation is subsequently discussed in detail.

2.2.1. Normalised stress state characteristics

The deformation and failure behaviour of steels is strongly affected by the stress state. For an efficient characterisation of the stress state two normalised variables are frequently used: the stress triaxiality η and the Lode angle θ. The stress triaxiality is defined as the ratio of the hydrostatic to the equivalent stress (Eq. 2.34). It therefore implicitly considers I_1 and J_2.

$$\eta = \frac{\sigma_H}{\sigma_e} = \frac{\frac{1}{3}I_1}{\sqrt{3J_2}} \tag{2.34}$$

The stress triaxiality is large for stress states with a high share of hydrostatic stresses. A high triaxiality is induced by notches and sharp cracks. An smooth round tensile bar induces a stress triaxiality of $\eta = 0.33$ before necking while cracked samples reach triaxialities of $\eta \sim 2.0 - 4.0$ [25].

However, the stress triaxiality does not consider the full stress state because J_3 is not included. A full consideration of the stress state can be achieved by introducing the Lode angle. Its meaning is illustrated in Fig. 2.5a. In the principal stress state the deviatoric plane is perpendicular to the hydrostatic axis formed by $\sigma_1 = \sigma_2 = \sigma_3$. For a given hydrostatic stress σ_H, the stress triaxiality is characteristic for a circle around the hydrostatic axis. This circle contains axisymmetric as well as shear-dominated stress states. The Lode angle now allows a definition of the stress state on the triaxiality circle and thereby a precise characterisation of the loading situation. The Lode angle θ is defined as:

$$\cos(3\theta) = \xi = \frac{3\sqrt{3}}{2}\frac{J_3}{J_2^{\frac{3}{2}}} \tag{2.35}$$

$$\theta = \frac{1}{3}\arccos(\xi) \tag{2.36}$$

The Lode angle is normalised for a convenient handling. Bai and Wierzbicki give the definition of

the normalised Lode angle parameter $\overline{\theta}$ as [26]:

$$\overline{\theta} = 1 - \frac{2}{\pi} \arccos \xi \tag{2.37}$$

The normalised Lode angle factor has a range of $-1 \leq \overline{\theta} \leq 1$. Axisymmetric tensile stress states exhibit values of $\overline{\theta} = 1$, axisymmetric pressure states of $\overline{\theta} = -1$, and plane strain and pure shear stress states like torsion of $\overline{\theta} = 0$. The experimental differentiation between $\overline{\theta} = 1$ and $\overline{\theta} = -1$ is difficult, but the difference between both seems to be small for many steel grades. Therefore, symmetric normalised formulations are available as well. An example is the deviatoric shear variable ω defined by Nahshon and Hutchinson [27]:

$$\omega = 1 - \xi^2 \tag{2.38}$$

ω has a range of $0 \leq \omega \leq 1$ and is maximal for plane strain and pure shear stress states and zero for axisymmetric stress states. An illustration of the relation between $\overline{\theta}$ and ω is given in Fig. 2.5b.

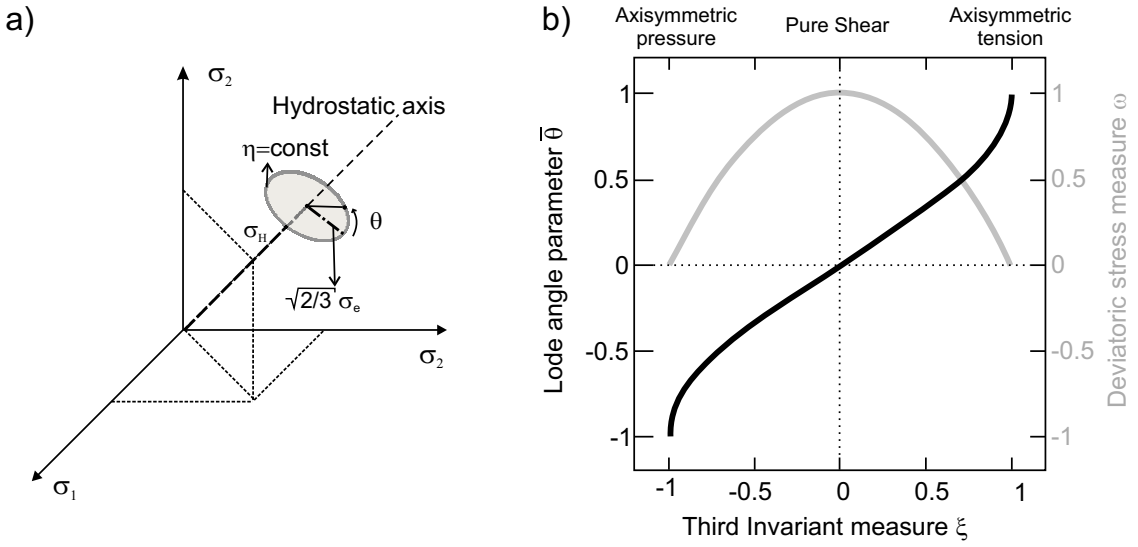

Figure 2.5.: a) Schematic illustration of the Lode angle in principle stress space. b) Illustration of the relation between $\overline{\theta}$ and ω. Figure adapted from [28].

2.2.2. Fracture mechanisms

2.2.2.1. Cleavage fracture

Cleavage fracture is characterised by a separation of atomic bonds along crystallographic planes. It is only observed in steels with a body centred cubic (bcc) crystal lattice and takes place on crystal planes that are the least closely packed [13]. Cleavage fracture is induced within a grain if the maximum normal stress reaches the critical stress for a suitably oriented crystal plane. The initiation of cleavage fracture is favoured by dislocation pile-ups at grain boundaries. These are caused by microplasticity within grains and lead to local stress concentrations that help to overcome the critical stress and induce cleavage. In face centred cubic (fcc) crystal lattices there is a

large number of densely packed sliding planes available so that microplasticity is induced instead of cleavage [9].

Once initiated, cleavage fracture may progress with high velocity and under little energy consumption. The surface of a cleavage fracture is characterised by flat facets formed out of the fracture planes of individual grains as displayed in Fig. 2.6. The fracture surface has a glittering visual appearance because light meeting these fracture planes is reflected unidirectionally for each individual plane. The activation of the cleavage fracture mechanism is favoured by low temperatures and high strain rates in the material [13]. In most cases, brittle behaviour on the macroscopic scale coincides with cleavage fracture and macroscopic ductile failure is induced by microscopic void formation. However, a ductile deformation behaviour of a tensile sample with a pronounced overall plastification may still result in a final cleavage fracture, as recently shown by Golisch [29].

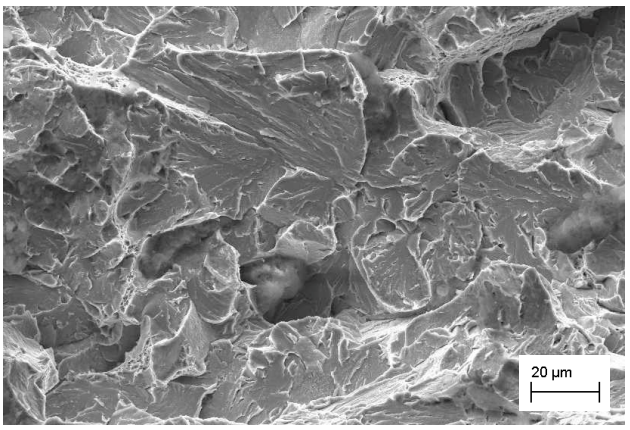

Figure 2.6.: Mixed fracture surface with a large share of cleavage fracture showing the typical planar structure.

2.2.2.2. Ductile failure

Ductile failure is the prevailing fracture mode under plastic deformation. The underlying mechanism is the formation of voids in the material. This process is characterised by a strong interaction of mechanics and microstructure [30]. The process of ductile crack formation is usually subdivided into three stages which are not strictly separated but interact during the deformation process [30]:

- Void nucleation
- Void growth
- Void coalescence

Void nucleation is initiated at second-phase particles like non-metallic inclusions and precipitates. Under large plastic deformation, the yielding behaviour of particles and the surrounding matrix deviates. Voids are formed by either decohesion of matrix and particle or by particle cracking. Void formation begins at larger particles. Void nucleation at Manganese Sulfides (MnS) inclusions can be observed shortly after the onset of plastic deformation in steels, but also other types of large particles may initiate early void nucleation. At smaller inclusions, e.g. carbides, void nucleation is initiated after significant plastic deformation. Void nucleation is influenced by the stress state, the

mechanical properties of the constituents, the strength of the matrix-particle interface, the shape of the particles, and their orientation towards the main loading direction [23, 30].

Voids grow with progressing plastic deformation. This process is dominated by stress triaxiality. A multi-axial stress state favours the volume growth of existing voids contrary to a uniaxial stress state. Consequently, the void growth rate is higher for larger stress triaxialities. The void volume may also decrease in pressure dominated stress states under low triaxialities. The shape of the growing void is strongly influenced by the stress triaxiality as well as the shape of the initiating particles. MnS inclusions, which are elongated due to rolling processes in steel production, may induce large crack-like defects at low deformation if they are oriented disadvantageously to the loading direction [23, 30].

Void coalescence begins when two neighbouring voids have grown near enough to each other to interact. Two basic mechanisms can be distinguished [30]:

- Void impingement
- Void sheeting

Void impingement describes the direct coalescence of two neighbouring voids. This can either happen by an internal necking of the remaining material ligament (Fig. 2.7a) or by the formation of a shear band (Fig. 2.7b) in the remaining material. Void sheeting refers to the coalescence of two voids by the formation of secondary voids on a population of smaller inclusions like carbides (Fig. 2.7c) [23, 30]. A recent study of Barsoum and Faleskog investigated the influence of the stress state on the activation of internal necking or void shearing in structural steels. They found that for high stress triaxialities larger than unity internal necking is the dominant mechanism. It is characterised by large and deep dimples of the fracture surface. For low triaxialities around 0.5 they found smaller, elongated dimples on the fracture surface that were sheared off. At intermediate stress triaxialities both mechanisms seemed to compete [31]. Barsoum and Faleskog suggested that a consideration of the Lode angle is necessary for distinguishing between both mechanisms. Figure 2.8 shows examples of all void coalescence mechanisms. For comprehensive essays on mechanisms and experimental evidence the reader is referred to Garrison and Moody as well as Seidenfuß [23, 30]. Compact overviews can be found in the textbooks of Rösler, Bleck, and Berns [9, 13, 15].

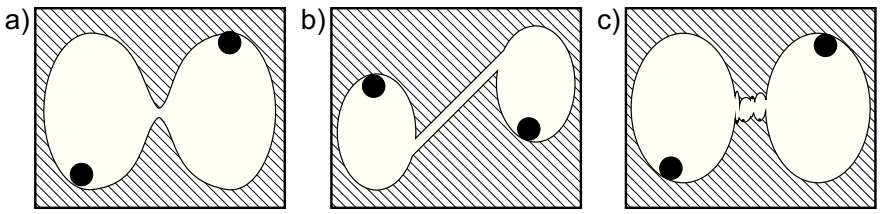

Figure 2.7.: Schematic illustration of void coalescence mechanisms. Void impingement by a) internal necking b) shear band formation and void sheeting by c) formation of secondary voids. Figure adapted from [23].

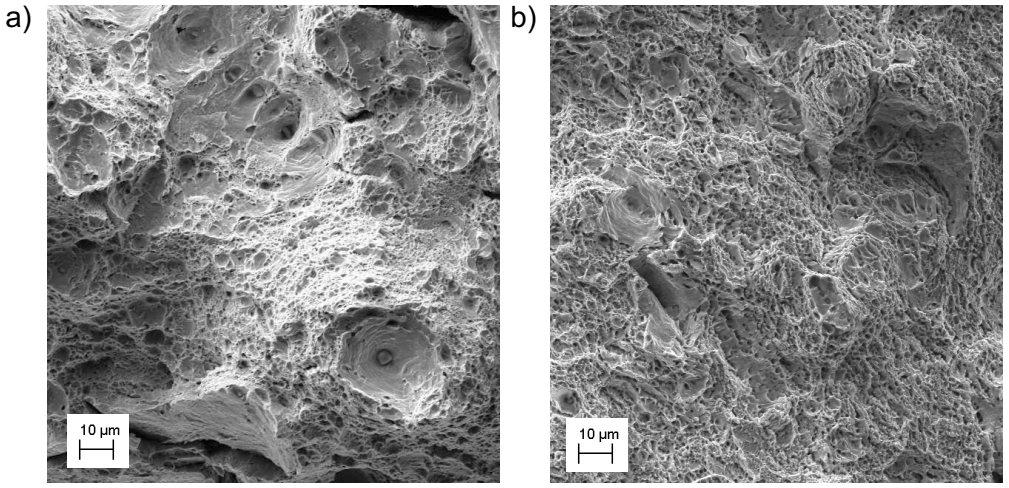

Figure 2.8.: Typical fractography of a) void coalescence by internal necking and the formation of secondary voids in the middle of a notched round bar sample and b) void coalescence by shearing in the shear lips of a notched round bar.

2.2.3. Experimental investigation of ductile damage

The sample types typically used for the characterisation of ductile failure properties are smooth and notched round bars, plane strain specimens, shear specimens, Charpy samples, and fracture mechanics samples like the Single-edge-notched-bending (SENB) samples. They are displayed in Fig. 2.8.

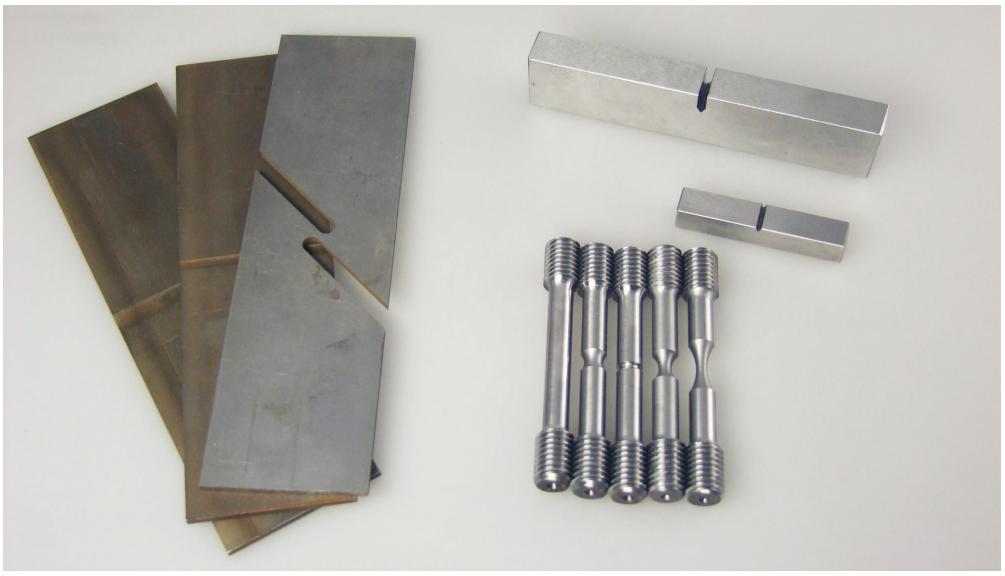

Figure 2.9.: Sample types for characterisation of ductile failure properties (from left to right): Notched plane strain specimens, shear sample, smooth round bar, notched round bars with varying ligament and radius, SENB and Charpy specimens.

Smooth and notched round bars Tensile tests on smooth round bars (SRB) provide information yielding behaviour and the ductility [30]. For all axisymmetric tensile stress states the

normalised Lode angle has values of $\overline{\theta} = 1$ and $\omega = 0$ in the rotation axis. The stress triaxiality in smooth round bars is $\eta = 0.33$ before necking and increases with the formation of a neck [25]. Notched round bars (NRBs) allow a variation of stress triaxiality. The notch in combination with the axisymmetric geometry creates a three-dimensional stress state that limits the plastic deformability and increases stress triaxiality. The formation and growth of voids is accelerated and the ductility is limited compared to unnotched specimens [25, 30].

The typical ductile failure mode of smooth and notched round bars is the cup-cone fracture (Fig. 2.10a). It usually starts in the centre of the specimen and propagates in a zig-zag-mode by changing its path on planes with high shear loading. This results in a crack surface that appears to be normally orientated to the tensile load. When the crack has grown large enough so that the remaining material ligament forms a ring, the stress state in the ligament changes to a two-dimensional stress state and the sample fails by developing shear lips under approximately 45° to the loading direction. In sharply notched specimens there is a competition between the high triaxiality in the central axis of the sample and the plastic strain concentration at the notch ground. Consequently, cracks may also be induced at the notch ground [32, 33].

Plane strain and shear samples Many constructions made of heavy plate materials are rather subjected to plain strain states than to axisymmetric stress states due to the large wall thicknesses. Sample geometries for assessing the corresponding failure behaviour are typically flat with a thickness of 6-3 mm and of a width of 25-50 mm. This induces a plain strain state in the centre of the specimen because the material cannot contract freely in the width direction. Consequently, these samples exhibit normalised Lode angle parameters of $\overline{\theta} = 0$ and $\omega = 1$ in their centre. To study the influence of stress triaxiality, plane strain samples can also be used with notches (e.g. [34]). The failure of these samples typically takes place by slanted fracture, comparable to the shear lips of a NRB (Fig. 2.10b).

Early studies on plane strain samples were performed in the 1970s and found a significantly earlier failure in plane strain than in axisymmetric tension [30, 35]. Since 2004, damage mechanics research focused on failure in this regime. Bao and Wierzbicki performed pioneering work by showing that the failure mode shifted to shear fracture for low triaxialities [36]. In the following

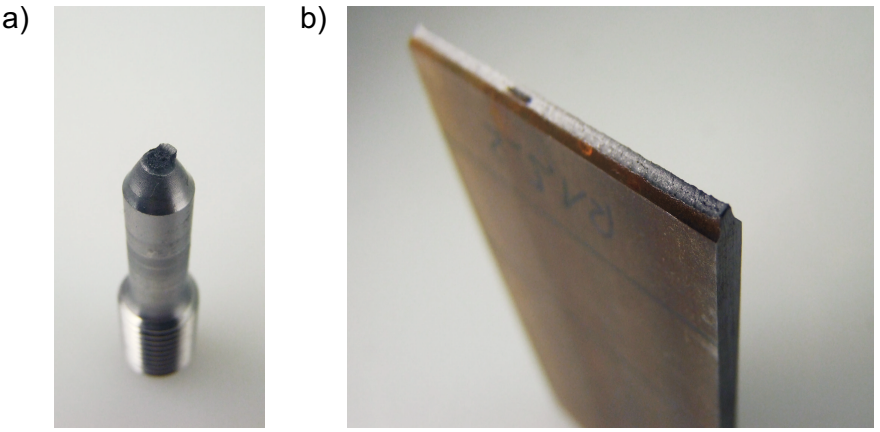

Figure 2.10.: a) Cup-cone fracture surface of a notched round bar b) slanted fracture surface of a notched plane strain specimen.

year, studies of Barsoum and Faleskog and Bai and Wierzbicki confirmed that failure strain is significantly smaller under shear-dominated stress states and in plane strain. These findings can be correlated very well to the Lode angle influence [26, 31].

In addition to plane strain samples, varying concepts for testing under $\overline{\theta} = 0$ are applied. Examples are shear samples that can be used in tensile testing machines, such as the one displayed Fig. 2.8. Moreover, tubes tested under pure torsion [37], and tubes containing a double-notch for testing under a combination of tension and torsion [31] are reported in the literature. The investigations on failure behaviour in the lower triaxiality regime led to the development of new ductile failure models, being presented in Section 2.3.

Fracture mechanics samples Stable ductile crack propagation has to be guaranteed for a safe component operation of cracked structures. This is assessed by fracture mechanics. The two most common sample types are the compact tension specimens (CT) and the single edge notched bending specimens (SENB). Both sample types contain a notch in which a fatigue pre-crack is initiated by cyclic loading. In the final testing it is possible to either determine the load at which unstable, brittle failure is initiated, or to assess the stable crack propagation speed [9, 15]. In the middle of fracture mechanics specimens prevails a plane strain state with high triaxialities of up to $\eta = 3.0$ [25].

Charpy test A minimum operation temperature for components is defined by standards for steel constructions to avoid brittle failure. This transition temperature is determined in Charpy impact toughness tests at varying temperatures. The Charpy tests measure the energy consumed in breaking a notched sample. Additionally, force and deflection can be recorded in an instrumented Charpy test. The failure behaviour of bcc materials will vary from complete cleavage fracture in the lower shelf, to a mixture of brittle and cleavage fracture in the transition region, to complete ductile failure in the upper shelf depending on the testing temperature. The transition region is defined to start at an impact energy of 27J and the associated temperature while the upper shelf is defined by the maximum impact energy [13]. An analytical description of this curve is e.g. provided by Wallin [38].

2.3. Damage mechanics methods

The following section shortly introduces the history of the local approaches of damage mechanics as well as their basic structure. Subsequently, an overview on common models is provided with an intensified discussion of phenomenological and porous plasticity models to be used in this study. An introduction to the implementation of damage mechanics within the Finite Element Method concludes this section.

2.3.1. Introduction and overview

The first engineering discipline to deal with the prediction of brittle and ductile failure was fracture mechanics. The frequent catastrophic failure of the Liberty ships in World War II, induced by weld

flaws and stress concentrations, fostered its establishment in the 1950s [39]. Two general concepts are available:

- Linear-elastic fracture mechanics: Based on initial studies by Griffith [39, 40] the research group of Irwin developed methods to predict whether an initial crack would result in an unstable propagation [39, 41]. The central variable is the stress intensity factor K. It characterises the stress state at a crack tip in dependence of the crack length and the value of the applied remote stress field. It can be compared to the material's resistance which is determined on fracture mechanics samples. Analytical formulas enable the relation between the varying geometries of the component and the sample. This method is only valid without significant plastic deformation.
- Elastic-plastic fracture mechanics: Since many components experience plastic deformation, in the 1970s these approaches were developed. The crack tip opening displacement (CTOD) by Wells [39,42] makes use of the blunting of a sharp crack to describe the plastic influence. The J integral developed by Rice relates to the dissipated energy [39,43]. Both methods can predict ductile stable crack growth.

The methods of fracture mechanics are nowadays mature and widely applied, a comprehensive overview can be found in [39]. However, there are some essential limitations in the application fracture mechanics:

- Only an assessment of the load-bearing capacity of cracked structures is possible. Flawless structures or material with micro-defects cannot be characterised.
- A prediction of crack initiation is not possible.
- The use of correlation functions and global quantities like the remote stress field is very well suited for known loading situations and the transfer between standard application situations and standard sample geometries. The applicability to complex geometries or loading situations is limited.

Contrary to the global approach of fracture mechanics, the methods of damage mechanics aim at a local description of failure initiation and development. This is achieved by the consideration of micromechanical processes with the help of continuum mechanics. Pioneering work was performed in the late 1970s by McClintock as well and Rice and Tracey [30]. McClintock provided descriptions for the growth rate of holes based on analytical studies and found a strong dependence on stress triaxiality and the hardening properties of the material [44]. These findings were confirmed by investigations of Rice and Tracey, who applied variational principles. They concluded that a "moderate and high stress triaxiality leads to an amplification of relative void growth rates over imposed strain rates by a factor depending exponentially on the mean normal stress" [45]. A comparison of both studies to experimental investigations on NRB by Hancock and Mackenzie showed that the influence of stress triaxiality was well captured and that the failure strain of NRBs could be described in exponential dependence of stress triaxiality [46].

Today a large variety of damage mechanics models is available. Figure 2.11 gives an overview on the most important model types.

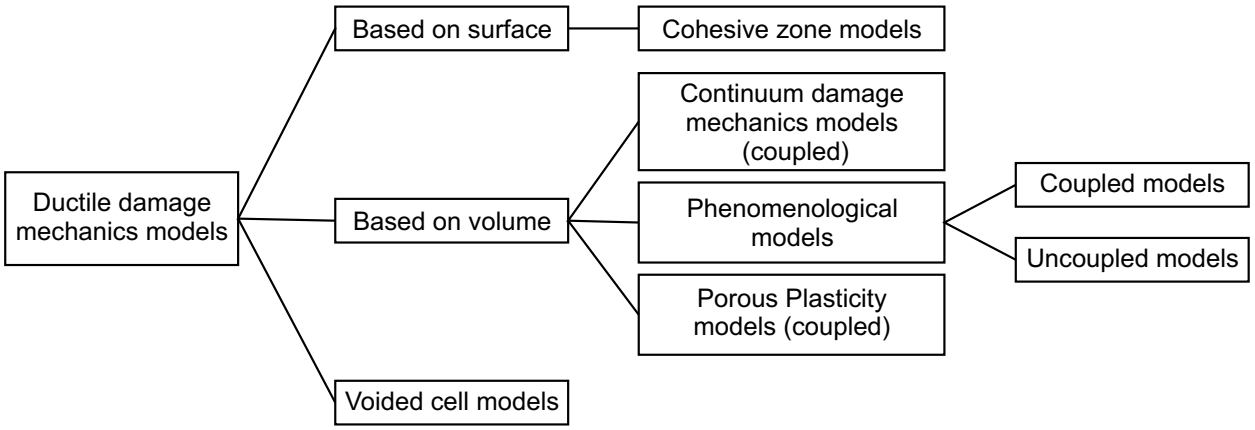

Figure 2.11.: Overview on ductile damage mechanics models, partly adapted from [47]

Crack growth can be modelled effectively by the surface-based cohesive zone models. However, their application is limited to situations where the crack path is known in advance. Voided cell models consist of a finite element model that contains a void or an array of voids. Periodic boundary conditions are required in these models. This requirement can often be simplified to keeping the cell walls straight when assuming a regular void distribution. Voided cell models play an important role in the research on ductile damage mechanisms as they allow systematic studies of the influencing parameters (e.g. [48–50]). They are frequently used to calibrate the parameters of homogenised volume-based damage mechanics models (e.g. [51–53]). Additionally, they can help to improve the formulations of the homogenised models (e.g. [54, 55]).

Volume-based models characterise the constitutive behaviour of a local material point in dependence of the stress state, the yield properties of the material and a damage variable D. The local failure of a material point and thereby the initiation and progression of a crack is described as a result of progressing local damage in the material. Volume based models can be classified into:

- Uncoupled models: The damage variable increases under ongoing deformation, but has no effect on the mechanical response of the specimens. Damage softening is ignored.
- Coupled models: The material's stiffness and yield strength decrease with increasing damage.

Table 2.1 gives an overview on the related formulations assuming failure of a local material point after a critical amount of damage D_{crit}.

Table 2.1.: Examples of model formulations for coupled and uncoupled models

Model formulation	Yield potential	Damage evolution	Failure definition
Uncoupled	$\Phi = \sigma_e - \sigma_y \leq 0$	$D = f(\varepsilon_{ij}, \dot{\varepsilon}_{ij}, T...)$	$D \geq D_{crit}$
Coupled	$\Phi = \sigma_e - \sigma_y(1-D) \leq 0$	$D = f(\varepsilon_{ij}, \dot{\varepsilon}_{ij}, T...)$	$D \geq D_{crit}$

Three main types of volume-based damage mechanics models can be distinguished: Continuum damage mechanics models, phenomenological models, and porous plasticity models.

Continuum damage mechanics models The framework of continuum damage mechanics (CDM) models was established by Lemaitre [56]. The damage variable D is defined as the "surface density of microcracks and intersections of microvoids" in the considered plane [57]. Lemaitre introduced an effective stress to account for the loads acting on the undamaged material:

$$\tilde{\sigma}_{ij} = \frac{\sigma_{ij}}{(1-D)} \tag{2.39}$$

One of the strengths of this model group is that due to the thermodynamic consistent formulation it can be extended for anisotropic damage and damage closure as well as brittle and fatigue damage [57]. A correlation of the damage variable D to microstructural features is however not possible since the model derivation is performed solely on macroscopic, homogenised considerations. Comprehensive overviews on this model type and its various extensions can be found in [57, 58].

Phenomenological models Phenomenological models do not consider micromechanical or thermodynamic theories but try to reproduce broad sets of data accurately by a suitable mathematical description. One of the first phenomenological models for ductile failure was formulated by Johnson and Cook [59, 60]. They performed tests on iron, copper and steel materials under elevated strain rates. NRB and torsion samples were considered. They defined an empirical definition for the failure strain:

$$\varepsilon_f = [D_1 + D_2 \exp(D_3 \eta)] [1 + D_4 \ln \dot{\varepsilon}] [1 + D_5 T] \tag{2.40}$$

Consistent with the findings of Hancock and Mackenzie [46] an exponential dependence of the failure strain from stress triaxiality was found (Fig. 2.12a). Additionally, a formulation for the flow curve in dependence of strain, strain rate and temperature T was provided. The damage evolution was calculated in an incremental form depending on the current strain increment $\Delta\varepsilon$:

$$D = \sum \frac{\Delta\varepsilon}{\varepsilon_f} \tag{2.41}$$

Final failure, resulting in element deletion, was assumed to happen at $D = 1$. The Johnson-Cook (JC) model has successfully been applied in a large range of applications and may also be used without the formulations for strain rate and temperature dependence.

Recent investigations by Bao and Wierzbicki revealed that the exponential dependence of the failure strain does not hold true anymore in the low triaxiality range [36]. Bai and Wierzbicki could show that for a suitable description of the failure behaviour the Lode angle factor has to be considered [26]. Similar to Johnson and Cook they provided a modular formulation of their damage model. A flow curve formulation in dependence of the stress state was given employing the constants c_η, c_θ^s, c_θ^{ax} , η_0, m, and the Lode angle dependent function γ:

$$\sigma_y = \sigma(\overline{\varepsilon}^p) \cdot [1 - c_\eta(\eta - \eta_0)] \left[c_\theta^s + (c_\theta^{ax} - c_\theta^s) \left(\gamma - \frac{\gamma^{m+1}}{m+1} \right) \right] \tag{2.42}$$

Additionally the failure strain was defined in the space of stress triaxiality and Lode angle factor

in dependence of six factors D_i (Eq. 2.43). It forms a failure locus in the $\eta - \overline{\theta}$-space (Fig. 2.12b).

$$\varepsilon_f = \left[\frac{1}{2}(D_1 e^{-D_2\eta} + D_5 e^{-D_6\eta}) - D_3 e^{-D_4\eta}\right]\overline{\theta}^2 + \frac{1}{2}(D_1 e^{-D_2\eta} - D_5 e^{-D_6\eta})\overline{\theta} + D_3 e^{-D_4\eta} \quad (2.43)$$

A symmetric formulation of this failure strain locus was also given. It does not differentiate between pressure and tensile axisymmetric stress states:

$$\varepsilon_f = \left[D_1 e^{-D_2\eta} - D_3 e^{-D_4\eta}\right]\overline{\theta}^2 + D_3 e^{-D_4\eta} \quad (2.44)$$

The JC and BW models are both uncoupled models. However, in some modern multiphase steel materials, e.g. dual phase steels, damage is induced early on brittle secondary phases. Therefore, uncoupled formulations might not be sufficient. Lian et al. developed a coupled modification of the Bai-Wierzbicki model (BW), the modified Bai-Wierzbicki model (MBW) [47, 61]. It employs the same flow rule as the BW model but uses Eq. 2.43 as an initiation strain ε_i instead of the failure strain ε_f. After damage initiation the damage is characterised by an evolution law until final failure at D_{crit} and $\overline{\varepsilon}^p_f$ (Eq. 2.45). The damage evolution is hereby defined by the current yield strength, the characteristic length L and the fracture energy G_f.

$$D = \begin{cases} 0 & \overline{\varepsilon}^p \leq \varepsilon_i \\ \int \frac{\sigma_y L}{2G_f} d\overline{\varepsilon}^p & \varepsilon_i < \overline{\varepsilon}^p < \overline{\varepsilon}^p_f \\ D_{crit} & \overline{\varepsilon}^p \geq \overline{\varepsilon}^p_f \end{cases} \quad (2.45)$$

The main advantage of phenomenological models is that they can be applied very effectively due to their straightforward formulation. This holds especially true for uncoupled models. However, the transferability to other loading situations, geometries and materials cannot be taken for granted and needs to be verified for each application field because no thermodynamic or micromechanical considerations are included [23].

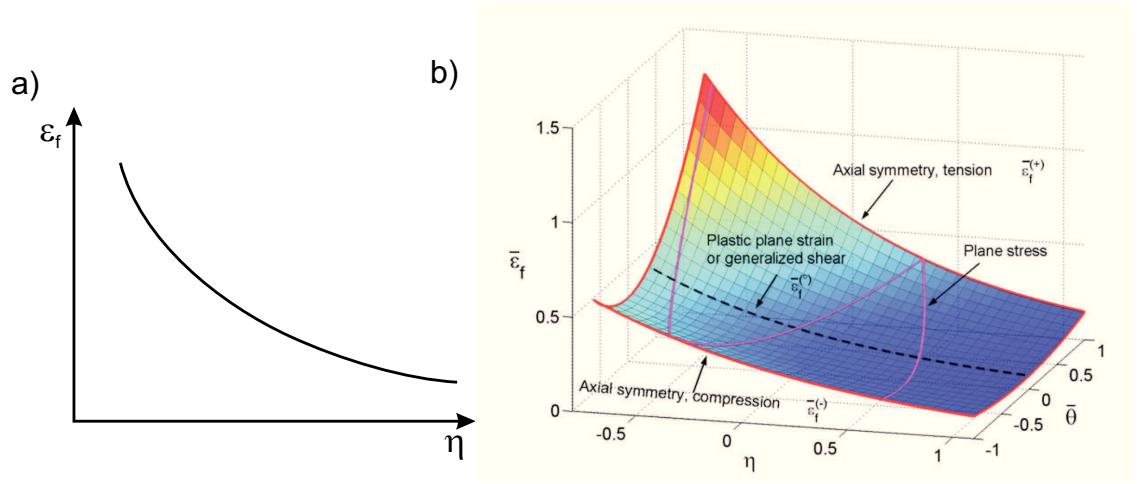

Figure 2.12.: Schematic illustration of a) the JC failure strain definition and b) the BW failure strain definition (taken from [26]).

Porous plasticity models Porous plasticity models are based on micromechanical considerations about the behaviour of voids in remote stress fields. They were derived from these by the application of homogenisation methods. This concept was firstly proposed by Gurson in 1977 [62]. He investigated the behaviour of a spherical void in a spherical matrix and derived a homogenised description of a yield potential that incorporated an idealised void volume fraction f as damage variable (Eq. 2.46).

$$\Phi = \left(\frac{\sigma_e}{\sigma_y}\right)^2 + 2f\cosh\left(\frac{3}{2}\frac{\sigma_H}{\sigma_y}\right) - 1 - f^2 \leq 0 \tag{2.46}$$

From this consideration it follows that the evolution of the void volume fraction f is dependent on the volumetric plastic strains $\dot{\varepsilon}^p_{kk}$ [23]:

$$\dot{f} = (1-f)\dot{\varepsilon}^p_{kk} \tag{2.47}$$

The initial form of the Gurson model proved to be not directly applicable since void coalescence was not considered. Phenomenological extensions by Tvergaard and Needleman [54, 63] formed the today most widely used form of this damage mechanics model, the Gurson-Tvergaard-Needleman (GTN) model. It will be used within this thesis and is presented in detail in the following section.

The Gurson model only considers spherical voids. Based on Gurson's studies Gologanu, Leblond and Devaux formulated a model that considers also ellipsoidal void shapes, see Benzerga and Leblond for an overview [25]. Another porous plasticity model was provided by Rousselier based on thermodynamic and micromechanical considerations, see [23] for details. The main advantage of porous plasticity models is their micromechanical foundation. This supports a transferability to other loading situations and geometries. However, in their derivation significant simplifications have to be made to obtain homogenised analytical descriptions. Therefore, the transferability has to be checked with caution [23].

Porous plasticity models and most other damage mechanics models provide modified yield potentials and internal state variables, such as damage, which are given in incremental formulations. The integration of the stress and strain increments is performed within the framework described in section 2.1. It can be performed with explicit or implicit numerical procedures. Most plasticity and damage mechanics models are integrated implicitly by the radial-return algorithm. For a detailed description the reader is referred to [20, 24]. For the GTN models this radial return algorithm was implemented by Aravas [64], whose formulations are used within this thesis.

2.3.2. The GTN model

In this study the GTN model is applied in its basic and an extended version. It is one of the most widely used damage mechanics models and has also been incorporated in several commercial finite element codes. In the following, the model's structure, its calibration and properties will be discussed.

Model structure In 1981 Tvergaard investigated the capability of the Gurson model to predict shear band formation in comparison to voided cell models [63]. He introduced three empirical

fitting parameters q_i into the yield potential (Eq. 2.48) with which he could calibrate the Gurson model so that the results of the cell model studies were met well. In this formulation void coalescence was still not being considered. Tvergaard and Needleman therefore suggested the introduction of an effective void volume fraction f^* (Eq. 2.50). Its growth is accelerated by a factor κ after reaching a critical void volume fraction f_c to account for void coalescence and material failure [54]. Additionally, Tvergaard and Needleman used a nucleation law for secondary inclusions from Chu and Needleman [65] besides the void growth formulation (Eq. 2.49). This nucleation law is formulated as a Gaussian distribution function in dependence of the volume fraction of possible nucleation sites f_N, the nucleation strain ε_N and the standard deviation S_N. These equations form the today well-known and frequently used GTN-Model. It is implemented in commercial FE-packages and therefore usable in engineering practice:

$$\Phi = \left(\frac{\sigma_e}{\sigma_y}\right)^2 + 2f^* q_1 \cosh\left(\frac{3}{2} q_2 \frac{\sigma_H}{\sigma_y}\right) - (1 + q_3 f^{*2}) \leq 0 \tag{2.48}$$

$$\dot{f} = (1-f)\dot{\varepsilon}^p_{kk} + \frac{f_N}{S_N\sqrt{2\pi}} \exp\left[-\frac{1}{2}\left(\frac{\overline{\varepsilon}^p - \varepsilon_N}{S_N}\right)^2\right] \dot{\overline{\varepsilon}}^p \tag{2.49}$$

$$f^*(f) = \begin{cases} f & f \leq f_c \\ f_c + \kappa(f - f_c) & f > f_c \end{cases} \tag{2.50}$$

When the effective void volume fraction f^*_u is reached the element is assumed to have failed and the stress carrying capacity is set to zero. By setting $\Phi = 0$ and assuming $q_3 = q_1^2$ in Eq. 2.48 it can be found that:

$$f^*_u = \frac{1}{q_1} \tag{2.51}$$

The value of f^*_u corresponds to a final void volume fraction of f_F. The phenomenological void coalescence model by Tvergaard and Needleman (Eq. 2.50) can either be controlled by prescribing the acceleration factor κ or the final void volume fraction f_F. Both interact in Eq. 2.52. Figure 2.13a shows a graphical representation of the evolution of f^*.

$$\kappa = \frac{f^*_u - f_c}{f_F - f_c} \tag{2.52}$$

The GTN yield potential forms a spheroid in the principal stress space (Fig. 2.13b) that grows and shrinks corresponding to the current value of f.

The GTN model in total has nine parameters to be calibrated that can be clustered as follows [67]:

- The initial void volume fraction f_0: Within the GTN model, it is assumed that a certain amount of voids is present at the beginning of plastic deformation. The initial void volume fraction f_0 represents the starting value of the damage variable f.
- The void nucleation parameters f_N, ε_N, S_N: These three parameters control the nucleation of secondary voids according to the Gaussian distribution and interact within the distribution function.
- The void coalescence parameters f_c, κ: Both parameters control the accelerated void growth to account for void coalescence and failure.

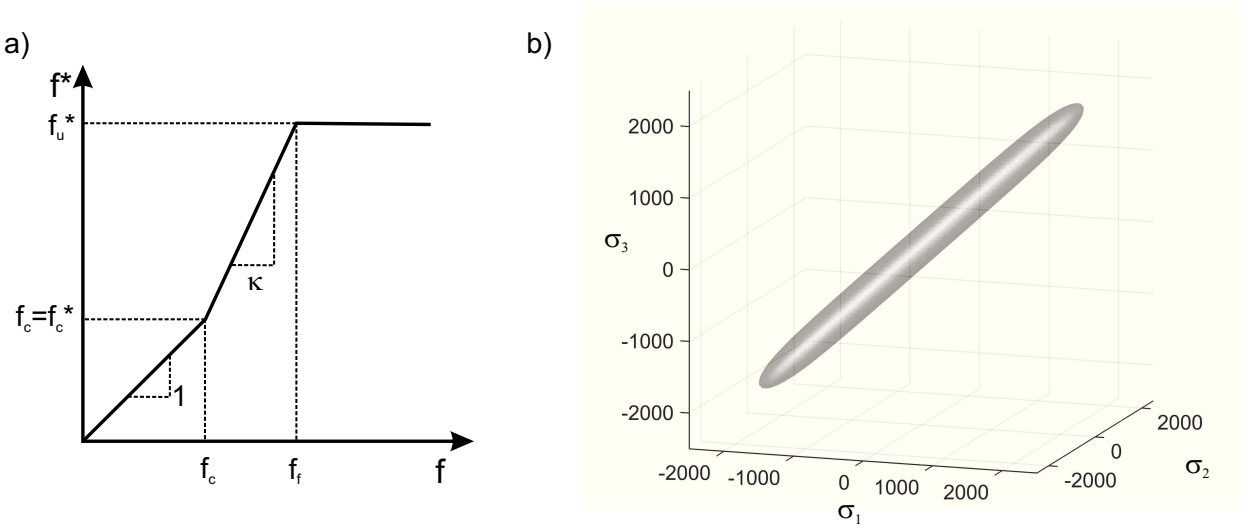

Figure 2.13.: a) Schematic illustration of the evolution of f^* in dependence of f. Figure adapted from [66]. b) Yield potential of the GTN model in principal stress space.

– The empirical fitting parameters q_1, q_2, q_3: The fitting parameters are directly incorporated in the yield potential. Tvergaard initially proposed values of $q_1 = 1.5$ and $q_2 = 1.0$ as well as the relation $q_3 = q_1^2$, which will be used in the following.

Additionally, the GTN model exhibits a pronounced mesh size dependence. In reality the damage state of a certain point interacts with the surrounding material. In experimental investigations it can be seen that ductile damage localizes during the failure process into a zone whose width is typical for the material and represents a characteristic length. This is different in the common formulations of damage models, including the GTN model. Within these so-called local formulations stress and strain in one material point are only influenced by the local state variables, e.g. damage, of this material point. The states of the neighbouring material points are not considered. Consequently, after the onset of damage-induced softening the deformation localizes in only one row of elements since the surrounding elements are then stronger and unload.

From this point on the FE solution is mesh-dependent because the dissipated energy depends on the element volume. The smaller the element size the smaller the dissipated energy. From a mathematical point of view the correlated mechanical boundary value problem, which belongs to the class of elliptic partial differential equations, loses its ellipticity and becomes ill-posed. As a result, there is no more unique solution to the differential equations. This means that the solution depends on the mesh size [23, 68].

There are two solutions to this problem. The first one is the re-formulation of damage mechanics models and their implementation into the FEM such that they are able to directly consider the characteristic length and the damage state of the environment. Such non-local models are currently under intensive research. Mostly, a damage gradient formulation is introduced. Such formulations for the GTN model are for example given by Reusch [68] and Linse et al. [69]. The implementation of these models requires considerable expertise and the programming of user-defined element formulations. When applying a non-local Rousselier model to large-scaled samples, Seidenfuß also met significant problems since the formulation of the non-local model was computationally

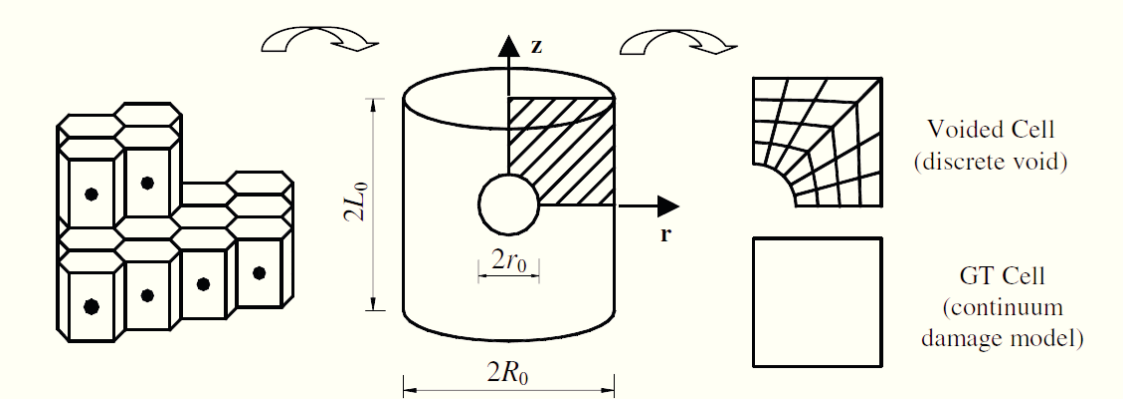

Figure 2.14.: Schematic illustration of axisymmetric voided and continuous cell model simulations. Figure from [50].

too expensive for a three-dimensional representation of the samples [23].

The second, pragmatic solution is to keep the mesh size constant in the zones of damage localization during the simulations. This means that the mesh size then represents the characteristic length. It has to be calibrated as an additional parameter. Seidenfuß gave an overview on studies showing that this approach delivers reliable engineering solutions for many applications [23]. He summarised that the usually calibrated mesh sizes are in the order of 0.1 mm. This approach will be pursued within this thesis.

Parameter calibration For the calibration of the GTN model parameters two main strategies can be found in the literature. The first approach is to compare the simulation of voided cell models to the results of alike but voidless cell models containing the GTN model (Fig. 2.14). This approach is often used to investigate the general structure of the GTN model. Cell model studies of Tvergaard led to the introduction of the empirical fitting parameters [63]. Koplik and Needleman investigated at which point voided cell models subjected to triaxial loads shifted into a uniaxial straining response and compared this point with the outcome of GTN cell model studies to define a coalescence criterion [48]. Voided cell models can be built based on different assumed void arrangements. Hexagonal arrangements enable axisymmetric idealisations (Fig.2.14).

Kuna and Sun investigated the results of the selected idealisation in comparison of GTN simulations and voided cell models. They concluded that cubic, hexagonal, and axisymmetric void arrangements lead to reasonable agreement. Axisymmetric arrangements hereby yielded slightly softer responses [49, 70].

Faleskog et al. and West et al. calibrated the empirical fitting parameters on cell model simulations and reported a slight dependence of this parameter on the stress triaxiality [51, 53]. Kim et al. found a similar effect for f_c [50]. Recent studies of Tvergaard investigated the mechanisms of shear-dominated failure [71]. To sum up, this approach is used to investigate the general structure of the model and its capability to capture certain failure modes. Due to the inherent idealisations its suitability for the calibration of actual material parameters is limited [23].

The second calibration strategy is the comparison of experimental tests with varying geometries to the corresponding simulations with a subsequent iterative parameter fitting. This strategy is

regularly applied [25,72]. The magnitude of f_0 is hereby often defined as the content of dominating inclusions [73]. Since the GTN model strongly idealises the micromechanical processes, a direct transfer of such metallographically determined values may be limited [72,74]. For HSLA steels the content of MnS inclusions is often considered as initial void volume fraction f_0 while the content of secondary carbides may be chosen for f_N [23, 73, 75].

The remaining parameters can be determined in comparison with tests of varying geometries to cover different stress states [73]. Tests on smooth and notched round bars are regularly used to cover the influence of stress triaxiality (e.g. [72, 74]). The internal length parameter, respectively the mesh size, can be calibrated on fracture mechanics samples since the stable crack growth enables an adaption of the simulation results to the crack propagation energy [76].

Model properties and applications One of the strengths of the GTN model is its micromechanical basis although this is limited by the phenomenological modifications. As the general model structure is, in contrast to purely phenomenological models, based on a general consideration of void mechanics, a transferability to other loading situations can be assumed within certain limits.

One of the weaknesses is the large number of parameters and the resulting non-uniqueness of the calibrated parameter sets. Zhang proved this non-uniqueness in an investigation on smooth, notched and centre cracked tensile specimens [74]. In addition, he investigated whether the specimen types could be modelled equivalently well by either considering pure void growth in the GTN model or pure void nucleation of secondary voids. He found that both approaches could describe the simulation of smooth round bars equivalently good with different parameter sets [74]. Bonora demonstrated the non-uniqueness in a sensitivity study on smooth round bars. He also concluded that the consideration of multiaxial stress states is necessary for a calibration of the GTN model [72]. Springmann and Kuna used a numerical optimisation algorithm to identify optimised parameter sets. The algorithm could identify global minima of the error function for the flow curve and the hardening exponent that can consequently be determined uniquely. For all other parameters only local minima of the error function were found; this proves the non-uniqueness of the parameter selection [77]. A European numerical round robin performed in 2001 also showed that parameter sets determined from the same results may vary [78]. Besides such systematic studies, the sensitivity of the GTN model towards the impact of individual parameters was mostly investigated within studies directed at other purposes. Xue et al., Tu et al. and Hütter et al. investigated for example the impact of individual parameters on modified versions of the GTN model to explore the required values [79–81].

Besides the drawback of a complicated parameter calibration the GTN model is one of the most often applicated damage mechanics models. As Steglich summarises, the application of the GTN model to smooth round bars, notched round bars and fracture mechanics samples is nowadays a standard procedure [73]. Lesser studies are available for the simulation of Charpy tests. They mostly focused on the simulation of the ductile-brittle transition behaviour by the combination of the GTN model with a brittle fracture criterion (e.g. [82–89]) and did not investigate the sensitivity towards the GTN parameter selection. In this study GTN-based Charpy simulations are used. Therefore, the sensitivity will be investigated.

2.3.3. Implementation of damage mechanics models into the Finite Element Method

Damage mechanics models provide local descriptions of the material behaviour. Therefore, they have to be used in a framework which assesses the global behaviour of a construction. This is the Finite Element Method. This method is nowadays the standard application for manifold mechanical problems. It is available in a large variety of commercial programs; see Zienkiewicz for a thorough overview on the method [90].

Mechanical problems consist of systems of partial differential equations that have to be solved for the whole region of the problem. The central approach of the FEM is to subdivide the region into finite elements. Local solution functions are defined for each element. The solution is only known at the nodes of the element and is interpolated in between. The local solution functions are reassembled in a large matrix system of all nodes which is finally solved. The main equation of a FE-system is formed by the stiffness matrix $\overline{\overline{K}}$, which is assembled from the individual element stiffnesses, the displacement vector $\overline{u}$ and the vector of the external forces $\overline{F}$ [20]:

$$\overline{\overline{K}} \cdot \overline{u} = \overline{F} \tag{2.53}$$

FE systems are solved for the displacements u. The most straightforward way for solving Eq. 2.53 is an inversion of the stiffness matrix. However, this is only possible as long as the stiffness matrix is independent of the deformation. For nonlinear material behaviour this is not the case. For plastic material behaviour the equilibrium has to be formulated in increments to allow for a consideration of the history dependence. Consequently, Eq. 2.53 may be reformulated as a residuum [20]:

$$\Psi_{n+1} = \overline{\overline{K}}_{n+1}(\overline{u}_{n+1}) \cdot \overline{u}_{n+1} - \overline{F}_{n+1} = 0 \tag{2.54}$$

This residuum can then be solved by implicit iteration algorithms. Most frequently used is the Newton-Raphson-Algorithm. It finds the solution in an iterative procedure by forming a tangent stiffness matrix to the current load point (Fig. 2.15a). One weakness of the Newton-Raphson-Algorithm is that it cannot converge if the tangent stiffness matrix is horizontal (Fig. 2.15b). This happens when the global system experiences softening. An alternative, which is able to follow softening behaviour, is the arc-length method. It is also referred to as Riks algorithm. It defines an additional constraint for tracking the solution through softening behaviour and solves the resulting system for the displacement and the corresponding load factor simultaneously. Details can be found in [91]. Implicit solution algorithms are unconditionally stable and are used for static problems [20].

For elastoplastic or damage mechanics models the stiffness matrix is dependent on the amount of plastic deformation. The residual formulation is then not formulated in dependence of the product $\overline{\overline{K}} \cdot \overline{u}$ but in dependence of an internal force vector representing the internal structural resistance:

$$\Psi_{n+1} = \overline{F}^{int}_{n+1} - \overline{F}_{n+1} = 0 \tag{2.55}$$

This internal force vector is the central point of interaction between the material constitutive response and the structural response. Within the course of a FE computation the global structural

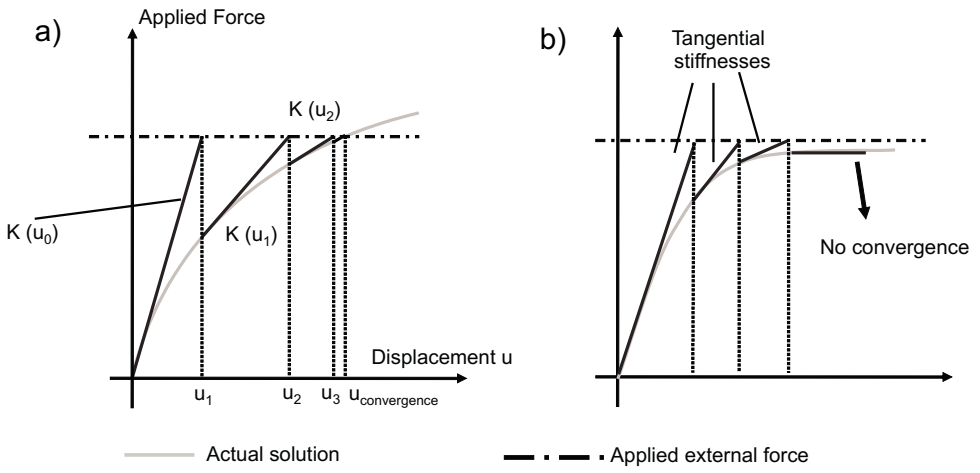

Figure 2.15.: a) Schematic illustration of the Newton-Raphson-Algorithm in FEM and b) the corresponding convergence difficulties for horizontal tangent stiffness matrices. Figure adapted from [20].

response is solved first and an overall strain increment $\Delta\varepsilon$ is determined. This is used in conjunction with the current stress and strain state as an input for the integration of the material subroutines [24]. In the commercial FEM program Abaqus that is used in this thesis this is performed in the user defined subroutine UMAT for implicit integration.

For a dynamic system the overall formulation of a FE system is similar but includes additionally the mass matrix M and the damping matrix D.

$$\overline{\overline{M}} \cdot \ddot{\overline{u}} + \overline{\overline{D}} \cdot \dot{\overline{u}} + \overline{\overline{K}} \cdot \overline{u} = \overline{F} \tag{2.56}$$

Due to the more complicated structure of the dynamic formulation, which includes time-dependent variables, implicit solution procedures cannot be applied. The time dependency may be solved by an explicit integration of acceleration and velocities by truncated Taylor series expansions:

$$\overline{u}_{n+1} = \overline{u}_n + \Delta t \dot{\overline{u}}_n + \frac{1}{2}\Delta t \ddot{\overline{u}}_n \tag{2.57}$$

As mass and damping matrices are usually diagonalised, Eq. 2.56 can be easily decoupled by inserting such formulations and the system becomes solvable, see [90, 92] for details. However, the application of such procedures is only conditionally stable. Consequently, only small time steps are admissible. Explicit solution algorithms are preferably used for dynamic procedures. Similar to implicit systems, the integration of an elastoplastic constitutive behaviour is performed by considering an internal force vector. The respective determination of the plastic reaction is performed in a VUMAT subroutine [24].

Damage mechanics models shall be used for the failure prediction of HSLA steels in this thesis. An overview existing studies for this purpose is given in the following.

2.4. Structural failure prediction for HSLA steels

HSLA steels were developed from the 1960s on. Major developments were the introduction of microalloying concepts and improved production processes, e.g. in the field of secondary metallurgy. By these measures the inclusion content could be significantly reduced [93]. HSLA steels are characterised by an excellent strength and toughness. They are available nowadays as commercial grades with yield strengths up to 1300 MPa. For structural steels they are classified until grade S960Q with a yield strength of 960 MPa in EN 10025. In pressure vessel design the strongest allowable grade of EN10028 is P690Q with a yield strength of 690 MPa. Low strength HSLA steels usually have a ferritic-pearlitic microstructure. High strength steels have mostly bainitic or martensitic microstructures. HSLA steels may be produced by normalisation, thermomechanical rolling or quench and temper processes. See [9, 93] for an overview.

High strength steels are more prone to failure after small deformation than low strength steels. Therefore, the introduction of these grades was accompanied by intensive studies on their safe application. Many of these were performed at RWTH Aachen University. The initial studies focused on the prevention of brittle failure by applying fracture mechanics methods. They defined toughness requirements for a safe application. For high strength steels ductile crack initiation may occur before plastic collapse. Therefore, complementary investigations on the prediction of ductile crack initiation have been performed as well. These studies partially form the base of today's regulations in the toughness assessment of the Eurocode 3 for structural steel work, EN 1993, and the pressure vessel design code EN 13445. Since the concept of this study is based on these findings, a short overview is given in the following. An overview of the current use of damage mechanics models for burst pressure prediction concludes this chapter.

2.4.1. Previous internal studies

2.4.1.1. Studies on the resistance to brittle failure

The structural safety of high strength steels was investigated at the Department of Ferrous Metallurgy in fracture mechanics tests (e.g. SENB tests), Charpy tests and tensile tests on smooth round bars (SRB) and NRB. The validation was performed on component-like pre-cracked wide-plate samples (WP) at a 12 MN tensile machine at the Department of Ferrous Metallurgy. An example is shown in Fig. 2.16. Such wide-plates usually have a total sample length of approximately 2.5 m, including the clamping section. The relevant length with the testing cross section is about 0.5 m. The sample width is 200 mm - 300 mm and the thickness varies typically from 30 mm to 80 mm. Fatigue pre-cracks can be added. The final test is performed as a tension test. The sample can be cooled by copper plates so that brittle failure can be induced.

An overview on selected studies is given in Table 2.2. Early studies of Halim, Hubo and Liessem [32, 95, 96] showed that fracture mechanics tests predicted conservative results for the component failure. Partially, the results were even considered to be overconservative. A correlation of the results of fracture mechanics transition temperatures and Charpy transition temperatures was determined that allows a simplified toughness assessment, as for example today included in the

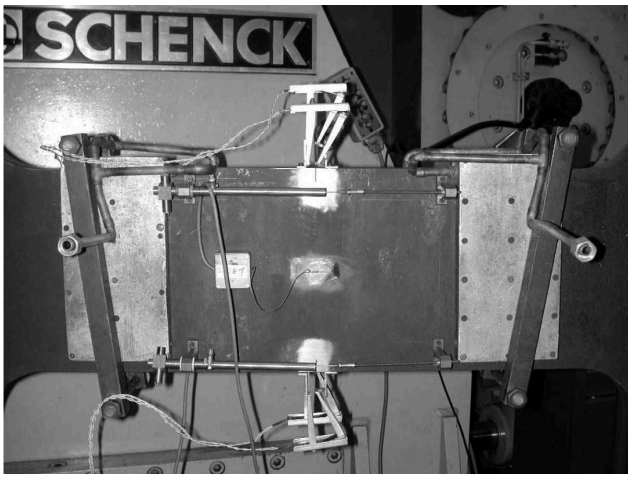

Figure 2.16.: Large-scale pre-cracked tensile sample with a height of 200 mm. The sample is cooled by copper plates at the limits of the test section. The fatigue pre-cracks are located at the end of the two outer notches. Crack mouth opening displacement is measured by clip gauges. Figure from [94].

design rules of the Eurocode 3 (EN 1993). Beltrami and Langenberg broadened the methodology by using probabilistic approaches and applying the FEM for a more precise characterisation of the loading situation [97, 98]. Niessen and Buchholz used these methods to perform thorough assessments of the performance of fracture mechanics concepts for high strength structural and pressure vessel steels [94, 99]. They could prove the safe applicability and discussed strength and weaknesses of current methods for toughness assessment.

Based on these and further studies, simplified concepts for avoiding brittle fracture by requiring minimum Charpy impact toughnesses and service temperatures are nowadays included in the relevant standards, such as the Eurocode or EN 13445. In EN 13445 however, the application of these simplified concepts is limited to steel grades with a maximum yield strength of 500 MPa. In summary, the large amount of studies shows that a safe application of high strength steels is possible and that a high strength does not necessarily result in a low failure resistance.

2.4.1.2. Studies on the prediction of ductile failure

The previous internal studies on the prediction of ductile failure focused on ductile crack initiation and crack growth in pre-cracked samples, see Table 2.3 for an overview. A central approach investigated by Holland, Arndt, Schlüter and Achenbach [33, 100–102] is the so-called damage curve. It describes a critical strain to failure in dependence of the stress triaxiality. This is equivalent to the Johnson-Cook criterion. The experimental determination of the damage curve defines which event is characterised by the defined critical strain. The studies presented in Table 2.3 mostly used interrupted tests on NRBs for the determination of the damage curve. For this procedure one sample was loaded until failure while subsequent tests were stopped before failure. The middle plane of the samples was metallographically investigated to find the instance of void coalescence. Metallographic investigations and stopped testing were performed iteratively so that the point of first void

Table 2.2.: Selected internal studies on the prediction of brittle failure in HSLA steels.

Reference	Experiments	Aims	Summary
Halim, 1989, [32]	– St 52, cast steel – SRB, NRB, CT, WP, burst test on a gas valve made of cast steel	– Correlate ductile failure properties of tensile and fracture mechanics tests. – Investigate transferability of fracture mechanics prediction to component scale.	– No simple correlation between tensile and fracture mechanics tests. – Small scale fracture mechanics tests leads to conservative predictions on large scale components and in burst tests, partially overconservative results.
Hubo, 1990, [95]	– 16 commercially available steel grades – Yield Strength levels: 235, 355, 500 and 690 MPa – SRB, CT, Charpy, WP	– Assess whether the constitutive behaviour varies with the strength level.	– Hardening behaviour is similar for steel grades of different strength classes even under different temperature levels. Toughness properties vary significantly for different strength levels. Scatter of toughness properties less for high strength than for low strength steels. – In WP made of high strength steels stable ductile crack growth may initiate before maximum force. – Failure behaviour of WP can be predicted by fracture mechanics methods, partially overconservative results.
Liessem, 1996, [96]	– 29 commercial HSLA steels, yield strengths: 355, 500, 690, 890 MPa – SRB, Charpy, SENB, WP	– Achieve a correlation between toughness values determined in Charpy and fracture mechanics tests.	– Correlation proposed and validated. – Failure behaviour of WP can be predicted by fracture mechanics methods, similar overconservativities as Hubo.
Beltrami, 1995, [97]	– Results from Liessem	– Investigation of the loading situation for WP samples with FEM to compute the required toughness.	– A slight reduction of allowable stresses by the factor 0.9 reduces the required toughness significantly. – Procedure enables definition of toughness requirements.
Langenberg, 1995, [98]	– Historical steels manufactured around 1900 – NRB,SENB, WP	– Development of a method to judge the remaining lifetime of bridges built around the year 1900. – Evaluation of a database including 400 historical steels	– Approach: Combination of toughness requirement via FEM and statistical description of materials resistance and application of probabilistic safety concepts. – Approach successfully validated on WP made from a demounted bridge. – Transfer to modern steel grades on results of previous studies successful.
Niessen, 2000, [99]	– 20 water quenched HSLA steels, yield strengths: 690, 890, 960 MPa – SRB, Charpy, SENB, WP	– Investigate how the location of specimen extraction of small scale specimens impacts the toughness prediction for WP.	– Small scale samples extracted from the surface usually show the worst fracture toughnesses. – The region with the lowest toughness value determines the failure behaviour of WP. – Slight variations of the Y/T ratio have no influence on the resulting toughness.
Buchholz, 2006, [94]	– P500Q, P690Q – Base material and weld seams – SRB, Charpy, SENB, WP	– Investigate whether the failure of high strength pressure vessel steel can be reliably predicted by fracture mechanics concepts.	– High strength pressure vessel steels can be safely applied. – The fracture mechanics concepts deliver conservative results. – The correlations of fracture toughness and initiation temperature can be applied.

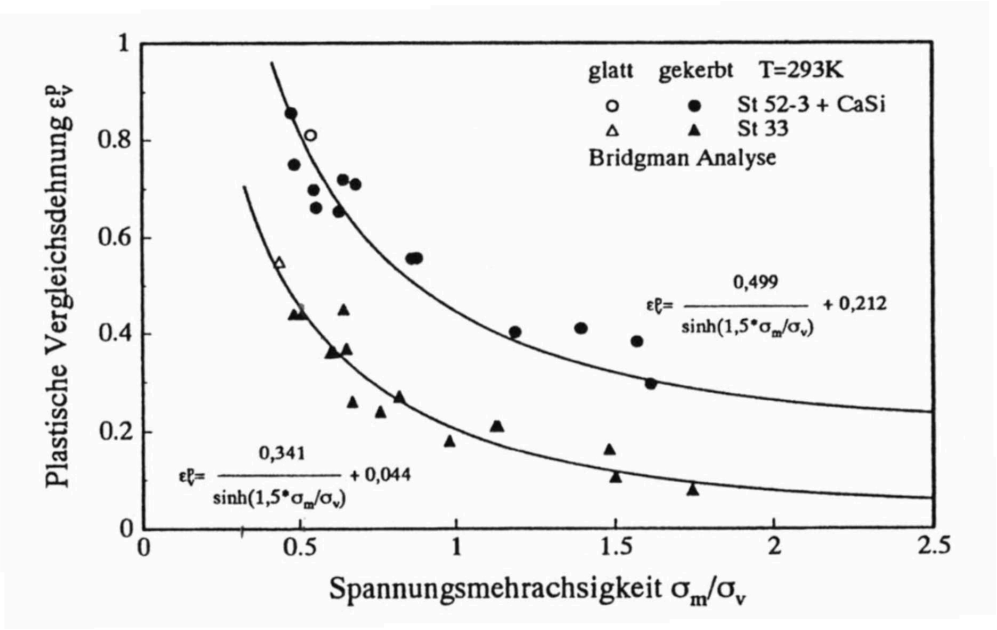

Figure 2.17.: Derived damage curves as a characterisation of damage initiation for St52 and St33, Figure from [100].

coalescence could be found. The corresponding local values of equivalent plastic strain and stress triaxiality were obtained by either analytical approaches or FE computations. The designation damage curve is appropriate because this procedure of determination actually tries to characterise the onset of void coalescence. An example provided by Holland is displayed in Fig. 2.17. Arndt also proposed density measurements on notched round bars for a determination of the damage curve while Münstermann used the direct current potential drop method (DCPD) for a determination of the void nucleation strain [66]. Using the damage curve for structural failure prediction, as tested by Arndt, was not successful. Holland and Achenbach outlined the impact of cleanliness on the overall level of the damage curve. The damage curve is only valid for proportional loading as Arndt showed.

Münstermann, Thönnessen and Nonn explored damage mechanics modelling by the coupled GTN model [66, 103, 104]. The calibration of the GTN parameters on microstructural features, as investigated by Thönnessen and Münstermann, was not completely successful. Nonn showed that a transfer of the GTN parameters was possible if the mesh size remained small, e.g. in the surrounding of a crack tip. However, this requested a large amount of computational resources and a long runtime compared to the simpler cohesive zone model [104].

In summary, the studies showed that damage mechanics models were able to predict the ductile failure of HSLA steels in general. The damage curve, representing strain-based ductile failure criteria, was successfully calibrated on steel grades covering all strength levels. However, a transfer to the prediction of structural failure included challenges which were not solved.

Table 2.3.: Selected internal studies on the prediction of ductile failure in HSLA steels.

Reference	Aims, methods and investigated steels	Summary
Holland, 1993, [100]	– St 52, St 33 – Investigation whether the damage curve is a suitable ductile failure description. – Damage curve calibration: Stopped NRB tests, density measurements on SRB.	– Cleanliness is reflected in overall level of damage curve (St 52 > St33). – Both methods for damage curve derivation lead to comparable results.
Arndt, 1997, [101]	– St 550, St 690 – Investigation, how a nonproportional loading path affects the validity of the damage curve and if the damage curve can predict structural failure. – Damage curve from stopped experiments on pre-loaded and re-manufactured NRBs. – Additionally: SENB, WP, bolted joint	– Non-proportional loading paths strongly affect the failure behaviour and limit the validity of the damage curve. – Damage curves could not predict the failure behaviour of WP and low-triaxiality shear failure in bolted connections. Only high triaxiality failure region in bolted joint was correctly predicted.
Schlüter, 1997, [33]	– StE460, StE690, 22 NiMoCr 37 – Investigation of the impact of temperature, strain rate and microstructure on the damage curve. – SRB, NRB, Charpy, SENB, WP, damage curve by stopped tests and density measurements	– Distance between coalescing voids is in the same order of magnitude as distance between secondary particles. It is independent of strength or toughness. – SENB samples are not suitable for damage curve derivation due to the varying stress state. A slight variation of deformation speed has no impact on the damage curve. Temperature variation has a strong impact.
Achenbach, 1999, [102]	– S460M, Deep drawing steel – Investigation of microstructural feature's impact on the damage curve – Modification of microstructure of S460M by heat treatments – Derivation of damage curve by stopped tests on NRB	– Damage curve for different microstructures show strong variations in the low triaxiality regime but are comparable above $\eta \geq 1.5$, possibly an effect of varying yield properties. – Deep-drawing steel with strongly reduced inclusion content has an overall higher level of the damage curve.
Münstermann, 2006, [66]	– S355, S690, S890, P460Q, P690Q – Investigate transferability of GTN model parameters, that were only calibrated on microstructural features to different sample types. – Metallographic and SEM investigations, DCPD method for ε_N, cell models for f_c. – Numerical derivation of damage curve: Simulation of NRB, evaluation at $f = f_c$. – Validation on NRB, CT, deep drawing test	– Transfer of parameter set calibrated on microstructural features successful for NRB with varying geometry, but not for CT and deep drawing tests. Conclusion: GTN model is applicable but has weaknesses in the low triaxiality regime. – Numerically derived damage curves not comparable to experimental ones. – Application of GTN parameter set in a pressure vessel simulation predicted 2.7 times higher failure pressure than design pressure.
Thönnessen, 2009, [103]	– X70 pipeline steel, SRB, Charpy – Complete microstructure-based characterisation of the GTN model and subsequent simulation of Charpy tests without adiabatic heating, application of Orowan criterion for lower shelf simulations	– Small carbides induce void formation. – General course of Charpy force-displacement curves can be reproduced in simulations but peak force is overestimated and load drop predicted too early. Failure simulation in lower shelf partly successfull but failure predicted too early.
Nonn, 2009, [104]	– Hybrid-laser weld connections of S355, EH36 and RQT701 – Comparison of fracture mechanics concepts to damage mechanics simulations with GTN and cohesive zone model. Consideration of cleavage fracture by a Beremin criterion. – Mini tensile samples, NRB, Charpy, SENB, WP	– Force-displacement behaviour successfully reproduced, crack initiation toughness partly overestimated. Cohesive zone model shows shorter calculation time than GTN model – Small-scale experiments and simulations predict much more conservative values than WP tests. GTN transfer to WP tests successful with fine mesh around crack tip. GTN and Beremin mesh size requirements cannot be fulfilled together.

2.4.2. Burst pressure prediction by damage mechanics

The burst pressure of cylindrical, flawless pressure vessels and pipelines without additional elements is traditionally predicted by analytical formulas. Studies that compared the analytical predictions to the results of burst tests showed that in general a good prediction quality can be achieved for this simple case [105–108]. Once more complex geometries are considered, finite element studies gain importance. The bibliography of Mackerle proves that simulation is a well-accepted and regularly used tool for predicting the failure behaviour of pressurised structures [109]. The application of simulations within the DBA framework shows that the loading situation can be covered more precisely (e.g. [10, 11, 110]) than in analytical considerations.

Damage mechanics models have to be used if ductile failure shall be included in simulations in addition to plastic deformation. Successful examples mostly consider structures with initial defects. Dybwad et al. and Sandvik et al. simulated the full-scale failure behaviour of cracked pipeline segments with the GTN model [111, 112]. However, in both cases the failure initiation spot was predefined so that the mesh could be strongly refined in the respective model region. Dotta et al. even limited the application of the GTN model to a single layer of elements near the crack tip in similar studies. They could predict the burst pressure with moderate accuracy [113]. Pavankumar et al. explicitly investigated the transferability of damage mechanics parameters, considering the GTN and Rousselier model, from CT specimens to the failure behaviour cracked components. They found that the crack growth in the component was reasonably well predicted and the parameters could be transferred [114]. Summing up, it can be stated that the application of damage mechanics models in pre-cracked, large-scale components is feasible since a fine mesh is only needed around the small defect. A parameter calibration in similar stress states of small and large scale components allows a transfer of parameters between these scales. However, if less concentrated initial defects are present, a fine mesh is required in a larger region and the poor computational efficiency of these models will lead to excessive calculation times.

Consequently, studies on larger defects, e.g. corrosion defects, mostly use simpler damage models. Oh et al. used a Johnson-Cook-like critical strain criterion in dependence of stress triaxiality to predict the ductile failure of pipelines with corrosion and gouge defects [115]. They calibrated the failure strain on laboratory NRB samples. The simulation was validated in comparison to full scale experiments. The failure could be correctly predicted regardless whether it was induced before or after global plastic instability. Due to the encouraging results they used simulations with this simple and efficient failure criterion to perform a parameteric study and proposed a new analytical assessment formula for this kind of defects. This would usually have required a large number of costly burst tests. This approach is similar to the one pursued in this study.

Coppola et al. investigated a corrosion defect in a pipe that was tested under combined bending and internal pressure [116]. In failure simulations they applied also an efficient critical strain criterion, which considered the dependence of stress triaxiality and Lode angle. The burst pressure under this complicated loading scenario could be well reproduced. Consequently, efficient critical strain criteria are suitable for damage modelling in uncracked structures with larger defects.

Recent studies of Schruff focused on the failure prediction for pressure vessels without initial defects made from HSLA steels [8]. He explored opportunities to predict pressure vessel failure for the steel grades P355N, P500Q and P690Q by the application of damage mechanics. The focus

was hereby set on using damage mechanics to derive nominal failure criteria that subsequently might be used in probabilistic safety assessments.

To achieve this, Schruff proposed a method to derive nominal, lower-bound damage curves for pressure vessel simulations. The underlying idea was to use the micromechanically motivated GTN model to reproduce the material behaviour of steels with varying quality. By artificially deteriorating GTN model parameters such that they just meet nominal requirements, the behaviour of a virtual lower-bound material can be assessed. The nominal requirements of EN 10028 for a steel grade P690Q demand, besides the nominal strength, a minimum Charpy impact toughness of 60J at 20°C. Since crack initiation and propagation properties are characterised in a Charpy test, Schruff [8] proposed to refer to this requirement when defining lower-bound failure criteria. For this, he modified previously calibrated GTN parameter sets in the simulation of Charpy tests until the minimum requirement of 60J was met. However, as explained above, the GTN model is not suitable for a prediction of ductile failure in uncracked, large structures due to its limited computational efficiency. Therefore, Schruff suggested using the GTN simulations to derive nominal damage curves. Figure 2.18 displays a scheme of the procedure.

Schruff could show that this nominal damage curves always were below experimentally derived ones. He could therefore demonstrate the general applicability of the concept but concluded that further investigations on the validity and reproducibility of the results were necessary. He listed the non-consideration of adiabatic conditions and the unclear impact of the non-unique GTN parameter selection on the results as weaknesses of his approach. However, the correlation to nominal ductile failure properties is innovative and enables the application of damage mechanics concepts within probabilistic safety concepts. This procedure is therefore adapted in this study.

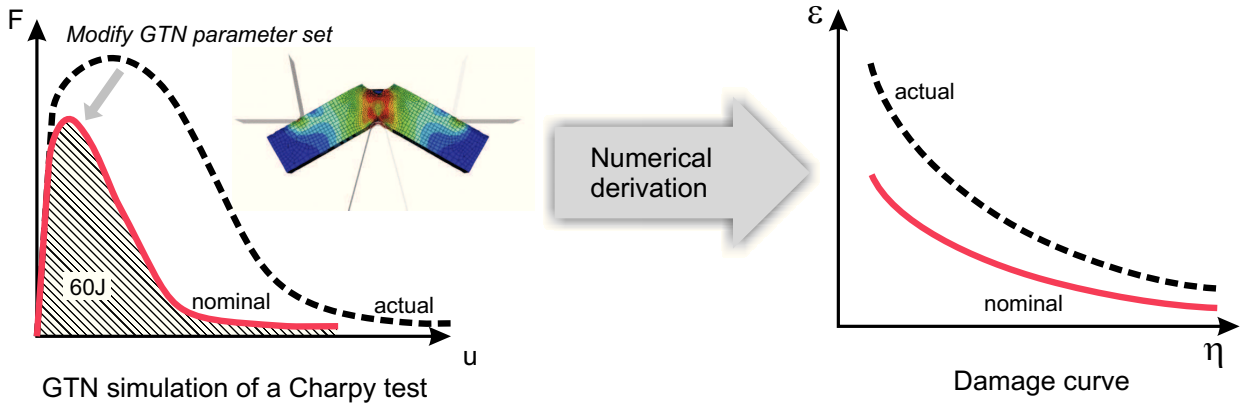

Figure 2.18.: Scheme of the procedure developed in [8] for the derivation of nominal damage curves.

2.5. Summary

The presented studies from the literature show that damage mechanics models are suitable to model the ductile failure behaviour of high strength structural steels. The transfer between the failure prediction on small scale laboratory samples and large-scale components and structures remains a challenge. For now it was only successfully mastered when the failure initiation site is known in

advance by a pre-crack. For components without such localised defects only very efficient simple models can be used. Critical-strain criteria, respectively damage curves, are a well-tested approach to predict ductile failure in an efficient way. The approach of Schruff provides a concept how to link these criteria to nominal toughness requirements defined in the standards. However, the current concept has several weaknesses, such as the non-consideration of adiabatic conditions and concerns about the reproducibility of results due to the non-unique GTN parameter selection. In addition, this approach does not consider the Lode angle influence. Studies of the last decade have shown that it is very important to consider this variable in the low triaxiality regime. The missing Lode angle consideration may also explain a part of the difficulties in scale-bridging damage mechanics models in the low triaxiality region. Finally, the concept has not been tested versus full-scale failure tests.

The available studies therefore provide a good basis to investigate a comprehensive concept for structural ductile failure prediction, but significant extensions have to be made. Additionally, a developed concept has to be demonstrated in a full scale failure test. The investigations performed in this thesis aim at solving these challenges. An overview of the performed investigations is provided in the following chapter.

3. Outline of the study

The aim of this study is to provide a comprehensive modelling concept for the ductile failure prediction in large scaled components that can be used within probabilistic safety concepts. One of the fundamental challenges in this task is scale-bridging the ductile failure prediction from the mm scale, on which ductile failure can be well predicted by laboratory tests and damage mechanics simulations, to the m scale, on which the modelling of large components has to be very efficient and robust. Another aspect to be investigated is how lower-bound assumptions of ductile failure criteria can be reliably derived from the nominal material requirements given in EN 10028. To fulfil this aim, manifold investigations have been undertaken. They can be grouped into four basic steps (Fig. 3.1) that are presented in the following.

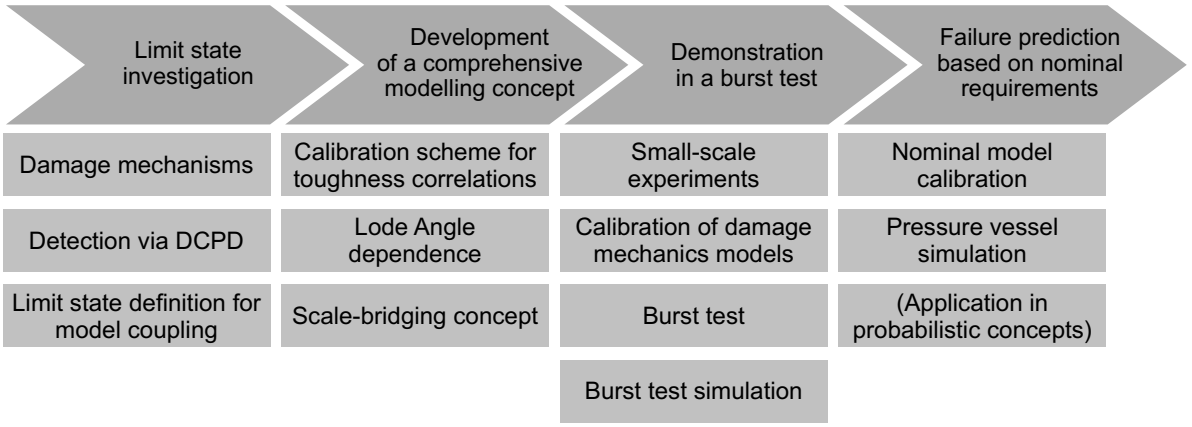

Figure 3.1.: Overview on the performed investigations. The application of probabilistic concepts was performed by project partners in the accompanying research project.

1. Limit state investigation: The evolution of ductile failure is a continuous process. However, only simple, efficient failure criteria, such as damage curves, are suitable for large-scaled component simulations. These define individual limit states. It therefore needs to be investigated which limit state is suitable for the characterisation of ductile failure on the component scale. Furthermore, it needs to be examined how this limit state relates to investigations performed on laboratory samples. Thus, the relevant damage mechanisms in HSLA pressure vessel steels were explored. Previous studies used the direct current potential drop method (DCPD) for an experimental characterisation of damage states [8, 66]. Therefore, it was tested whether it can be used in this study. Based on these findings, a suitable limit state for the simulations on the component scale was defined.
2. Development of a comprehensive modelling concept: As outlined in Chapter 1, three main requirements on a modelling concept arise from the intention to substitute burst tests in

probabilistic safety concepts with damage mechanics simulations. These are a high computational efficiency in large scale simulations, the reliable consideration of all relevant stress states and loading situations, and the possibility to derive a lower-bound failure criterion from nominal requirements. An approach that fulfils all these requirements was developed within this thesis. The basis for this modelling concept is formed by the previous studies of Schruff [8]. It was extended and adapted to the requirements of ductile failure prediction in pressure vessels considering the following aspects:

- Calibration scheme for toughness correlations: In this study, simulations with Gurson models shall be used to correlate efficient ductile failure criteria with real and nominal toughness levels. One of the major drawbacks of the procedure developed in [8] is that the GTN parameter selection is non-unique. This might have an influence on the derived damage curve and thereby cause non-reproducible results. To establish a framework for a reliable numerical derivation of critical strains, a sensitivity analysis for the GTN parameter selection was performed and a calibration scheme was defined that avoids non-uniqueness. Additionally, the model was extended to include the simulation of adiabatic loading conditions. This is crucial for a correct simulation of Charpy impact toughness tests because they are characterised by high strain rates and energy dissipation.
- Consideration of Lode angle dependence: The previous implementation neglected this aspect. However, pre-studies have proven that failure in thick-walled pressure vessels takes place in a plane-strain stress state, in which Lode angle effects on ductile failure are significant. The procedure was therefore extended to consider Lode angle dependence by the implementation of a modified version of the GTN model.
- Scale-bridging concept: Strain-based criteria for ductile failure shall be applied in the component simulation. However, in large-scaled simulations models the mesh size may strongly vary. Since the computed strains may depend on the base length, which is determined by the mesh size, approaches for compensating this were developed.

3. Demonstration in a burst test: To gain the acceptance of standardisation committees and pressure vessel designers for the developed procedure, its prediction capabilities also have to be demonstrated in a burst test. Additionally, such a test can provide an example for the applicability of high strength pressure vessel steels. Therefore, a demonstrator pressure vessel was built from the high strength steel P690Q in the accompanying research project FOSTA P950 [117]. It was tested until failure in a burst test. Laboratory samples were manufactured from the pressure vessel materials and tested. These small-scale tests served as a basis for the calibration of the damage mechanics models. After calibration these were applied in a full-scale simulation of the pressure vessel to examine the prediction quality.
4. Failure prediction based on nominal requirements: Nominal strain-based failure criteria were derived from the requirements of EN 10028. They were tested in pressure vessel simulations to explore the applicability of the procedure. The derived nominal failure criteria were used as an input for the application of probabilistic concepts in the accompanying research project.

The materials used within these investigations are introduced in the following chapter. Methods and results are presented in groups according to these four basic steps in Chapter 5 to Chapter 8.

Models based on the initial formulations of Gurson play a key role within the study. Throughout this study, the following designations will be used:

- The terms “Gurson models” or “Gurson simulations”: These terms shall refer to the group of model formulations derived from Gurson’s initial studies in general. They include extensions, such as formulations for void nucleation and coalescence as well as additional terms for Lode angle dependence. The designation is deliberately vague because these extensions may be used in different combinations. The terms shall imply that the described procedures could also be used with other model combinations. The terms do not refer to models that have significantly altered the structure of the Gurson model, for example the models considering void shape.
- Specific designations of model versions, for example the GTN model. The complete model formulations will be provided along with the introduction of the designation.

4. Materials

4.1. Demonstrator pressure vessel

In the accompanying research project FOSTA P950 a pressure vessel was designed and built to demonstrate the applicability of high strength steels in pressure vessel design [117]. The vessel was manufactured from two commercial P690Q steel grades. The design of the vessel features a nozzle as a typical detail, a cylindrical vessel body and ellipsoidal heads (Fig. 4.1). It has a length of 3382 mm, a diameter of 1200 mm and a wall thickness of 50 mm in body and nozzle and 38 mm in the heads. Body and nozzle were manufactured from the identical material while the heads originate from a different material producer. After forming, the nozzle was quenched and tempered a second time to remove deformation effects. The longitudinal weld seams in body and nozzle as well as the weld joint of body and heads were manufactured by submerged arc welding. The weld joint of body and nozzle was produced by manual arc welding with covered electrodes. The vessel was closed by a cover welded on the nozzle in which filling and ventilation valves were inserted. All weld seams were tested 100% with ultrasonic and magnetic particle testing. No defects were reported. After manufacturing, the vessel was heat treated for stress relief at 575°C for five hours. Sample welds were produced from the body, head, and nozzle-body weld joints for characterising the weld properties. These samples were heat treated together with the vessel to ensure equivalent properties.

The vessel therefore consists of two base materials and three relevant weld seams. Acronyms will be used for material identification in the following (Table 4.1, Fig. 4.1). Due to the time-consuming production process of the vessel some sample material of the heads was used for preparatory and general investigations before the final heat treatment. To distinguish between these states two acronyms (dvI and dvIII) are used although the material has the same chemical composition.

Table 4.1.: Nomenclature of the characterised vessel materials. *Material was heat treated for stress relief together with the vessel.

Acronym	Type	Description
dvI	Base material	Material of the heads without any heat treatment, used for preliminary studies.
dvII	Base material	Material of vessel and nozzle*
dvIII	Base material	Material of the heads*
dvIV	Weld seam	Work samples of the weld joint of nozzle and vessel body*
dvV	Weld seam	Work samples of the longitudinal vessel body weld seam*
dvVI	Weld seam	Work samples of the weld joint of body and heads*

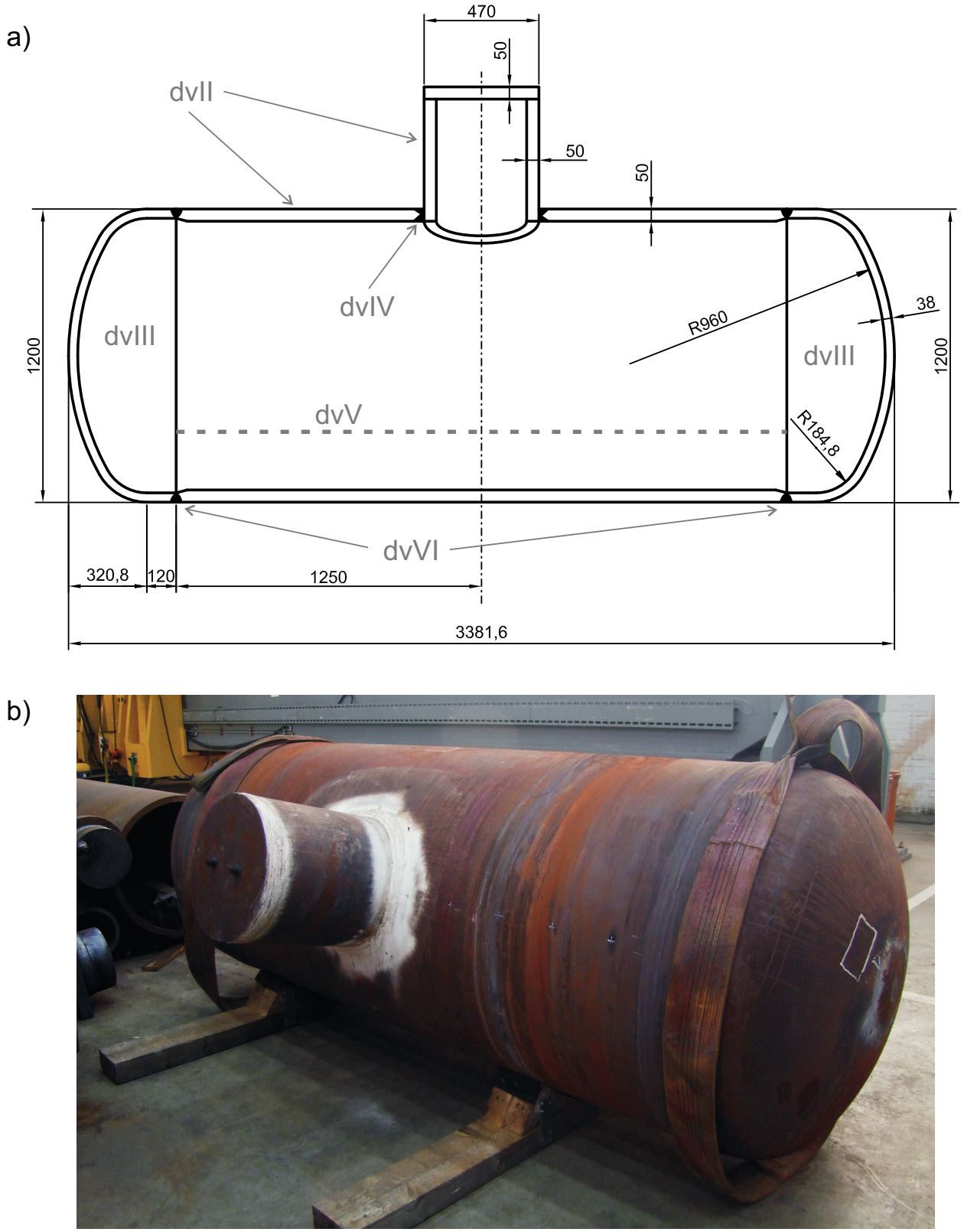

Figure 4.1.: a) Dimensions of the demonstrator pressure vessel in mm. The material acronyms are marked in grey. b) The completed vessel after manufacturing and heat treatment.

The design pressure of the vessel according to EN 13445-3 is 226.3 bar, see [117] for a detailed computation. The critical part according to the design criteria is the transition from body to nozzle. The minimum material requirements for a material P690Q according to EN 10028 are given in Table 4.2.

Table 4.2.: Nominal requirements of EN 10028-6 for the mechanical properties of P690Q.

	Minimum $R_{p0.2}$ or R_{eH} [MPa]			R_m[MPa]		Min. ε_f [%]	$AV_{20°C}$ [J]
Thickness t [mm]	$t \leq 50$	$50 < t \leq 100$	$100 < t \leq 150$	$t \leq 50$	$100 < t \leq 150$	-	-
Nominal requirements	690	670	630	770 - 940	720 - 900	14.0	60

4.2. Basic characterisation of pressure vessel materials

Base materials The base materials are both bainitic steels. Table 4.3. lists the chemical composition and Table 4.4 the mechanical properties. Comparing the properties to the nominal requirements given in Table 4.2 reveals that strength as well as toughness requirements are fulfilled and partially exceeded. Results of toughness tests at different temperatures are provided in Section A.2 in the Appendix. Figures 4.2 and 4.3 show the microstructure in light (LM) and scanning electron microscopy (SEM).

Table 4.3.: Chemical composition of the base materials, product analysis in percentage by weight.

	C	Si	Mn	P	S	Cr	Mo	Ni	Al	Cu	Nb	Ti	V
dvII	0.159	0.29	1.27	0.013	<0.001	0.41	0.24	0.12	0.071	0.02	0.024	0.003	0.006
dvIII	0.088	0.41	1.65	0.008	<0.001	0.16	0.43	0.52	0.085	0.04	0.025	0.003	0.028

Table 4.4.: Mechanical properties of the base materials.

	$R_{p0.2}$ [MPa]	R_{eH} [MPa]	R_{eL} [MPa]	R_m[MPa]	ε_u [%]	ε_f [%]	AV_{RT} [J]
dvII	-	791	786	841	6.2	19.0	195
dvIII	795	-	-	855	6.8	20.0	170

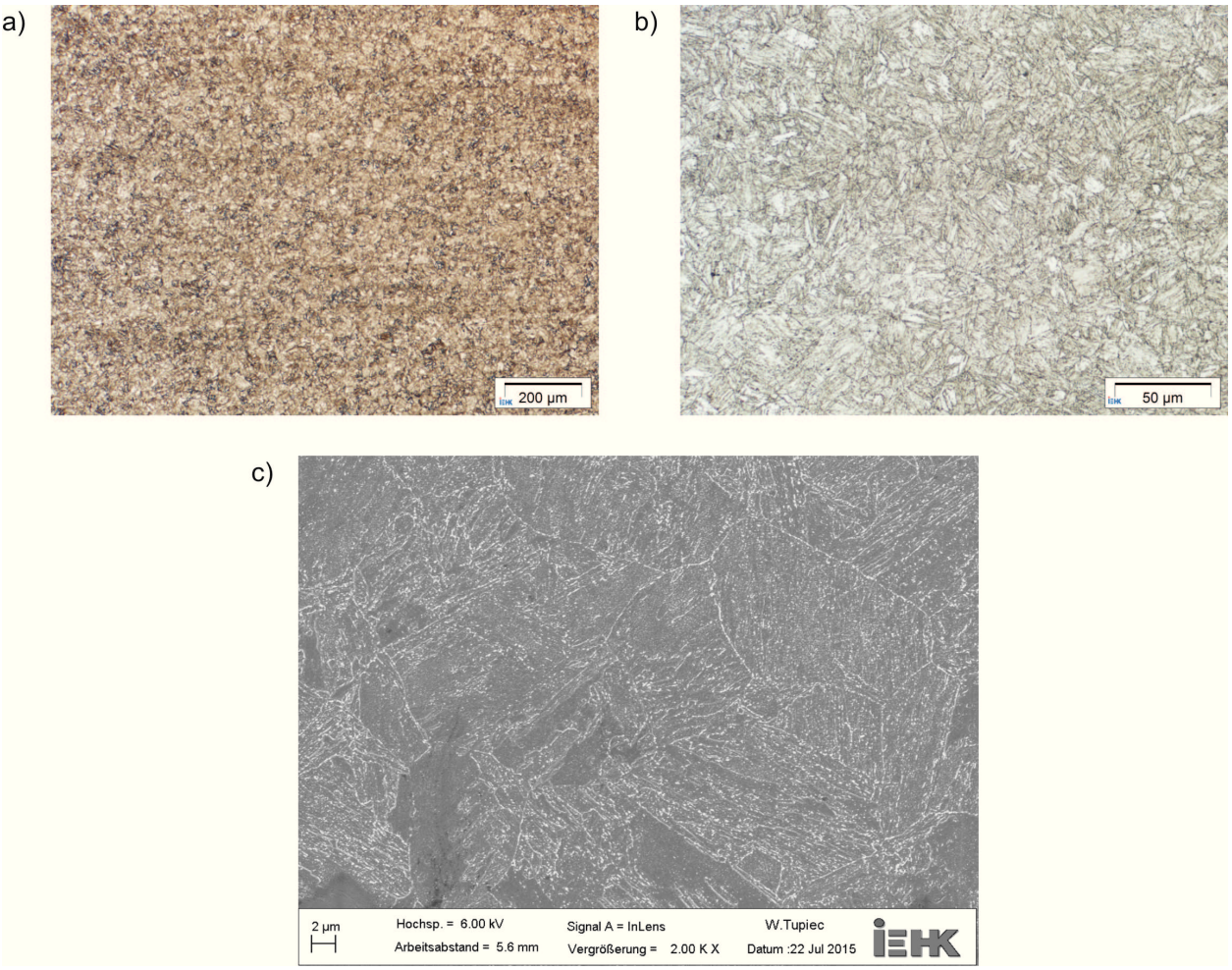

Figure 4.2.: Nital etched microstructure of dvII in LM (a-b) and SEM (c).

Weld seams The weld seams at the nozzle transition, the head transition and in the vessel body were investigated in detail on provided work samples. Tables 4.5 and 4.6 list the chemical composition of the weld seams. Detailed results of the toughness tests are provided in Section A.2 in the Appendix.

Table 4.5.: Chemical composition of the weld seams, product analysis in percentage by weight.

	C	Si	Mn	P	S	Cr	Mo	Ni	Al	Cu	Nb	Ti	V
dvIV	0.057	0.19	1.99	0.008	0.002	0.51	0.52	1.82	0.004	0.03	0.002	0.004	0.016
dvV	0.053	0.35	1.44	0.009	<0.001	0.54	0.49	2.06	0.017	0.07	<0.001	<0.001	0.007
dvVI	0.062	0.33	1.43	0.008	<0.001	0.52	0.48	1.91	0.018	0.06	0.003	<0.001	0.008

Table 4.6.: Mechanical properties of the weld seams.

	$R_{p0.2}$ [MPa]	R_{eH} [MPa]	R_{eL} [MPa]	R_m[MPa]	ε_u [%]	ε_f [%]	AV_{RT} [J]
dvIV	-	782	776	843	8.0	20.6	115
dvV	-	723	721	789	8.3	19.7	108
dvVI	692	-	-	797	9.0	22.0	130

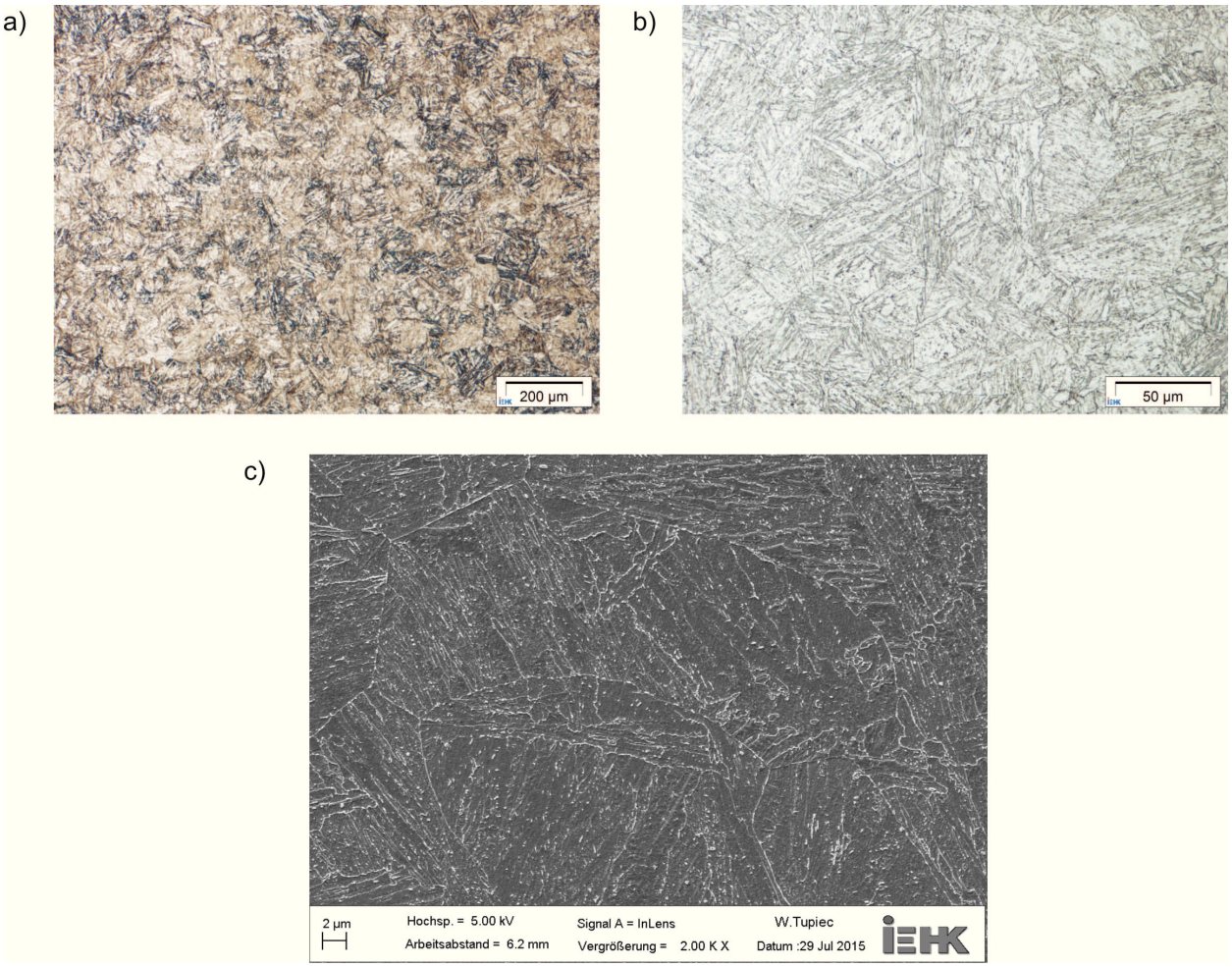

Figure 4.3.: Nital etched microstructure of dvIII in LM (a-b) and SEM (c).

The microstructure around the weld seams shows the typical distribution of weld metal, coarse and fine grained zone as well as heat affected zone (HAZ) as displayed in Fig 4.4 a,c,e. The microstructure of the weld seams is also bainitic as can be seen in Fig.4.4 b,d,f and in additional graphs provided in the Appendix A.1.

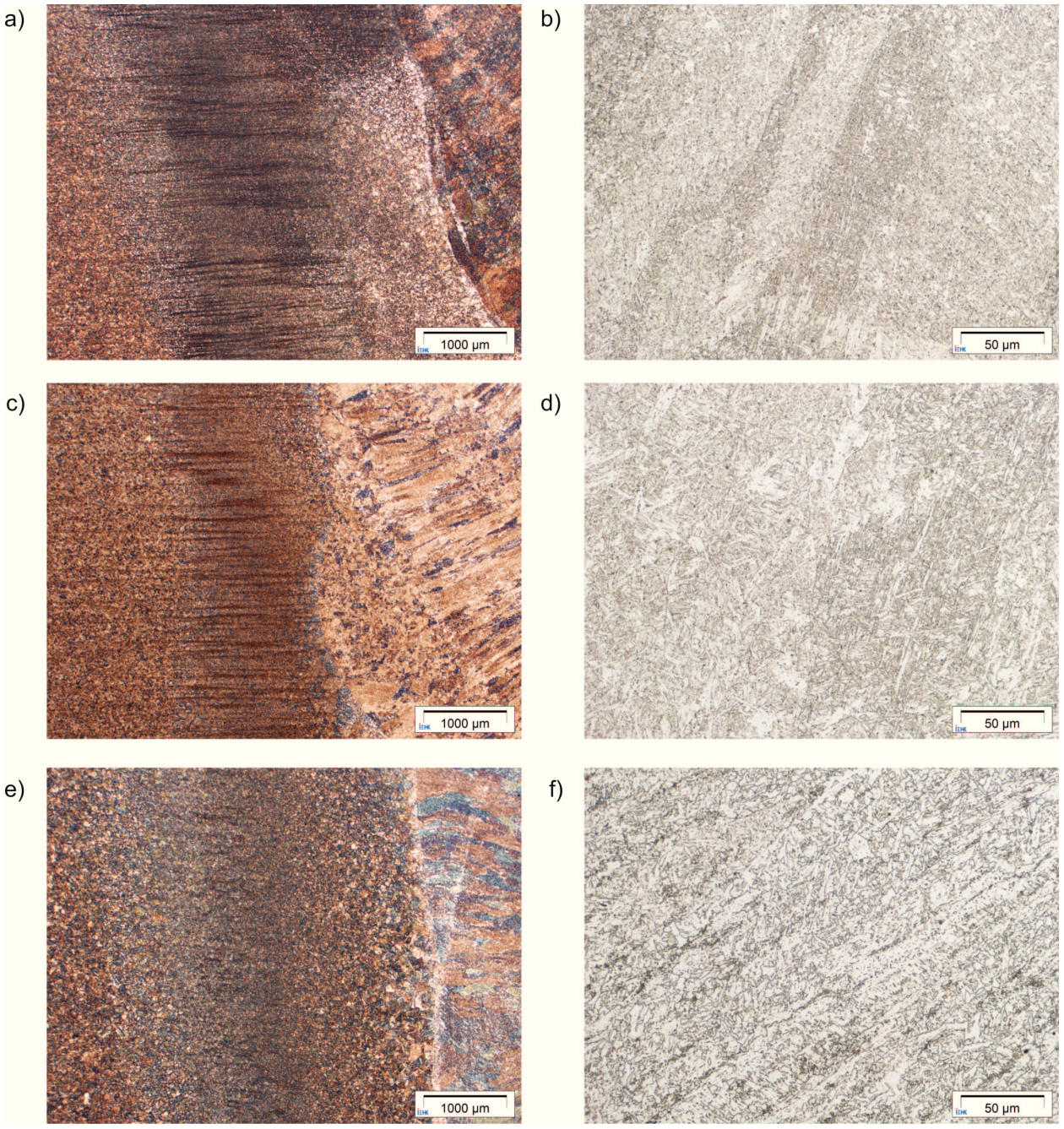

Figure 4.4.: Nital etched microstructure of a) weld region of the nozzle weld joint (dvIV), b) weld seam of dvIV, c) weld region of the body weld joint (dvV), d) weld seam of dvV, e) weld region of head weld joint (dvVI), f) weld seam of dvVI.

The deviation of properties within weld and heat affected zone was explored by performing a hardness mapping on a MicroDur system that measures the Vickers hardness HV1 by the ultrasonic contact impedance procedure (UCI). The results were evaluated by the plotting program DPlot. Macroscopic photographs of the weld joints with overlaid hardness mappings are given in Fig. 4.5. For all weld seams the hardness of base material and weld seam is similar, but the HAZ is softer. To quantify these hardness values, intervals were identified that included most of the results of a typical region. The interval width was hereby defined to be 10 HV1. The results listed in Table 4.7 consequently specify the medium value of the ± 5 HV1 interval that covers the typical

hardness for each region. This was investigated for HAZ, base metal and weld seam material.

Table 4.7.: Typical intervals for hardness values in the respective regions.

Material	Hardness in HV1 ±5 HV1		
	Base metal	Weld seam	HAZ
dvIV	290	310	240
dvV	280	290	250
dvVI	280 (dvII) / 290(dvIII)	290	245

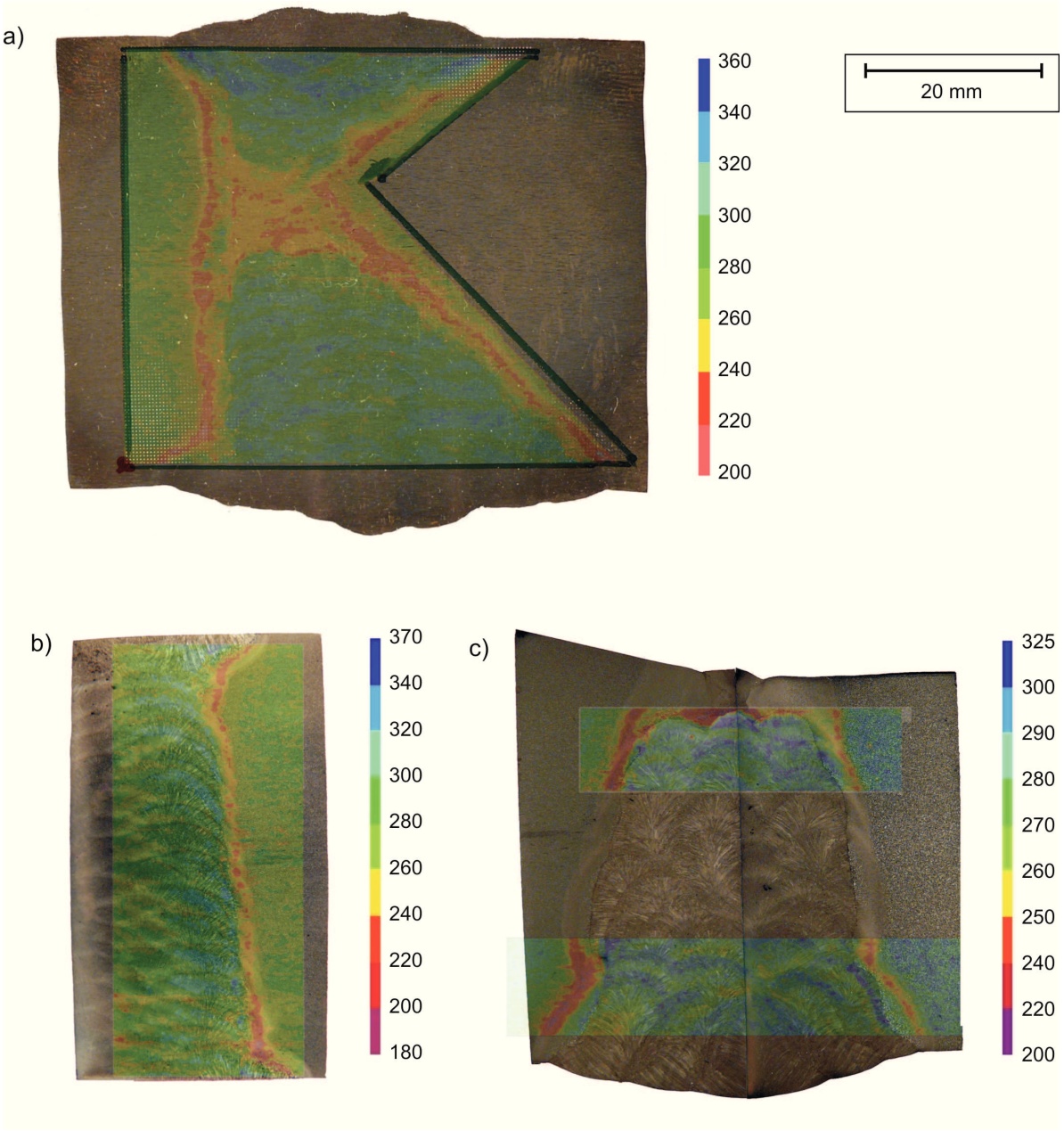

Figure 4.5.: Macroscopic preparations and hardness mapping results (in HV1) of a) nozzle weld joint (dvIV) b) body weld joint (dvV) c) head weld joint (dvVI). Result intervals are partly irregular to enhance the visibility of results.

4.3. Further materials

As the pressure vessel design and manufacturing was a time-consuming process, the material in the final stage of heat-treatment was not available at the beginning of the studies. Therefore, two available substitute materials were used. They are introduced in the following.

Some share of the head material, which was not heat treated for stress relief, was used for preparatory and general studies. As the chemical composition is not affected by the heat treatment, it is identical to the one of dvIII given in Table 4.3. The mechanical properties, as displayed in Table 4.8, indicate that only the toughness is affected by the heat treatment. This is in accordance with studies of Hanus [118]. A full comparison of the toughness values is given in Appendix A.2 along with metallographic investigations that hint at only minor changes in the microstructure.

Additionally, a pressure vessel steel P500Q previously used by Schruff was applied in this study. Tables 4.9 and 4.8 list the chemical composition and mechanical properties, details can be found in [8].

Table 4.8.: Mechanical properties of additional materials, values for P500Q from [8].

	$R_{p0.2}$ [MPa]	R_{eH} [MPa]	R_{eL} [MPa]	R_m[MPa]	ε_u [%]	ε_f [%]	AV_{RT} [J]
dvI	805	-	-	859	7.6	20.5	211
P500Q	-	604	599	682	7.8	20.2	223

Table 4.9.: Chemical composition of P500Q, taken from [8].

	C	Si	Mn	P	S	Cr	Mo	Ni	Al	Cu	Nb	Ti	V
P500Q	0.164	0.32	1.17	0.009	<0.001	0.02	0.10	0.05	0.058	0.03	0.023	0.004	0.003

4.4. FE programs and test setups

The FE simulations in this study were performed with the commercial FE software package Abaqus by Dassault Systèmes, Versailles, France, versions 6.12 and 6.14. The experimental investigations featured tensile tests in quasi-static mode, high-speed tensile tests, fracture mechanics and Charpy tests for all investigated materials. The tensile tests were performed on tensile testing machines of Zwick, precisely a Zwick100 with a maximum force of 100kN, and a Zwick1484 with a maximum force of 200kN. The high-speed tensile tests were conducted at a RoellAmsler high speed-testing machine with a maximum force of 12kN. Charpy tests were performed on an instrumented 300J hammer with a striker mass of 19.81 kg and an impact velocity of 5500 mm/s. Fracture mechanics tests were performed on servohydraulic testing machines with force capacities of 60kN and 400kN.

In the following chapters the methods applied for the individual investigations are introduced in the following chapters along with the results according to the four basic steps defined in Chapter 3.

5. Limit state investigation

The first step towards a comprehensive modelling concept was the investigation of the limit state, which included three individual aspects (Fig. 5.1). First, the relevant damage mechanisms in high strength pressure vessel steels were examined. As described in Chapter 2, the general mechanisms of ductile damage are well-known from studies of the 1970s to the 1990s. However, the steels produced today are characterised by an excellent purity and a fine-tuned microstructure. Therefore, the extent of damage and the characteristics of its development in the investigated steel should be re-checked to ensure that the limit state for the structural failure modelling is selected appropriately.

Second, the in situ detection capabilities of the DCPD were investigated. Previous studies used the DCPD method on modified fracture mechanics samples and NRB to experimentally derive damage curves [8, 66]. However, it needs to be examined whether the DCPD is also applicable to steels with such a low inclusion content. Third, the modelling concept shall include a coupling of the strain-based failure criteria with Gurson simulations in order to refer damage curves to real and nominal toughness levels. To foster reliable and reproducible results, this coupling needs to be based on an appropriate limit state definition. The methods applied for investigating these aspects are introduced in the following section; the results are presented subsequently.

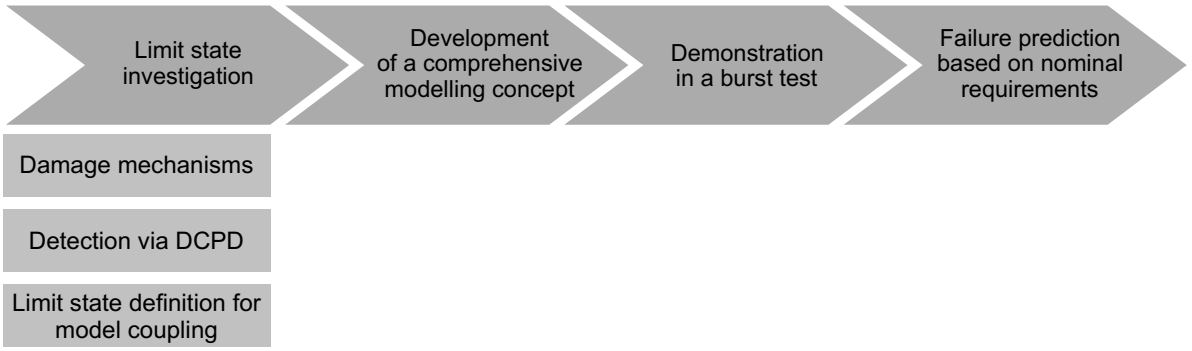

Figure 5.1.: Overview on the presented limit state investigation.

5.1. Methods

5.1.1. Assessment of relevant damage mechanisms

Classical methods to investigate the mechanisms of ductile failure are optical and scanning electron microscopy (SEM) [25]. Recently, also microtomography methods gain importance in the investigations of failure mechanisms as they can provide three-dimensional information (e.g. [119–122]).

Within this study, the approach of Arndt was adapted for the assessment of the damage mechanisms [101]. It includes tensile tests on notched round bars which are stopped at different deformation grades. Subsequent metallographic investigations give evidence about the damage development. In addition, one sample could be investigated with microtomography to validate the metallographic investigations.

The ductile damage development within the pressure vessel steel was investigated on samples made from previously obtained material of the heads, dvI. The sample geometries were derived from the basic form of the B8x40 sample type of DIN EN 50125, a round bar with an outer diameter of 8mm. However, the samples were manufactured with an increased length of 90 mm to provide more space for adding the potential equipment. Three different notch geometries were manufactured (Table 5.1). They were tested on electric tensile testing machines under quasistatic conditions. The deformation was recorded by an optical extensometer. After performing firstly tests until failure, subsequent tests were stopped at the force maximum, shortly before failure, and halfway between force maximum and failure.

Table 5.1.: Nomenclature of NRB of dvI used for the investigation of ductile damage.

Acronym	Notch ligament	Notch radius
L4R2	4mm	2mm
L4R6	4mm	6mm
L6R6	6mm	6mm

As a next step, the notch region of the samples was grinded to the central plane (Fig. 5.2). However, the preparation of the samples by pure polishing was not successful. The polishing process seemed to dislocate material into existing voids, thereby close them and prevent detection via microscopy. Therefore, the procedure described in [101] was applied. The samples were first polished, then etched for 10s with a 3% HNO_3-solution and then polished again with 1µm diamond paste. The intermediate etching removed the material caps over the voids and made them visible in microscopy. The area fraction of the existing voids was subsequently evaluated by image processing in the commercial program FIS Olympus Analysis.

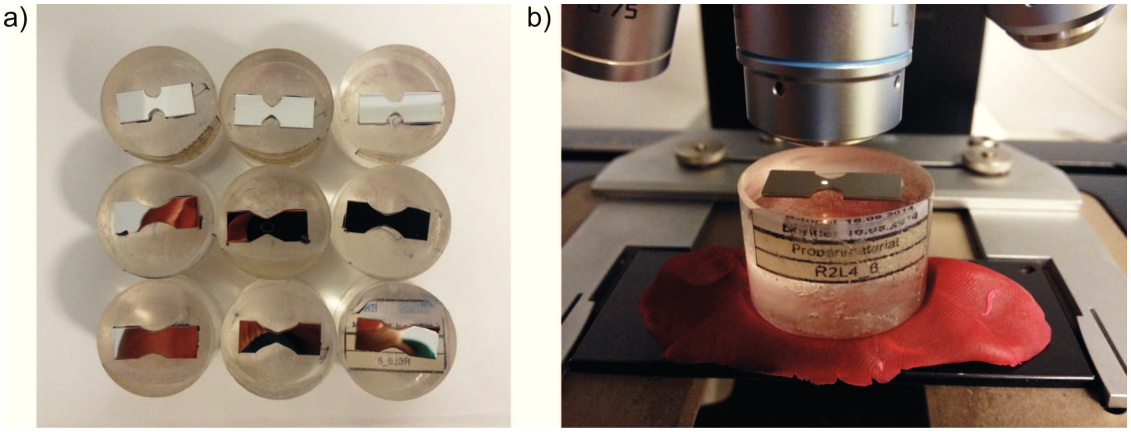

Figure 5.2.: a) Polished samples of stopped tensile tests. b) Investigation via microscopy.

5.1.2. Detection of ductile damage via the DCPD

Additionally, it was explored whether the amount of ductile damage could be measured in situ within the damage mechanics test. Lemaitre and Dufailly were the first ones to provide a systematic proposal of destructive and non-destructive methods for the quantification of ductile damage in 1987 [123]. Out of their proposed methods, measurements of the elastic modulus, the micro-hardness and the electrical potential are used most frequently. Alves used these methods on a mild structural steel [124]. The damage values detected by the different methods varied significantly. He corrected the modulus measurements with respect to deformation. This significantly improved the results. Bonora et al. [125] used finite element simulations to account for the sample deformation in modulus investigations. Tasan et al. found that indentation-based measurements require a previous heat treatment to remove plasticity-induced effects like strain hardening [126–128]. In addition, they reported that different methodologies yielded strongly varying absolute values for the damage state. In summary, these studies show that measurements of ductile damage may be strongly deteriorated by other effects, especially under severe plastic deformation.

Potential measurements are a standard methodology in fracture mechanics for assessing crack growth during a test. The effective cross section is reduced by crack growth and void formation. This induces an increased resistance. Consequently, the resistance of the sample and the measured voltage increases. The relevant procedures are standardised, e.g. in ASTM E647. For fatigue applications often alternate current is applied since it is more sensitive to surface defects due to the skin effect. For ductile crack growth, the direct current potential drop method is applied. It has the advantage that it may be applied in situ. Studies by Ljustell on strongly deformed fracture mechanics samples indicated the need for an explicit consideration of the plastic deformation in DCPD measurements [129].

Münstermann and Lian used the DCPD in NRB for the detection of ductile damage [61, 66]. They did not consider possible effects of deformation. Yet, plastic deformation might deteriorate the results as the cross sections of such specimens are also strongly reduced by necking. Zhang et al. assumed that the effect of deformation could be described as a linear function of local strain. This share was subtracted from the measured potential to identify the influence of damage [130, 131]. However, previous studies of the author of this thesis gave evidence that most of the potential effects can be attributed to the plastic deformation of samples if the DCPD is applied for measuring ductile damage in uncracked samples [132].

This was further investigated within this study. A methodology was developed to separate the effect of plastic deformation and damage on DCPD measurements. Thus, an assessment of the validity of DCPD measurements for ductile damage quantification in NRB could be performed. For the application of the DCPD method, a constant current is induced into a sample during testing while the voltage is measured between two points. The clampings are electrically isolated (Fig. 5.3a).

The principle of the developed methodology is to identify the share of resistance increase that is induced by pure deformation. By this, it is possible to subtract the effects of deformation from the voltage increase and identify the share of a possible damage influence. The basic relations are provided by Ohm's law. The resistance of a non-uniform conductor can be computed as a series circuit of infinitesimal slices [133]. Figure 5.3 illustrates the principle. Consequently, the

resistance can be formulated as:

$$R = \lim_{N\to\infty} \sum_{i=1}^{N} \rho \frac{\Delta x}{A_i} = \int_0^L \rho \frac{dx}{A(x)} \approx \sum_{i=1}^{N} \rho \frac{\Delta x}{A_i} \tag{5.1}$$

Equation 5.1 shows that the resistance depends on the cross section function, the length and the resistivity ρ. It can readily be applied on notched round bars if the current cross section function is known throughout deformation history. The cross section can be obtained by digital image correlation or by an FEM simulation. This was tested in pre-studies for a structural and a pipeline steel, see [132] for details. It could be shown that for notched round bars a simulation with a von Mises yield condition could well capture the notch ground deformation. The resistance increase and the resulting effects on the measured voltage were computed by Eq. 5.1 and compared to the experimental results. Measured and computed voltage showed a similar course throughout deformation but could not reliably be matched (Fig. 5.4).

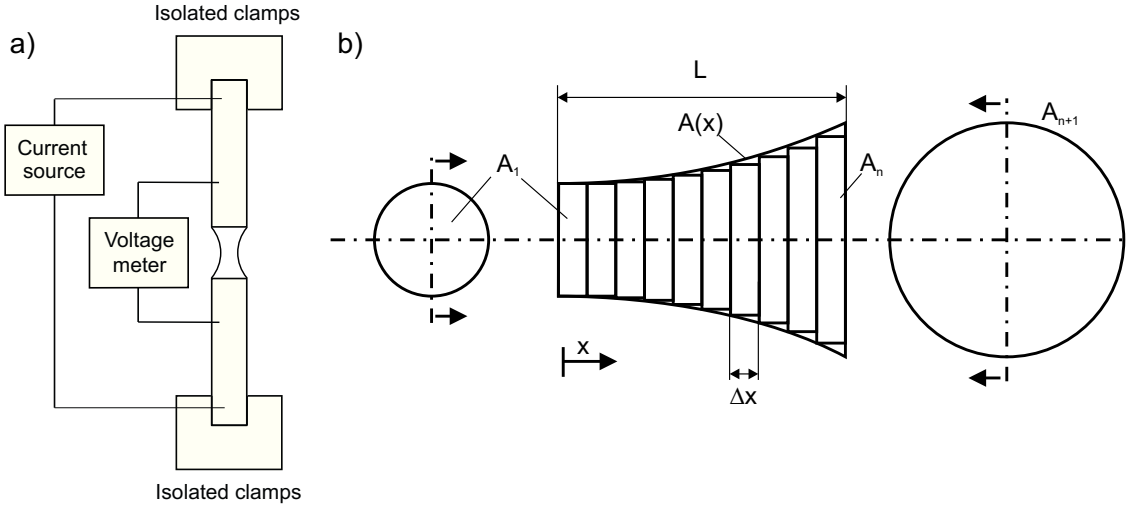

Figure 5.3.: a) Illustration of a setup for applying the DCPD in notched round bars. b) Scheme for the calculation of the resistance of a non-uniform conductor. Figure adapted from [133].

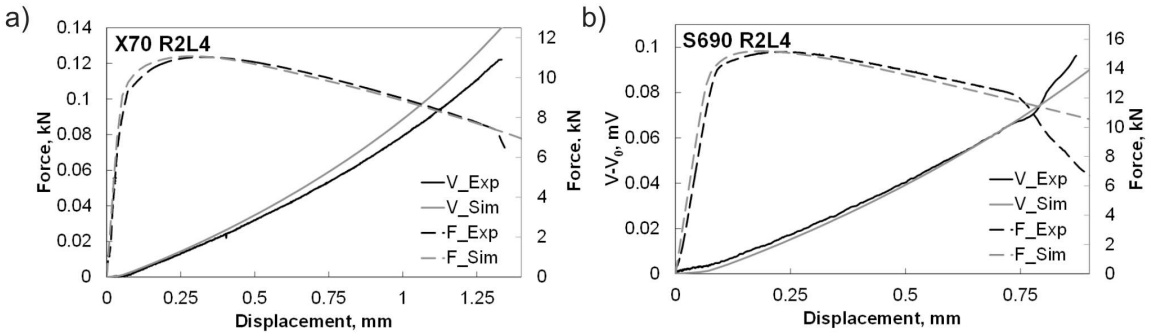

Figure 5.4.: Comparison of measured and computed resistance according to Eq. 5.3 based on a simulated deformation for a) pipeline steel X70 and b) structural steel S690 [132].

To further optimise this method two approaches were pursued: First, an optimisation of the test

setup (Fig. 5.5) was performed. The main improvements were achieved by an optimisation of the equipment. A more precise current source (Keithley 2200-20-5) was purchased. It provides a current output precision of 0.05%. The detection range of the operated nanovoltmeter (Keithley 2182) was adapted to 10mV and the internal analogue low-pass filter was activated. The test setup was isolated from air ventilation by Styrofoam to prevent temperature changes. Copper rods were used as contact points for the nanovoltmeter instead of clamps to have a precise contact point. By this, a measurement accuracy of approximately 1µV could be achieved. This is an acceptable precision considering that a NRB, which is subjected in this setup to a current of 1 A, experiences a voltage increase of around 100µV during an experiment.

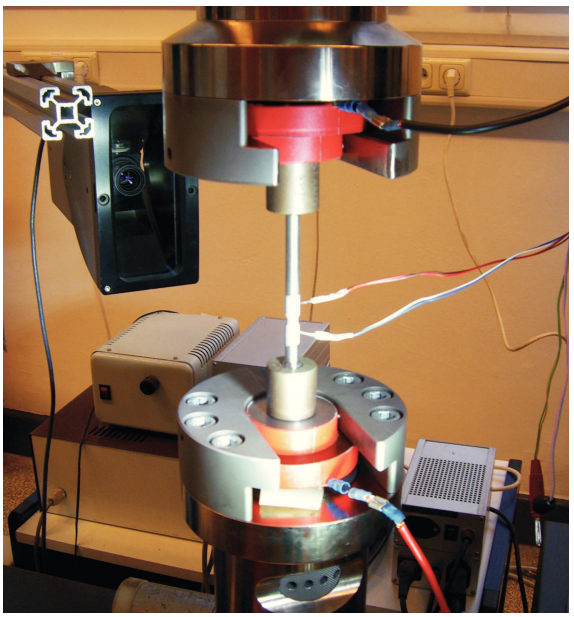

Figure 5.5.: Optimised test setup for DCPD measurements. Isolated clampings and a notched round bar sample with attached copper rods.

Second, the potential rise induced by deformation was computed more precisely by obtaining it through a coupled electrical-mechanical FEM simulation. The mathematical description of electrical and thermal fields also consists of systems of partial differential equations. These can be solved by FEM [20]. Coupled electrical-mechanical-thermal FEM simulations are available within Abaqus. As temperature measurements proved stable conditions, only mechanical-electrical simulation were performed. The NRB samples were hereby idealised by using axial symmetry. Figure 5.6a displays the model and the imposed boundary conditions schematically. The electric current was induced on the top of the sample at the same location where the displacement was prescribed. In the symmetry plane, where the sample was fixed in length direction, the sample was grounded.

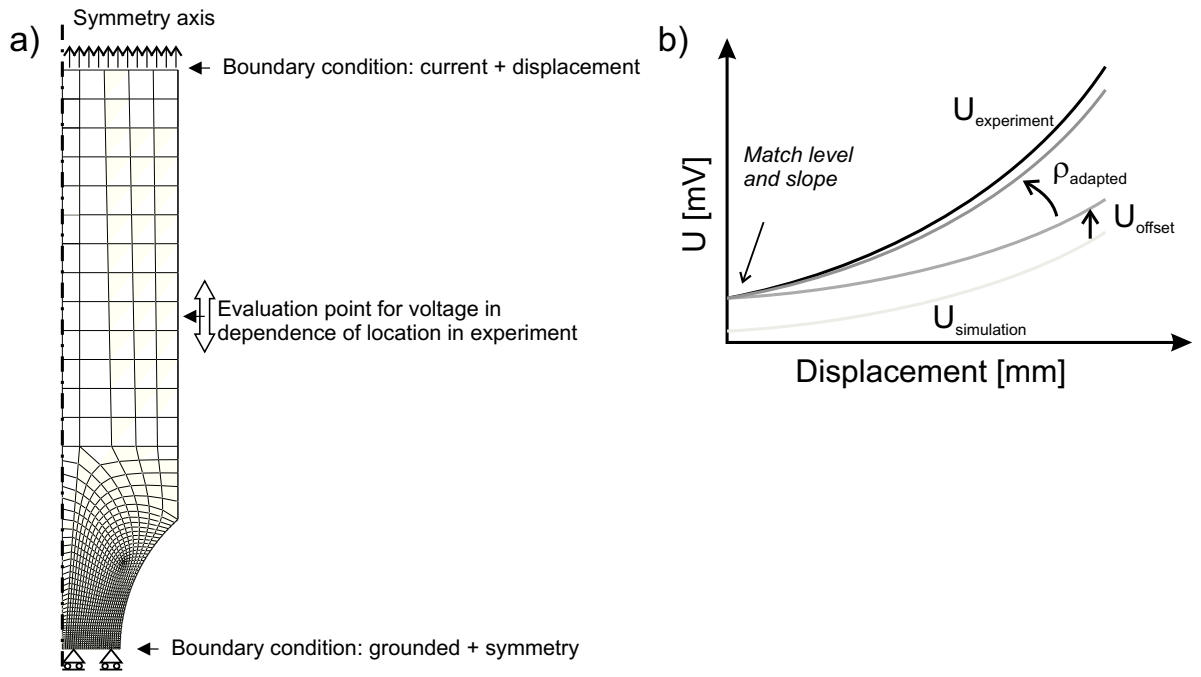

Figure 5.6.: a) Axisymmetric simulation model for electrical-mechanical simulations b) Post-processing of simulation results to match the actual resistivity and measurement distance of an experiment.

During the evaluation of the simulations the electric potential was obtained at the same location where the copper rods were fixed in the experiment. Besides the mechanical properties, the resistivity ρ had to be provided to the simulation. The resistivity depends on the current room temperature and might therefore vary slightly. However, as Eq. 5.1 shows, it is only a multiplicative factor to the result. Therefore, a resistivity of $\rho = 1\Omega mm^2 m^{-1}$ was defined in the simulations and the results were later adapted to the experiments. Moreover, differences between experiment and simulation with regard to the potential measurement distance strongly influenced the results. Such differences occur due to the limited precision in acquiring the copper rod distance as well as the discrete location of nodes in the FE model. These differences contributed to the overall result only as an additive factor because the measurement location was outside the notched region. Therefore, the results were also adapted to the experimental results in the aftermath.

This approach for post-processing is illustrated in Fig. 5.6b. First, the differences in potential measurement location were adapted by an additive factor U_{offset} and second the resistivity ρ was adapted. Both variables were modified such that the level and slope of the experimentally measured potential were matched at the beginning of deformation. This is justified by the assumption that during elastic and early plastic deformation no influence of damage can be expected.

Tensile tests were performed on notched round bars with geometries according Table 5.1. The applied constant current was 1A. This induced measured voltage levels of around 0.2 mV. The deformation speed was 0.2 mm/s. The copper rods were placed approximately 5mm outside the notched region of the sample. The DCPD measurements were performed on experiments subsequently evaluated to determine whether simulated and measured significantly deviate. This would then be an indication that significant damage could be detected. By this approach it is therefore

possible to differentiate between damage and deformation-induced effects on potential measurements.

5.1.3. Limit state definition for model coupling

A central approach of the presented study is to use Gurson simulations to derive nominal, strain-based failure criteria that are suitable for an application in large-scaled component simulations. Consequently, the strain-based failure criteria have to be derived from Gurson simulations. This can be achieved by using cell element models as shown in previous studies [8, 75].

Voided cell models and cell elements are widely used to calibrate and develop Gurson models as explained in Section 2.3.2. Cell elements contain one single finite element and, for example, the GTN model with a complete parameter set. Other versions of Gurson models can be used equivalently. Fully periodic boundary conditions would be required to exactly reproduce the behaviour of a continuum with only one element. However, they can be idealised if the cell walls are kept straight and the forces are applied in normal direction. A further simplification is possible by using axisymmetry, which is acceptable for small void volume fractions [49]. Figure 5.7a displays such an axisymmetric cell element. The cell element can be subjected to a constant load scenario by controlling the ratio of the acting loads. Consequently, the reaction of the embedded constitutive model to this stress state can be very well assessed. The stress state in axisymmetric cell models is characterised by a Lode angle of $\overline{\theta} = 0$ while the stress triaxiality η is a function of the stress ratio [53]:

$$\alpha = \frac{F_1}{F_2} = \frac{3\eta - 1}{3\eta + 2} \tag{5.2}$$

Thus, axisymmetric cell models can detect the constitutive response of the GTN model under different loading situations. This can be used to couple GTN simulations with critical strain criteria [8, 75]. For this purpose, the cell elements are subjected to stress states with characteristic stress triaxialities. The constitutive response for each triaxiality is evaluated, as illustrated in Fig. 5.7b,c. For a certain point, which is assumed to be critical, the plastic equivalent strain is extracted. This is repeated for varying triaxiality levels. By this, the critical strain can be constructed as a function of stress triaxiality. The advantage of this procedure is that by a modification of the GTN parameters it is then possible to derive critical strain criteria for non-existing, virtual materials. This can be used for a reference to nominal properties. However, the resulting Johnson-Cook-like failure strain curve strongly depends on the selection of the critical state.

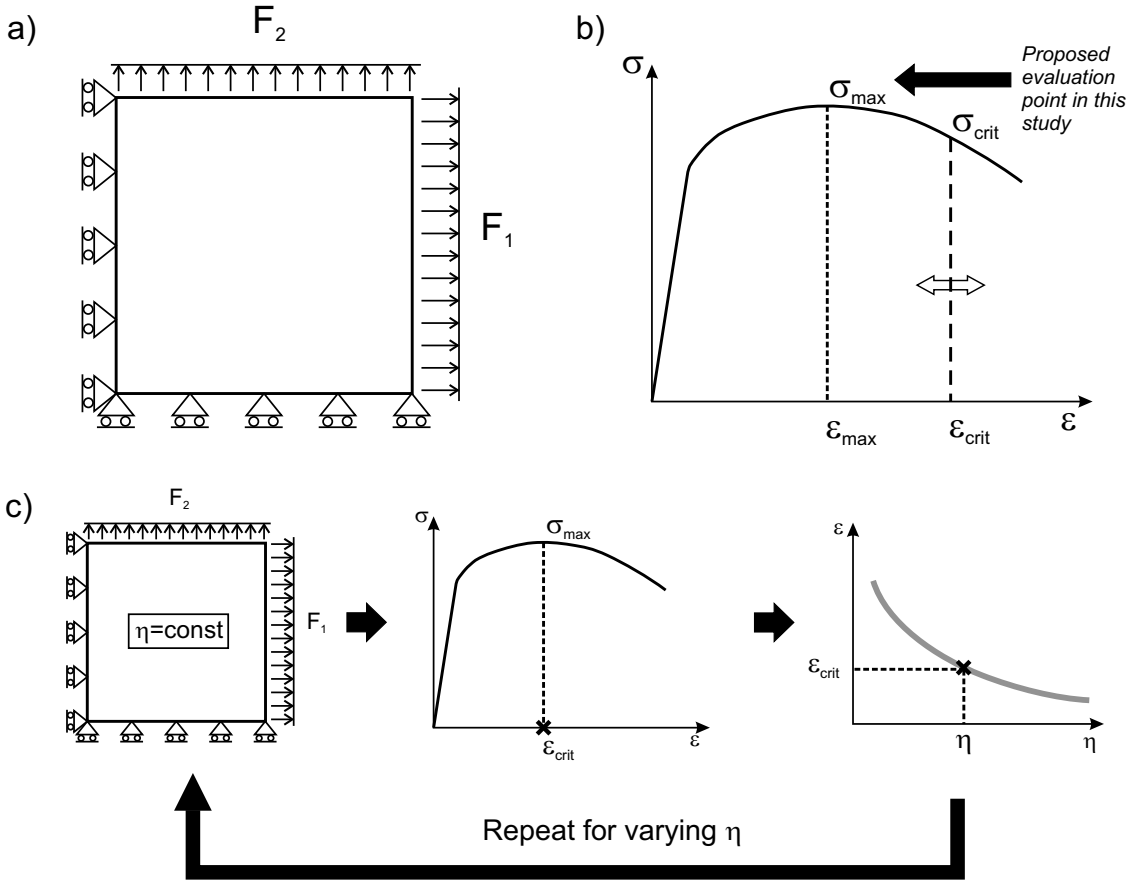

Figure 5.7.: a) Axisymmetric cell model, b) evaluation of the constitutive response, c) derivation procedure for limit strains proposed in this study.

Schruff defined in his study the critical point to be the instance when the deformation behaviour of a multi-axially loaded cell element turns into unilateral deformation. This deformation pattern was frequently used in the literature (e.g. [48, 50]). In voided cell models this assumption is justified since it characterises the collapse load of a material with such a void pattern. However, for cell elements with an embedded GTN model the collapse point is strongly influenced by the selection of the coalescence parameters of the GTN model. These do not fully reflect stress state dependency of ductile failure.

Therefore, a different definition was proposed and used within this study. It is based on considerations about ductile failure in large-scale structures and components. In their study on slant fracture in heavy plates Nielsen and Hutchinson pointed out that ductile failure in such constructions is preceded by the localisation of plastic deformation in what they refer to as “geometrical necking” [134]. This necking can be assessed by large elements and simple constitutive models within the FEM. In real components or structures its location is usually predetermined due to cross section transitions or local weak points like bolt holes. Within this geometrical neck ductile damage starts to accumulate and localise subsequently as well. For large plates, as investigated by Nielsen and Hutchinson, this takes place as a shear localisation in a small planar band. This damage localisation then induces crack growth and thereby final failure. Thus, if a critical strain criterion or a damage curve shall characterise the onset of ductile structural failure this localisation must be the basis of the definition.

Ductile damage is incorporated in the constitutive response of the cell element because the GTN model is a fully coupled model. Consequently, the localisation of ductile damage is indicated by the onset of softening because then the influence of local damage outweighs the local hardening capacity of the material. Therefore, in this study the local onset of softening, represented by the strain at the maximum stress in the constitutive response of the cell element, is proposed and tested as the definition of the critical point for a numerical derivation of critical strains by Gurson simulations.

This definition differs from the ones of damage curves [101] or failure strain curves [60]. The proposed definition tries to capture the instance where the micromechanical damage development begins affecting the structural response. It therefore represents a limit state. To underline this difference, the critical strains in dependence of stress triaxiality will in the following be referred to as limit strain curve instead of damage curve or Johnson-Cook criterion. The final procedure used in this study for the derivation of the limit strain curve is schematically displayed in Fig. 5.7c.

5.2. Results

5.2.1. Relevant damage mechanisms

Stopped tensile tests were performed on samples of the material dvI as described in 5.1.1 to assess the relevant damage mechanisms for the pressure vessel steels. In the following, the force-displacement curves of the tests are presented along with images of the metallographic investigation of the samples central planes (Figs. 5.8 , 5.9, A.11). In all three investigated geometries no relevant amount of voids had formed at the force maximum. At an intermediate displacement stage, approximately midway between force maximum and failure, the development of distributed, small voids was detected. Shortly before failure the voids grew significantly larger in geometries L6R6 (Fig 5.8) and L4R2 (Fig. A.11 in the Appendix). Contrary to that, geometry L4R6 (Fig. 5.9) exhibited less void growth.

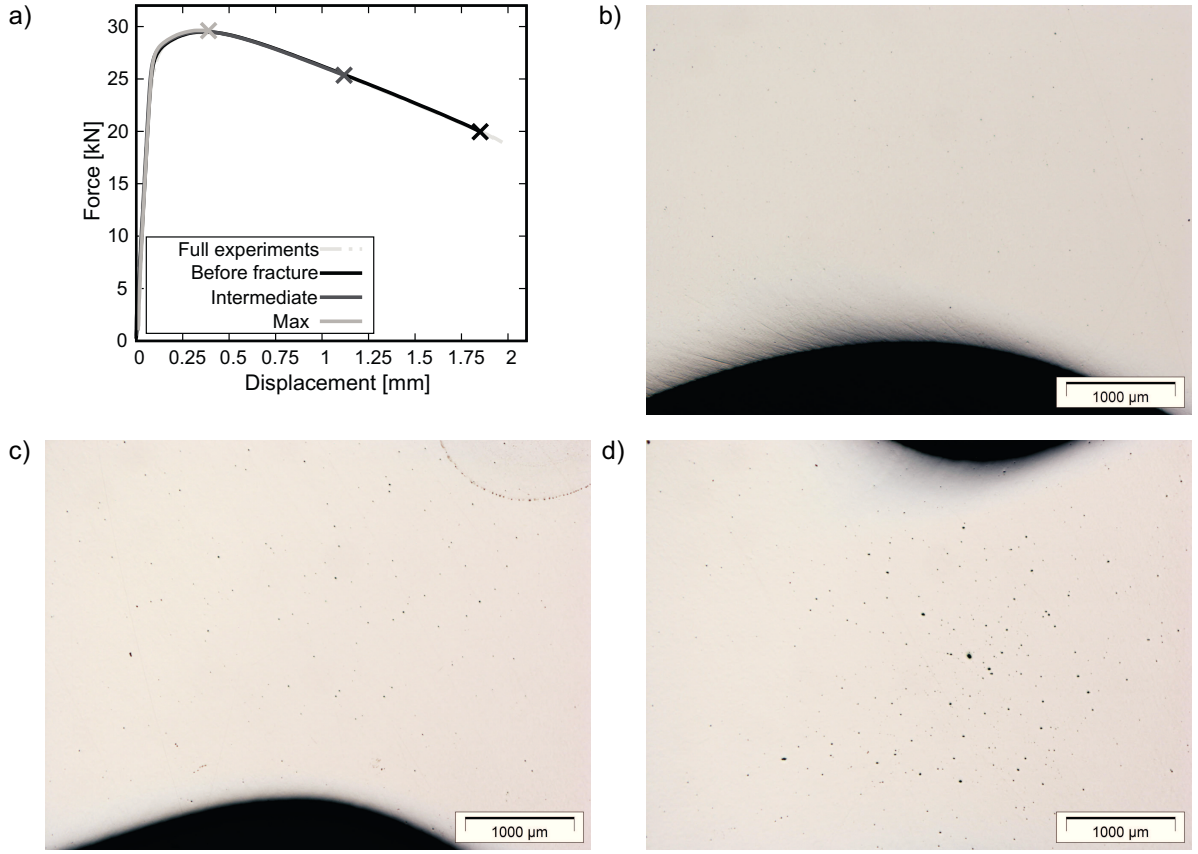

Figure 5.8.: Results of stopped tensile tests on the geometry L6R6: a) Force-displacement curve as well as prepared central sections of stopped experiment at b) force maximum, c) midway between force maximum and failure, d) immediately before failure.

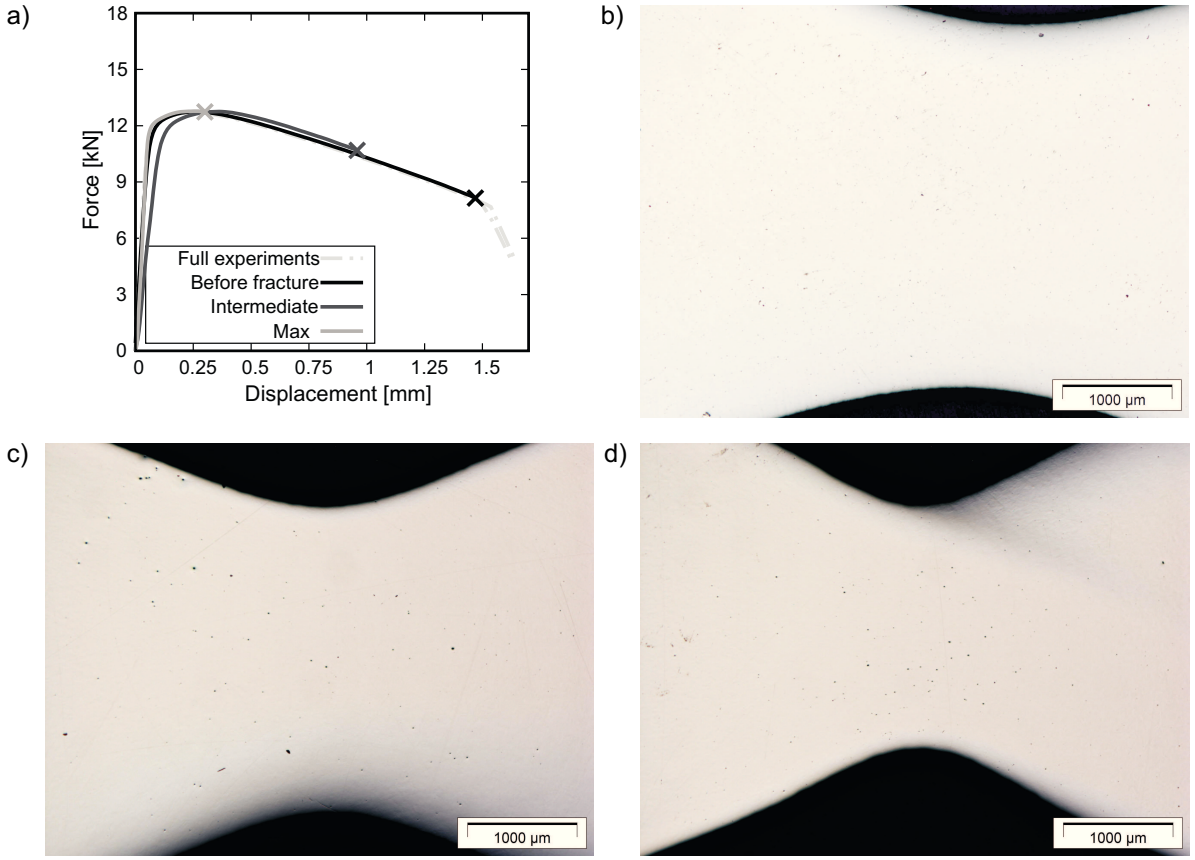

Figure 5.9.: Results of stopped tensile tests on the geometry L4R6: a) Force-displacement curve as well as prepared central sections of stopped experiment at b) force maximum, c) midway between force maximum and failure, d) immediately before failure. The slight deviation of the modulus in the sample stopped midway between failure and force maximum resulted from a different base length of the extensometer.

The area fractions of voids in the final deformation stage were evaluated by the image processing software FIS Olympus Analysis. The notch ground region near the centre was investigated. The absolute values of void area fraction hereby may depend on the magnification that also influences the investigated region. Consequently, it was determined on images with a magnification of 25 and 100 for comparison. The expected variation between the magnification was confirmed (Table 5.2). Because the lower magnification covers in this case a larger region, the results are considered to be more relevant. The L6R6 geometry exhibited the largest void area fraction with a share of 0.37%.

Table 5.2.: Area fractions of voids measured on the central section of specimens stopped shortly before failure.

Geometry	Area fraction of voids shortly before failure [%]	
	25x	100x
L6R6	0.37	0.26
L4R2	0.32	0.14
L4R6	0.17	0.09

However, the metallographic investigations, although cautiously grinded to the central plane, only

evaluate one section. Three-dimensional investigations, such as microtomography, are necessary to check whether important volumetric information is missed by this procedure. One sample of the geometry L4R6, which was also stopped shortly before failure, could be investigated as a demonstration sample at Carl Zeiss Microscopy LLC, Pleasanton, California, USA[1]. The sample was scanned using a ZEISS XRadia Versa 520. A square rod of 3mm side length that included the entire notch region was taken from the initial sample (Fig. 5.10). This was necessary to achieve a higher possible resolution in the scanning process.

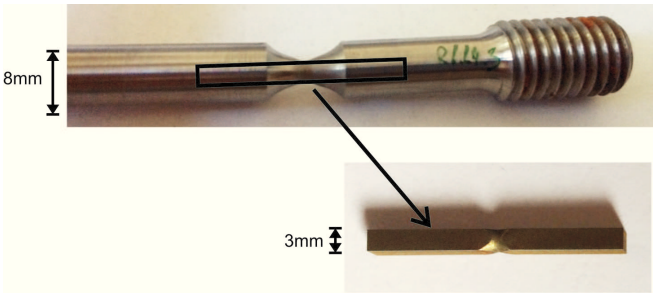

Figure 5.10.: Extraction of the notch region for the investigation by microtomography.

An overview scan, which covered the notch region, was performed using a voxel size of 3.5 µm. Subsequently, a small region at the centre of the sample was scanned with a smaller voxel size of 0.85 µm. The analysis of the results was performed with the software Dragonfly Pro by Object Research Systems, Inc., Montreal, Canada. The scanned volumes are presented in Fig. 5.11.

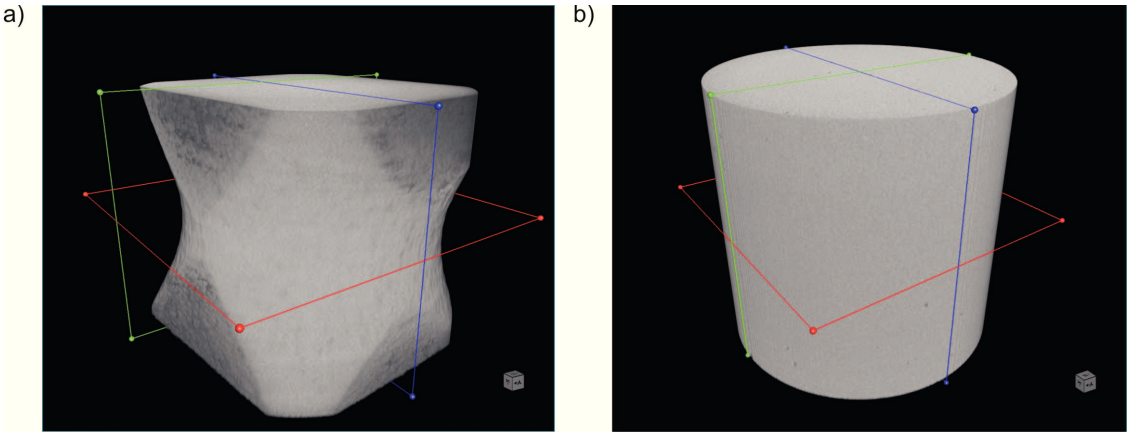

Figure 5.11.: Overview on the scanned regions: a) Larger region of approximately 3.5mm height and 2.6 mm side length, scanned with a resolution of 3.5 µm. b) Smaller region in the notch centre of 0.85 mm height and 0.8 mm side length, scanned with a resolution of 0.85 µm. The blue, red and green markings indicate cutting planes along which virtual cross sections can be investigated as displayed in the following figures.

[1]The scans were performed by Alyssa Browning, Carl Zeiss Microscopy LLC, Pleasanton, California, USA.

The results for the large region are displayed in Fig. 5.12. Only 25 voids were identified that had sizes larger than 3x3x3 voxels. 13 out of the 25 detected voids had volumes between 1000µm³ and 3000 µm³, which is equivalent to diameters of 8-12 µm. The two largest voids exhibit ellipsoidal shapes. The length of their major axis is approximately 100 µm while their minor axes are 30 µm to 70 µm long. Obviously, only a few large voids were present shortly before failure. No crack formation could be detected. Most of the damage could not be captured with such a coarse resolution. Consequently, the central region was scanned with a finer resolution.

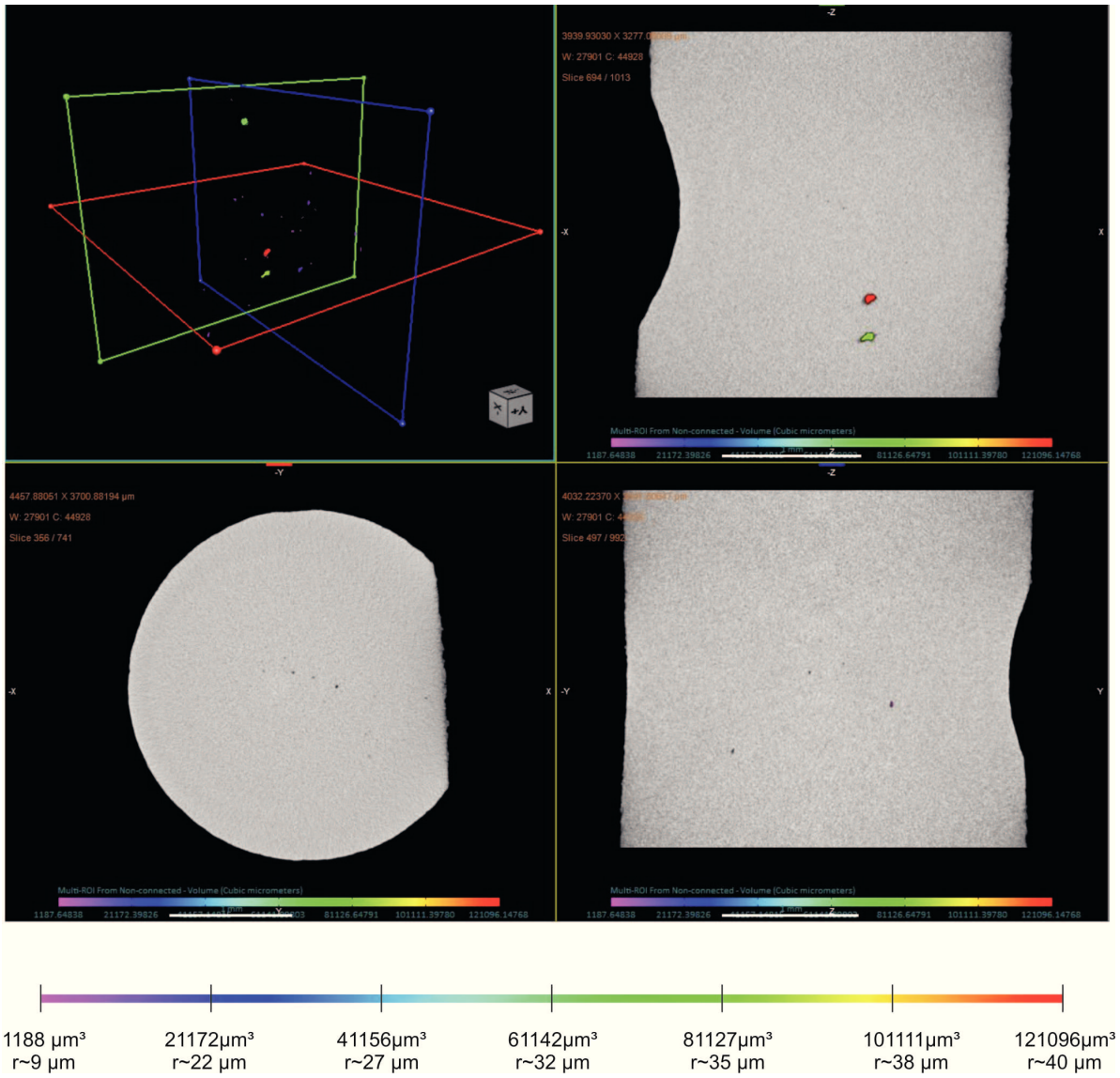

Figure 5.12.: Results of the scan covering the whole notch region including the volume distribution of the identified voids and virtual cross sections (top right: green plane, bottom left: red plane, bottom right: blue plane). Only a few larger pores were identified. The approximate radius sizes were calculated by averaging spherical diameters and cubic side lengths that correspond to each volume.

The smaller region was scanned with a voxel size of 0.85µm. The results are presented in Fig. 5.13. Much more voids could be detected at this resolution. The minimum size of voids considered in the analysis was 3x3x3 voxels. The analysis of the void volume distribution showed that 35% of

the voids were smaller than 50 µm³, 23% had sizes between 50µm³ and 100µm³. This means that the majority of the voids is very small. Only 7 out of 926 detected voids possessed volumes above 5000µm³, corresponding to diameters of 15µm and above. The largest detected void had a void volume of 15690µm³ and a diameter of 20 µm. The total void volume fraction in this region was determined to be 0.06%.

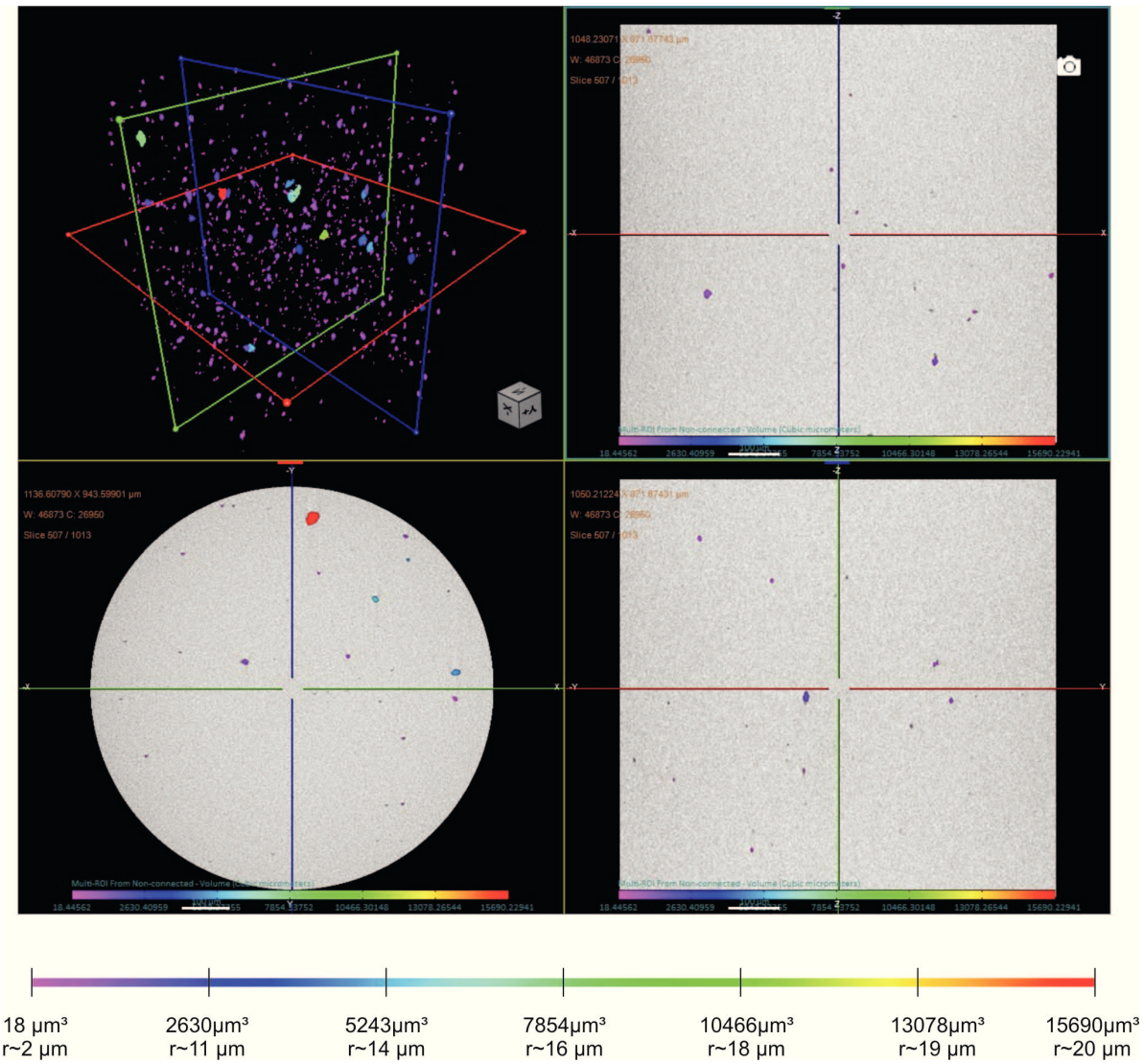

Figure 5.13.: Results of the detail scan of the central region including the volume distribution of the identified voids and virtual cross sections (top right: green plane, bottom left: red plane, bottom right: blue plane).The approximate radii were calculated by averaging spherical diameters and cubic side lengths that correspond to each volume.

These three-dimensional investigations confirm the findings made by the metallographic investigations. The void volume fractions are even lower than the determined area fractions. With both approaches only distributed, small voids could be detected even shortly before failure.

The presented results underline that ductile damage in modern HSLA steels consists as expected of the classical stages of void nucleation, growth and coalescence. Yet, only small, distributed voids are present throughout the majority of the deformation history due to the low inclusion content. The constitutive response of the material is dominated by its plastic properties. Only very

shortly before failure, the deformation localises and a relevant amount of voids is created and starts growing and coalescing. The area fractions which can be detected at this stage are still below 1%. Similar findings have been reported by Daly et al. [135] for a reactor pressure vessel steel and by Tasan et al. [128] for a DP600 steel. Consequently, the damage values or void volume and area fractions detected in reality seem to be lower than the ones predicted by Gurson or cell model studies. These give typical values for void coalescence of a few percent. This difference can be explained by the inherent model idealisations, such as the assumption of regular void distributions.

This finding supports the selection of the onset of local softening as the limit state for model coupling. The local growth of larger voids, as e.g. displayed in Fig. 5.8d, results in a local softening if the neighbourhood of a large void is considered as a homogenisation zone. Thus, the proposed limit state might be set in relation to the micrographs. Local softening may for steels of this high purity be a better choice for the limit state definition than void coalescence because a significant amount of void coalescence is detected very late in the failure process. The local onset of softening therefore represents a reasonable assumption for the limit state.

5.2.2. Assessment of the detection capabilities of the DCPD

Within his study, Schruff used CT samples with modified thickness in combination with the DCPD in order to assess the critical state of damage initiation. However, the traditional sample geometries for the derivation of Johnson-Cook-like critical strain criteria are notched round bars. They have the advantage that they characterise an uncracked state and thereby relate much more to damage mechanics. Therefore, the calibration of GTN model parameters was performed in this study on NRB.

To assess whether the DCPD is able to capture the damage development in NRBs, the newly developed method described in Section 5.1.2 was applied. In the following, results are presented for the geometries L4R6 and L6R6 providing two samples per geometry. Fig. 5.14 plots the experimental results of force and potential measurement as a function of the displacement in black. The results of force and potential from the electrical-mechanical simulation are displayed in grey. The simulation results have been adapted to the level of the experimental values at the beginning of the experiment by the procedure described in 5.1.2. Table 5.3 lists the corresponding adaptation values.

Table 5.3.: Applied adaptation factors for matching the potential start level of experiment and simulation

	L4R6_4	L4R6_5	L6R6_4	L6R6_5
U_{offset}[mV]	-0.002561	-0.005465	-0.011795	-0.013312
$\rho_{adapted}[\Omega mm^2 m^{-1}]$	0.285	0.285	0.300	0.300

Theoretically, the measured potential should exceed the simulated values in the late stages of deformation due to the cross section reduction induced by void formation. For the results of the two samples of the geometry L4R6 (Fig. 5.14a,b) this could only be observed after the load drop in the experiment. At this point the sample had already failed and was just breaking apart. Before the load drop, the measured and simulated potential match perfectly. Similar findings were achieved

in the samples of the geometry L6R6 (Fig. 5.14c,d). Here, the testing machine stopped recording the data immediately after the load drop. Therefore the final deviation is missing, and the data matches perfectly until failure.

Consequently, the entire potential rise detected in the investigated samples could be attributed to the deformation which was covered by the simulation as well. This result was achieved despite the existence of voids that was proven by the stopped experiments. Hence, the effect of the existing voids on the potential seems to be too small to affect the measured potential. This finding is in accordance with analytical studies performed by Tada et al. [136]. They used analytical equations to estimate which influence small, distributed, penny-shaped cracks had on a measured potential. They reported that 450 cracks with a mean diameter of 23 µm² were required per mm³ material volume to induce a 1% rise in the measured potential. This implies an effective crack area of approximately 0.75mm² per mm³. The number and diameter of voids in the NRB before the load drop do not reach these numbers. Consequently, it can be concluded that the DCPD cannot measure the actual damage state within NRB tests.

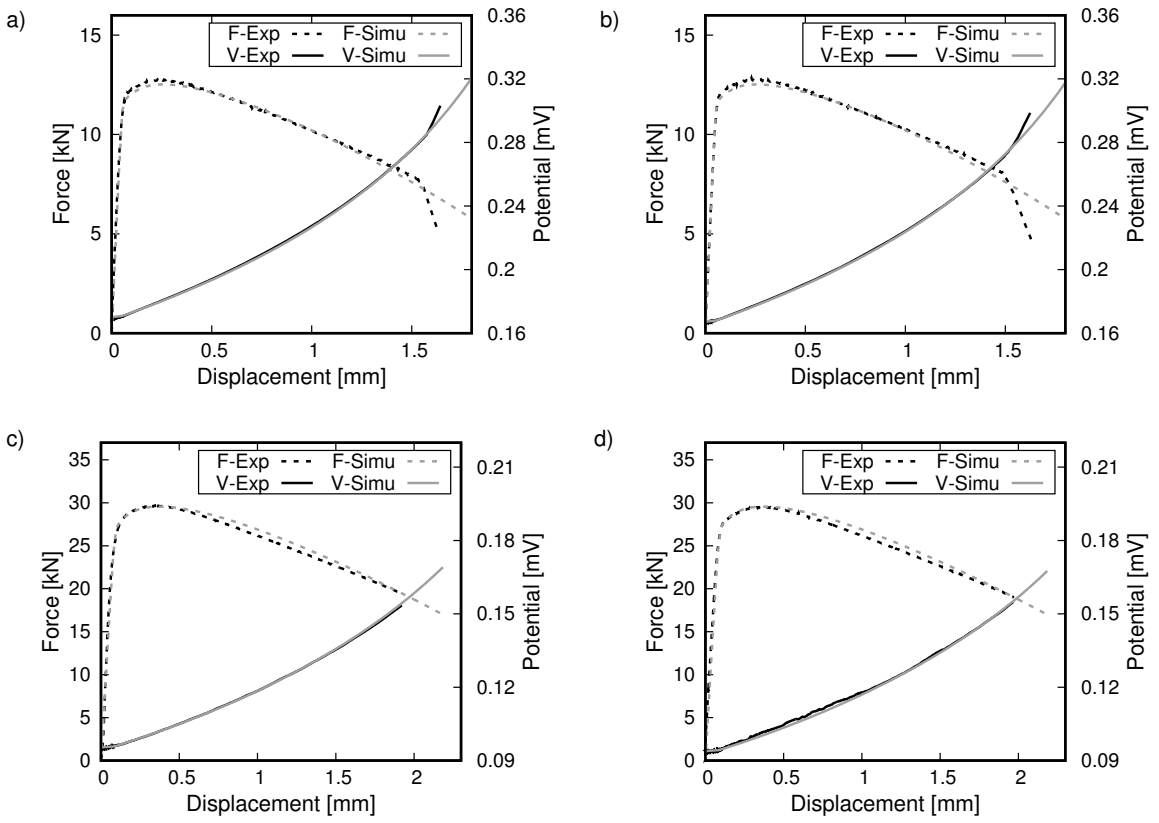

Figure 5.14.: Results of tensile tests with potential measurements as well as the simulation results of force and potential on NRB of the geometry L4R6 (a: L4R6_4, b: L4R6_5) and L6R6 (c: L6R6_4, d: L6R6_5).

5.3. Summary

The metallographic investigations showed that void formation takes place only in the very late stages of deformation for steels with such a low inclusion content. Consequently, the plastic properties dominate the failure process. Based on these findings and theoretical considerations, the onset of local softening is defined as the limit state which shall be used in the modelling concept. An application of the DCPD for the detection of this limit state seems not feasible. Based on the selected limit state definition, the modelling concept was developed. This is presented in the following chapter.

6. Development of a comprehensive modelling concept

Three main aspects were explored to form a comprehensive modelling concept (Fig. 6.1). One focus was defining a framework for the reliable toughness correlation. A key approach of the presented study is to use Gurson models for referring to nominal toughness levels by simulated Charpy tests. An artificial deterioration of the Gurson parameters enables the correlation of parameter set and nominal toughness level. Due to their micromechanical motivation, Gurson models form a better basis for such a procedure than phenomenological models. However, their parameter selection is non-unique and might therefore influence the results. Thus, a calibration scheme was explored to enable a reliable toughness correlation. A second aspect explored was the extension of the procedure with regard to Lode angle effects. Finally, the application of limit strain curves may lead to problems when using them in large-scaled components with varying mesh sizes. A possible solution was proposed. The applied methods are explained below, followed by a presentation of the corresponding results.

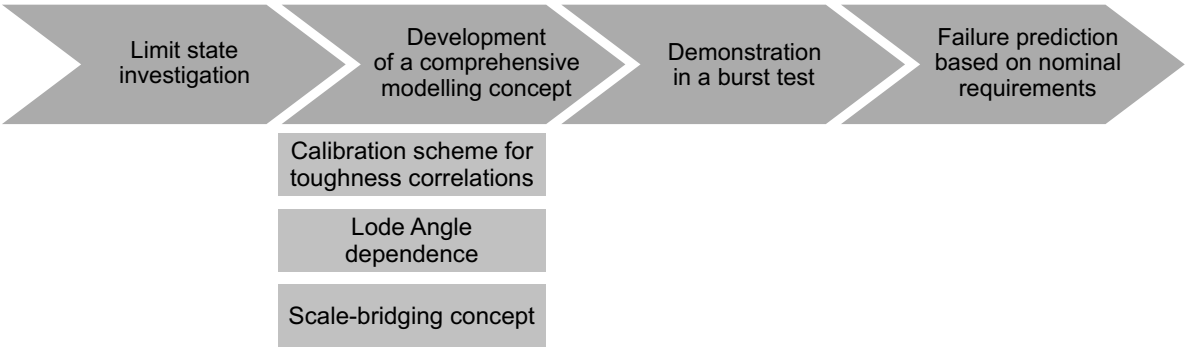

Figure 6.1.: Overview on the investigations for a comprehensive modelling concept.

6.1. Methods

6.1.1. Calibration scheme for toughness correlations

As stated in [8], the procedure of correlating GTN simulations with limit strains suffers from the non-uniqueness of the GTN parameter selection. This non-uniqueness may lead to the fact that different damage curves are derived from an identical toughness level. To overcome this weakness, a calibration scheme is investigated and proposed. The aim is to minimise the non-uniqueness in the GTN parameter determination and thereby also in the derived limit strains. To achieve this, the sensitivity of the entire procedure with respect to the GTN parameter selection was investigated.

6.1.1.1. Sensitivity analysis

The sensitivity analysis was performed on the material P500Q. From [75] a calibrated parameter set and a flow curve were available that were used as a reference. All tests relevant for the numerical derivation of limit strain curves were included in the sensitivity analysis. Therefore, NRB, Charpy, and cell element simulations were considered. Adiabatic heating was neglected in the Charpy simulations to reduce the simulation effort.

The NRB sample was based on B8x40 samples. It had a cylindcrical length of 48 mm, a notch radius of 2.61 mm and a notch ligament radius of 2.18 mm. For its simulation an axisymmetric model was employed in a quasi-static Abaqus/Explicit analysis. CAX4R elements and the built-in implementation of the GTN model were used. The Charpy simulation model consisted of a standard Charpy-V-sample according to EN ISO 148. Striker and bearing were simulated as rigid solids. The striker was equipped with a point mass and an initial velocity. The contact definitions between sample and bearings were assumed to have a friction coefficient of 0.01 due to the polished sample surfaces. The simulations were performed as dynamic analyses in Abaqus/Explicit using C3D8R elements and the built-in implementation of the GTN model.

The cell element was designed with a height and length of 1mm; since stress-strain curves are extracted as an output, its dimensions are irrelevant. It consisted of one axisymmetric element of the type CAX8R and was modelled within an Abaqus/Standard analysis. This allowed for using the Riks algorithm for load control. The Riks algorithm is a convenient way to ensure a constant load ratio for a constant triaxiality while being able to simulate softening [137]. The GTN model was embedded by a UMAT user subroutine for Abaqus that was available at the department.

All relevant GTN parameters were varied in a one-factor-at-a-time-analysis to a maximum as well as a minimum value. The variation values were selected based on literature studies (e.g. [50,72,74]) within the common range for each type (Table 6.1). Since the flow curve itself also represents a significant influence, the initial Hollomon extrapolation was modified in overall stress level by a simple parallel shift of ± 100 MPa. Additionally, the hardening exponent was varied (Table 6.2). Furthermore, the mesh size influence on the simulation of NRB and Charpy tests was assessed by simulations of varying mesh sizes. From the results of the sensitivity analysis, a calibration scheme was proposed to reduce the influence of the non-unique parameter selection.

Table 6.1.: Selected variations of GTN parameters for the sensitivity analysis

Parameter	f_0	f_N	S_N	ε_N	f_c	κ	q_1	q_2
Reference value [75]	0.00185	0.00215	0.4	0.12	0.015	1.1	1.5	1
Max value	0.01	0.015	0.6	0.3	0.05	3	2.5	1.5
Min value	0.0005	0.0005	0.1	0.05	0.005	1	1	0.5

Table 6.2.: Selected variations of the flow curve for the sensitivity analysis

Parameter	$\sigma_y(\overline{\varepsilon}^p)$ [MPa]	n
Reference value [75]	$978(\overline{\varepsilon}^p)^{0.134}$	0.134
Max value	$978(\overline{\varepsilon}^p)^{0.134}+100$	0.2
Min value	$978(\overline{\varepsilon}^p)^{0.134}-100$	0.05

6.1.1.2. Validation of the calibration scheme and implementation of adiabatic loading conditions

To assess whether the proposed calibration scheme can fulfil the aims, additional experiments on the steel P500Q were conducted. The parameter set from [75] was re-calibrated according to the defined calibration scheme. NRB samples with a length of 40mm, a base diameter of 8mm, a ligament diameter of 6 mm and notch radii of 1.5 mm, 3mm, and 8mm were produced and tested. Five tests were performed for each geometry. The fracture mechanics test was performed on a standard 1-CT-sample according to ASTM E399-12. The sample had a sharp fatigue pre-crack with an average depth of 26.21 mm. Tensile tests on elevated temperatures were performed on smooth B8x40 samples in a temperature range from 50°C to 250°C. Moreover, five high speed tensile tests were performed at strain rates of 150/s and 250/s. The samples for high speed testing were also based on B8x40 tensile samples but had a testing region with a reduced diameter of 4mm on a length of 20mm to reduce the testing forces. Charpy tests were conducted at room temperature to test whether the re-calibrated model can reproduce the toughness behaviour of a pressure vessel steel.

Since a complete comparison with a Charpy tests requires a consideration of adiabatic loading conditions, an existing implementation of the GTN model in a user defined subroutine VUMAT was adapted accordingly. Temperature softening as well as strain-rate-induced hardening have to be considered under adiabatic conditions. To this purpose, formulations used by Hosten were adopted [16]. For temperature softening an exponential factor formulation in dependence of three fitting parameters c_T^i was used:

$$f(T) = c_T^1 \exp(-c_T^2 T) + c_T^3 \tag{6.1}$$

The mechanisms of thermally activated flow induce material hardening under moderate strain rates. This hardening can be characterised by a logarithmic formulation:

$$f(\dot{\overline{\varepsilon}}^p) = c_{\dot{\varepsilon}}^1 \ln \dot{\overline{\varepsilon}}^p + c_{\dot{\varepsilon}}^2 \tag{6.2}$$

For very high strain rates, the effect of dislocation damping can be considered by an additive factor so that the complete formulation as given by Hosten then reads:

$$\sigma_y(\overline{\varepsilon}^p, \dot{\overline{\varepsilon}}^p, T) = \left[\sigma_y(\overline{\varepsilon}^p) \cdot f(\dot{\overline{\varepsilon}}^p) + c_{\dot{\varepsilon}}^3 \dot{\overline{\varepsilon}}^p\right] \cdot f(T) \tag{6.3}$$

This formulation was implemented into the hardening calculations of the GTN VUMAT. The VUMAT used the algorithm of Aravas [64] for the numerical integration of the GTN model formulations. This algorithm is based on a Newton-Raphson scheme for solving the system of nonlinear equations imposed by the GTN model formulations. Consequently, the corresponding partial derivations of this algorithm, which include the hardening value, had to be adapated to the new formulations as well.

All tests were simulated with the re-calibrated parameter set to check whether they can sufficiently reproduce the behaviour. The derived limit strain curve was then compared to the one derived in [75]. Results are presented in Section 6.2.

6.1.2. Consideration of Lode angle influences

Plane strain states often prevail in thick-walled constructions produced from heavy plates, such as pressure vessels. As introduced in Chapter 2, such states are characterised by a significantly lower failure strain. To ensure a safe application of the newly developed modelling concept it is therefore necessary to consider Lode angle influences. Consequently, the previously developed methodology was extended. As the numerical derivation of critical strains involves two central aspects, GTN and cell element simulations, both had to be modified. The first step was to extend the GTN simulations towards Lode angle dependence.

6.1.2.1. Implementation of a Lode angle dependent Gurson formulation

As detailed in Section 2.3, studies in the field of damage mechanics consider possible Lode angle influences since 2008. Such model formulations have also been investigated for Gurson models. Several formulations were provided for example by Xue [138], Nahshon and Hutchinson [27], and Gao et al. [139]. Jackiewicz [140] compared the Xue and the Nahshon-Hutchinson (NH) formulations and found that they could be equally well fitted to experimental data. The NH model was successfully tested on DH36 steels [79], Weldox 420 and 960 steels [141], and aluminium [142]. However, Nielsen and Tvergaard found that the NH modification overestimated the Lode angle influence for high stress triaxialities and therefore proposed a slight modification. This model version, in the following referred to as Nielsen-Tvergaard model (NT), was successfully tested by Dunand and Mohr on a TRIP780 steel [28]. It could reproduce the deformation and failure behaviour of samples covering a wide variety of stress states. A comparison with micromechanical investigations by voided cell elements proved that the NT model, although the extension formulation is phenomenological, can cover the micromechanical deformation modes reliably [55].

Due to their wide acceptance in the Gurson community, model formulations based on the proposal of Nahshon and Hutchinson were selected for this study. It was tested whether the original formulation by Nahshon and Hutchinson or the extension by Nielsen and Tvergaard was more suitable for the application in the proposed modelling concept. The formulations of the NH and NT model are given in the following. Both adopt the yield potential and void coalescence law from the GTN model without alterations:

$$\Phi = \left(\frac{\sigma_e}{\sigma_y}\right)^2 + 2f^* q_1 \cosh\left(\frac{3}{2} q_2 \frac{\sigma_H}{\sigma_y}\right) - (1 + q_3 f^{*2}) \leq 0 \tag{6.4}$$

$$f^*(f) = \begin{cases} f & f \leq f_c \\ f_c + k(f - f_c) & f > f_c \end{cases} \tag{6.5}$$

The equations for the computation of κ (Eq. 2.52) and f_u^* (Eq. 2.51) are valid likewise. The modification for Lode angle dependence is included in the damage evolution law. It contains, additional to the void growth term of the GTN model, a shear damage term (Eq. 6.6). The nucleation law according to Chu and Needleman according to Eq. 2.49 is not included here but can be used in combination.

$$\dot{f} = (1 - f)\dot{\varepsilon}_{kk}^p + \dot{f}_{shear} \tag{6.6}$$

The NH and NT formulations employ different formulations of this shear damage term. In the NH model, the shear damage term (Eq. 6.8) is given in dependence of the function $\omega(\sigma_{ij})$ as introduced in Eq. 2.38 as a measure for the third invariant, respectively the Lode angle. In addition, a scaling factor k_ω, the current value of f, and a normalised deviatoric strain measure $\frac{s_{ij}\dot{\varepsilon}^p_{ij}}{\sigma_e}$ derived from Eq. 2.28 are included in the term.

$$\dot{f}_{shear} = k_\omega f \omega(\sigma_{ij}) \frac{s_{ij}\dot{\varepsilon}^p_{ij}}{\sigma_e} \tag{6.7}$$

Nielsen and Tvergaard introduced a function ω_0 instead of using $\omega(\sigma_{ij})$ (Eq. 6.8). It diminishes the influence of the shear damage term in high triaxiality regions. They used a simple linear interpolation function $\Omega(\eta)$ so that ω_0 is defined by Eqs. 6.9 and 6.10. As long as the stress triaxiality η is smaller than a boundary value η_1, the shear damage term is fully active. If the stress triaxiality is larger than the second boundary value η_2, the shear damage term vanishes, and the original formulation of the GTN model is active. In between η_1 and η_2, the influence of the shear damage term is decreased linearly.

$$\dot{f}_{shear} = k_\omega f \omega_0 \frac{s_{ij}\dot{\varepsilon}^p_{ij}}{\sigma_e} \tag{6.8}$$

$$\omega_0 = \omega(\sigma_{ij}) \cdot \Omega(\eta) \tag{6.9}$$

$$\Omega(\eta) = \begin{cases} 1 & \eta < \eta_1 \\ \frac{\eta - \eta_2}{\eta_1 - \eta_2} & \eta_1 \leq \eta \leq \eta_2 \\ 0 & \eta > \eta_2 \end{cases} \tag{6.10}$$

The NH model introduces only one additional parameter, the scaling parameter for the damage function, k_ω. The NT formulation adds two boundary values for the triaxiality functions, η_1 and η_2. Due to the consideration of the third invariant these models, in contrast to the original GTN model, predict damage development under pure shear stress states. Yet, this also implies that the variable f is no longer tied to the plastic volume change and that is has to be considered as a phenomenological damage term rather than an effective void volume fraction [79].

The available UMAT and VUMAT formulations of the GTN model were modified for the implementing the NH and NT model formulations. Xue et al. [79] and Achouri et al. [143] showed that splitting the plastic strain tensor into a volumetric and an isochoric part, which is a basic element of Aravas integration algorithm [64], can be used for the numerical implementation of Eq. 6.8 as well. Within the VUMAT and UMAT subroutines, which are based on the solution procedures of Aravas and Zhang [144], the derivatives for the Newton-Raphson algorithm as well as for the formulation of the material stiffness matrix were modified accordingly. This was only necessary for derivations that contain the modified variables or are performed with respect to them. Since the yield potential is not modified, no alterations on its direct derivations were required. Both implementations were successfully validated in comparison to analytical solutions for simple loading cases, which are provided in [143, 145].

6.1.2.2. Implementation of three-dimensional cell elements

Cell elements can likewise be used in a cubic form (e.g. [51]). A three-dimensional cubic cell element allows the variation of stress triaxiality and Lode angle [146]. Consequently, such a cell element was employed in this study (Fig. 6.2). By varying the ratio of the forces, the Lode angle and the stress triaxiality can be defined arbitrarily. Table A.1 lists ratios of the applied forces that induce certain stress states. The load was applied via the Riks algorithm and the cell model consisted of a C3D20R element. The cell model was used in combination with a UMAT of the NH or NT model. The constitutive response was obtained and evaluated at the onset of softening. Thereby, the procedure of the numerical derivation provided limit strains in the 3D-space of strain, stress triaxiality, and normalised Lode angle factor. As a result, a limit strain locus was derived instead of a limit strain curve. For its mathematical description, the symmetric formulation of Bai and Wierzbicki (Eq. 2.44) was adapted. Consequently, the equation for the derived limit strain locus is:

$$\varepsilon_c = \left[D_1 e^{-D_2\eta} - D_3 e^{-D_4\eta}\right] \overline{\theta}^2 + D_3 e^{-D_4\eta} \tag{6.11}$$

The combination of a Lode angle dependent Gurson model and the three-dimensional cell elements enables the consideration of Lode angle effects in pressure vessel simulations. Yet, in some cases an adaptation of the limit strains to the mesh size might be required. This is discussed in the following section.

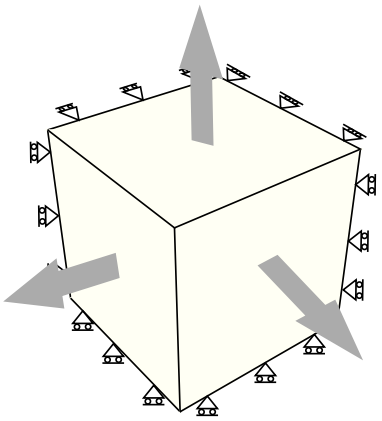

Figure 6.2.: Schematic illustration of a three-dimensional cell element.

6.1.3. Scale-bridging concept

6.1.3.1. Problem description and literature study

Strain-based failure criteria, like the Johnson-Cook criterion or the limit strain curve, are robust and effective. However, they have the fundamental disadvantage that the computation of strains depends on the selected base lengths in localisation zones. Figure 6.3 illustrates the corresponding relations. The critical strains according to the previously described procedure characterise the onset of softening within a pronounced neck. Once necking has occurred, all deformation takes place within the smallest cross section of the neck. As a result, very high local strains are achieved.

Since the limit strain curve refers to these local strains, it is also characterised by a high strain level. In the large-scale simulation of a pressure vessel, deformation will also localise in suitable regions. These are for example cross section transitions such as the one from nozzle to vessel body. However, due to computational requirements the achievable mesh size is limited. If the deformation is however distributed on an element of 2mm length, the computed resulting strain will be much smaller than if it would be distributed on an element of 0.1 mm. Consequently, the critical strain might not be achieved although in reality failure may occur.

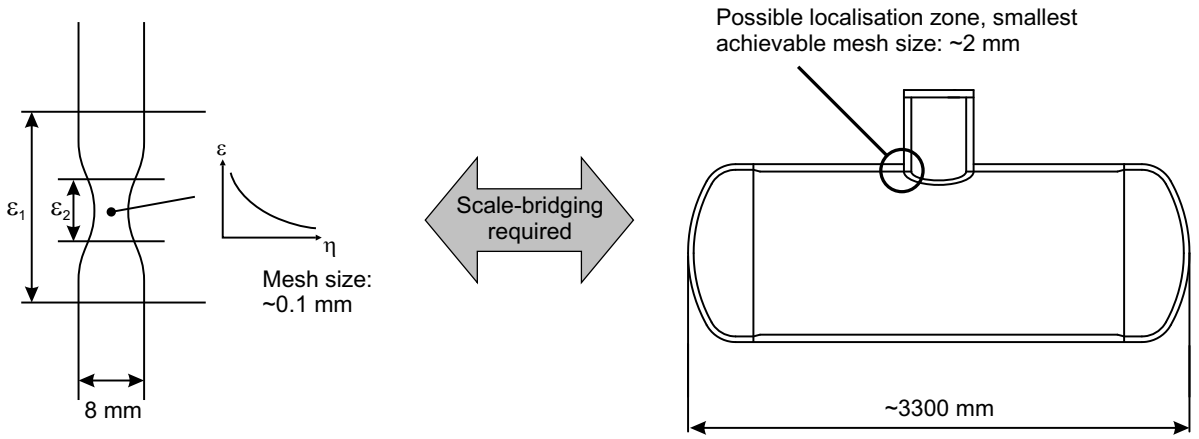

Figure 6.3.: Illustration of the dependence of the strain computation on the base lengths within localisation zones and the need of scale-bridging.

Such problems rarely arise in classical studies on damage mechanics because they are mostly concerned with the correct reproduction of the failure behaviour in laboratory samples. Contrary to that, research fields that deal with the failure prediction of very large structures regularly meet this problem. Examples can be found in studies on the failure of large-scaled ship structures (e.g. [147,148]). These are mostly modelled with large shell elements. Such elements cannot reproduce the formation of necking zones because they are smaller than the element size. Consequently, adaptation strategies, which correlate a current strain in the shell element to a failure strain, are under ongoing research. Walters [149] summarised that classical correlation functions used for such purposes refer the failure strain of a larger element ε_{fShell} to the ratio of the element length l_e and thickness t via two constants A and B:

$$\varepsilon_{fShell} = A + B\frac{t}{l_e} \tag{6.12}$$

Hereby, the constant A mostly represents the strain outside the necked region, while B is a multiplicative correction of the failure strain. Walters, as well as other studies (e.g. [150]), points out that a consideration of stress triaxiality might be necessary. In summary, these studies correct the failure strains by multiplying functions in dependence of the element size. Yet, these functions were developed for shell elements. Within the pressure vessel simulation, solid elements will be used. Consequently, the approaches are not directly transferable. No similar approaches for solid elements were available to the author's knowledge.

6.1.3.2. Solution approach

One possibility to circumvent this problem is the use of submodelling. This technique is already implemented within Abaqus. Hereby, a global large-scale model is simulated with a coarse mesh. Subsequently, a smaller region of interest is defined. The displacements that this region's boundaries experienced throughout deformation history are transferred on the corresponding cut-out of the global model. This cut-out can then be remeshed with smaller elements and be simulated with the stored displacements as imposed load so that the reaction of the global model is preserved, but a finer mesh can be achieved. However, this approach is also time-consuming and not suitable for an application in a large number of analyses within a probabilistic safety concept. Therefore, the possibility of using a scaling function similar to the ones used for ship-structures was investigated.

To find a solution approach, the theoretical development of strains in a simplified setting was considered. It was assessed how engineering and true strain develop if a constant displacement u is applied to different base lengths l, as schematically displayed in Fig. 6.4a. The results (Fig. 6.4b), computed according to Eqs. 2.2 and 2.5, point out that the achievable strain values strongly reduce with increasing base length. Eq. 6.13 indicates that a formulation of the strain as a function of the base length under constant deformation may be formulated in dependence of the inverse of the base length:

$$\varepsilon(l) = \frac{u}{l} = f(l^{-1}) \tag{6.13}$$

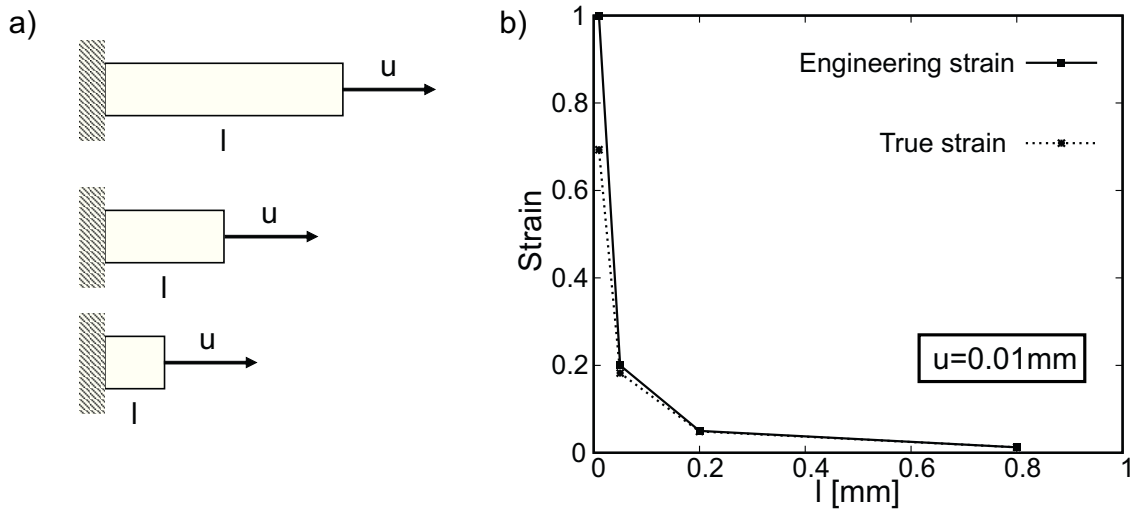

Figure 6.4.: Development of engineering and true strain if an element of varying length l is subjected to the same displacement of u=0.01mm.

The simplified setting should be similar to the situation in a neck, since the deformation only takes place in a small region. To verify this, a further investigation a similar study was performed on the simulation of a L4R2 NRB made of the material dvI. For this purpose, the deformations were extracted from the simulation at different locations, as schematically displayed in Fig. 6.5a. The resulting true strains for different gauge lengths, illustrated by ε_1 and ε_2, were calculated and compared to the local strain of the central element ε_{local}. The results, displayed in Fig. 6.5b, can be well correlated to a power function of the form $\varepsilon(l) = 0.384 \cdot l^{-0.951}$.

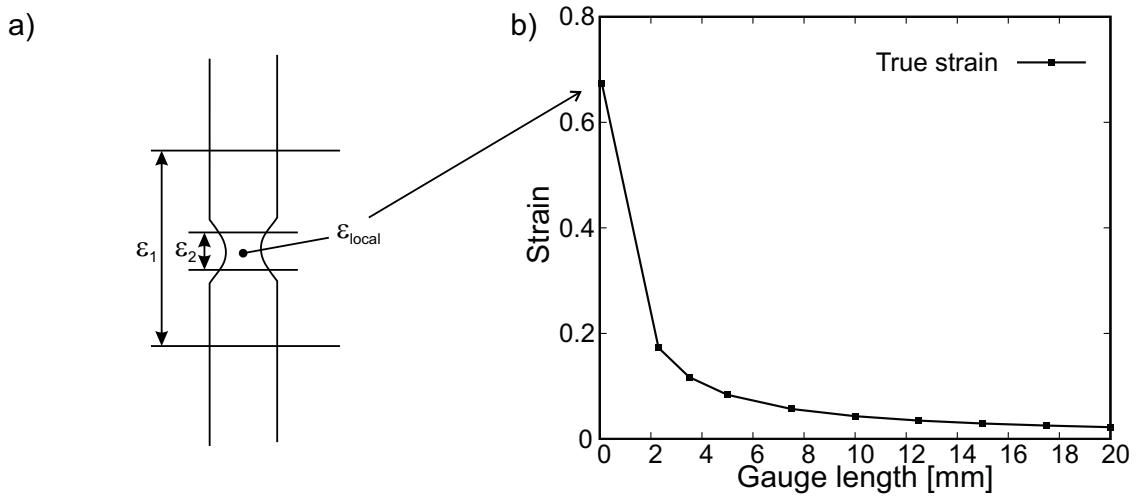

Figure 6.5.: Computed true strain values from varying gauge lengths in the simulation of a NRB.

In summary, power laws seem to be promising formulations for possible scaling limit strain criteria. Such formulations were thus explored within this study for a use in pressure vessel simulations. To achieve this, the development of equivalent plastic strains in dependence of the mesh size was analysed in the more complex loading situations that were present in the large-scale vessel simulation. The results are consequently not presented in this chapter but in Section 7.2.4.

6.2. Results

6.2.1. Calibration scheme for reliable toughness correlations

The selection of GTN model parameters influences the numerically derived limit strain curves. Since this selection is non-unique, different parameter sets may be able to reproduce identical results in Charpy simulations but lead to different numerically derived limit strains. This must be avoided. Therefore, a sensitivity analysis was performed to assess the impact of the parameter selection. The aim was to develop a calibration scheme for a reliable numerical derivation of limit strains and guidelines for the parameter modification to meet nominal toughness levels. The results are presented in the following.

6.2.1.1. Sensitivity analysis

The sensitivity analysis was performed, as described in Section 6.1.1.1, by varying one parameter at a time and keeping the others constant. This procedure was performed on simulations of a NRB, a Charpy test and the cell element because these simulation types are central to the proposed modelling concept. The cell element was simulated for stress triaxialities from $\eta = 0.5$ to $\eta = 2.5$ in steps of 0.5. The limit strains were extracted at the onset of softening and analysed for their sensitivity as well. In some cases, the GTN model did not predict softening for a triaxiality of $\eta = 0.5$; consequently, no limit strain could be derived. Additionally, the development of the equivalent stress and the void volume fraction f^* throughout the deformation history was evaluated from cell element simulations subjected to $\eta = 1$ and $\eta = 2.5$ to gain more detailed insights on the impact of individual parameters.

The results are clustered in the following according to the parameter groups given in Section 2.3.2: The initial void volume fraction, the void nucleation parameters, the void coalescence parameters, and the empirical fitting parameters. Additionally, the influences of flow curve variations and different mesh sizes were tested.

A general assessment of quantitative sensitivities is not feasible because the absolute values of the simulation results depend strongly on the selected reference values. Therefore, the performed analysis aimed at establishing the qualitative relations and interdependencies of parameter selection and simulation results.

Influence of the initial void volume fraction f_0 The reference value of f_0 was determined by metallographic investigations in [8]. A variation to $f_0 = 0.01$ and $f_0 = 0.0005$ was performed within the sensitivity analysis. Figure 6.6 displays the results. Within the NRB simulation, f_0 exhibited a strong influence on the load drop in the force-displacement curve (Fig. 6.6a). The overall force level, including the maximum force, was only slightly affected. Contrary to that, a variation of f_0 strongly impacted the maximum force as well as the dissipated energy, represented by the area beneath the force-displacement curve, in the simulation of a Charpy test (Fig. 6.6b).

The cell element simulations revealed which influence a varying f_0 exhibits on a derived limit strain curve. A substantial influence of f_0 on the derived limit strains was detected for almost all

tested values of stress triaxiality, as displayed in Fig. 6.6c. The strain level varied by 34% at a triaxiality of $\eta = 1$. This difference decreased with increasing triaxiality and vanished at $\eta = 2.5$.

The detailed analysis of the development of stress and void volume fraction offers an explanation for this strong impact. Figure 6.6d plots the equivalent stress and the effective void volume fraction f^* as functions of the equivalent plastic strain. The results are provided for two cell element simulations subjected to stress triaxialities of $\eta = 1.0$ and $\eta = 2.5$. It is evident that in both cases there is a strong effect of f_0 on the resulting stress level whereas for $\eta = 2.5$ the position of the maximum stress with respect to strain is constant. Therefore, the derived strain is not affected while for $\eta = 1$ a significant shifting of the maximum position takes place.

In summary, the selection of f_0 has a strong influence on all investigated simulations. Significant effects on the load drop point in NRB simulations, the maximum force and dissipated energy in the Charpy simulation and the overall level of derived limit strains in cell elements were found.

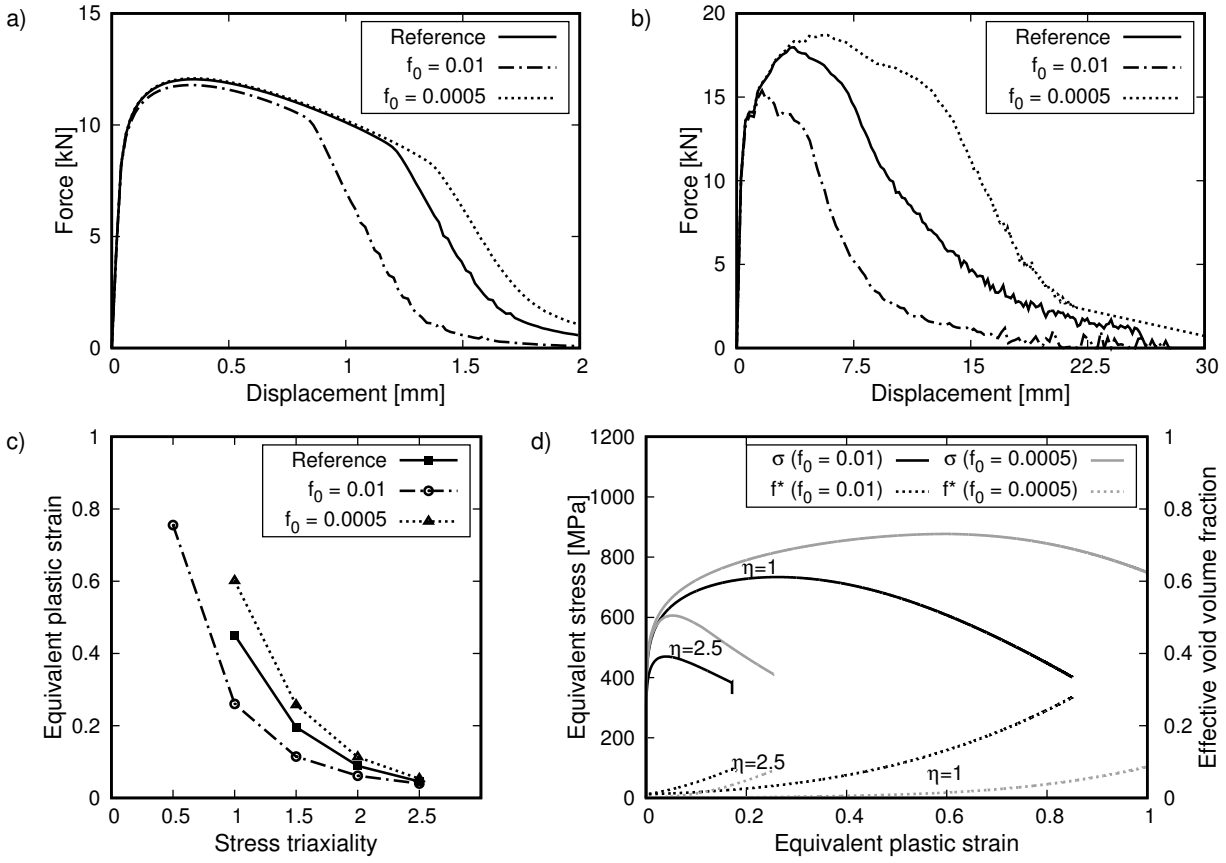

Figure 6.6.: Influence of f_0 on a) NRB and b) Charpy simulations, c) the derived limit strains from and d) σ_e and f^* within cell element simulations for η=1.0 and $\eta = 2.5$.

Influence of the void nucleation parameters f_N, ε_N and S_N The three void nucleation parameters were originally introduced by Chu and Needleman and shall describe the nucleation of smaller voids at secondary particles [65]. The formulation uses a Gaussian distribution function including the volume fraction of possible nucleation sites f_N, the nucleation strain ε_N, and the standard deviation S_N. Consequently, these three parameters strongly interact within this function.

The reference value of $f_N = 0.00215$ was determined in [8] as the area fraction of secondary carbide particles. It was varied to $f_N = 0.015$ and $f_N = 0.0005$ within the sensitivity analysis. The variation extent is similar to the previously described variation of f_0. The results are provided in Fig. 6.7. The main effect of f_N on the simulation of a NRB is a modification of the load drop point (6.7a). In this case no decrease of the overall load level was detected although the variation of the input parameter was similar to the one of f_0. Comparable observations were made in the simulation of the Charpy test. The impact of the variation on the maximum force and the dissipated energy is much weaker compared to the one of f_0. The limit strains, which were derived from cell model simulations, also revealed these effects. The difference in strain level at a triaxiality of $\eta = 1$ was only 12%. This is significantly smaller than under a comparable variation of f_0 (Fig. 6.7c). It vanished for higher stress triaxialities. This is also reflected in the development of stress and void volume fraction within the cell element (Fig. 6.7d).

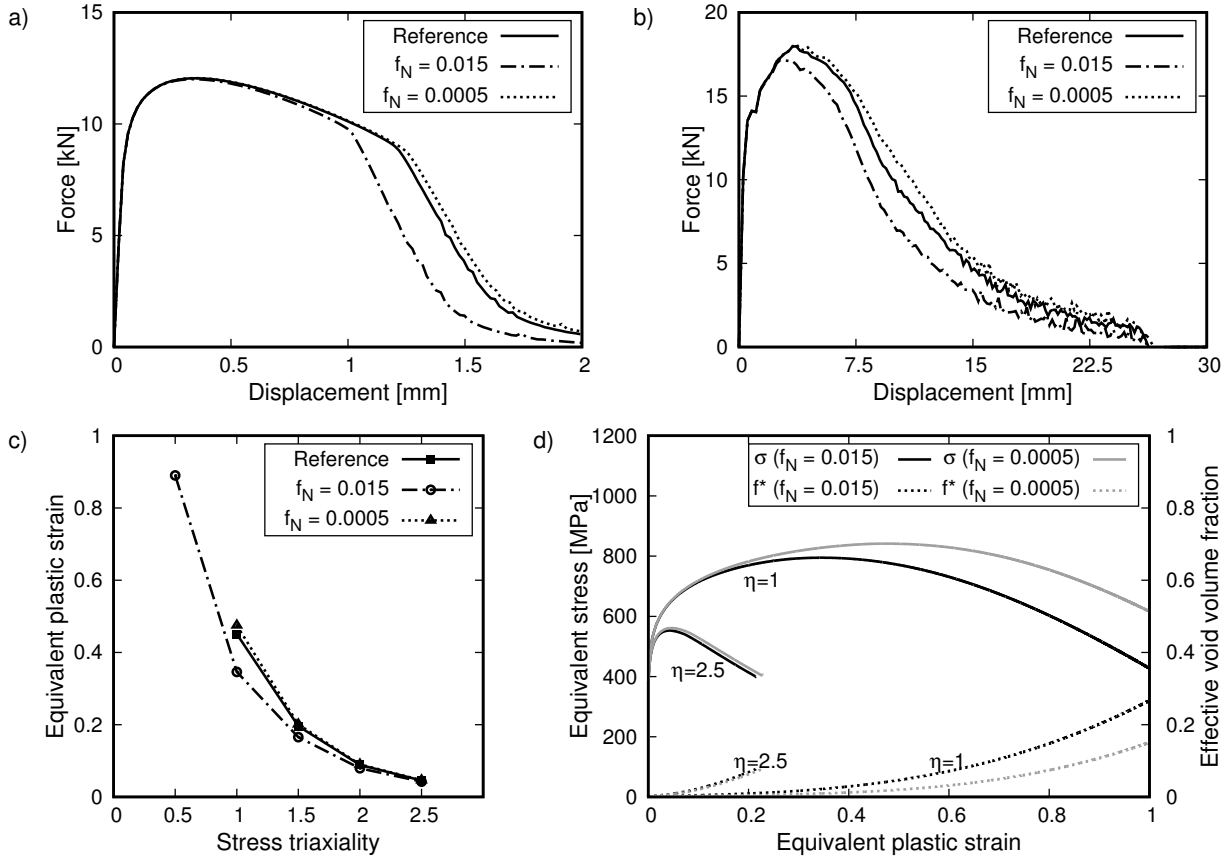

Figure 6.7.: Influence of f_N on a) NRB and b) Charpy simulations, c) the derived limit strains from and d) σ_e and f^* within cell element simulations for η=1.0 and $\eta = 2.5$.

A variation of ε_N and S_N at the reference value of $f_N = 0.00215$ resulted in minimal differences

as evident from the derived limit strains in Fig. 6.8. No significant influences on the NRB or Charpy simulations were found at this metallographically determined value of f_N; see the full results provided in the Appendix in Figs. A.12 and A.13. The sensitivity study of both parameters was repeated for an increased value of $f_N = 0.015$ to establish their qualitative influence on the derived limit strains.

The results are plotted in Figs. 6.9 and 6.10. The difference from the reference limit strains is a consequence of this increased f_N. Under these conditions, S_N exhibited a moderate impact on the constitutive answer and the derived strains. However, the impact of ε_N was still minimal even for such increased values of f_N . This was probably caused by the combination of f_N and the reference value of $S_N = 0.4$. The presented effects underline the strong interactions that the nucleation parameters are subjected to. Nonetheless, the overall level of impact on the results seems to be less strong than the one of the initial void volume fraction.

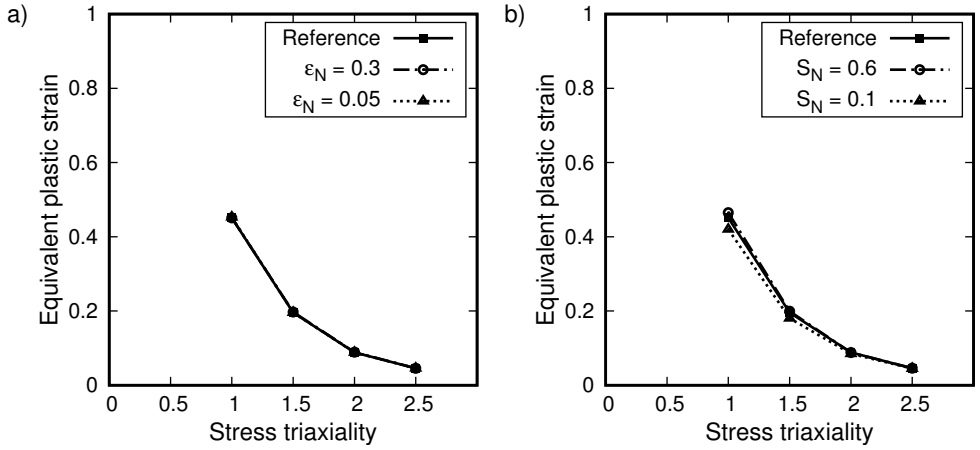

Figure 6.8.: Derived limit strains from cell element simulations with $f_N = 0.00215$ under a variation of a) ε_N and b) S_N.

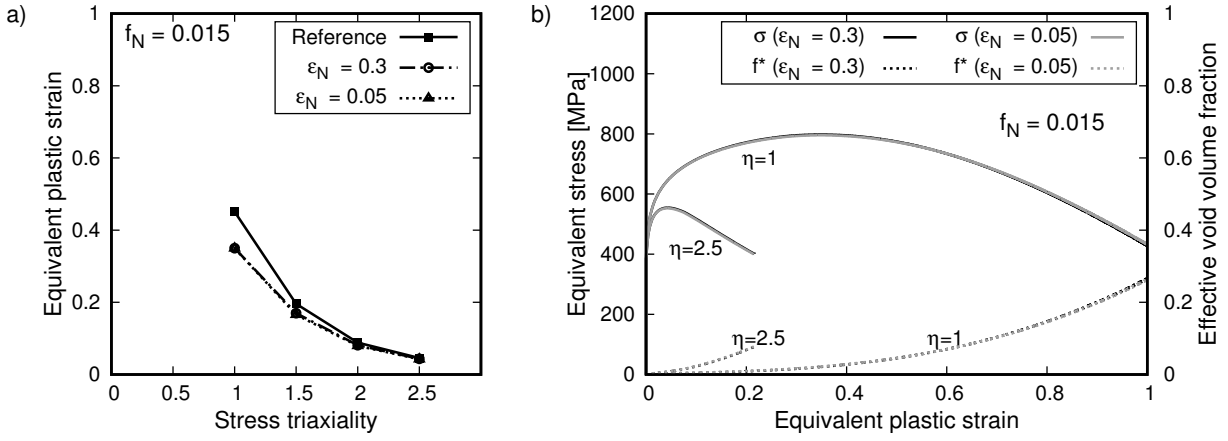

Figure 6.9.: Influence of ε_N (with $f_N = 0.015$) on a) derived limit strains from and b) σ_e and f^* within cell element simulations for η=1.0 and $\eta = 2.5$.

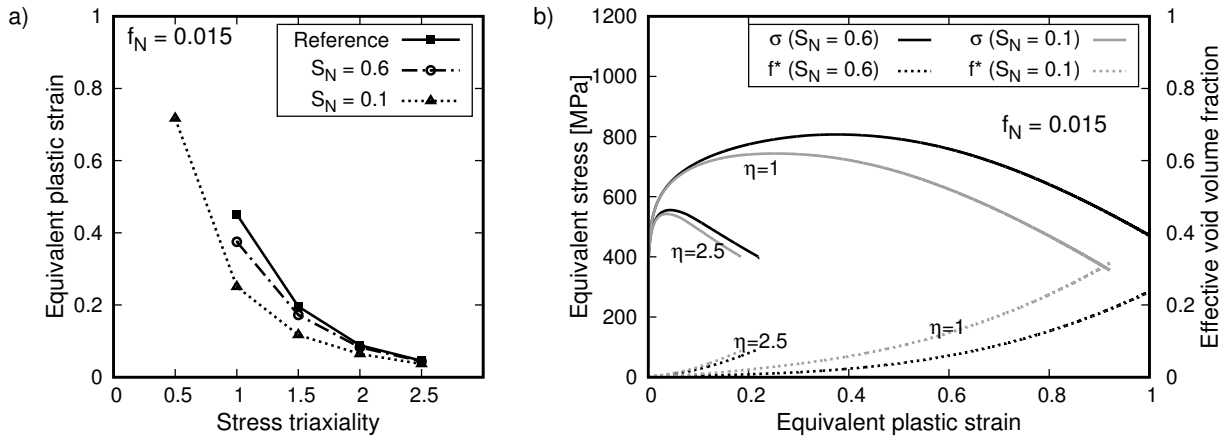

Figure 6.10.: Influence of S_N (with $f_N = 0.015$) on a) derived limit strains from and b) σ_e and f^* within cell element simulations for η=1.0 and $\eta = 2.5$.

Influence of the void coalescence parameters f_c and κ Interaction effects are known as well between the two void coalescence parameters [74]. The critical void volume fraction f_c determines the onset of the void growth by the factor κ. Subsequently, κ controls the constitutive response in the final stages of deformation. The effect of κ on the simulation results is presented in Fig. 6.11.

The acceleration factor was varied between values of $\kappa = 1$, which effectively means no acceleration or an effective deletion of the parameter, and $\kappa = 3$. Similar to f_0 and f_N, effects of a variation of κ on the load drop point in NRB and maximum force and dissipated energy in Charpy simulations were found. The extent of the resulting effects is rather strong, comparable to the one of f_0. Despite this strong impact on force-displacement curves, almost no effect on the derived limit strains could be observed (Fig. 6.11c). A maximum difference of 6% at $\eta = 1$ was found. This striking result can be explained by a closer investigation of the stress-strain development in the cell element (Fig. 6.11d). Since κ rather influences the slope of softening than its onset, the derivation of limit strains was not affected by its variation.

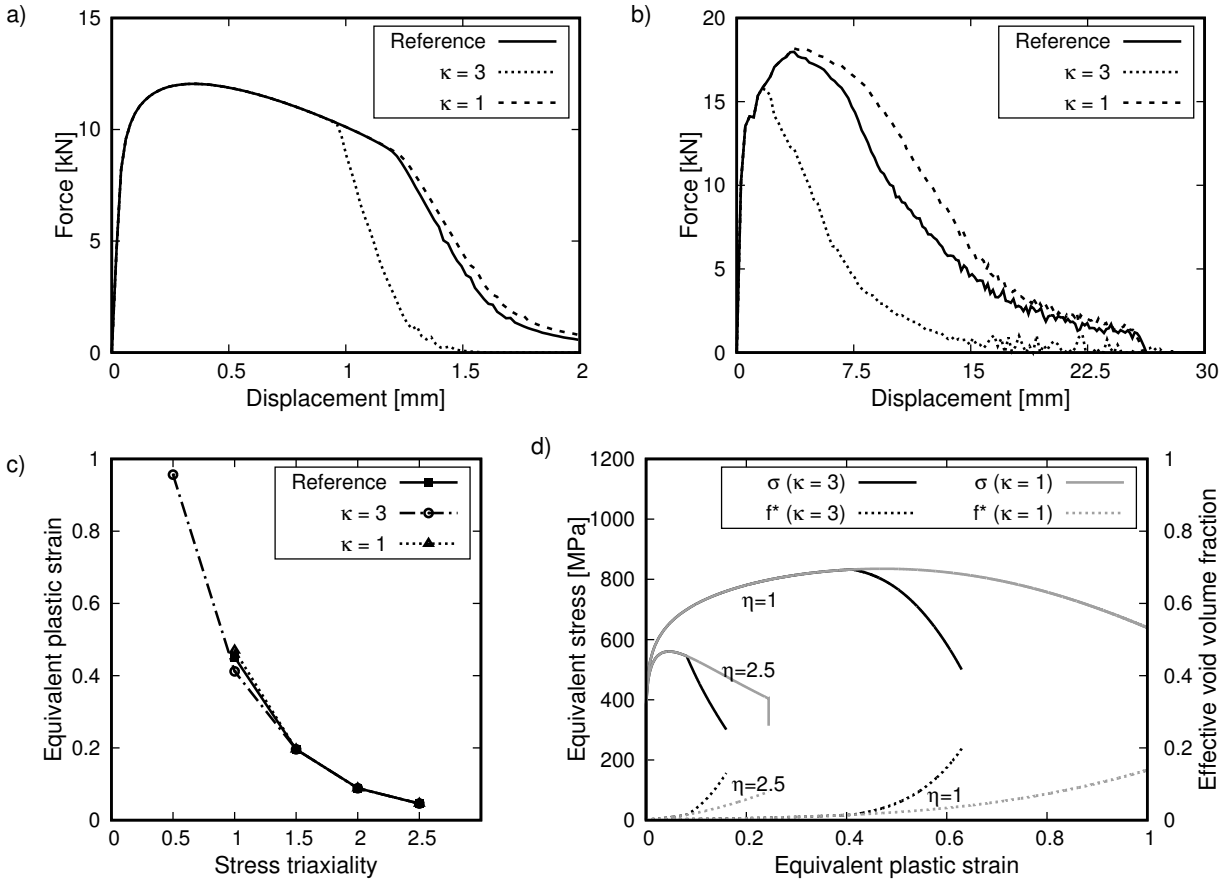

Figure 6.11.: Influence of κ on a) NRB and b) Charpy simulations, c) the derived limit strains from and d) σ_e and f^* within cell element simulations for η=1.0 and $\eta = 2.5$.

Within the reference parameter set an initial value of $\kappa = 1.1$ was calibrated. The use of this low acceleration factor in the sensitivity analysis diminished the influences of f_c on the results, as evident from the cell element simulations in Fig. 6.12. Consequently, the sensitivity analysis for f_c was repeated for an increased value of $\kappa = 3$ to establish the qualitative influence of f_c on the simulation results.

The results are plotted in Fig. 6.13. Significant influences of f_c on load drop point in NRB, as well as maximum force and dissipated energy are obvious. The investigation of cell elements revealed that an f_c larger than reference value does not strongly influence the derived limit strains. Contrary to that, a low f_c strongly influenced the course of the stress strain curve and the onset of softening. In summary, it was found that the parameters f_c and κ strongly interact, but that a suitable selection of them may minimise the influence of the parameter selection on the derived limit strains.

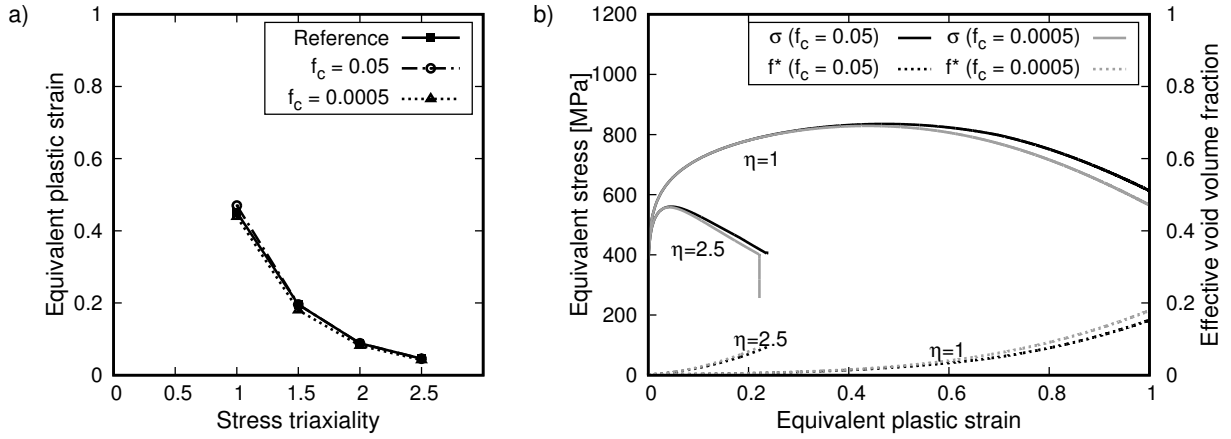

Figure 6.12.: Influence of f_c on a) derived limit strains from and b) σ_e and f^* within cell element simulations for η=1.0 and $\eta = 2.5$.

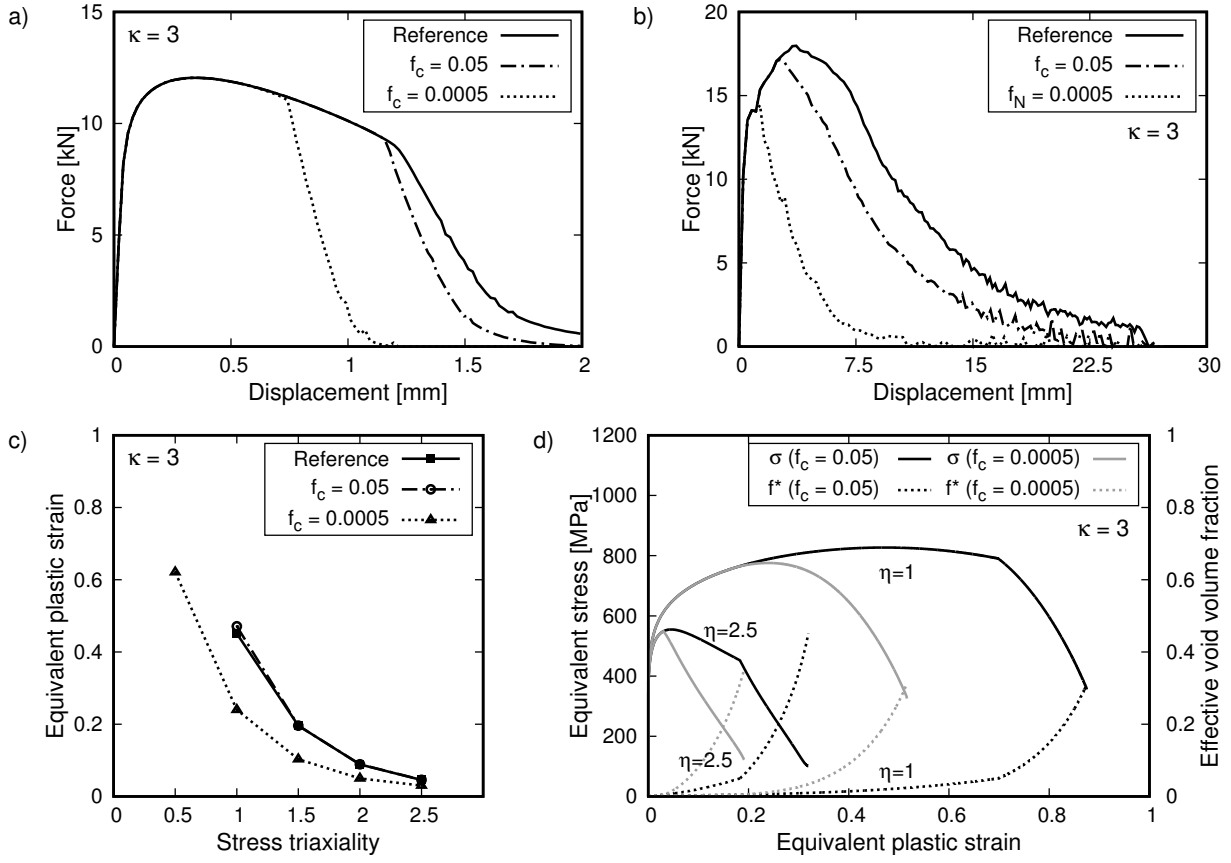

Figure 6.13.: Influence of f_c for $\kappa = 3$ on a) NRB and b) Charpy simulations, c) the derived limit strains from and d) σ_e and f^* within cell element simulations for η=1.0 and $\eta = 2.5$.

Influence of the empirical fitting parameters q_1 and q_2 The empirical fitting parameters q_1 and q_2, introduced by Tvergaard [63], are incorporated directly in the yield potential (Eq. 2.48). The assessment of their influence proved that both exhibit a massive influence on all simulation results (Fig. 6.14 and 6.15) as well as the derived limit strains. Failure is accelerated by an increase of either q_1 or q_2.

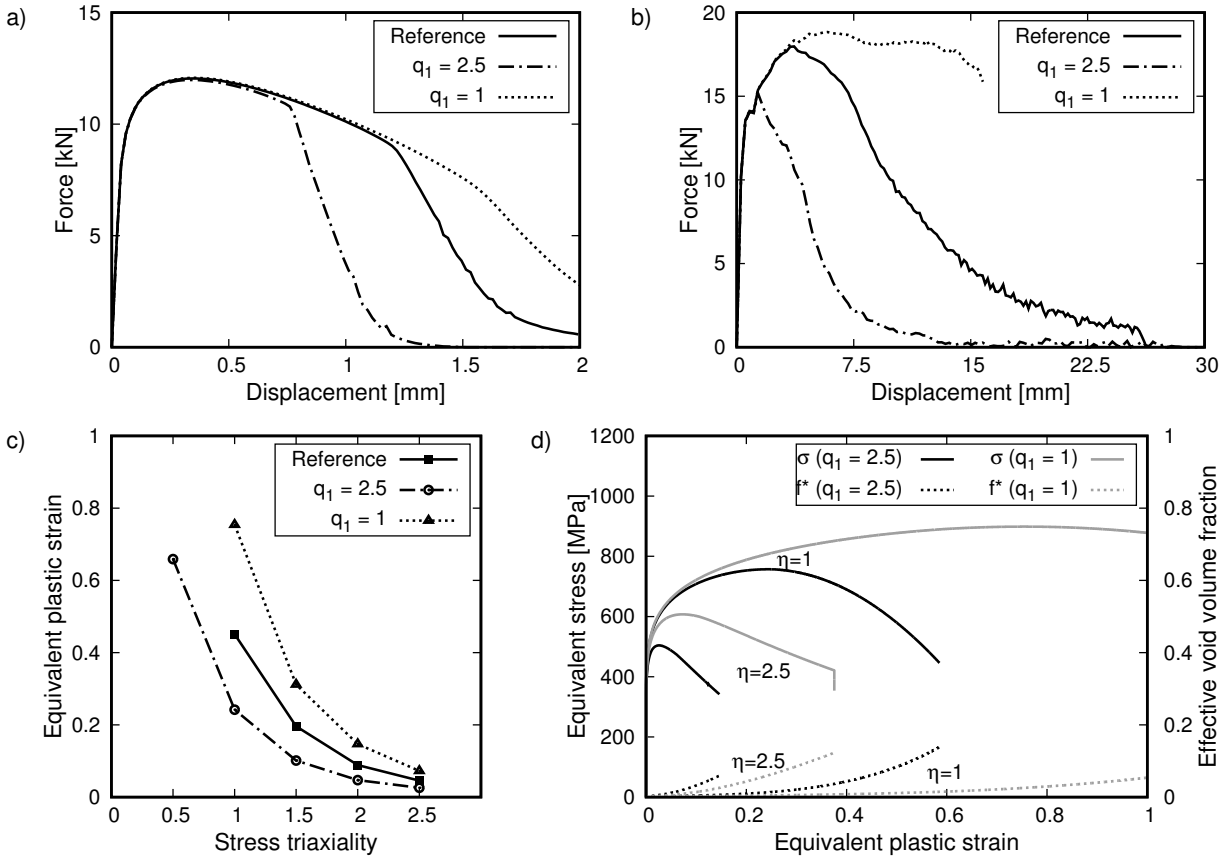

Figure 6.14.: Influence of q_1 on a) NRB and b) Charpy simulations, c) the derived limit strains from and d) σ_e and f^* within cell element simulations for η=1.0 and $\eta = 2.5$.

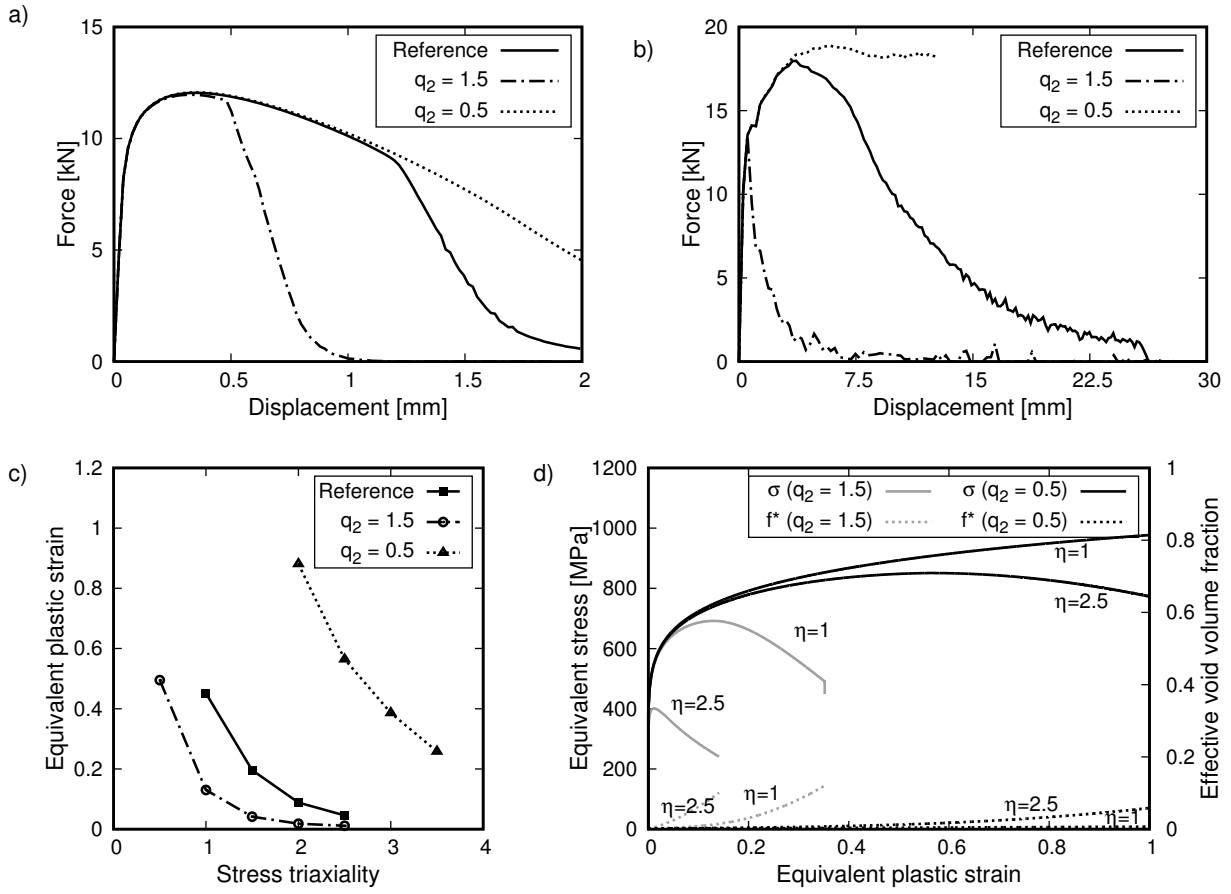

Figure 6.15.: Influence of q_2 on a) NRB and b) Charpy simulations, c) the derived limit strains from and d) σ_e and f^* within cell element simulations for η=1.0 and $\eta = 2.5$.

Influence of the flow curve The flow curve formulation within the Hollomon or Ludwik extrapolation has two distinct features: the overall level of stress and the hardening exponent. As the flow curve forms the basis of each FE simulation and each constitutive model, it obviously has great influence on all results. It was therefore tested how the derivation of limit strains is influenced by a variation of the flow curve. Figure 6.16 displays the results for a variation of the overall stress level. The cell element simulations reveal that such a shift of the flow curve exhibits no influence on the derived limit strains because the strain at maximum stress is not affected. Contrary to that, a strong influence of the hardening exponent on the derived limit strains was found (Fig. 6.17). Because the hardening exponent strongly influences the onset of softening, the level of the derived limit strains was scaled in an almost linear fashion over all stress triaxialities by the hardening exponent. A reliable determination of the hardening exponent is therefore crucial.

Influence of the mesh size An important indirect parameter when using local Gurson formulations is the mesh size as explained in Section 2.3.2. NRB and Charpy simulations form central parts of the investigated simulation procedure. Therefore, their dependence on the selection of the mesh size in the critical region, where elements are being deleted, was investigated. For NRB it was found that the mesh size only exhibits a limited influence on the slope of the force drop (Figures 6.18). For the Charpy simulations a stronger influence on the dissipated energy and a minor

impact on the maximum force could be detected (Fig. 6.19).

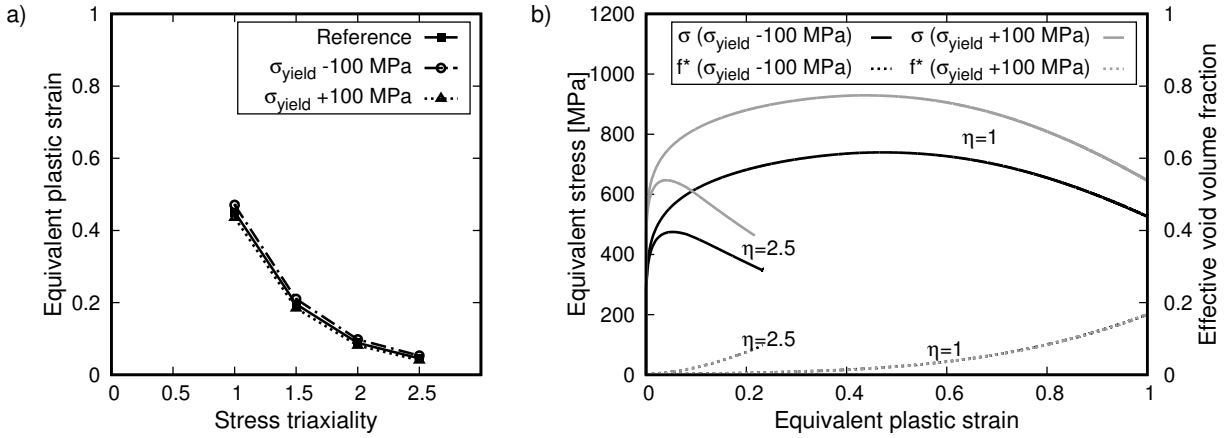

Figure 6.16.: Influence of the overall level of the stress-strain curve on a) derived limit strains from and b) σ_e and f^* within cell element simulations for η=1.0 and $\eta = 2.5$.

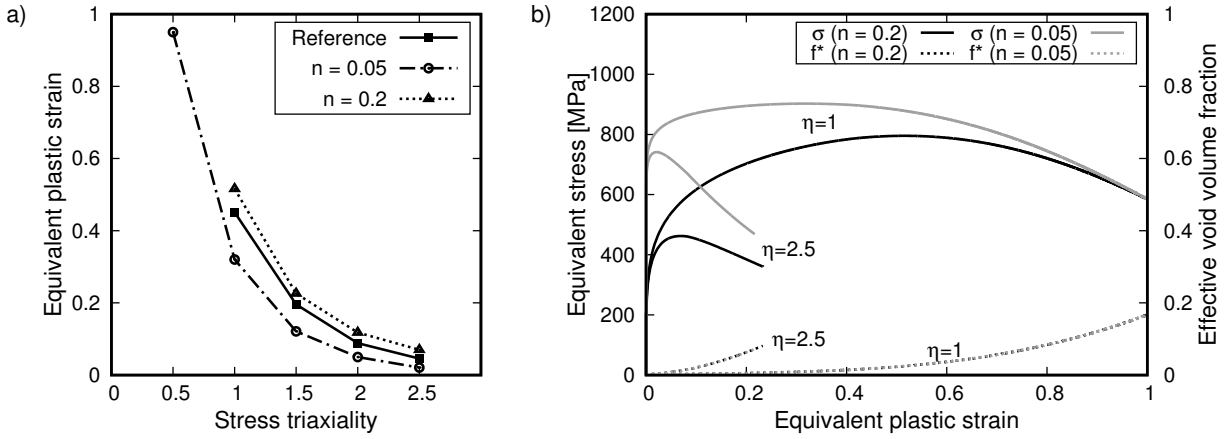

Figure 6.17.: Influence of the hardening exponent on a) derived limit strains from and b) σ_e and f^* within cell element simulations for η=1.0 and $\eta = 2.5$.

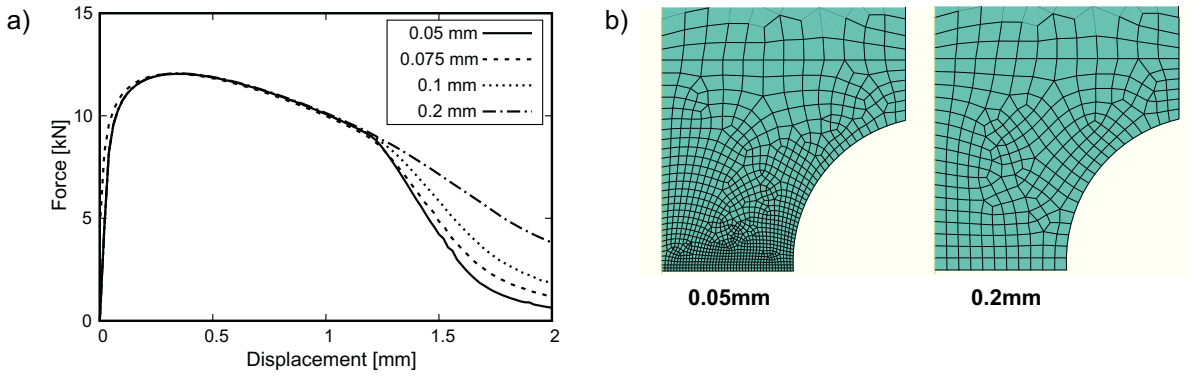

Figure 6.18.: a) Influence of the mesh size on the force-displacement curve in NRB simulations. b) Mesh examples

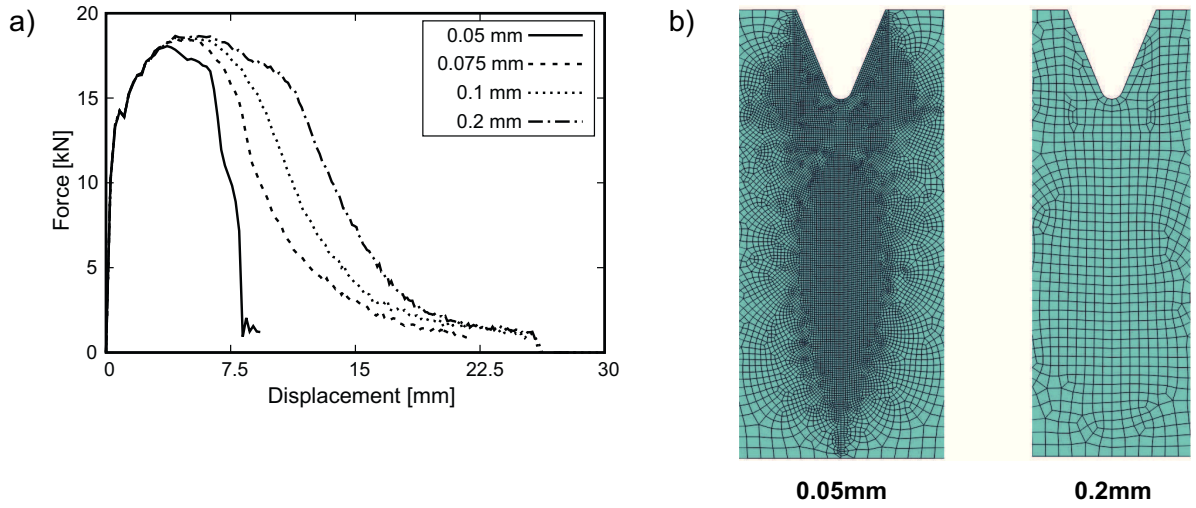

Figure 6.19.: a) Influence of the mesh size on the force-displacement curve in Charpy simulations. b) Mesh examples

6.2.1.2. Preliminary discussion and proposal of a calibration scheme

The qualitative impact of the individual parameters was assessed; the results are summarised and discussed in the following.

All considered simulation types were strongly affected by a variation of the initial void volume fraction f_0 throughout the complete deformation history. Changing f_0 evenly deteriorates or improves the simulated performance of the sample, for example in terms of load level and failure onset. A higher f_0 induced earlier failure and lower derived limit strains. No direct interactions with other parameters were observed. In general, the difference between f_0 and f_c determines the possible deformation from the beginning until the onset of accelerated failure. The relation between these two parameters has to be selected carefully. The obtained results match very well the results of a large number of studies available in the literature (e.g. [72, 74, 80, 151]).

Strong interactions were detected between the three parameters f_N, ε_N and S_N of the void nucleation law. The possible influence of ε_N and S_N is scaled by the absolute value of f_N. It is negligible in combination with metallographically determined values of f_N but becomes more significant for larger values of f_N. This was also demonstrated by Bonora, who simulated tensile tests with pure nucleation [72]. High values of ε_N or S_N may delay the nucleation of secondary voids to unrealistically high strain values that do not occur during deformation. This diminishes the influence of f_N. In general, the strong interaction effects within this parameter group foster the introduction of non-uniqueness to the parameter determination and corresponding simulation results.

The coalescence parameters f_c and κ were found to have a strong influence on the final failure phase of simulations. Additionally, interaction effects between the two parameters are evident. The parameter κ is only active after f_c is reached. Therefore, a high f_c may limit its influence. Additionally, a small value value of κ leads to the fact that the whole void coalescence formulation has a very limited impact on the results. On the other hand, a very high value of κ may induce unrealistically fast failure. The combination of both parameters can be used to control the onset of the load drop point in NRB without affecting the overall load level. Within the literature, values for

f_c were investigated by cell model studies on collapse loads (e.g. [25,48]). These report values up to $f_c = 0.06$. However, values up to $f_c = 0.15$, as initially proposed by Tvergaard and Needleman [54], were successfully used (e.g. [54, 112, 134]). Only small influences on numerically derived limit strains were found for the moderate value range of f_c and κ in this study.

The empirical fitting parameters q_1 and q_2, using the common assumption $q_3 = q_1^2$ [63], revealed a massive influence on all simulation results. The reason is that they are directly incorporated in the yield potential. The strong impact of this parameter group leads to the fact that they can compensate the influence of almost every other parameter group. Consequently, they foster a non-uniqueness of the simulation results. Many studies investigate possible relations of the q-parameters to hardening properties ([48, 51, 52]), void shape effects [58], and the stress state ([50, 53]) without clear results. Initially, Tvergaard proposed values of $q_1 = 1.5$ and $q_2 = 1.0$ [63]. Follow-up studies of Koplik and Needleman proposed improved values of $q_1 = 1.25$ and $q_2 = 1.0$ [48]. Analytical considerations were used by Leblond to derive a theoretical value of $q_1 = 4/e = 1.477$ [25]. Although the q-parameters may be used to compensate special plasticity effects like anisotropy, a large number of application-oriented studies used the values initially proposed by Tvergaard with success [23, 58, 151].

The hardening exponent was found to exhibit a unique influence on the derivation of limit strains. This agrees with the findings of Springmann and Kuna who proved this by using optimisation algorithms [77].

It is well known that for Gurson models the mesh size has to be constant in the region of element deletion [151]. The mesh size determines the dissipated energy because finer elements are deleted earlier. Especially the element height orthogonal to the crack growth direction is relevant for this [76, 152]. Additionally, the mesh in the crack region has to be fine enough to properly resolve the stress state. A minor influence of the mesh size was detected in NRBs, which are therefore suitable for a first parameter calibration. The simulation of Charpy tests exhibited a mesh size sensitivity after the force maximum. Table 6.3 summarises the results of the sensitivity analysis for the GTN parameters.

Table 6.3.: Summarised results of the sensitivity analysis for the GTN parameters. *For certain ranges of parameter selection.

Parameter	f_0	f_N	S_N	ε_N	f_c	κ	q_1	q_2
Influence on derived limit strain curve	Strong	Weak	Weak	Weak	Weak*	Weak*	Strong	Strong
Influence on Charpy simulation	Strong	Weak	Weak	Weak	Strong	Strong	Strong	Strong
Direct interactions with other parameters	No	Yes	Yes	Yes	Yes	Yes	No	No

A calibration scheme was proposed based on these results. Its application shall minimise possible influences of non-uniqueness on the correlation between toughness simulations with the Gurson model and derived limit strains. For a direct calibration of parameters from experimental results the following recommendations are given:

- The order of magnitude of f_0 may for many steel grades be determined from the volume content for non-metallic inclusions. Slight modifications of this value are acceptable because the inclusion content also varies within real materials.
- Bonora proved that identical behaviour can be modelled with or without the law for secondary void nucleation [72]. Although secondary void nucleation is a well-known microstructural mechanism, the implemented formulations are purely phenomenological and do not consider the actual micromechanical processes [23]. Additionally, the sensitivity study showed that this parameter group fosters the introduction of non-uniqueness due to its strong interaction effects. Therefore, it is recommended not to use the nucleation function within this modelling concept.
- The void coalescence parameters f_c and κ should be calibrated by comparing experimental results and simulations of NRBs. The aim is to meet the load drop point at the end of the experiment. For a reliable derivation of limit strains it is favourable to choose f_c such that it is reached after the stress maximum in cell element simulations. An upper bound of $f_c = 0.15$ should be observed to avoid a strong violation of micromechanical relations. Moderate values in the range of $1.2 < \kappa < 2$ are recommended to ensure a balanced consideration of void coalescence. The final value should be selected with care as it exhibits a strong influence on Charpy simulations.
- The q-factors are likely to introduce non-uniqueness into the simulation results due to their large influence. If it is necessary for an adequate modelling, they could be modified with great care to introduce e.g. void shape effects. However, for many structural steels this is not relevant. Therefore, it is suggested to use the initial values of Tvergaard and not modify them to prevent the introduction of non-uniqueness to the results.
- Flow curve and hardening behaviour can be uniquely determined from common tensile tests.
- The mesh size can be very well calibrated in the comparison of experiment and simulation of fracture mechanics tests due to the limited energy dissipation zone [23, 76].

In addition, conclusions from the sensitivity analysis for the derivation of nominal parameter sets were drawn. The modification of the GTN parameters is in general arbitrary and many parameters enable the artificial deterioration of parameter sets so that a certain Charpy impact toughness is achieved. However, the following guidelines are proposed to minimise non-uniqueness and establish a clear framework for the derivation of nominal properties:

- The derivation of nominal properties should be performed based on existing parameter sets that were derived from experiments on a steel of the investigated grade. This ensures a well-justified starting point for a modification of the GTN parameters.
- The hardening exponent exhibits a strong influence on the derived limit strain curve. Hubo showed in his studies that the hardening behaviour is similar for HSLA steels of varying quality [95]. Therefore, the hardening behaviour should be adapted from experimental investigations on the corresponding steel grade.
- The overall strength level should be adapted to the nominal yield strength of the material. This is required because the overall strength level strongly influences the dissipated energy in Charpy simulations.

– The GTN parameters should be kept constant except for a modification of f_0. An increase of the initial void volume fraction evenly deteriorates the mechanical properties of the material without introducing further non-uniqueness. Additionally, this is covered by the micromechanical motivation of the GTN model because a material with higher inclusion content usually exhibits worse properties. An increase of f_0 also reduces the difference to f_c and thereby implicitly assumes an earlier failure onset.

This calibration scheme presents a framework to derive nominal assumptions suitable for the modelling of a high number of large-scaled components.

6.2.1.3. Testing of the proposed calibration scheme

To assess whether the proposed calibration scheme can adequately reproduce the failure behaviour of high strength steels, additional experiments were performed on the material P500Q. A new parameter set was calibrated and the derived limit strains were compared to the ones derived from the previously defined parameter set [75]. Furthermore, the implementation of adiabatic conditions was tested in the simulation of high speed tensile tests and Charpy tests.

The calibration of GTN parameters was performed according to the proposed calibration scheme. Table 6.4 lists the final parameter set.

This parameter set was calibrated within the simulation of three NRB geometries. Figure 6.20 underlines that the results of experiments and the corresponding simulations match very well. The onset of softening in the central element of the simulations is marked by a cross. The mesh size was calibrated on the experimental results of a CT test with a fatigue pre-crack of 26.21 mm depth. A mesh size of 0.15 mm led to an acceptable agreement of simulation and experiment (Fig. 6.20d).

Based on this calibrated parameter set, the corresponding limit strains were derived according to the methodology presented in Section 5.1.3. A comparison of these to previous results [75] shows that the limit strain curve derived from the re-calibrated parameter set matches these results very well for $\eta > 1$ (Fig. 6.21). The maximum deviation at $\eta = 1$ is only 11% even though the strains derived in [75] are based on a very different parameter set. This deviation can be avoided by the future application of the calibration scheme.

In addition, the common approach of deriving limit strains was pursued. Hereby, the limit or failure strains are extracted from the NRB simulation in the instance that is considered critical. Within the traditional Johnson-Cook-concept this instance is for example is total failure [60]. Other definitions are e.g. the instance of void coalescence as in the damage curve according to Arndt [101]. For the presented concept, the strains and stress triaxialities should be obtained at the onset of local softening, as marked by the cross in Fig. 6.21. This was tested in three NRB and one CT simulation. The results, marked in Fig. 6.21, match the derived limit strain curve very well. The numerical derivation of limit strains based on parameter sets calibrated according to the proposed scheme thus produces reliable results.

Table 6.4.: Re-calibrated parameter set for steel grade P500Q

Parameter	f_0	f_N	S_N	ε_N	f_c	κ	q_1	q_2
Calibrated value	0.001	0	0	0	0.15	1.4	1.5	1

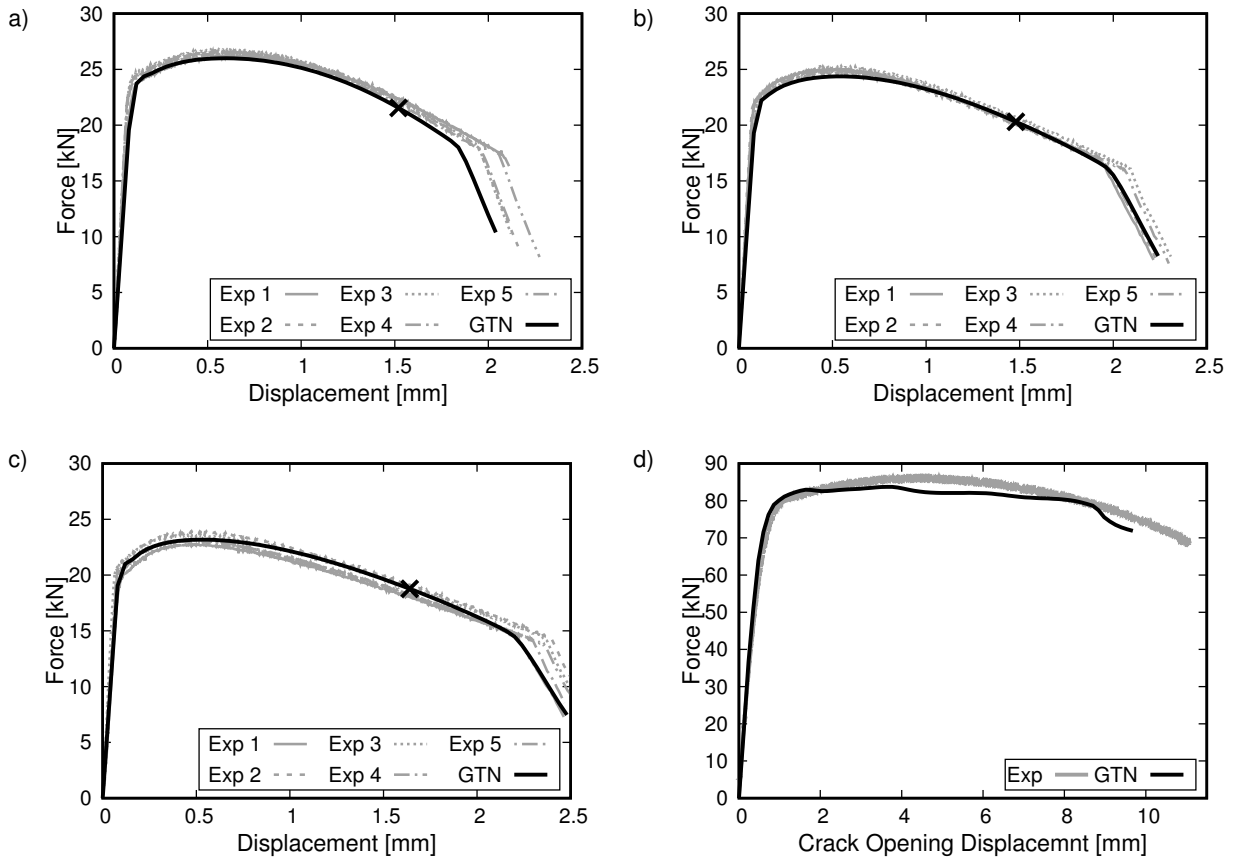

Figure 6.20.: Force-displacement curves of experiment and simulations of NRB with a radius of a)1.5 mm b) 3mm c) 5mm. The crosses indicate the first occurrence of local softening. d) Comparison of simulation and experiment for the calibrated mesh size of 0.15mm in a CT test.

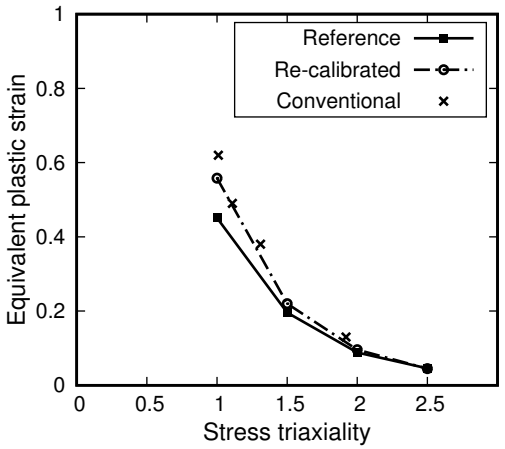

Figure 6.21.: Comparison of the limit strains derived from the reference GTN parameter set, the set re-calibrated according to the proposed calibration scheme and the strains derived conventionally from the simulation of NRB.

Furthermore, the implementation of temperature and strain rate dependence within the GTN model was tested for adiabatic conditions. To this purpose, additional temperature and tensile tests were performed and the parameters of Eqs. 6.1 and 6.2 were calibrated accordingly. These are listed in Table 6.5.

Table 6.5.: Re-calibrated parameter set for temperature and strain rate dependency.

Parameter	$c^1_{\dot{\varepsilon}}$	$c^2_{\dot{\varepsilon}}$	$c^2_{\dot{\varepsilon}}$	c^1_T	c^2_T	c^3_T
Calibrated value	0.008	1.076	0	1.12	0.0052	0.8

The results of an exemplary high speed tensile test and Charpy tests are compared to simulations with the extended implementation in Fig. 6.22. The course of the force-displacement curves were well met by the simulations. Only the force drop of the Charpy tests is slightly underestimated by the simulation. The implementation of adiabatic conditions was therefore successful.

These results demonstrate that parameter sets calibrated according to the proposed scheme can reproduce toughness levels in the simulation of a Charpy test. By using the proposed procedure, reproducible limit strain curves representing certain toughness levels can therefore be derived. However, some ambiguity prevails in the low triaxiality regime. It might be correlated to the fact that the Lode angle is not considered within this procedure. Therefore, the procedure was adapted; results are presented in the following.

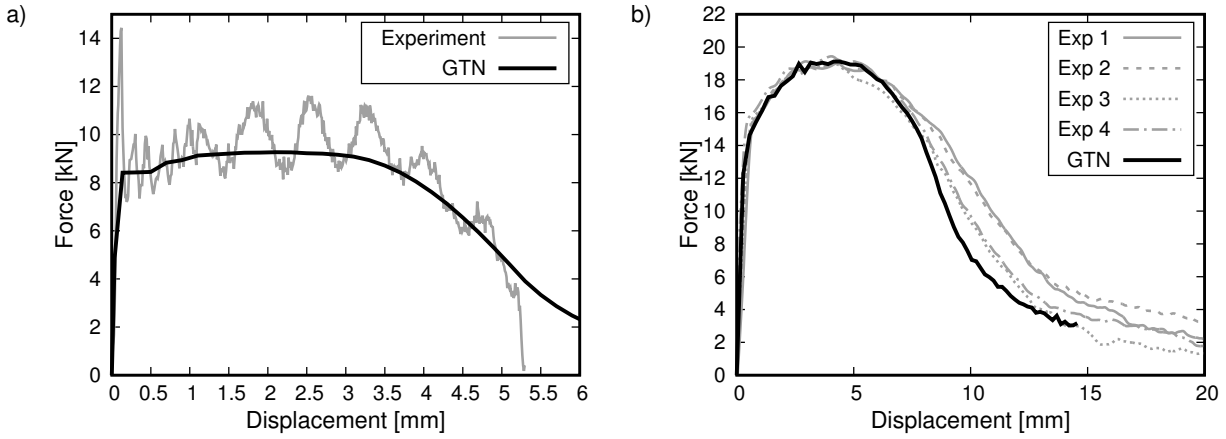

Figure 6.22.: Force-displacement curves of experiments and simulations performed with the re-calibrated parameter set for a) a highspeed tensile test at a strain rate of 250/s b) Charpy tests at room temperature.

6.2.2. Lode angle consideration

For the implementation of a Lode angle dependent Gurson model two formulations, by Nahshon and Hutchinson [27] as well as Nielsen and Tvergaard [153], were tested. The NH formulation was implemented first because it only introduces one additional parameter. Pre-studies on the material dvI were performed for testing the model implementations. The determination of the classical GTN parameters was performed according to the calibration scheme described above on the NRB tests used previously for the limit state investigation. The results are provided in Table 6.6.

Table 6.6.: On NRB simulations calibrated GTN parameter set for dvI.

Parameter	f_0	f_c	κ	q_1	q_2
Calibrated value	0.0015	0.05	1.5	1.5	1

Subsequently, plane strain tests were performed on samples with notch radii of 1.5, 3, and 8 mm. These were simulated with the NH model. Hereby, the value of k_ω was varied to establish its influence in conditions of $\overline{\theta} = 0$. Additionally, these samples were also simulated with a pure elastic-plastic material law and the original GTN model to assess the difference between the model formulations. The results for the samples with radii of 1.5 and 8 mm are plotted in Figs. 6.23 and 6.24. While the elastic-plastic simulation cannot predict any failure, the GTN simulation and the simulation using $k_\omega = 0$, which are identical, predict the failure onset far too late due to the non-existent or deactivated shear damage term. Nahshon and Hutchinson proposed a range of $0 < k_\omega < 3$ in a theoretical study on a low-strength steel with a much lower hardening exponent [27]. The results of the plane strain simulation indicate that these values are not applicable to the actual failure behaviour of high strength steels and that larger values of k_ω are required. A value of $k_\omega = 5$ seems a reasonable value for a failure prediction in this case.

Apart from the influence of k_ω, it can also be recognised in Fig. 6.23 that the load level and yield strength are overestimated by all simulations. This effect is also present in the 8mm radius sample (Fig. 6.24) although it is less pronounced. It is known that some steels exhibit a dependence of the yield point from the Lode angle while others do not (e.g. [37,61]). The micromechanical foundations of this phenomenon remain currently unclear. However, this effect is neither considered in the NH or NT model formulations nor in any other currently available extension of the Gurson model. They only consider a Lode angle influence on the damage development contrary to, for example, the phenomenological Bai-Wierzbicki model [26].

As discussed above, some authors describe that the empirical fitting parameters q_i may in Gurson models be used to characterise plasticity effects. Consequently, it was explored whether they could be used to compensate this effect. The results provided in the Appendix (Fig. A.14 and A.15) prove that even a strong modification of q_1 and q_2 does not affect the yield point, but would deteriorate all other simulation results. Therefore, this overestimation of the yield point has to be accepted as an intrinsic weakness of the available models. Modifications should be investigated in the future. Nonetheless, the implementation of the shear damage term provides a significant improvement of the failure prediction in plane strain state.

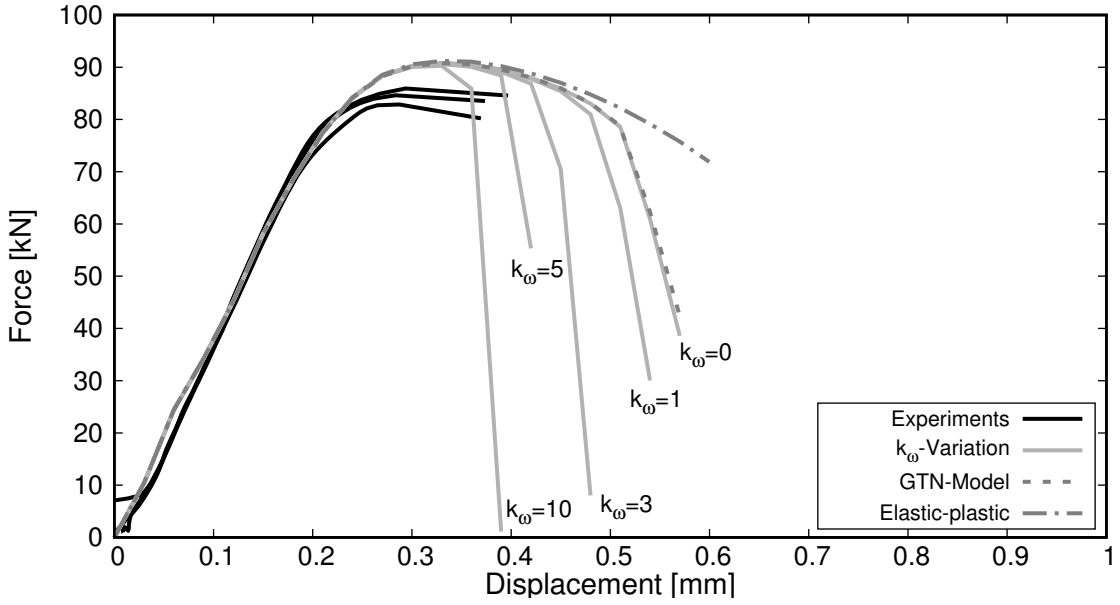

Figure 6.23.: Experimental results and simulations of plane strain samples with a radius of 1.5 mm, material dvI.

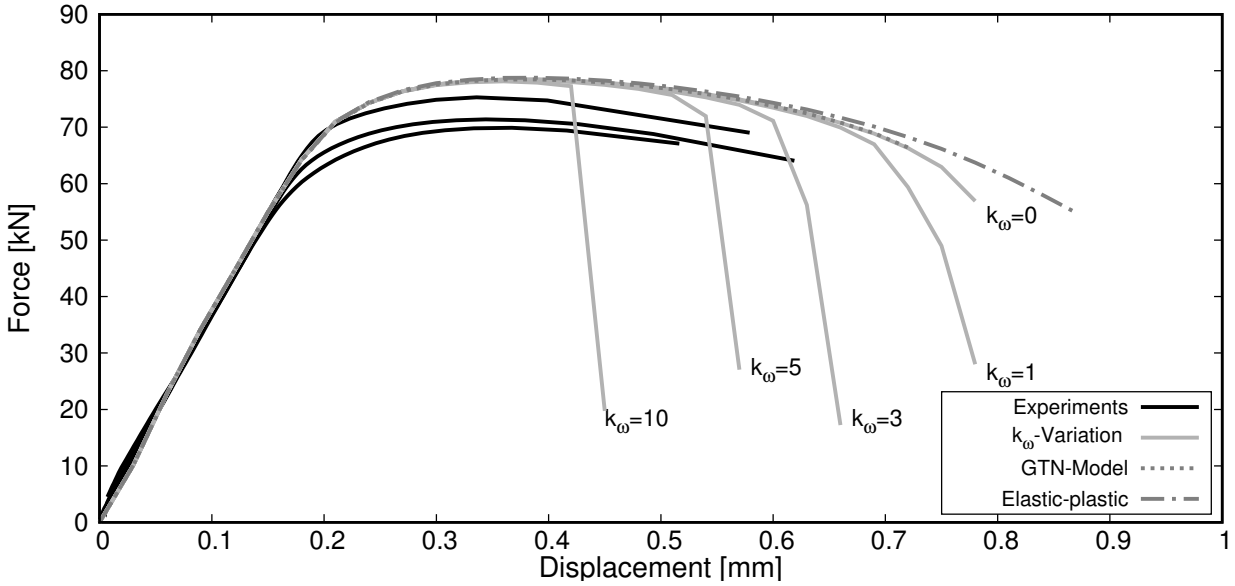

Figure 6.24.: Experimental results and simulations of plane strain samples with a radius of 8 mm, material dvI.

Further investigations were performed to complement the calibration scheme with respect to the new parameter. In general, the shear damage parameters should be calibrated on plane strain and shear specimens because they exhibit a stress state of $\overline{\theta} = 0$. In NRB simulations k_ω has no influence due to the axisymmetric stress state. Besides k_ω, a modification of f_c and κ could also influence the load drop in plane strains simulations, but it will not be possible to find matching solutions for NRB and plane strain. Consequently, the coalescence parameters should be calibrated on NRB and the shear damage term on plane strain and shear samples.

f_0 was identified as the lead parameter for an adaption of the parameter set to nominal values.

Therefore, it was analysed how the simulation of plane strain specimens is affected by a variation of f_0. The results (Fig. 6.25) support the selection of f_0 as the main modification parameter because it also evenly deteriorates the failure behaviour in the simulation of plane strain specimens.

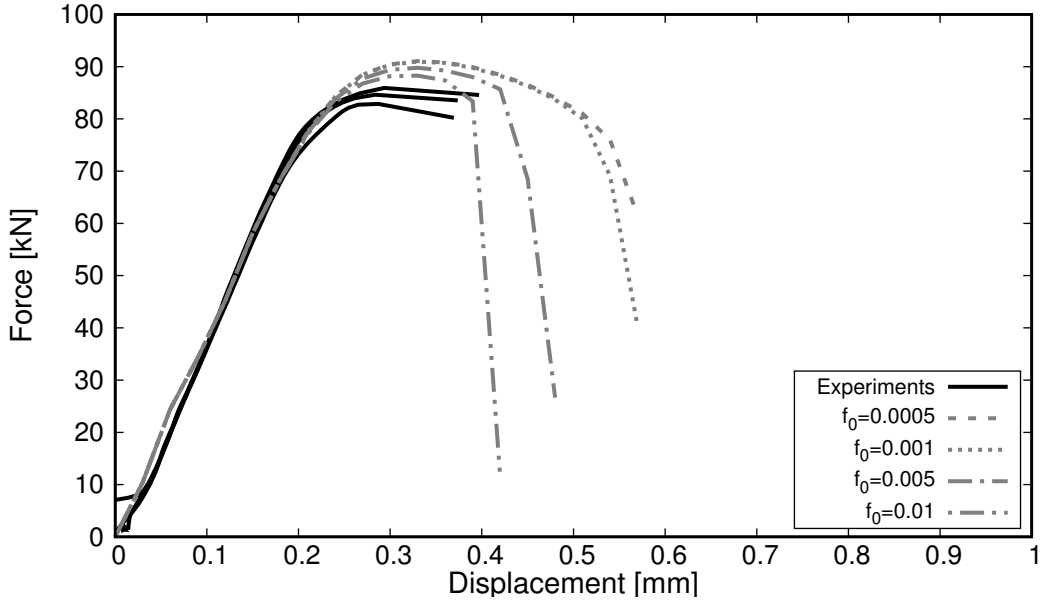

Figure 6.25.: Effect of a variation of f_0 on the simulation of plane strain samples with a radius of 1.5 mm using the NH model.

Finally, the ability of the NH model to simulate a Charpy test was assessed. The influence of k_ω was at first explored without a consideration of temperature and strain rate dependency. The simulation results (Fig. 6.26a) indicate that k_ω has a similar influence on the Charpy simulation like the coalescence parameters. Increased values of k_ω feature an earlier failure. The extent of the influence is quite pronounced. Subsequently, a simulation with the calibrated value of $k_\omega = 5$ and a consideration of strain rate and temperature dependence was compared to experimental results. The NH model predicts the failure onset much too early (Fig. 6.26b). While the consideration of Lode angle dependence is required for the simulation of plane strain samples, the NH model overestimates this influence for the Charpy tests. The stress triaxiality in front of the notch in Charpy specimens usually exhibits values of approximately $\eta = 1.5$. In the notched plane strain specimens the stress triaxiality is usually below one. Consequently, the NH model seems to overestimate the Lode angle influence for higher stress triaxialities. This is in accordance with the findings of Nielsen and Tvergaard that led to the formulation of the NT model [153].

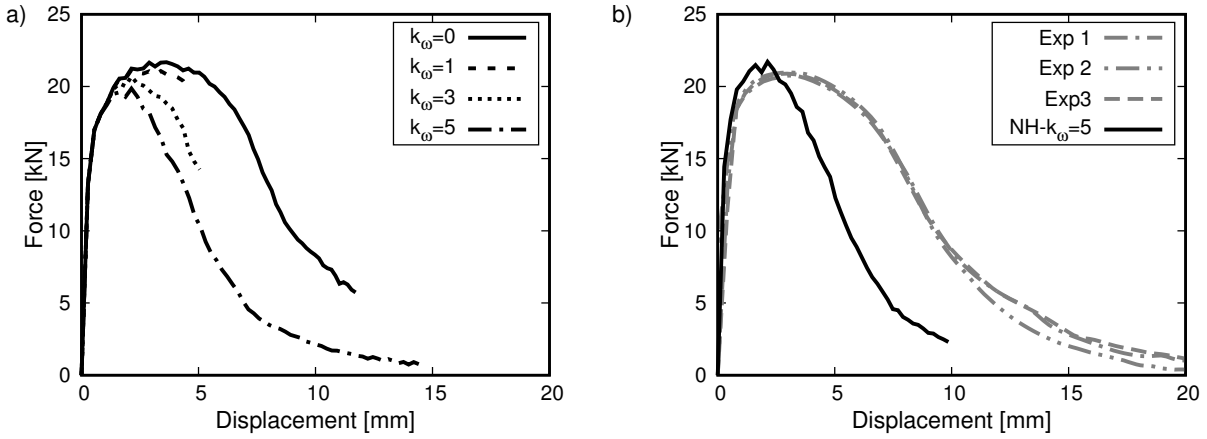

Figure 6.26.: a) Sensitivity analysis on k_ω in Charpy simulations. b) Comparison of an adiabatic NH simulation to experimental results of material dvI.

Therefore, the test of the NH model was considered not to be successful. Thus, the NT model was implemented. Its suitability was tested on the pressure vessel materials. Hereby, optimal parameters for the two boundary triaxialities were determined to be $\eta_1 = 0.8$ and $\eta_2 = 1.3$. These parameters allowed a successful simulation of the Charpy test while maintaining the ability to predict the onset of failure in plane strain samples. Only for sharp notched plane strain samples with a notch radius of 1 mm, the prediction quality was partially decreased. The results are omitted here as they are provided in the following section 7.2.1. Regardless of this model change, the results and conclusions on the calibration scheme, which were determined from the NH simulations, remain valid because NH and NT model show the same behaviour in the plane strain simulations. Consequently, the parameter k_ω should be determined on plane strain and shear samples and f_0 is the most suitable parameter for an adaptation to nominal requirements.

6.3. Summary

The comprehensive modelling concept was successfully developed. The sensitivity analysis identified the essential relations between the Gurson parameter selection on the one hand and the simulated toughness levels as well the derived limit strains on the other hand. On this basis the initial void volume fraction f_0 was selected as the main parameter for the simulation of virtual toughness levels, and a calibration scheme to avoid non-uniqueness of the results was proposed. Lode angle dependent formulations of the Gurson model were successfully implemented and tested to ensure a consideration of all relevant stress states. The model formulation by Nielsen and Tvergaard [153] proved to be most suitable. The calibration scheme was extended accordingly. Hence, a comprehensive framework for deriving nominal limit strain loci was successfully developed. Additionally, a scaling function for limit strains was proposed which can be tested in the simulation of the full pressure vessel.

7. Demonstration in a burst test

One of the main aims of this thesis is the demonstration of the developed modelling procedure in a burst test. For this, investigations were performed on two scales (Fig. 7.1). On the laboratory scale, tests on various samples made of the pressure vessel materials were performed and subsequently simulated to calibrate the NT model parameters. From these simulations the limit strain locus was then derived numerically. On the component scale, the burst test was performed on the demonstrator vessel. Test results as well as fracture surfaces were evaluated. The burst test was simulated using the limit strain loci. The results of simulation and test were compared.

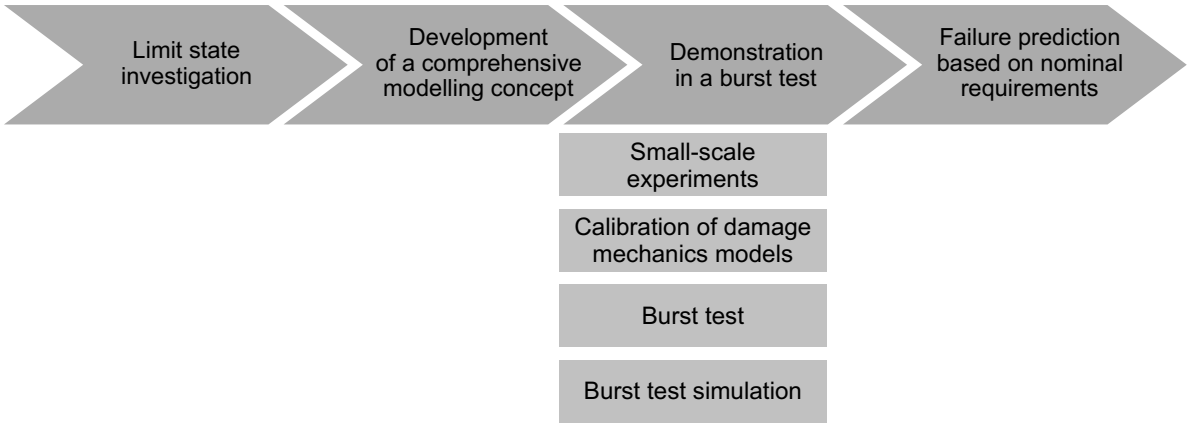

Figure 7.1.: Overview on the presented results on the burst test.

7.1. Methods

7.1.1. Experiments on laboratory samples

For the demonstration in a burst test, the damage mechanics models were calibrated on experimental results of the actual vessel material. To this purpose, tests on a variety of samples were performed. The materials dvII, dvIII, dvIV and dvV were fully characterised while limited investigations were performed on dvVI.

The material for all samples was heat treated for stress relief together with the pressure vessel itself. Samples from base materials were extracted preferably from a position at a quarter plate thickness if possible. Samples from weld seams were extracted such that the expected region of failure was located within the weld seam. This was guaranteed by polishing and etching the individual parts of the working samples before the blanks were extracted by sawing. For smooth round bars this induced that the whole sample was extracted from the weld seam (Fig. 7.2). Details on the applied test procedures are given in the following.

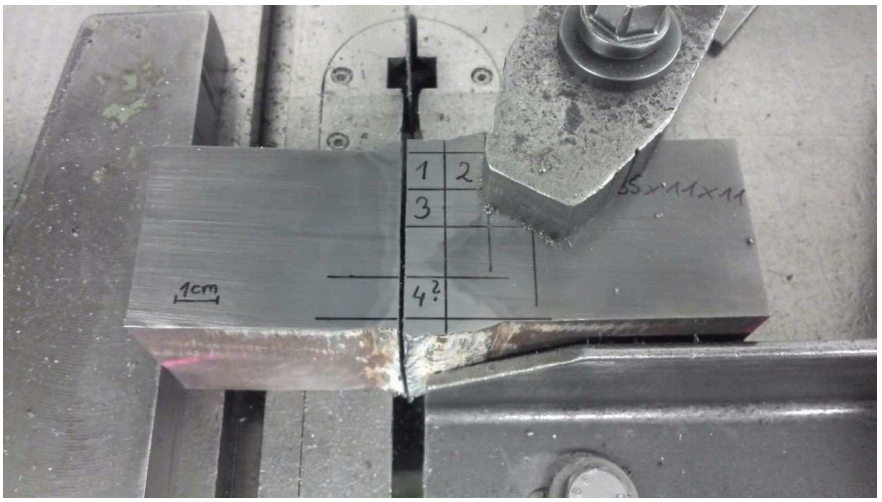

Figure 7.2.: Extraction for of blanks for milling B5x25 samples from the working sample of the nozzle weld joint, dvIV.

Content of non-metallic inclusions A common way to establish a starting value for f_0 in Gurson models is the determination of the fraction of non-metallic inclusions and second-phase particles in the steel. For all investigated materials this content was determined by investigating purely polished samples in light microscopy at a hundredfold magnification. The photographs were analysed by image processing to obtain the area fraction of the dark non-metallic inclusions.

Yield behaviour at varying temperatures and strain rates The yield behaviour under varying temperatures and strain rates was assessed in tensile tests. The basic yield behaviour at room temperature was determined in quasi-static tensile tests on smooth round bars of the shape B8x40, or for dvIV B5x25, according to DIN EN 50125 using optical extensometers. The temperature influence was assessed in tensile tests on the same specimens using a climate chamber to vary the ambient temperature. The displacement was measured by clip gauges on the sample. The resulting stress strain curves were evaluated at 5% strain to calibrate Eq. 6.1. The corresponding stress was extracted and compared to the stress at room temperature. The three fitting parameters c_T^i were fitted using the least-squares-method.

The effect of elevated strain rates on the hardening behaviour was assessed in high speed tensile tests. As described in 6.1.1.2 the cross section of the high speed tensile samples was reduced. Strain rates up to 250/s were tested. The resulting force-displacement curves were subsequently compared to simulations.

Notched round bars Notched round bars (NRB) with varying geometry were tested in quasi-static tensile tests. The sample geometries were also derived from the B8x40 form with varying ligament and notch radius. Table 7.1 contains the geometries that were used for studying the vessel materials (Fig. 7.3). Four geometries were tested for each material with at least three samples per geometry. The NRB were tested under quasi-static conditions using an optical extensometer. The resulting force-displacement curves were subsequently compared to simulations.

Table 7.1.: Nomenclature of NRB made of the pressure vessel materials used for the investigation of ductile damage.

Acronym	Notch ligament	Notch radius
L4R6	4mm	6mm
L4R18	4mm	18mm
L6R0.5	6mm	0.5mm
L6R1	6mm	1mm
L6R5	6mm	5mm

Plane strain and shear samples Plane strain (PS) and shear samples were manufactured to investigate the behaviour of the pressure vessel steel under shear-dominated loading conditions. All samples had a width of 50mm and a thickness of 3mm. The length was varied between 180mm and 130 mm, depending on the plate size. However, this only influenced the clamping length in the testing machine, which in both cases was sufficient. The plane strain samples were produced with 4 types of notch radii. Table 7.2 lists the geometries and acronyms. Three geometries were tested per material. Additionally, shear samples were produced from the same blanks. Shear samples have two overlapping notches; the exact geometry is given in the Appendix in Fig. A.10. Examples of the geometries are displayed in Fig. 7.3.

Table 7.2.: Nomenclature of the plane strain samples made of the pressure vessel materials used for the investigation of ductile damage.

Acronym	Notch ligament	Notch radius
PSR1	1.5mm	1mm
PSR3	1.5mm	3mm
PSR5	1.5mm	5mm
PSR8	1.5mm	8mm

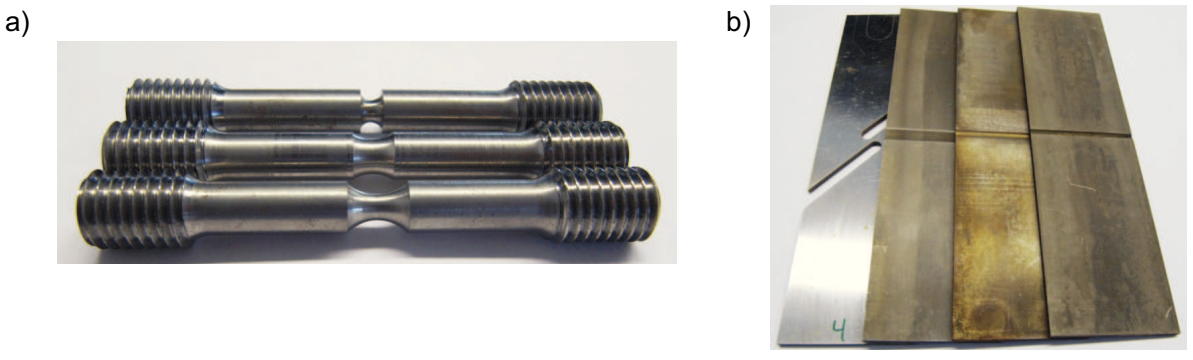

Figure 7.3.: Exemplary geometries of a) NRB b) plane strain and shear samples.

SENB tests SENB13x26 samples were manufactured. Fatigue pre-cracks were introduced and the samples were tested until a significant deformation was achieved. No brittle cracking occurred. Due to the high toughness and the resulting deformation, a significant displacement was detected in

the bearings, as can be seen in Fig. 7.4. This possible motion of the bearings had to be considered in modelling as well.

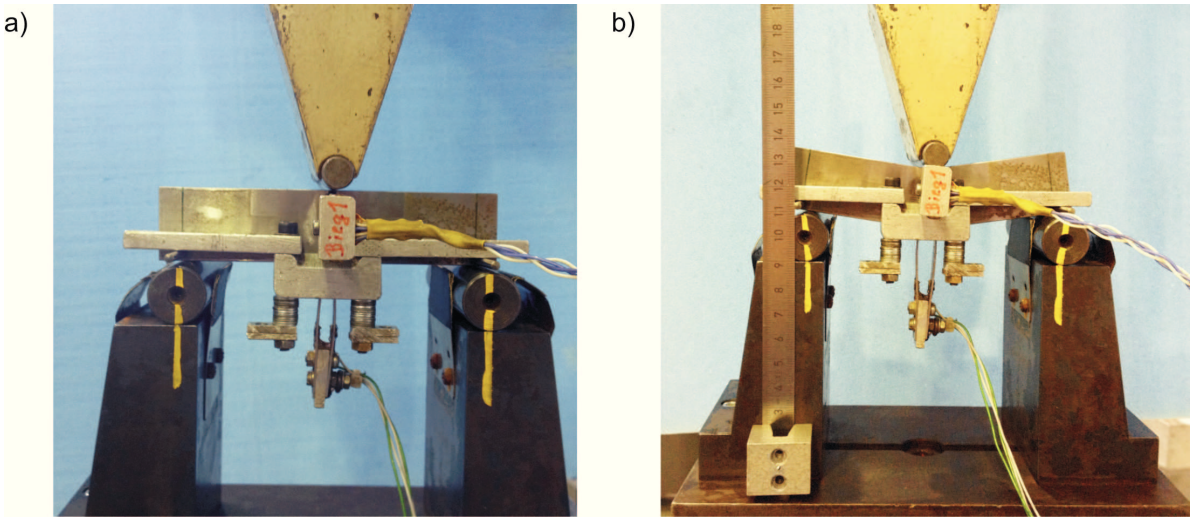

Figure 7.4.: SENB sample in the test setup with clip gauges a) before and b) after the test. The initial position of the cylindrical bearings was marked by yellow paint so that the displacement becomes visible.

Charpy tests Instrumented Charpy tests were performed on a 300 J hammer. For all materials tests at room temperature and at 7°C, the burst test temperature, were performed. For the base materials a range of temperatures between -196°C and room temperature was tested to assess the full transition behaviour. The results are provided in the Appendix, Section A.2.

7.1.2. Calibration of damage mechanics models

The NT model was calibrated for the materials dvII, dvIII, dvIV, and dvV on the performed tests. These were simulated and the parameters were modified iteratively until a sufficient agreement between measured and simulated force-displacement curves was achieved. All simulation models except for the cell elements were computed by the help of Abaqus/Explicit. In all 3D simulations the reduced linear element type C3D8R was used.

The NRB were simulated as axisymmetric half-models (Fig.7.5a). A simplification was also possible for the plane strain samples. During the iterative parameter calibration they were simulated by the help of CPE4 plane strain elements to reduce the computation time. While axisymmetric boundary conditions accurately represent a round sample, the assumption of the plane strain state does not hold true for the full width of plane strain samples. Therefore, a final validation of the parameter set was performed with a 3D analysis using one eighth of a sample as displayed in Fig. 7.5b. The shear samples were simulated using the entire geometry (Fig. 7.5c); only the thickness was reduced to half by the use of symmetry conditions.

SENB samples were simulated as 3D models with half thickness. The pre-crack was induced individually by the help of a crack seam definition. The cylindrical bearings were simulated with

elastic properties (Fig. 7.6). They were connected to the base surface and the sample by a friction coefficient of 0.1. This enabled the representation of the bearing displacement like in Fig. 7.4.

The high speed tensile test simulations used quarter models of the reduced cross section region. The testing velocity was applied as a boundary condition with a ramp-up time of 0.0001s. The Charpy model was identical to the one described in Section 6.1.1.1 except for the fact that the NT model was implemented via the VUMAT subroutine including strain rate and temperature dependence. After the successful calibration of the Gurson model parameters, these were used in cell element simulations to derive limit strain loci for the relevant vessel materials.

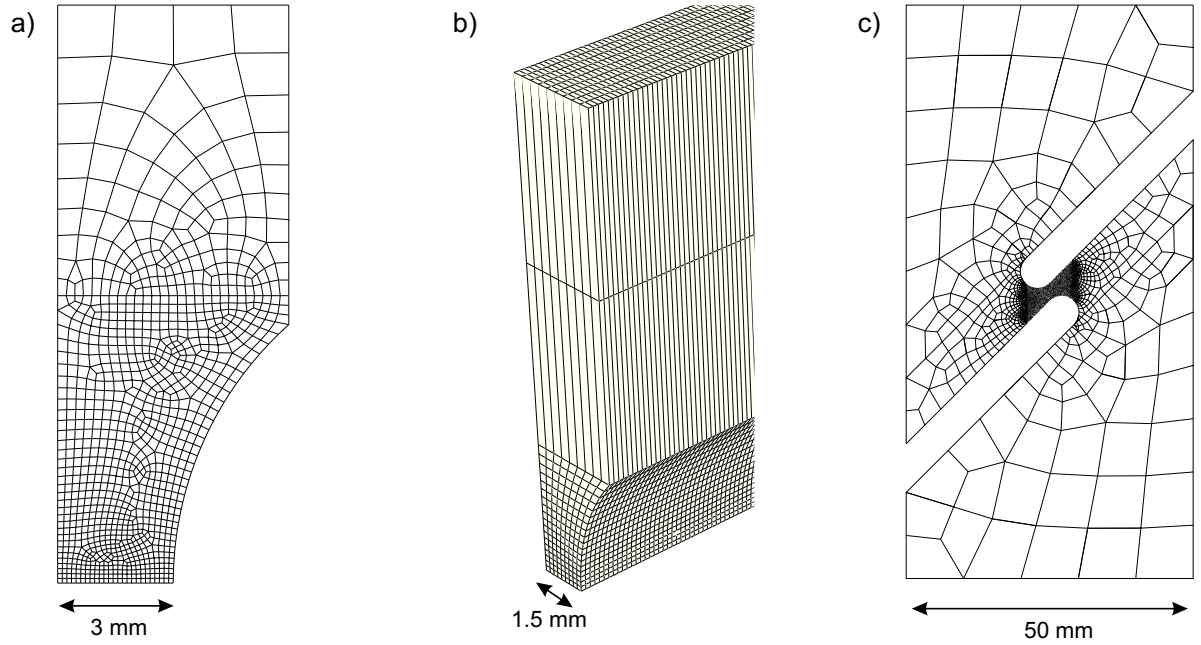

Figure 7.5.: a) NRB model b) PS model c) Shear sample model

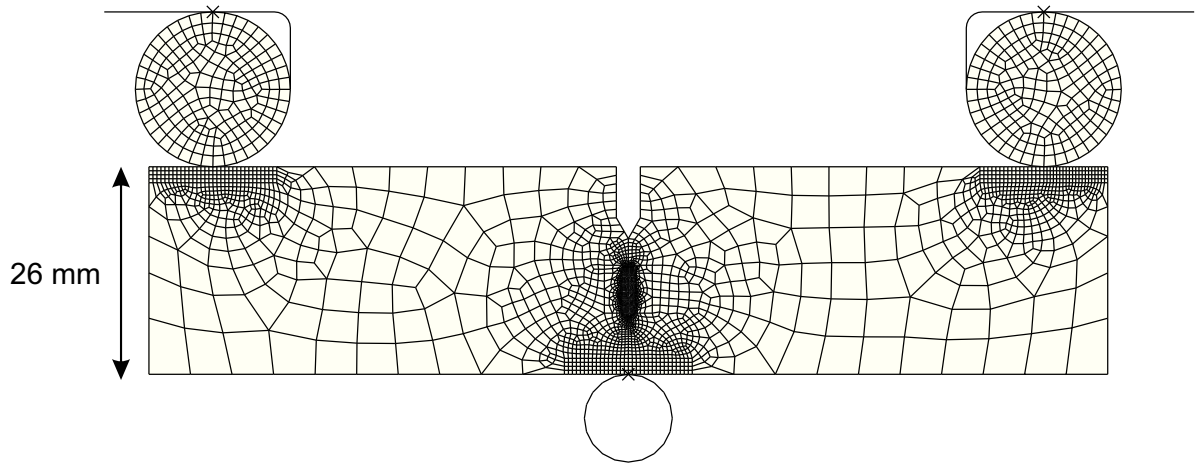

Figure 7.6.: Meshed SENB sample with explicitly modelled bearings.

7.1.3. Burst test

The burst test was performed on 30 January 2015 in the testing facility of the Salzgitter Mannesmann Forschung GmbH in Duisburg, Germany. The vessel was placed into a burst cavern and filled with water through the valves in the nozzle top. The vessel was instrumented with strain gauges and two wire displacement transducers for diameter measurements. Fig. 7.7 gives an overview on the applied measuring devices and shows the vessel before the test.

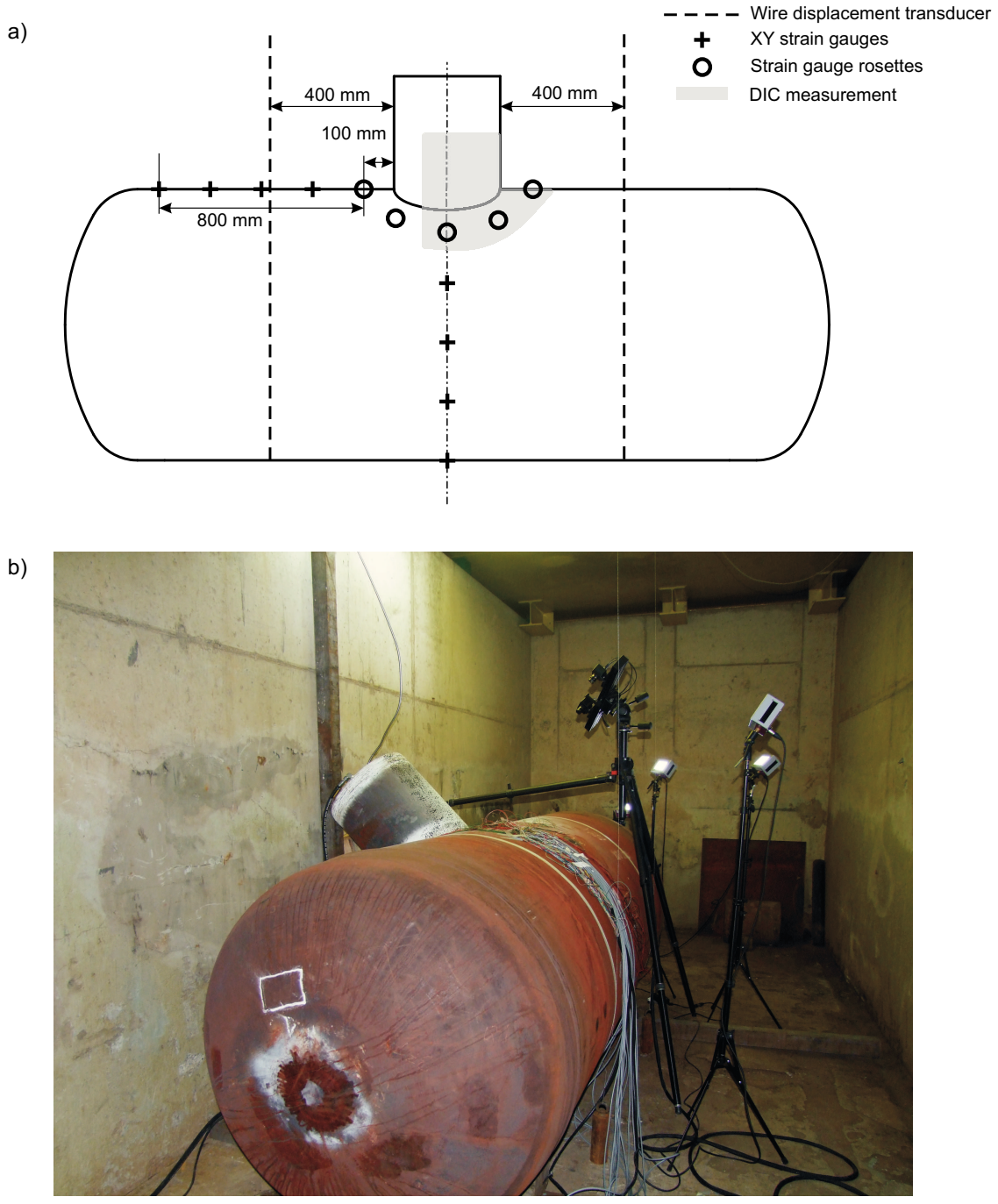

Figure 7.7.: a) Schematic illustration of the vessel instrumentation. b) The instrumented vessel in the burst cavern.

Moreover, during the elastic deformation of the vessel, the displacements at the transition from

nozzle to vessel were measured via digital image correlation (DIC) with a GOM ARAMIS system. Since the DIC system would have been destroyed by the burst event, the test was stopped in the elastic range at 400 bar. The pressure was reduced again to 300 bar, and the DIC system was demounted.

The applied strain gauges were suitable for high strains up to 20%. Strain gauge rosettes were placed around the nozzle cut-out while the longitudinal and circumferential straining of the vessel was recorded with XY-strain gauges. Details of the instrumentation are displayed in Fig. 7.8. Additionally, the applied pressure was recorded as well as the added water volume. A water-protected video camera was placed into the burst cavern to record the test and the bursting. The temperature of the vessel before the test was 7°C. For the burst test, the vessel was filled by high-pressure pumps until failure (Fig. 7.8d).

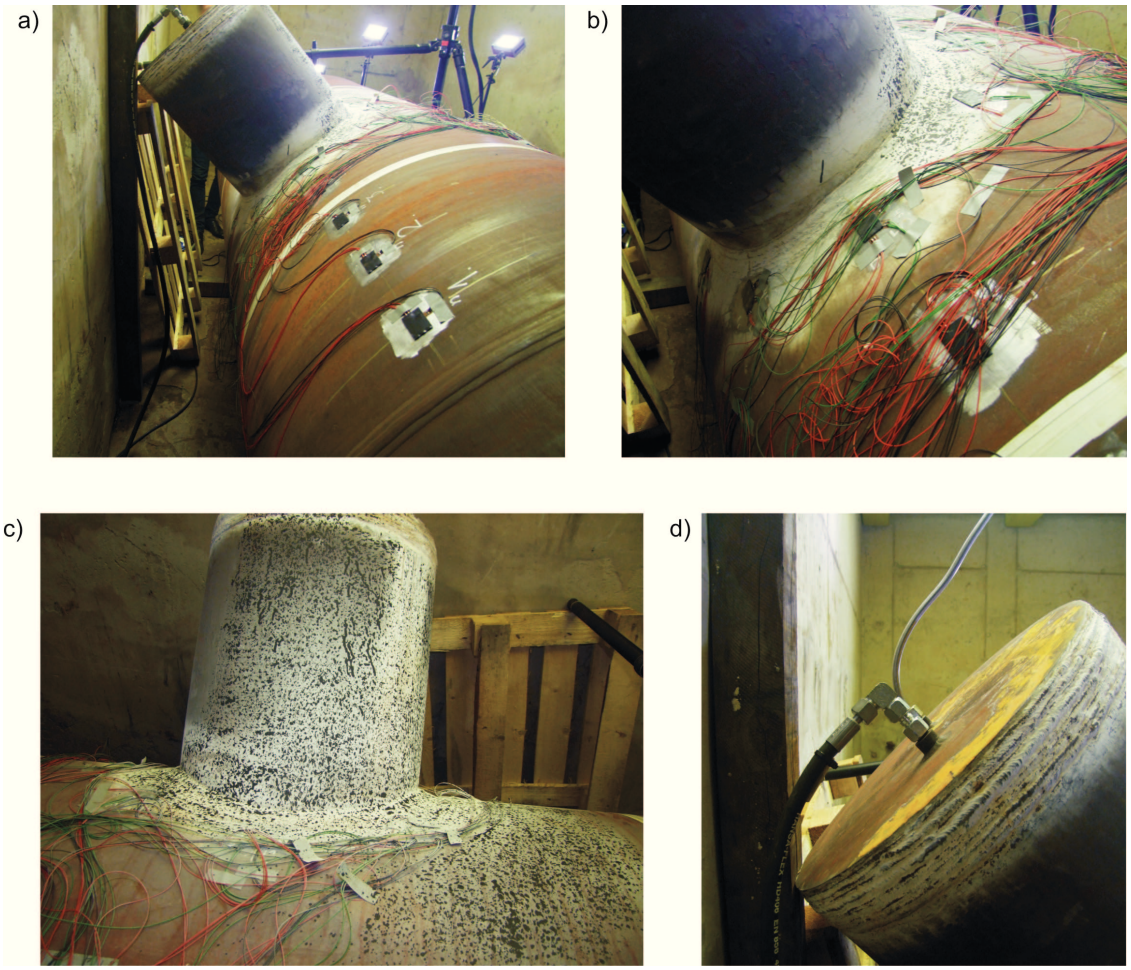

Figure 7.8.: a) Longitudinally positioned strain gauges, b) strain gauges at the nozzle-vessel transition, c) region prepared for DIC measurements, d) valves for filling and ventilation.

7.1.4. Full-scale failure simulation

The model for the full-scale failure simulation was developed within the accompanying research project FOSTA P950 [117]. A quarter of the vessel was simulated with symmetry conditions (Fig. 7.9a). The internal pressure was evenly distributed normal to the inner vessel surface. The computation was performed using Abaqus/Standard. The base materials and the relevant weld seams were explicitly modelled. C3D8R elements were used. The mesh was kept coarse in uncritical regions and refined in critical regions (Fig. 7.9b). Approximately one million elements were used within the model.

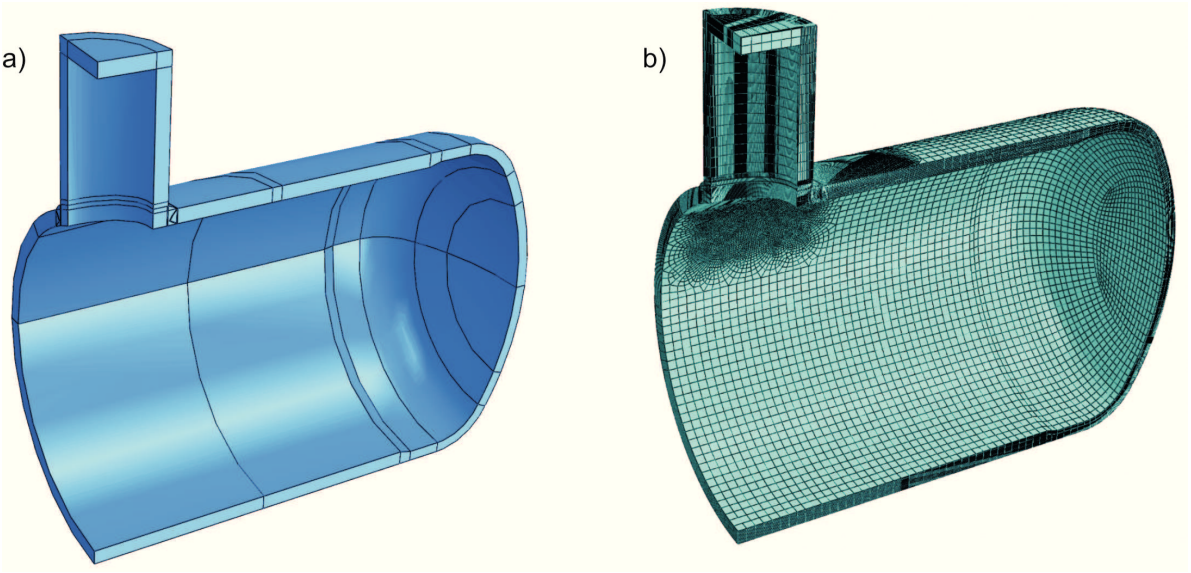

Figure 7.9.: Quarter model of the pressure vessel developed in [117]: a) geometry, b) mesh.

Their constitutive behaviour was described via a von Mises yield condition employing the derived flow curves. The limit strain locus was implemented via a subroutine for user defined variables, UVARM. This UVARM defined the ratio of the current plastic equivalent and the limit strain according to the stress state as an indicator for reaching the limit state:

$$L_{ind} = \frac{\overline{\varepsilon}^{p}}{\varepsilon^{c}(\overline{\theta}, \eta)} \tag{7.1}$$

If this limit indicator reached the value of $L_{ind} = 1$ during deformation, the vessel was assumed to have reached the limit state and therefore be close to failure. It has to be noted that this point does not necessarily coincide with the burst event. The limit state can be reached earlier since the limit strain corresponds to the onset of local softening. However, as a burst test is a load-controlled experiment local softening triggers failure reliably. Compared to the current, unclear limit state definitions, which indirectly relates to the yield point, this assumption is a significant improvement. In some cases, the exact moment when $L_{ind} = 1$ was reached could not be captured due to the automatic load stepping of Abaqus. In this case, the pressure was approximated by linear interpolation between the steps.

Equation 7.1 is a simplified version of the damage evolution rule of Johnson and Cook (Eq. 2.41) which only considers the stress state history in a limited fashion. However, as previous studies

have shown that in such pressure vessel simulations the stress state at the individual location is rather constant [12] this simplification does not affect the failure prediction significantly.

The full-scale failure simulations were used on the actual vessel geometry with the material properties and limit strain loci derived on the laboratory samples. Additional submodels were developed in [117] to compensate mesh influences and investigate scaling functions. The results of small and full scale investigations are presented in the following section.

7.2. Results

7.2.1. Experimental characterisation and numerical modelling of pressure vessel materials

In the following, the results of the experimental investigations on laboratory samples are presented along with the corresponding simulation results of the finally calibrated parameter sets. The sequence of investigations, which was defined based on the results of the sensitivity analysis, is illustrated in Fig. 7.10. During the iterative parameter calibration this sequence was repeated to achieve satisfactory results. Detailed results are presented for the base material of the vessel body, dvII, and the weld joint between vessel and nozzle, dvIV. Results for the base material of the heads, dvIII, and the longitudinal weld seam, dvV, are provided in the Appendix. Additionally, the material properties for the heat affected zone of the nozzle weld joint are discussed.

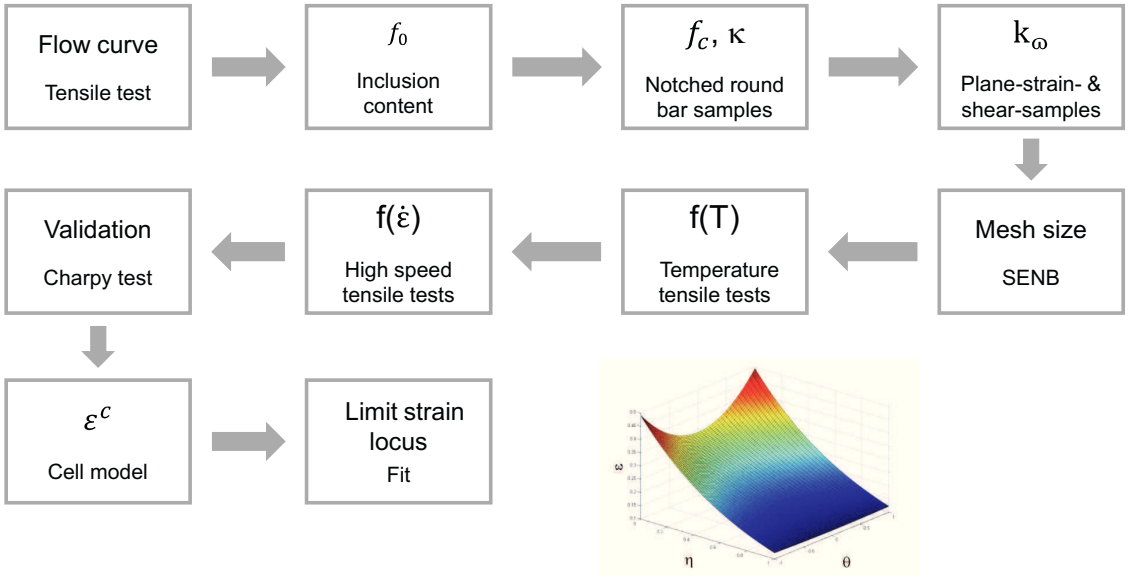

Figure 7.10.: Sequence of the performed investigations and simulations for the characterisation of the pressure vessel materials on the laboratory scale.

7.2.1.1. Base material of vessel body and nozzle (dvII)

The flow curve was extrapolated by means of a Ludwik formulation. Table 7.3 presents the corresponding parameters; the result is illustrated in Fig. 7.11a. Hereby, the discontinuous yielding of the experimental results was approximated by a smooth transition to avoid convergence problems of the VUMAT subroutine due to discontinuous derivations of the flow curve. The temperature dependence was fitted directly from experiments; results are presented in in Table 7.3 and Fig. 7.11b.

Table 7.3.: Parameters for the Ludwik extrapolation of the flow curve, strain rate and temperature dependency for dvII.

Parameter	σ_0 [MPa]	k_L [MPa]	n_L	c_T^1	c_T^2	c_T^3	$c_{\dot{e}}^1$	$c_{\dot{e}}^2$	$c_{\dot{e}}^3$
Calibrated value	448	685	0.153	0.456	0.00356	0.835	0.0052	1.036	0.04

Table 7.4.: Fitted NT parameter set for dvII.

Parameter	f_0	f_c	κ	q_1	q_2	k_ω	η_1	η_2	Mesh size
Calibrated value	0.002	0.015	1.5	1.5	1.0	3.8	0.8	1.3	0.06mm

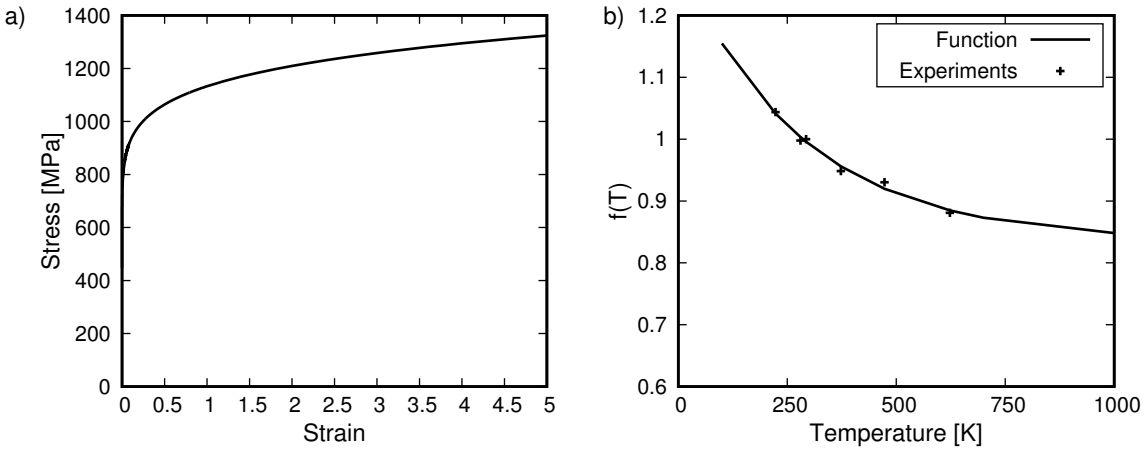

Figure 7.11.: a) Extrapolated flow curve and b) temperature dependence function of dvII.

All remaining parameters were fitted iteratively in the comparison of simulation and experiment. The final parameter set is provided in Tables 7.3 and 7.4. The inclusion content was determined from polished sections. An example is provided in Fig. 7.12.

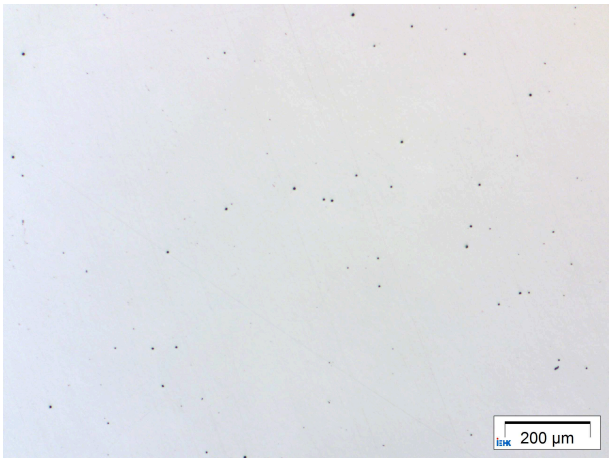

Figure 7.12.: Polished section of dvII for the determination of the inclusion content at a magnification of 100.

The average area fraction of the inclusion content was 0.095%. Starting from this, the value of the initial void volume fraction parameter was calibrated as $f_0 = 0.002$ in combination with $f_c = 0.015$

and $\kappa = 1.5$ in the NRB simulation. This parameter set can reproduce the experimental force-displacement curves of the tested NRBs with very good accuracy (Fig. 7.13). Only for the L6R0.5 geometry the force is slightly overestimated after the force maximum. The reason for this is the combination of an axisymmetric idealisation in the simulation and the sharp notch geometry. For such sharp notches, failure initiates in the notch ground not in the specimen's centre. Since an axisymmetric simulation cannot resolve differences along the circumference, the resistance of the sample is slightly overpredicted. In general, the good reproduction quality over a wide variation of notch radii and ligaments demonstrates that this parameter combination can predict the constitutive response of the material dvII reliably for varying stress states.

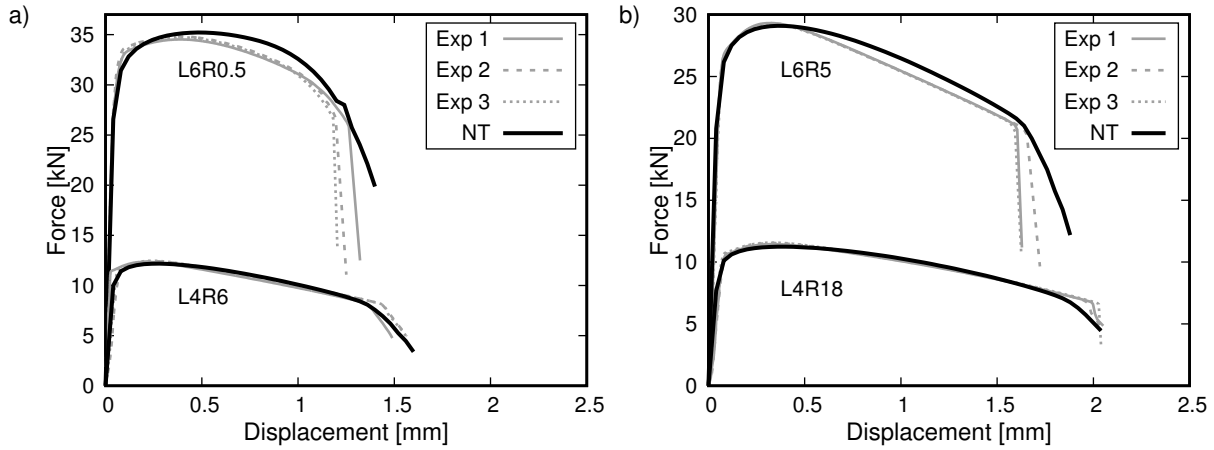

Figure 7.13.: Result of NRB simulation and experiments (dashed lines) a) L6R0.5 and L4R6 b) L6R5 and L4R18 of dvII.

The shear damage parameter k_ω, which is introduced by the NT model formulation, was fitted to the experimental results of shear tests and plane strain tests. The parameters $\eta_1 = 0.8$ and $\eta_2 = 1.3$, which proved to be suitable in the pre-studies, were applied here as well. The force-displacement curves of the simulations predict the onset of the load drop with very good accuracy for the PSR8 geometry and the shear test (Fig. 7.14) and with reasonable accuracy for PSR3. Only for the sharply notched PSR1 geometry the failure displacement is strongly overestimated. As discussed above, this is a result of the implementation of the NT model. The base metal dvII seems to exhibit a dependence of the yield properties on the Lode angle because the simulations overestimate the general force level. This cannot be covered by the NT model and therefore has to be accepted.

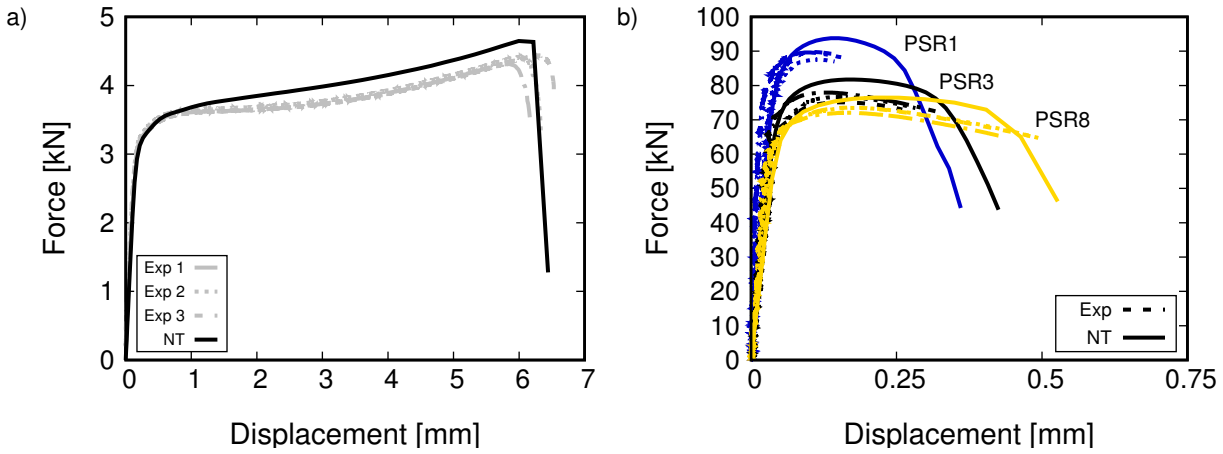

Figure 7.14.: Result of NRB simulation and experiments (dashed lines) of a) shear and b) plane strain samples of dvII.

The last parameter to complete the NT model formulation is the mesh size. It was fitted by comparing the results of SENB tests to simulations with the NT model. Figure 7.15a illustrates that for the calibrated mesh size of 0.06 mm the simulation can reproduce the test result with excellent accuracy. All three samples had similar lengths of the fatigue pre-crack (Exp 1: 13.36 mm, Exp 2: 13.34 mm, Exp 3: 13.15 mm, averaged according to ASTM 1820). Thus, it could also be shown that the NT model reliably covered stress states with a very high triaxiality.

Finally, the parameter set for the strain rate dependence was fitted to the results of high speed tensile tests. Figure 7.15b plots the results which show that the elevated force level due to strain rate hardening can be very well reproduced. Only the load drop displacement is slightly overestimated.

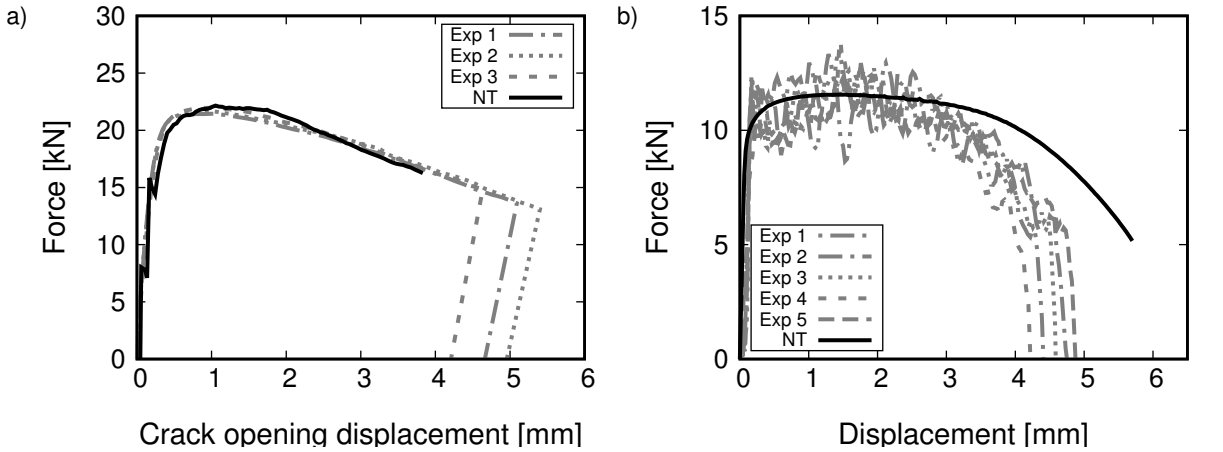

Figure 7.15.: Result of simulation and experiments (dashed lines) of a) SENB tests b) high speed tensile tests at a strain rate of 150/s of dvII.

The parameter set was validated in the simulation of a Charpy test at room temperature. The comparison of the force-displacement curves in Fig. 7.16 proves that the calibrated parameter set is able to reproduce the upper shelf toughness behaviour and that it was successfully fitted. The achieved accuracy is very good in all regions of the force-displacement curve.

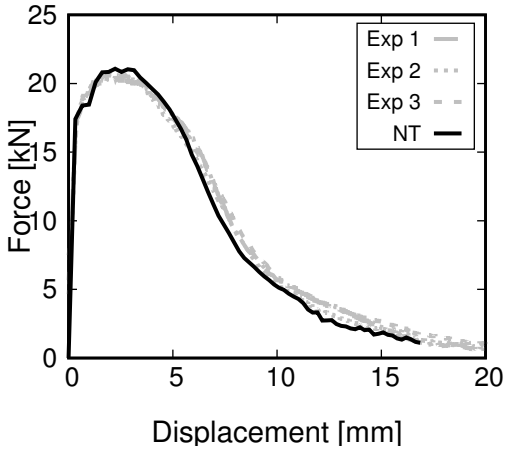

Figure 7.16.: Result of simulation and experiments for Charpy tests at room temperature of dvII.

In summary, the calibrated parameter set shows a good prediction quality for most experimental force-displacement curves. Perfect matching cannot be achieved for all samples if the model fitting is performed on such a wide range of stress states, loading conditions, temperatures and strain rates. Yet, a broad and robust prediction was provided. This is underlined by the well-matching Charpy simulation because this test incorporates constantly varying stress states, strain rates and temperatures.

Finally, the limit strain locus was derived according to the procedure described in Chapter 6. The symmetric formula of Bai and Wierzbicki (Eq. 2.44) was used for its mathematical description. The corresponding parameters were fitted by least squares optimisation. The resulting fit parameters of the limit strain locus (LSL) are listed in Table 7.5, the surface is plotted in Fig. 7.17.

Table 7.5.: Fitted LSL parameter for dvII.

Parameter	D_1	D_2	D_3	D_4
Calibrated value	2.738	1.882	0.7	1.182

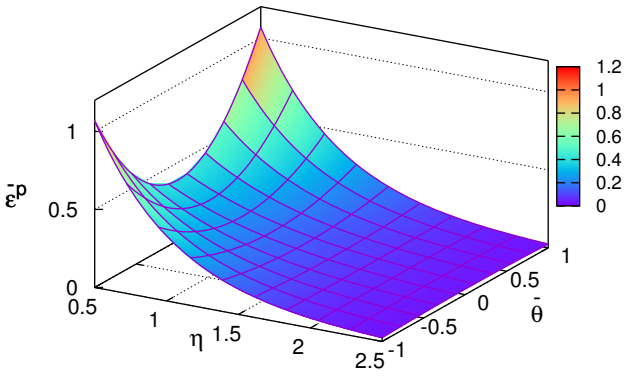

Figure 7.17.: Plotted limit strain locus of dvII.

7.2.1.2. Nozzle weld joint (dvIV)

The identical calibration approach was applied to the material of the nozzle weld seam, dvIV. The resulting parameter sets are provided in Tables 7.6 and 7.7. Flow curve and temperature function are displayed in Fig. 7.18.

Table 7.6.: Parameters for the Ludwik extrapolation of the flow curve, strain rate and temperature dependency for dvIV.

Parameter	σ_0 [MPa]	k_L [MPa]	n_L	c_T^1	c_T^2	c_T^3	$c_{\dot{e}}^1$	$c_{\dot{e}}^2$	$c_{\dot{e}}^3$
Calibrated value	435	775	0.19	1.05	0.0075	0.88	0.011	1.023	0.013

Table 7.7.: Fitted NT parameter set for dvIV.

Parameter	f_0	f_c	κ	q_1	q_2	k_ω	η_1	η_2	Mesh size
Calibrated value	0.001	0.002	1.67	1.5	1.0	5.0	0.8	1.3	0.06mm

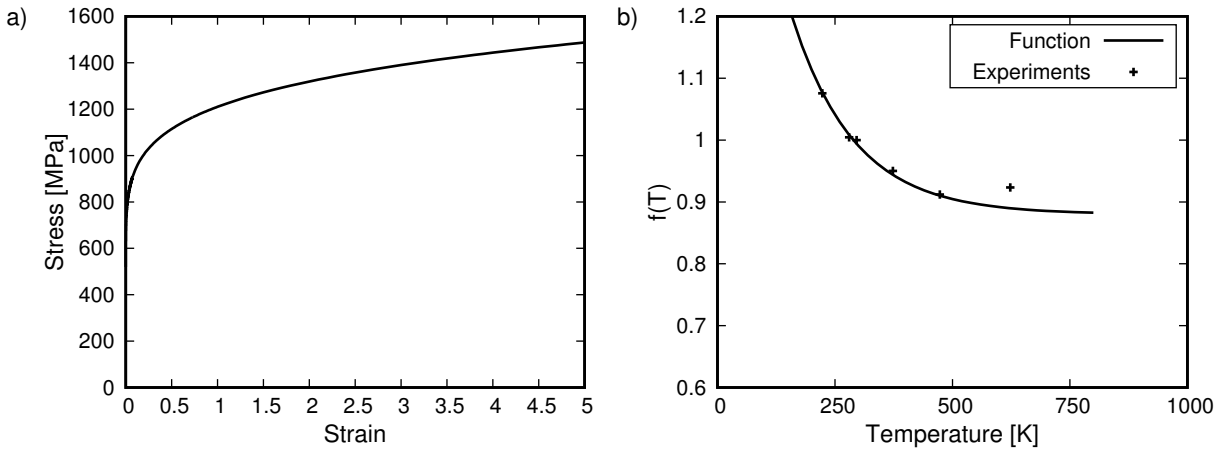

Figure 7.18.: a) Extrapolated flow curve and b) temperature dependence function of dvIV.

The metallographic investigation showed that only very finely dispersed non-metallic inclusions were present (Fig. 7.19). A very low area fraction of 0.01% was determined. Yet, such small inclusions are difficult to be captured by the measurement. The result therefore has to be treated with caution. The use of such a low value as initial void volume fraction f_0 diminishes any influence of the NT model. Therefore, an initial void volume fraction of $f_0 = 0.001$ was assumed.

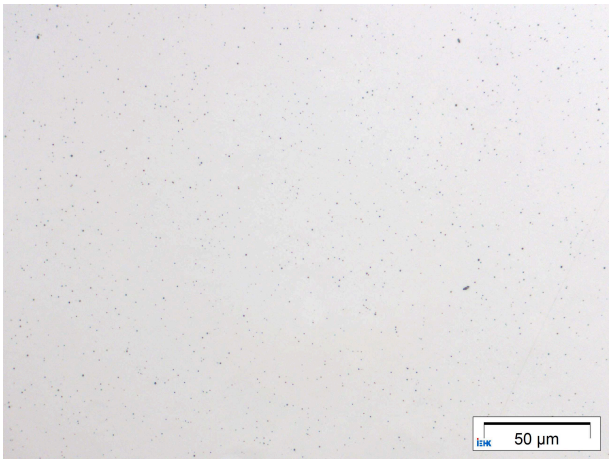

Figure 7.19.: Polished section of dvIV for the determination of the inclusion content at a magnification of 500.

As the samples were taken from a weld seam, the test results vary more than in the base material. In this case, the samples were extracted from the upper as well as the lower region of the K-weld seam. Nevertheless, the calibrated parameter set can reproduce the deformation and failure behaviour of the NRB samples very well (Fig. 7.20).

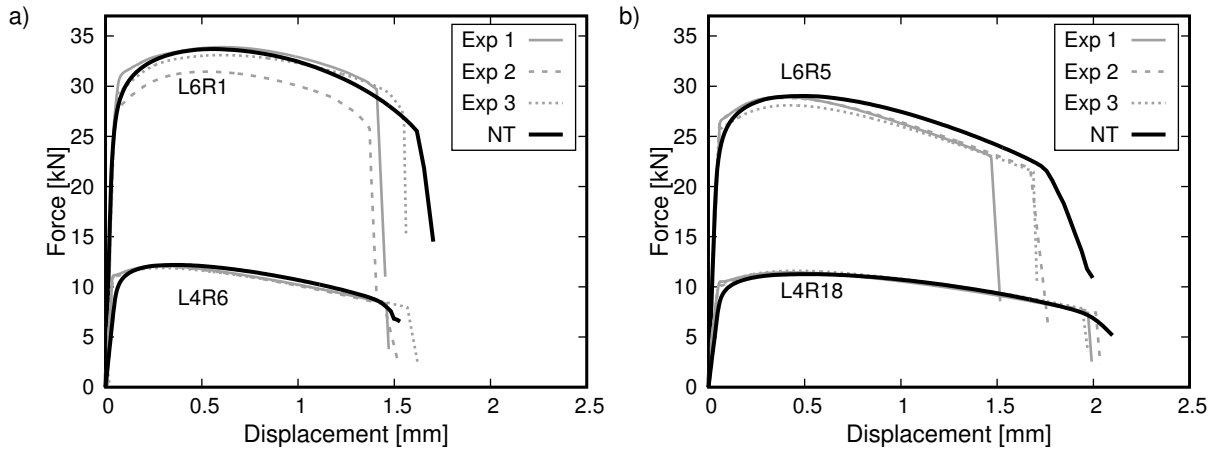

Figure 7.20.: Result of NRB simulation and experiments (dashed lines) a) L6R0.5 and L4R6 b) L6R6 and L4R18 of dvIV.

In the comparison of PS experiment and simulation (Fig. 7.21a) it can be seen that, contrary to the results of dvII, the difference in the yield point is not given for the material dvIV. This is in accordance with the findings of Bai et al., who showed that a Lode angle influence on the yield point is not present for all kinds of steels [37]. In this material, the yield point and load level could therefore be reproduced very well by the simulations. One argumentation in current discussions on such effects is that the Lode angle influence on yielding is caused by material anisotropy. This argumentation could be valid in this case as the base material dvII was rolled, which might cause anisotropy, while the weld metal was not. Yet, the base material was quenched and tempered which removes possible anisotropy effects. Further research into this topic could be beneficial. The failure displacement is predicted with very good accuracy for the geometries PSR3 and PS8

but overestimated for PSR1. In contrast to this, the failure displacement in the shear samples is slightly underestimated while the overall force-displacement curve is well met (Fig. 7.21b).

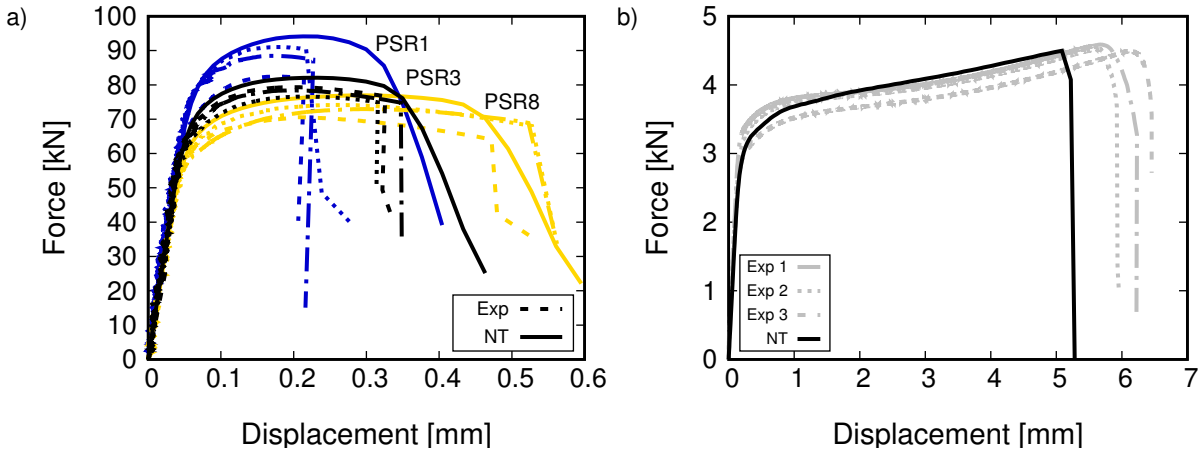

Figure 7.21.: Result of NRB simulation and experiments (dashed lines) of a) shear and b) plane strain samples of dvIV.

Strong variations due to heterogeneous weld properties could also clearly be detected within the experimental results on SENB specimens (Fig. 7.22a). The simulation, with an implemented crack length of Experiment 1, can predict the load level at the beginning of ductile crack extension very well. This is decisive for a correct calibration of the mesh size. It was therefore considered successful. The simulation predicts failure near the first load drop in Experiment 2, while Experiment 1 and 3 showed a deviating behaviour. The force-displacement curves of the high speed tensile tests could be well reproduced (Fig. 7.22b) except for a minor overestimation of the failure displacement.

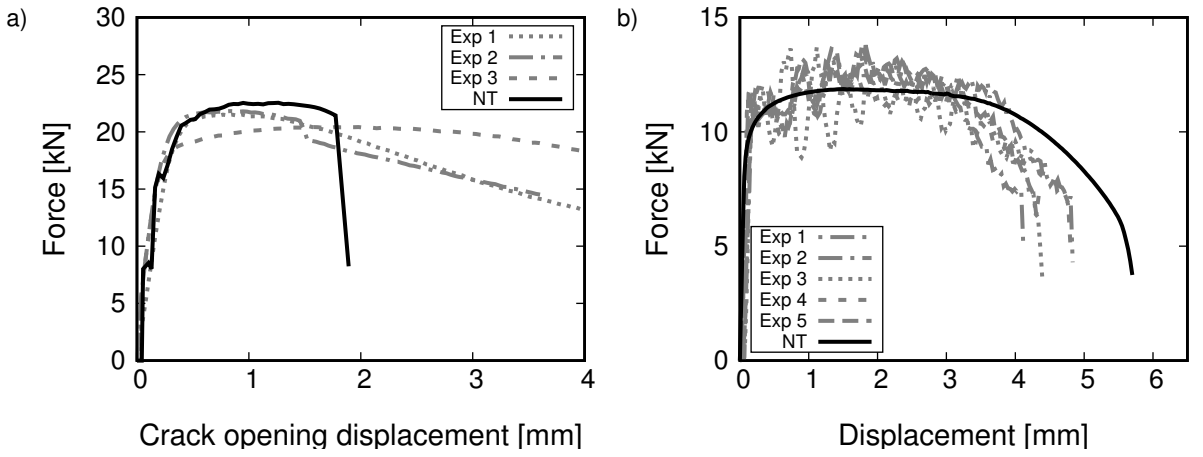

Figure 7.22.: Result of simulation and experiments (dashed lines) of a) SENB tests b) high speed tensile tests at a strain rate of 150/s of dvIV. Averaged crack lengths of the SENB samples was for Exp 1 13.31 mm, for Exp 2 12.9 mm, and for Exp 3 13.05 mm.

The calibrated parameter set could successfully reproduce the force-displacement behaviour in a Charpy test at room temperature (Fig. 7.23) and thereby represent the toughness level. The resulting LSL is presented in Table 7.8 and Fig. 7.24.

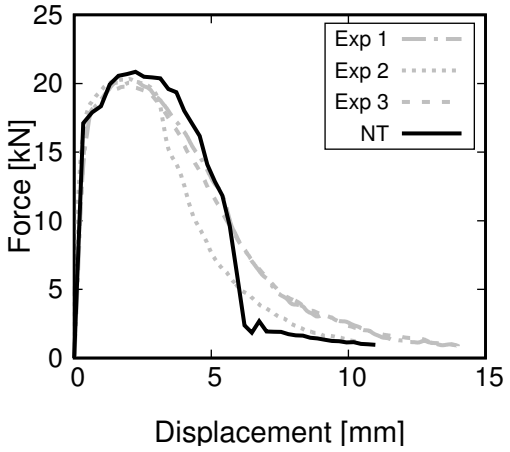

Figure 7.23.: Result of simulation and experiments for Charpy tests at room temperature of dvIV.

Table 7.8.: Fitted LSL parameter for dvIV.

Parameter	D_1	D_2	D_3	D_4
Calibrated value	2.291	1.831	0.6	1.083

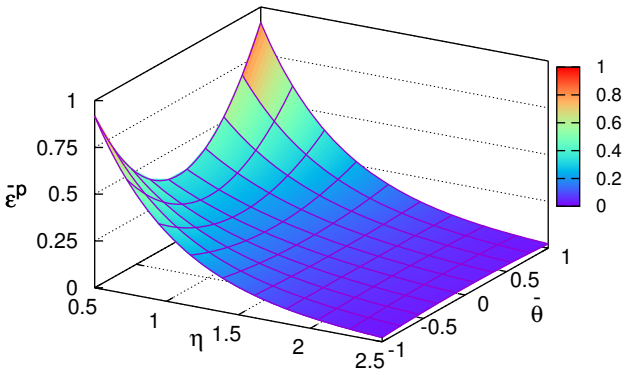

Figure 7.24.: Plotted local softening locus of dvIV.

7.2.1.3. Heat affected zone of the nozzle weld joint (dvIV)

The design of the pressure vessel predicted the transition from vessel body to the nozzle as the most critical location. Therefore, failure was expected within this region. As presented in Fig. 4.5, the heat affected zone of this weld seam is softer than the base metal or the weld seam itself. Consequently, also a lower flow curve can be expected as the correlation between hardness and yield strength for steels is well known. As a result, the heat affected zone is likely to be a weak spot in the structure and should be considered in the global pressure vessel model.

A common approach for this is to adapt the level of the flow curve according to a hardness ratio for weld seam modelling. In this study, the formulations presented by Sommer et al. [154] were

used. These are based on the idea of calculating an offset factor for the flow curve from the ratio of the HAZ hardness H_{HAZ} and the base metal hardness H_{bm} and the tensile strength of the base metal $R_{m,bm}$:

$$\sigma_{Offset} = R_{m,bm} \cdot \frac{H_{HAZ}}{H_{bm}} - R_{m,bm} = R_{m,bm} \cdot \left(\frac{H_{HAZ}}{H_{bm}} - 1 \right) \tag{7.2}$$

The flow curve is then corrected by:

$$\sigma_y(\overline{\varepsilon}^p)_{HAZ} = \sigma_y(\overline{\varepsilon}^p)_{bm} + \sigma_{Offset} \tag{7.3}$$

For the nozzle weld seam the average base metal hardness was 290 HV1 and the average HAZ hardness 240 HV1 (Table 4.7). This results in a hardness ratio of 0.83 and $\sigma_{Offset} = -154$ MPa. Consequently, the flow curve of the dvII base metal is reduced by 154 MPA. Fig. 7.25 displays the flow curves of dvII, dvIV and the derived one for the HAZ.

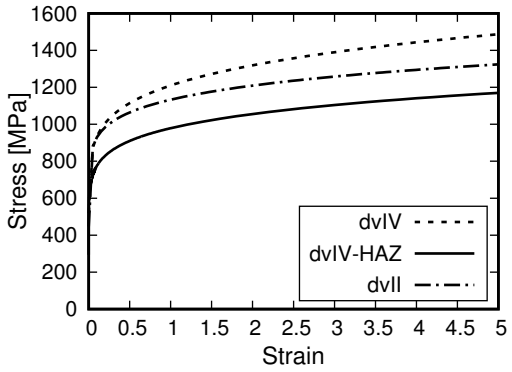

Figure 7.25.: Resulting extrapolated flow curve for the HAZ in comparison to the flow curves of dvII and dvIV.

The results of the sensitivity analysis showed that a parallel shift of the flow curve does not affect the derived softening locus. An experimental investigation of the failure properties of the HAZ is not feasible because its average thickness is approximately 2mm. Originally, the HAZ consists of base metal. Since the HAZ is softer, deformation should localise within it and therefore the limit strains would be reached earlier. Consequently, considering the strength reduction leads to already to conservative assumptions. The limit strain locus of the base metal dvII was therefore assumed for the HAZ without any further modification.

7.2.1.4. Summary of the results of the head material (dvIII) and longitudinal vessel weld joint (dvV)

The parameters for the materials dvIII and dvV were determined with identical procedures. Since they are not situated in the critical region for failure initiation, only the parameter sets of the results are provided in Tables 7.9-7.11. Full results including the comparison of experimental and simulations results are given in the Appendix (Section A.4.4).

Table 7.9.: Parameters for the Ludwik extrapolation of the flow curve, strain rate and temperature dependency for dvIII and dvV.

Parameter	σ_0 [MPa]	k_L [MPa]	n_L	c_T^1	c_T^2	c_T^3	$c_{\dot{e}}^1$	$c_{\dot{e}}^2$	$c_{\dot{e}}^3$
dvIII	467	663	0.151	1.16	0.00835	0.908	0.005	1.02	0.03
dvV	380	775	0.19	1.05	0.0077	0.88	0.01	1.07	0.01

Table 7.10.: Fitted NT parameter set for dvIII and dvV.

Parameter	f_0	f_c	κ	q_1	q_2	k_ω	η_1	η_2	Mesh size
dvIII	0.0015	0.015	1.5	1.5	1.0	3.0	0.8	1.3	0.12mm
dvV	0.001	0.002	1.67	1.5	1.0	5.0	0.8	1.3	0.08mm

Table 7.11.: Fitted LSL parameter for dvIII and dvV.

Parameter	D_1	D_2	D_3	D_4
dvIII	3.552	2.084	0.8451	1.148
dvV	2.374	1.835	0.639	1.2

7.2.2. Burst test and fractography

The burst test was performed as described in Section 7.1.3. In the following, the test results are presented along with a detailed analysis of the fracture surfaces. From this information, the failure sequence and the initiation site could be reconstructed.

7.2.2.1. Test results

Pressure, time and added water volume were measured during the burst test as global characteristics. The added water volume was hereby determined by the weight loss of the water supply tank, which was under ambient pressure. The course of the pressure development over time is plotted in Fig. 7.26. The filling stops, which were undertaken due to technical demands, such as demounting the DIC devices and switching supply pumps, are evident. The vessel burst at a pressure of 680 bar. The response of the pressure vessel to the load is clearly evident from Fig. 7.27 that plots the pressure as a function of the added water volume. The vessel was initially filled with 3105 l water. 147 l were added during the experiment. The global behaviour was linear until a pressure of approximately 570 bar. Subsequently, a global nonlinear, plastic behaviour was detected.

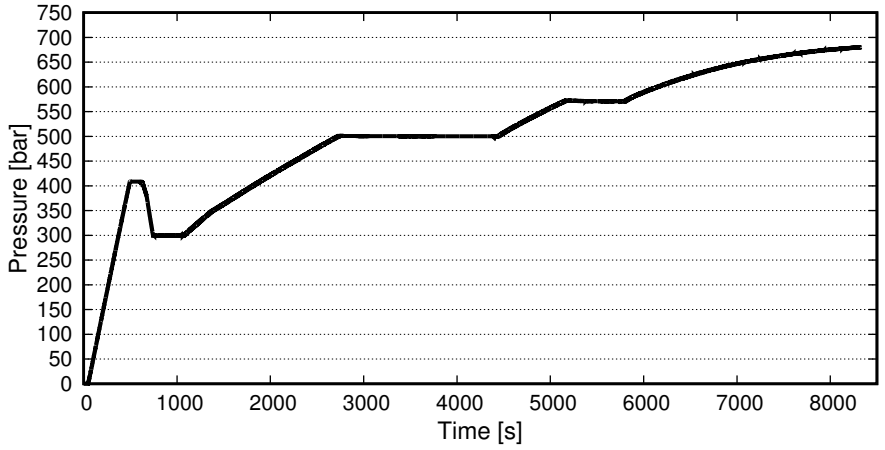

Figure 7.26.: Internal pressure of the vessel as a function of time.

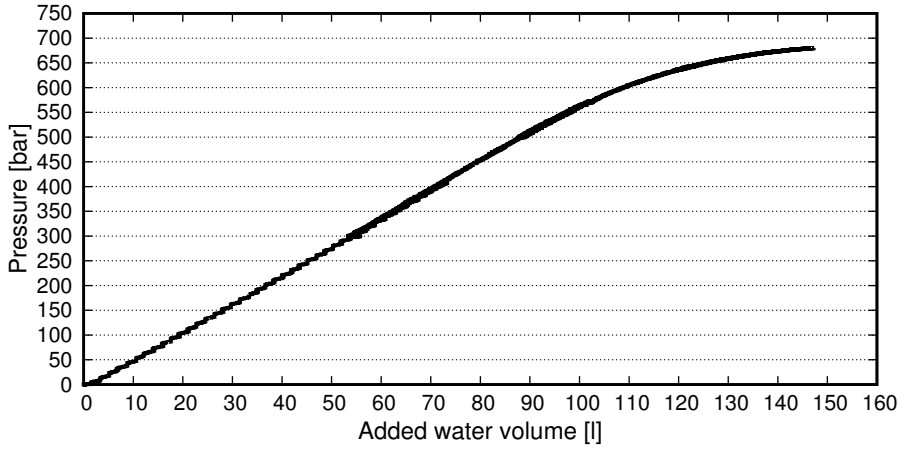

Figure 7.27.: Internal pressure of the vessel as a function of the added water volume.

Figure 7.28 shows the pressure vessel before and after the burst test in the burst cavern. The wall, which the vessel initially leaned against, showed a damaged region after the test. The vessel was turned over. A crack split one side of the vessel in half and extended into one of the heads. The nozzle was completely separated from the vessel.

Figure 7.28.: The pressure vessel in the burst cavern a) before and b) after the burst test.

Figure 7.29 provides detailed photographs of the crack path. The main crack split one half of the vessel and divided into two arms in the head. The nozzle was split as well. Some of the crack surfaces show signs of heat tinting. The accompanying video was made available on the internet [155]. On it, it can be seen that damp rose from the crack surfaces right after the burst test. Obviously, there was a significant amount of heat present due to the dynamic burst situation. The crack path in the vessel body could better be investigated after relocation of the vessel from the burst cavern (Fig. 7.29e). No additional cracks or defects were found in an inspection of the inner side of the vessel; all cracks proceeded fully through the wall.

Figure 7.29.: Details of the crack path: a) Crack in the vessel body, b) split end of crack in the front heading, c) split nozzle d) heat tinted material at the nozzle crack surface, e) crack path in the vessel body, visible after relocation from the burst cavern.

The deformation was measured during the experiment by strain gauges, wire displacement transducers, and in the beginning of the experiment by DIC. Technical problems with the wire displacement transducers prevented a reliable data recording in the beginning. After resetting the system during a filling stop, the measurements could be restored. At the end of the experiment the circum-

ferential strain measured was 0.36%. This is in accordance with the strain gauge measurements. The DIC measurements provide an overview on the deformation pattern in the nozzle transition region (Fig. 7.30). It is evident that the strongest deformation took place near the nozzle weld seam. A slight tendency for a buckle formation at the side of the vessel was detected.

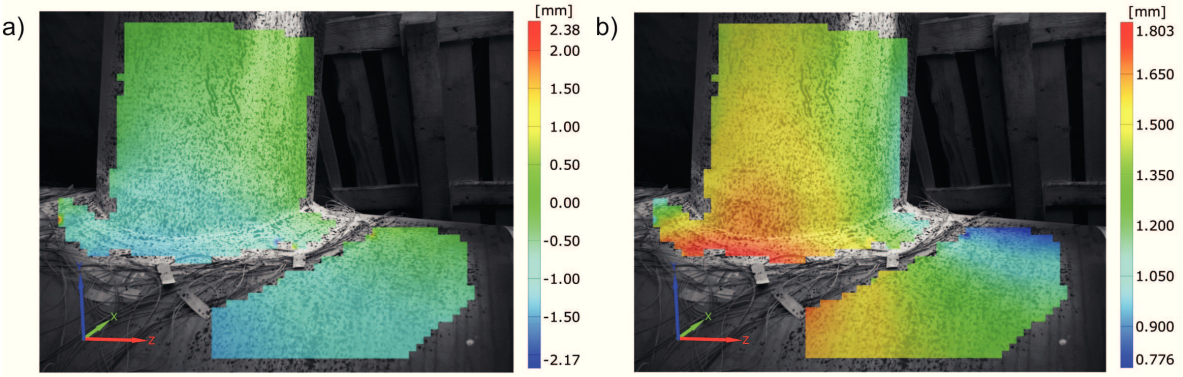

Figure 7.30.: Deformation at 400 bar measured via DIC: a) Deformation in x-direction (horizontal displacement perpendicular to the longitudinal axis of the vessel) b) Deformation in y-direction (height of the vessel). No significant deformation in z-direction (longitudinal axis of the vessel) was detected.

The deformation in the further course of the experiment was recorded by the strain gauges. The strain values that were recorded directly before bursting are presented in Fig. 7.31 along with the nomenclature. The XY strain gauges placed along the circumference recorded in general a low level of strains. The level of circumferential strains is approximately 0.3%. No relevant deformation in longitudinal direction was detected with these gauges. The slightly elevated L-displacement in U1 can be explained by the buckling tendency as also indicated by the DIC measurement.

The XY gauges placed on the longitudinal axis reveal that the deformation increased towards the nozzle. The circumferential (U) strain increases from the overall level of 0.3% to 2.7% before the nozzle in L4. Additionally, a negative longitudinal strain was detected. This indicates a strong localisation of deformation, which is in accordance with the deformation pattern after fracture. Rosette strain gauges recorded the deformation in the most highly loaded zone around the nozzle. The main crack formed between the strain gauges R1 and R8. All strain gauges around the nozzle measured high levels of circumferential strain between 4% and 5.5%. The strains detected in longitudinal direction were comparably lower with maximum values of 1%. The 45°-strain gauges recorded intermediate strains between 1.5% and 4%. The strain gauges R1, R5 and R8 show the highest levels of circumferential strain. The symmetry of the vessel is reflected in the fact that gauges opposite to each other seem to have experienced a similar deformation pattern. For example the longitudinal strain is highest for rosettes R1 and R5 while the 45°-measurement is lowest for R4 and R8. However, on the vessel side with the gauges R5-R8 and R1 a slightly higher level of strains was detected.

In general, it is evident that the deformation concentrated around the nozzle transition. A high level of plastic deformation was present leading to strain measurements of up to 5%. The corresponding base length of the strain gauges was 10mm. To reconstruct the failure initiation site, the deformation pattern has to be compared to results of an investigation of the fracture surfaces and the deformation after the burst test.

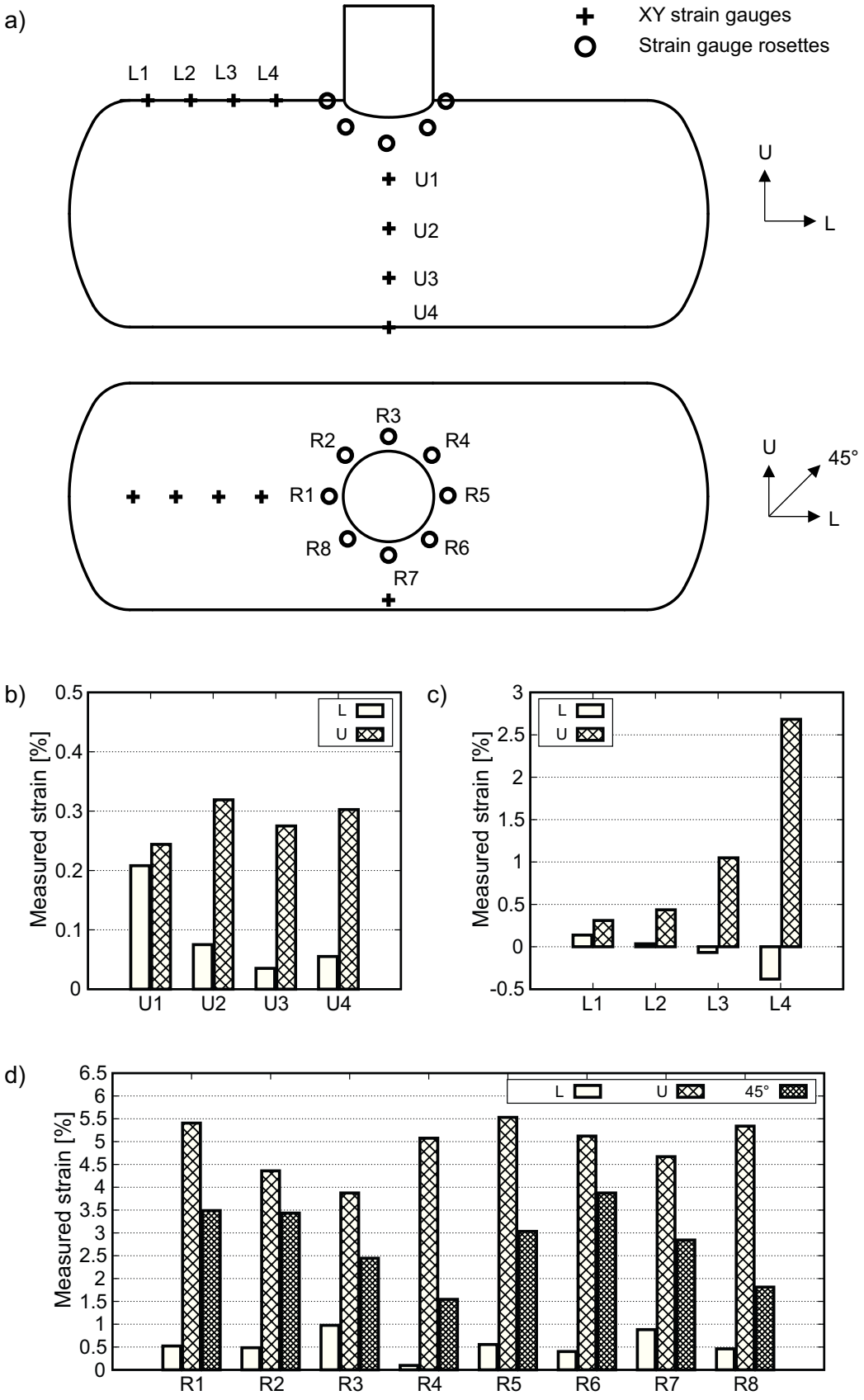

Figure 7.31.: a) Nomenclature of the strain gauges. Results of the measured strain immediately before bursting for strain gauges b) U1 - U4, c) L1 - L4, d) R1 - R8.

7.2.2.2. Fractography

For a full comparison of burst test result and simulation it is necessary to know the failure initiation site. Therefore, the pressure vessel was thoroughly examined in the aftermath of the experiment. All fracture surfaces were inspected and categorised. Typical regions were investigated in SEM to determine the fracture type. The deformations were classified and compared to the information available from the video and the position of the vessel in the burst cavern after failure.

Figure 7.32, to which the numbers in brackets refer in the following, shows the crack paths in vessel and nozzle. The side of the vessel, on which the circumferential strain gauges (U1-U4) were located, will in the following be called the front side of the vessel. The main crack in the body spreads from the hole of the nozzle location into one of the heads (1). It is located approximately 10 cm in front of the longitudinal axis of the vessel. The cut-out of the nozzle separation is on the front side characterised by a large region that was sheared off. It includes a part of the nozzle material that was separated from the nozzle itself (2). The rear side of the nozzle cut-out is characterised by an irregular, rugged appearance of the fracture surface with alternating regions of local heat tinting, smoothly sheared off partitions and coarse-grained fracture surfaces (3). A part of the nozzle material was separated from the nozzle and remained on the vessel body at the rear side of the main body crack (3a). This crack pattern is obviously reflected on the nozzle. Additionally, there is a longitudinal crack in the nozzle that extends into the weld seam at the top of the nozzle (4). Small cracks are visible on the edges of the nozzle weld seam no matter whether the remainders are located on the vessel or the nozzle (5). These small cracks are distributed all along the circumference of the nozzle. In Fig 7.32. exemplary but not all positions are marked. A closer investigation of such a crack by cutting showed that it proceeded through more than half of the material thickness in the weld seam. A detail picture is provided by Fig. 7.33e.

Typical fracture appearances could be classified according to the materials the crack ran through:

- dvII-body: Shear fracture with normal central region characterised by a significant amount of separations (Figure 7.33a). This fracture type is present in the main crack of the vessel body (1).
- dvII-nozzle: Shear fracture with pronounced shear lips or strongly plastified fracture edges and a planar, coarse-grained central region (Figure 7.33d). This fracture type is present in the splitting crack in the nozzle and on the nozzle material remaining on the vessel (2,3a, 4).
- dvIII: Coarse-grained, planar fracture surface with a straight course (Figure 7.33b). This fracture type can be found in the crack in the head (1).
- dvIV: Irregular, partially rugged fracture surface with alternating heat tinted areas, coarse-grained fracture regions and smooth, sheared-off surfaces (Figure 7.33c). This fracture surface is present along the broken weld-seam (3).

Typical examples for the fracture surfaces were cut out of the vessel and investigated in SEM. Most fracture surfaces showed ductile as well as cleavage fracture regions and could therefore be identified as mixed fracture. However, the share varied significantly. Figure 7.34a displays an example SEM picture from the main crack in the vessel body. Ductile fracture is clearly dominant. The coarse, granular fracture surfaces, as present in dvII-nozzle and dvIV, could be identified as mixed-mode fractures with a dominating share of cleavage fracture. An example from the

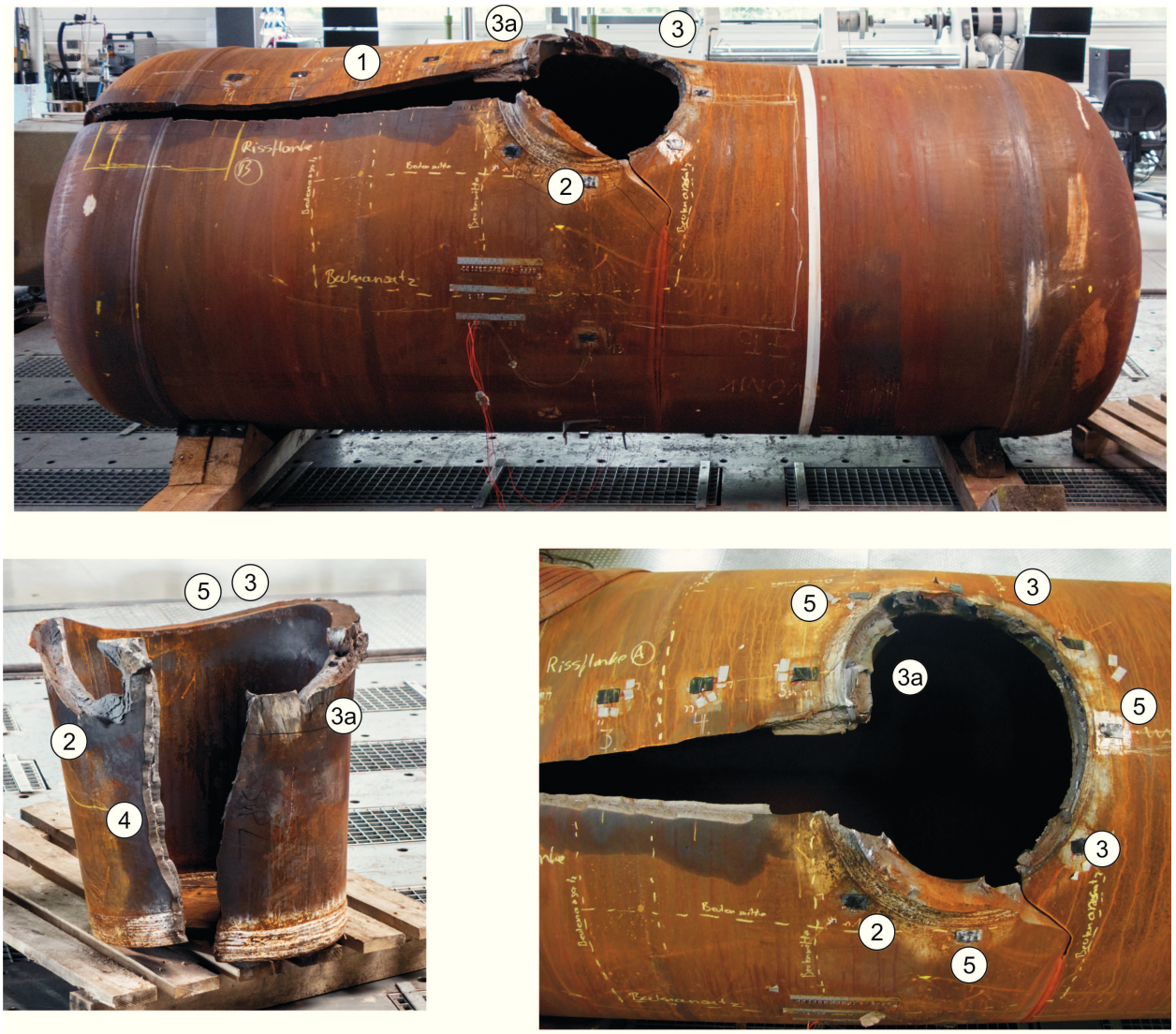

Figure 7.32.: Characteristic crack regions.

Figure 7.33.: Details of typical fracture surfaces in: a) dvII-body, b) dvIII, c) dvIV d) dvII-nozzle and e) detail of a small crack on the weld seam.

longitudinal nozzle crack is given in Fig. 7.34b. The shear lips showed purely ductile failure with sheared voids (Fig. 7.34c).

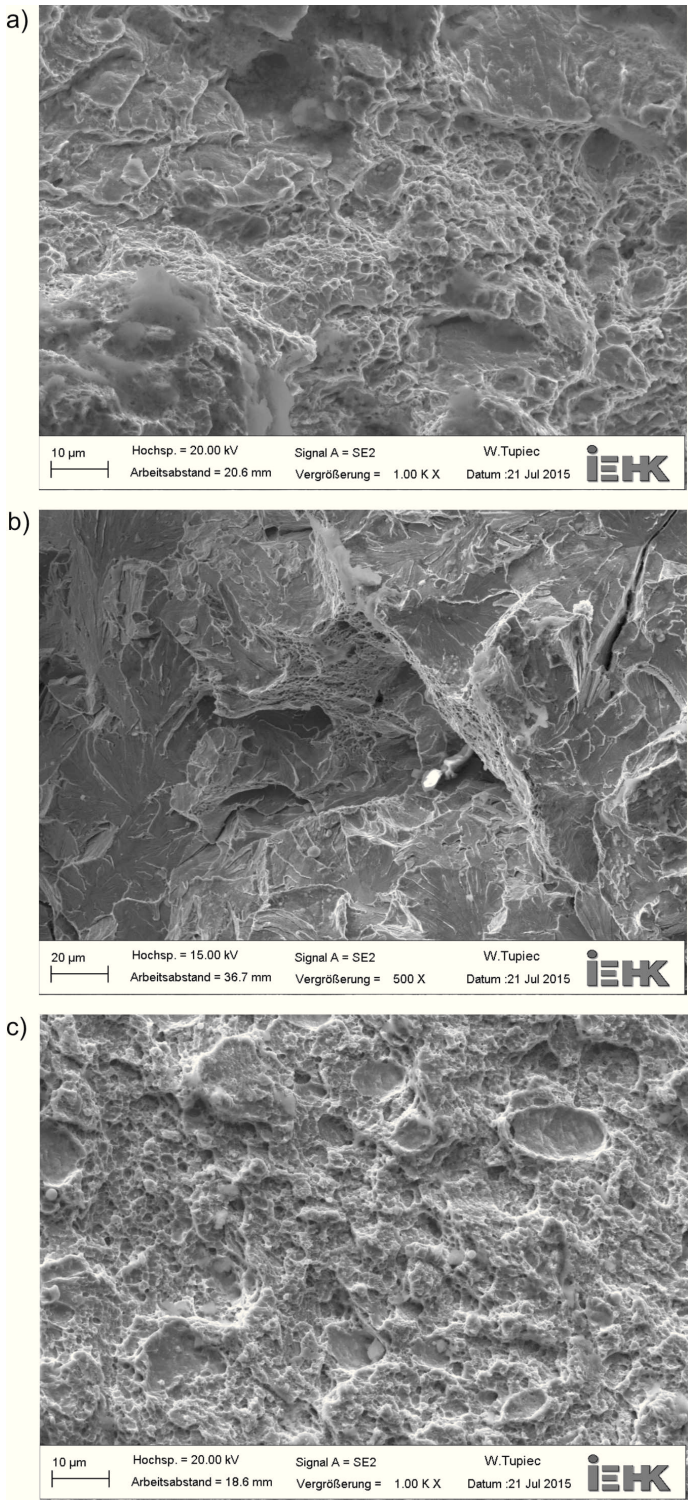

Figure 7.34.: SEM investigations of typical fracture appearances: a) mixed fracture with dominant ductile share in the vessel (dvII-body), b) mixed fracture with dominant cleavage share in the nozzle (dvII-nozzle), c) sheared voids on a shear lip (dvII-nozzle).

Figure 7.35.: Last frame of the test video in which the vessel is recognisable. The crack in the head is already visible while the nozzle, recognisable by the white paint on its top and marked by a red circle, is still in its place and uncracked.

7.2.2.3. Reconstruction of failure sequence and initiation site

The failure sequence and initiation site was reconstructed from the fractographic investigations presented above and a close investigation of the test video. On the test video [155] regular loud cracking noises can be heard in the last 10 minutes before failure. These can be correlated to the small cracks around the nozzle weld seam that formed but did not proceed. Obviously, the vessel could compensate these by a redistribution of the load. The last frame of the test video, in which the vessel is still recognisable, is displayed in Fig. 7.35. It is evident that at this point of time the crack had already proceeded into the head as water can be seen splashing out from it. However, behind this water jet, the white-painted top of the nozzle is visible below the filling valves and seems to be still intact. Also a portion of the nozzle itself is visible below that and seems to be still intact as well. Consequently, the failure initiation site must be located at the transition from nozzle to vessel. This is also the most highly loaded zone as indicated by the strain gauges (Fig. 7.31).

The combination of these evidences with the results of the fractographic investigation allow the reconstruction of the following, probable failure sequence (numbers in brackets refer to the nomenclature of Fig. 7.32):

1. Due to the high plastic deformation small cracks were initiated around the nozzle weld seam at local material inhomogeneities. This caused the cracking noises on the video. The load could be re-distributed by local plastification, the cracks were stopped and the pressure increased further.
2. At the point of failure initiation one of these small cracks started growing and became critical. First, the crack spread longitudinally along the body vessel into the head (1). In cylindrical pressure vessels, this is a typical pattern for crack formation because the circumferential

stresses have the highest magnitude.

3. The vessel body was opened by the leaking water. This induced a load on the nozzle and caused the crack to proceed longitudinally into the nozzle (4).
4. Although the nozzle was already split, the vessel body opened further and sheared off a large portion of the nozzle material (2). This crack sequence ended in a pure shear deformation of the vessel material. Since the nozzle was then separated from the opening motion of the vessel, it was not sheared open further.
5. Due to the force of the water jet, the nozzle was forced towards the rear side of the vessel and the remaining connection of vessel and nozzle was separated in a strongly dynamic crack propagation process (3,3a). This is proven by the heat tinted areas and the rugged appearance of the fracture surface in (3). The nozzle was fully separated and fell behind the vessel after damaging the wall.

According to this evidence the failure initiation spot is situated at the origin of the main crack in the vessel body at the weld seam. A close-up of this region is provided in Fig. 7.36. On it, a fan-like structure can be seen that has its origin in the HAZ of the nozzle weld seam. The further crack seems to have spread from this structure. In mixed fracture, these typical fracture lines indicate the crack propagation direction. This location is therefore assumed to be the origin of the crack. This is a justified assumption because the HAZ is also weaker than the base metal.

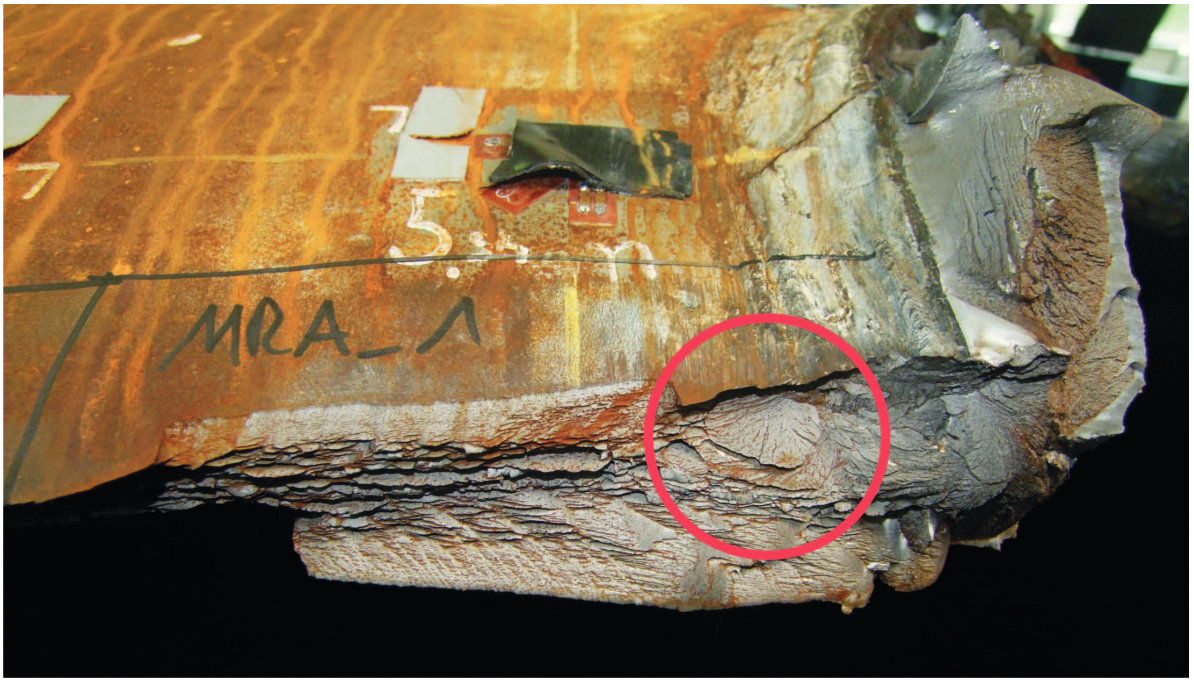

Figure 7.36.: Probable initiation site of failure. The fan-like structure in the HAZ of the weld seam, marked by the red circle, is the suspected crack origin.

The region was closely investigated in SEM (Fig. 7.37). On the origin of the fan-like structure the fracture surface shows a fully ductile appearance with typical void formation. The larger particle, which is visible in Fig. 7.37e, cannot be uniquely attributed to the material as it may also be a contamination. The voided structure of the fracture surface proves a ductile failure process.

Since this location is with high probability the failure initiation site, the assumption of a ductile failure initiation is well-justified. In summary, the failure sequence could be reconstructed and the probable initiation site shows a ductile fracture surface.

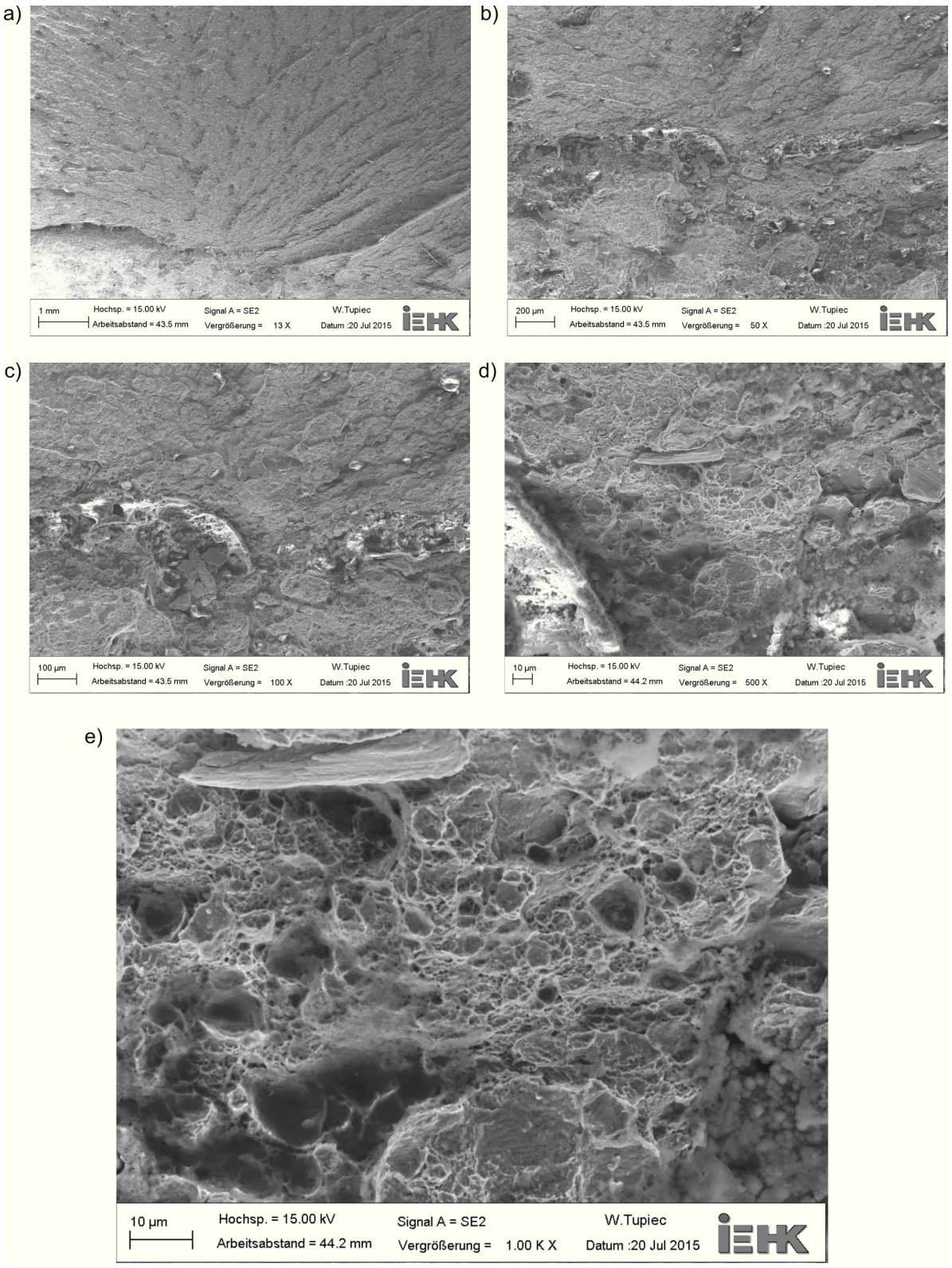

Figure 7.37.: Probable failure initiation site in a SEM investigation with increasing magnification (a-e).

7.2.3. Full scale vessel modelling and prediction result

As described in 7.1.4, the predictive capabilities of the developed modelling concept were tested in a simulation of the demonstrator pressure vessel. The results on full scale vessel modelling presented in the following section were created in cooperation with the Institute of Steel construction at RWTH Aachen University within the accompanying research project.

To allow a precise modelling of the nozzle weld joint, a section was extracted from the pressure vessel and prepared by etching (Figure 7.38a). This geometry was adapted in the FE model of the vessel provided by [117] (Figure 7.38b). The vessel model was combined with the limit strains and material properties of the pressure vessel determined in this study. Additionally, the proposed scaling function was tested.

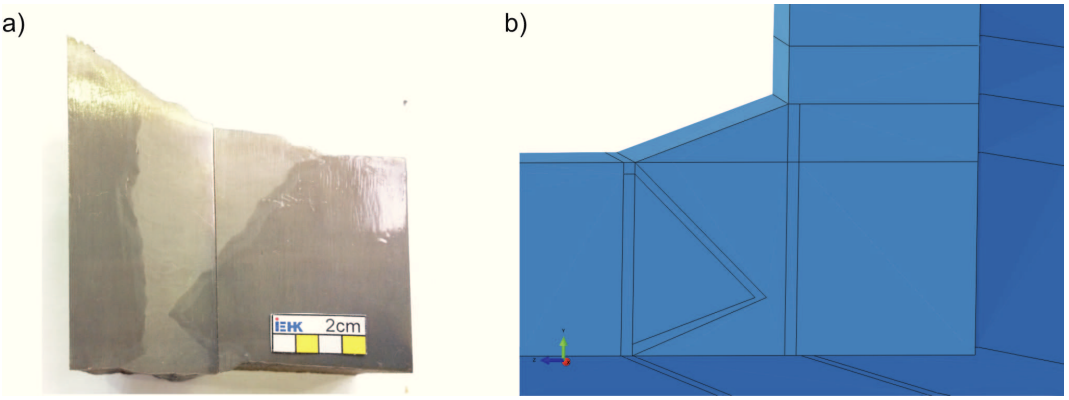

Figure 7.38.: a) Real geometry of the nozzle weld seam in the pressure vessel and b) idealisation in the pressure vessel model [117].

First simulations using the extrapolated flow curves and the limit strain loci of dvII and dvIV showed that the highest stresses and strains concentrated around the nozzle (Fig. 7.39). The highest local strains and the highest values of the limit indicator were reached at two positions around the weld (Fig. 7.40). These two positions will in the following be named as “Cut 1” and “Cut 2” because the FE model is cut at the respective locations for the evaluation. Cut 2 is near the central plane of the vessel, corresponding to the locations of the strain gauges R3, respectively R7 due to the symmetry. Cut 1 is located near the longitudinal axis. This corresponds to positions between the strain gauges R1 and R8 or equivalent positions due to symmetry. At these locations, small cracks in the weld seam were present, which confirms the suspected high loading. Cut 1 is close to the actual failure initiation site.

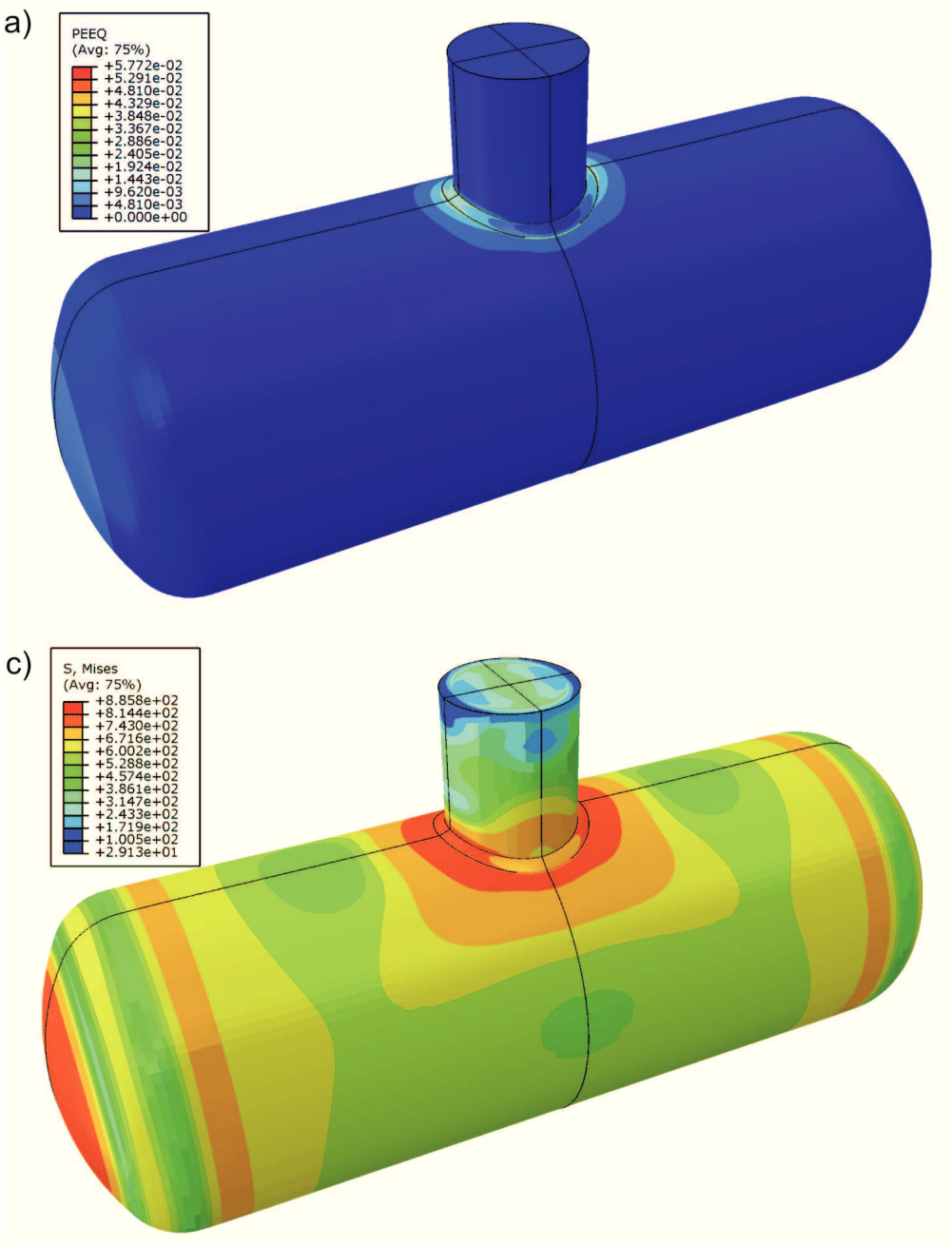

Figure 7.39.: a) Strain and b) stress distribution in the vessel at an internal pressure of 600 bar. The quarter model was mirrored for a better overview.

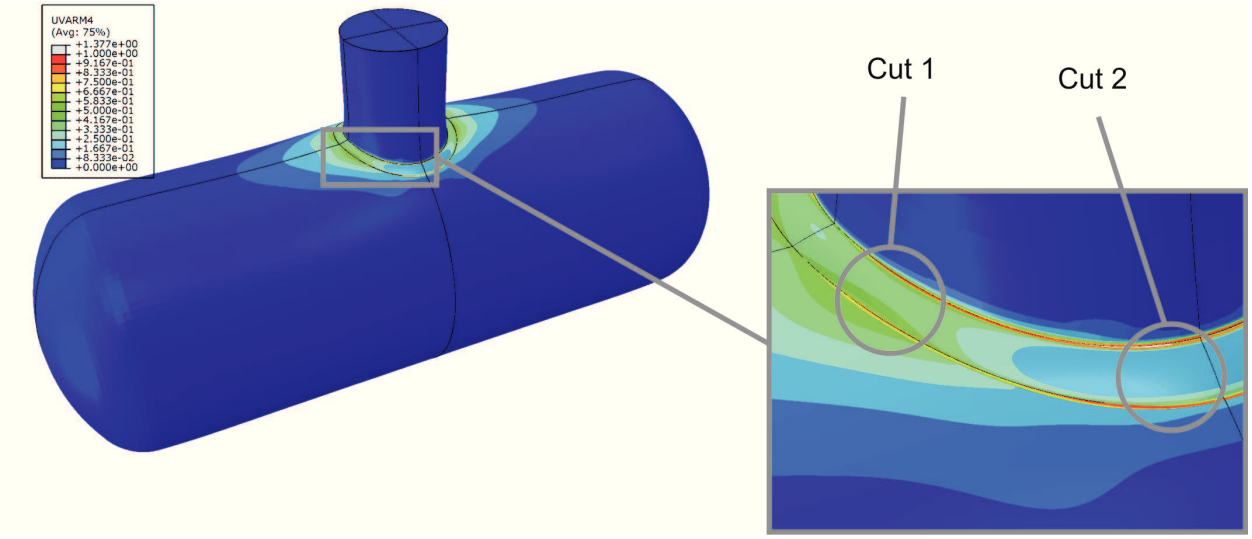

Figure 7.40.: Distribution of damage indicator values for HAZ and base material after reaching the limit state. Positions at which the limit indicator UVARM4 was reached first are marked by circles.

The initial simulations also proved the suspected strain localisation in the HAZ. This triggers a mesh dependency for strain-based failure criteria (Fig. 7.41). To investigate this, within the accompanying research project submodels were created from the original model [117].

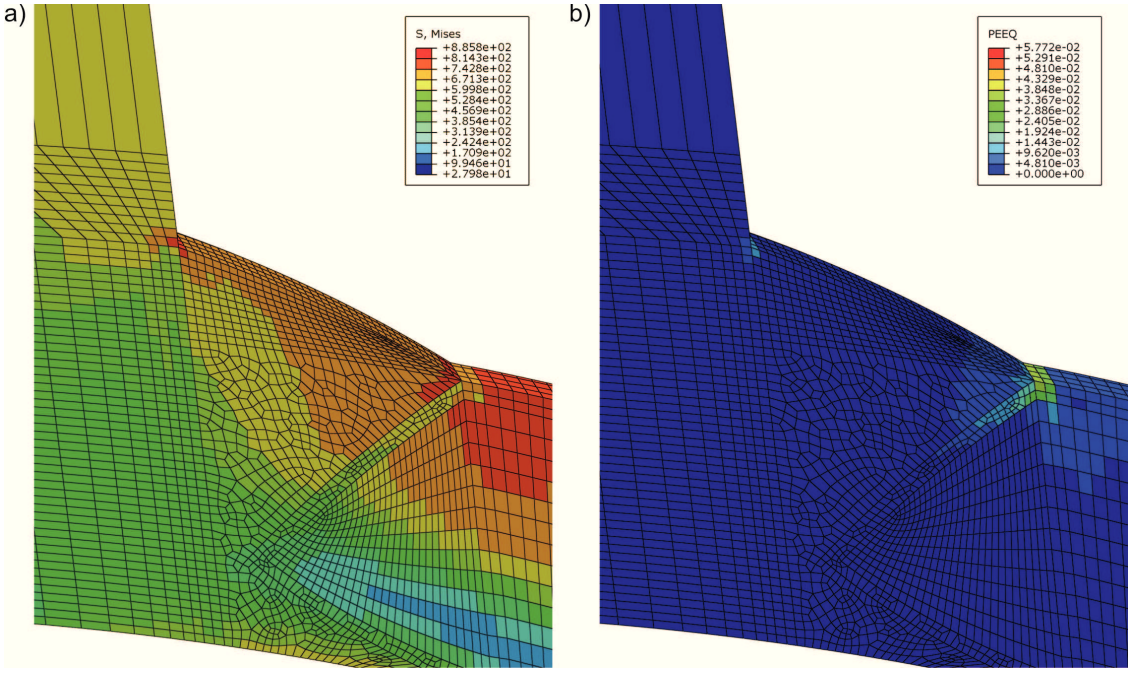

Figure 7.41.: a) Stress and b) strain distribution in Cut 1 in the nozzle weld seam and the HAZ at a pressure of 600 bar. In b) the strain localisation in the HAZ is clearly visible.

The submodelling technique allows re-modelling smaller partitions of an originally larger model with a finer mesh. To achieve the same loading situations, the displacements, which were computed in the original simulations, are prescribed on the boundary surfaces of the submodel. This

technique can be applied in several subsequent steps to achieve a high mesh resolution in an originally too large model.

The original pressure vessel model had a coarse mesh in uncritical regions and the mesh was refined to maximum 1.5 mm around the weld seam. In this configuration, the model reached a number of approximately one million elements. In a first submodelling step the weld seam region was extracted (Fig. 7.42a). Then Cut 1 and Cut 2 were isolated each in further submodels. The mesh was refined until the same mesh size as in the laboratory simulations, 0.06 mm, was reached (Fig. 7.42b-c), see [117] for details. For this element size, the limit strain locus is valid even in localised strain regions because it was derived on this mesh size on the laboratory samples. Consequently, the base length for strain calculation is equal and the results are comparable.

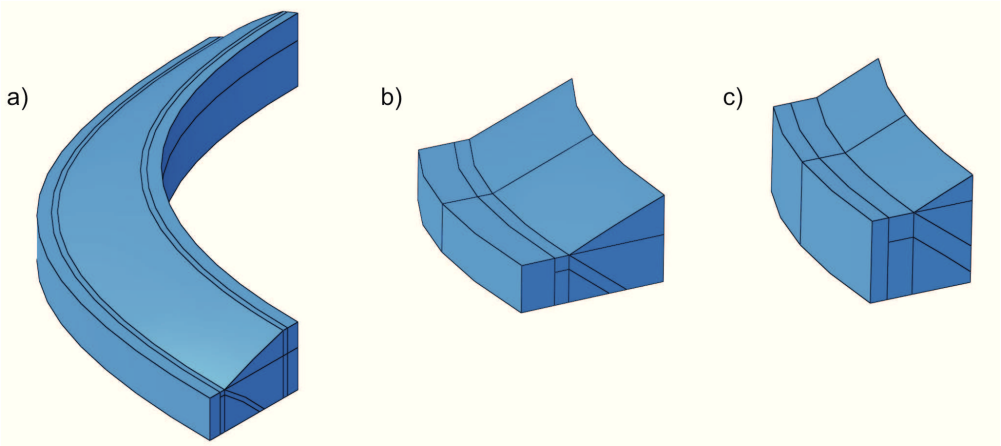

Figure 7.42.: Submodels developed in [117] for Cut 1: a) Complete submodel of the weld seam b,c) further refinements towards Cut 1.

The results achieved in the submodels for a mesh size of 0.06 mm are summarised in comparison to the burst pressure in Table 7.12. The limit indicator is reached first in Cut 2 and subsequently in Cut 1. Figure 7.43 displays the limit indicator in Cut 1. The predicted limit pressures do not characterise full failure but the onset of local softening, which subsequently leads to failure. Both limit pressures are beneath the burst pressure in a range smaller than 5% deviation. Additionally, the locations coincide with detected small cracks on the vessel and in the case of Cut 1 also with the actual failure location. The stress state in both locations was characterised by values of $0.65 < \eta < 0.7$ and $-0.01 < \overline{\theta} < -0.02$. Consequently, the consideration of the Lode angle effects was justified because the limit strains are lowest for these stress states. The stress triaxiality was constant throughout the deformation history and the Lode angle factor exhibited only minor variations. Therefore, the simplified definition of the limit indicator was valid.

Table 7.12.: Predicted limit pressures for Cut 1 and Cut 2 in comparison to the burst pressure.

Location	Pressure at $L_{ind} = 1$ [bar]	Total deviation from burst pressure [bar]	% deviation from burst pressure
Cut 1	669	-11	-1.6
Cut 2	653	-27	-4.0

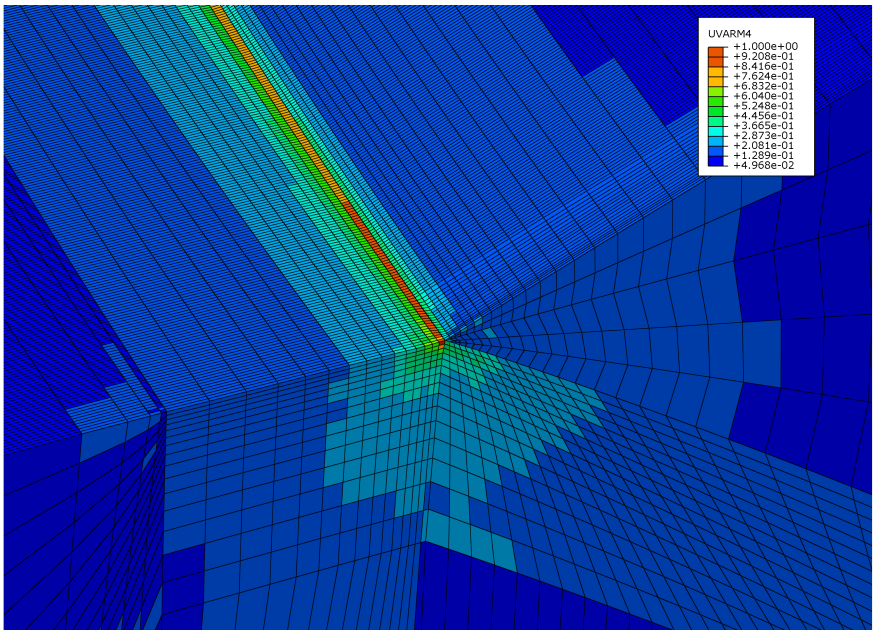

Figure 7.43.: Limit indicator in Cut 1 immediately before failure at a pressure 662 bar.

Figure 7.44 compares the simulation results to the outcome of the burst test. It is evident that the modelling approach is able to provide limit pressures that are close to the actual burst pressure. The plastic, nonlinear behaviour of the vessel could be successfully reproduced. The current design concepts strictly avoid plastic deformation in high strength pressure vessels, suspecting early failure. The burst test demonstrated that good-natured failure behaviour might as well be present in high strength pressure vessel steels and the developed modelling concept is able to represent this. In summary, the simulation could successfully reproduce the failure locations, and the predicted limit load is close the actual burst pressure. Hence, the developed modelling concept is able to predict much more realistic limit states than the current analytical approach.

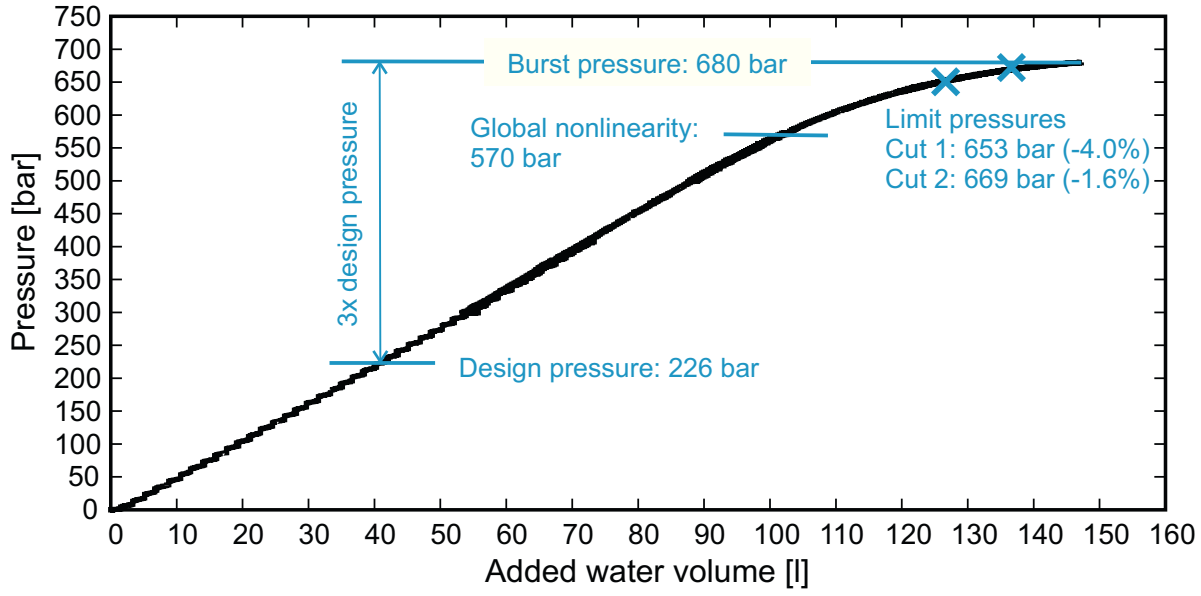

Figure 7.44.: Summary and comparison of the burst test and simulation results.

7.2.4. Test of the scaling function for limit strains

As previously described, the simulation capabilities of the modelling concept could successfully be demonstrated using submodelling. Yet, for an application in probabilistic safety concepts, an additional aspect has to be considered. In the numerous simulations that are required as input for the probabilistic safety assessment, it is not feasible to perform submodelling in each case. Therefore, the scaling function proposed in Section 6.1.3 was tested.

An evaluation at which global pressure the limit indicator L_{ind} was reached proved the suspected mesh dependency. Table 1 lists the global pressures at which the limit indicator was reached for each investigated mesh size. It is evident, that the predicted limit pressure depends on the mesh size.

Table 7.13.: Mesh dependency of predicted limit pressure. For Cut 1 the limit strain is not reached in the full model until the end of the simulation at 760 bar.

Model type & element size	Limit pressure Cut 1 [bar]	Limit pressure Cut 2 [bar]
Full model, 1.5 mm	-	731
Submodel 1, 0.5 mm	735	706
Submodel 2, 0.1 mm	687	663
Submodel 3, 0.06 mm	669	653

To test the scaling function, strains were extracted from the full model and the submodels at identical locations and at an identical pressure level. In this case, the previously determined limit pressure was selected. By this, the influence of the mesh size on the achieved localised strains could be investigated. A full model with a mesh size of 2.5 mm was employed additionally in order to use a broad spectrum of mesh sizes.

Figure 7.45a presents the results exemplarily for Cut 1. It is evident that the results show the same tendency as the theoretical considerations presented in Section 6.1.3. Therefore, a power law in dependence of the element size l_e was assumed as scaling function (Eq. 7.4). It was fitted to the results by the least squares method. The parameters $a = 0.3264$ and $b = -0.386$ provided a good approximation of the experimental results (Fig. 7.45b). The slight deviations result from a necessary extrapolation of the results to the same pressure level due to Abaqus automatic load stepping.

$$f(l_e) = a \cdot l_e^b \tag{7.4}$$

As a next step, the limit strains derived from the cell element simulations were multiplied with this function and thereby scaled. Subsequently, a LSL was fitted again to these scaled strains. This procedure was performed for all investigated mesh sizes. Table 7.14 lists the newly derived LSL parameters for each mesh size, and the LSL for dvII are plotted in 7.46.

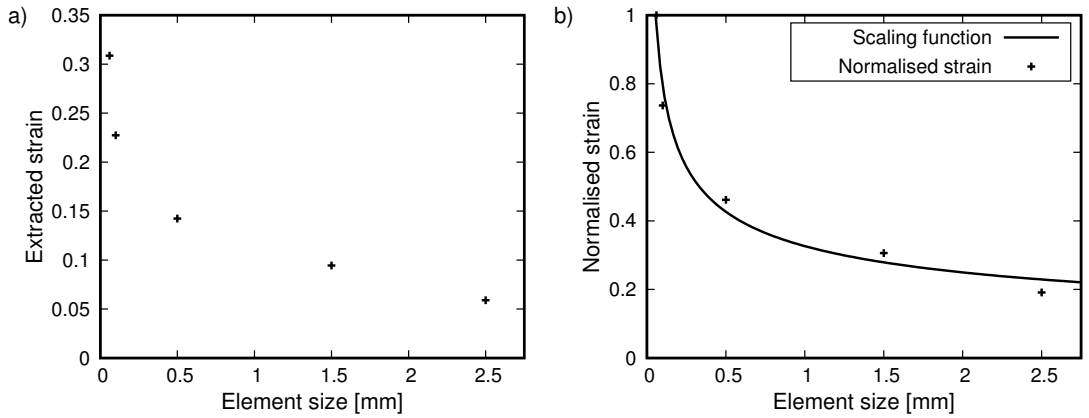

Figure 7.45.: a) Extracted strain values in the critical location of Cut 1 at a pressure of 669 bar.

Table 7.14.: Fitted LSL parameters for the scaled LSL of dvII and dvIV.

Material	Element size [mm]	D_1	D_2	D_3	D_4
dvII	0.06	2.738	1.882	0.7	1.182
dvII	0.1	2.174	1.882	0.5557	1.182
dvII	0.5	1.168	1.882	0.2986	1.182
dvII	1.5	0.7642	1.882	0.1954	1.182
dvII	2.5	0.6274	1.882	0.1604	1.182
dvIV	0.06	2.291	1.831	0.6	1.083
dvIV	0.1	1.819	1.831	0.4763	1.083
dvIV	0.5	0.9772	1.831	0.2559	1.083
dvIV	1.5	0.6394	1.831	0.1675	1.083
dvIV	2.5	0.525	1.831	0.1375	1.083

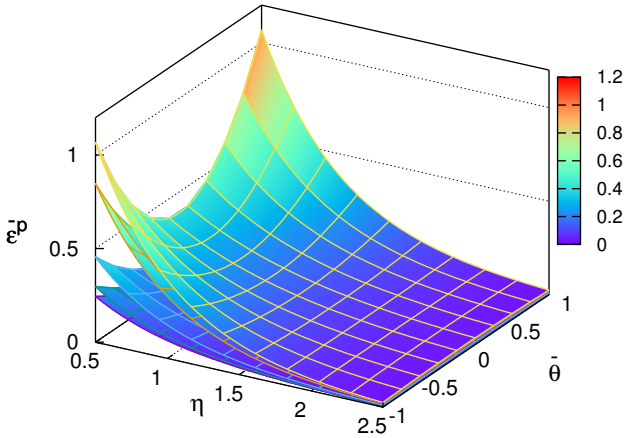

Figure 7.46.: Scaled LSL for dvII. The level of the LSL increases with decreasing mesh size.

These scaled LSL were then re-used in the submodel and full vessel simulations with the corresponding mesh sizes. The pressure at which the, now scaled, limit indicator was reached was

evaluated at the corresponding location. Table 7.15 lists the results for all investigated mesh sizes. It is evident that by the application of the scaling function the variation of predicted limit pressure could be reduced to below 1%. The same level of precision was achieved when calibrating the scaling function in Cut 2. Thus, the scaling function is able to replace submodelling.

It has to be noted that in pressure vessel models with coarse meshes but fully represented weld properties, location and pressure where the limit indicator is met first may vary slightly. This is caused by an interaction of weld properties, weld geometry, and mesh size which leads to varying conditions of strain localisation. Yet, all test simulations performed with the scaled LSL rendered conservative results which were below the limit pressures predicted in submodelling. In nominal studies the weld properties are neglected and the geometry is simplified because the standards make no specifications for the weld geometry. As a result, such local switching is prevented.

The proposed scaling function is therefore a suitable approach to compensate the localisation-induced mesh dependency. Consequently, if such a scaling function is applied, no submodelling is necessary for the application of probabilistic safety concepts. This enables an effective application of the LSL as limit criterion in simulations for probabilistic safety concepts.

Table 7.15.: Predicted limit pressures in the critical location of Cut 1 in models with different mesh sizes using the scaled LSL.

Model type & element size	Limit pressure with scaled LSL, Cut 1 [bar]	Deviation from reference [%]
Submodel 3, 0.06 mm	669	0 (set as reference)
Submodel 2, 0.1 mm	668	-0.15
Submodel 1, 0.5 mm	664	-0.75
Full model, 1.5 mm	666	-0.45
Full model, 2.5 mm	670	0.15

7.3. Summary

The results of the burst test show the high loading capacity of a pressure vessel made from high strength steels. They are compared to the simulation results in Fig. 7.44. A comparison of burst and design pressure proves that the design stress includes a triple safety against the burst event. The limit pressures provided by the full scale simulations predict the limit state conservatively within a 5% deviation from the actual burst pressure. Moreover, the correct failure locations were predicted. The prediction capabilities of the developed modelling concept were therefore successfully demonstrated. Additionally, the developed scaling function proved to be very well applicable in the pressure vessel. It enables an application of the modelling concept without using submodelling. Therefore, all requirements for using the simulations in probabilistic safety concepts are fulfilled by the developed modelling concept.

8. Failure prediction based on nominal requirements

The modelling concept for a numerical limit pressure prediction could successfully be demonstrated in the previous chapter. Therefore, the procedure for deriving nominal limit strains was tested on the basis of the demonstrator pressure vessel as well (Fig. 8.1). The parameter sets derived on the experimental results of the pressure vessel materials were modified to meet the nominal requirements. From this modified parameter set, a nominal limit strain curve was derived and applied in the simulation of the demonstrator pressure vessel using the scaling function. The result was compared to the burst test to judge whether an appropriate limit state was described. The scaled, nominal limit strain locus then provided the input for the application of probabilistic concepts in the accompanying research project [117], including manifold simulations on varying pressure vessel geometries. As most of the methods have been introduced in the preceding chapters, the procedures and results are presented together in the following.

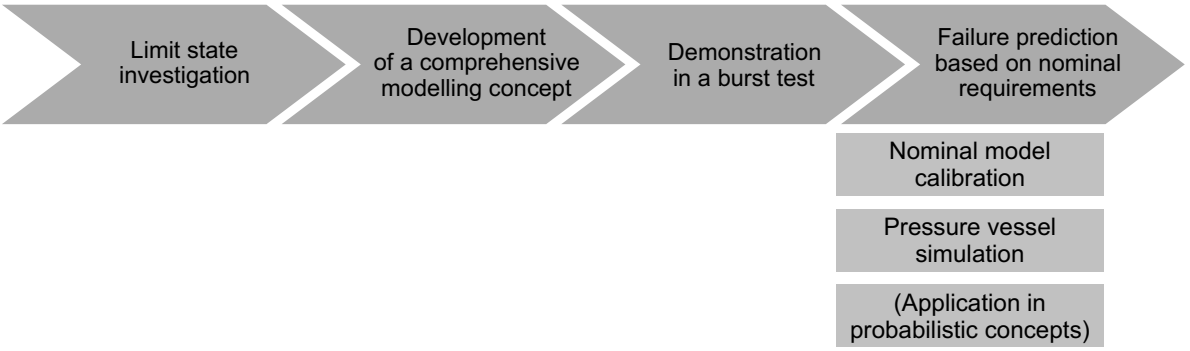

Figure 8.1.: Overview on the presented results on failure prediction based on nominal requirements.

8.1. Nominal model calibration

The nominal parameter set was determined according the calibration scheme proposed in Section 6.2. The experimentally calibrated parameter set of the material dvII was selected as a basis for the modifications. Firstly, the flow curve was adapted to the nominal requirements. As discussed in Section 6.2.1, the hardening behaviour can be assumed to be constant while the overall level has to be adapted such that the nominal yield stress of 690 MPa is met. The offset for the flow curve was calculated as the difference of the nominal yield strength and the lower yield strength $R_{eL} = 786$ MPa of dvII. Consequently, the flow curve was reduced by 96 MPa (Fig. 8.2).

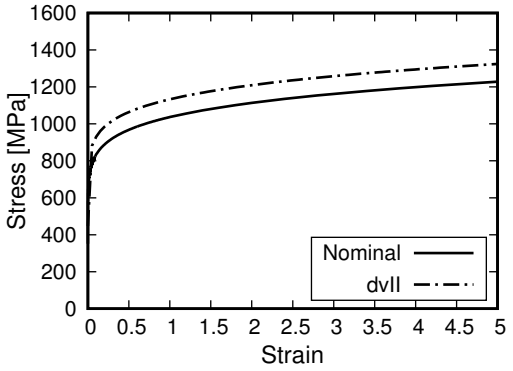

Figure 8.2.: Derived nominal flow curve for P690Q and the original flow curve of dvII in comparison.

Subsequently, this flow curve was used in the simulation of a Charpy test using the NT model. The originally calibrated parameter set of dvII was applied and the value of f_0 was modified on order to meet a dissipated energy that is similar to the nominal requirement of 60J (as introduced in Table 4.2). This was achieved for a value of $f_0 = 0.009$, for which the dissipated energy in the Charpy test was 64 J (Fig. 8.3). The Tables 8.1 and 8.2 summarise the derived nominal parameter set.

Table 8.1.: Nominal parameters for the Ludwik extrapolation of the flow curve, strain rate and temperature dependency.

Parameter	σ_0 [MPa]	k_L [MPa]	n_L	c_T^1	c_T^2	c_T^3	$c_{\dot{e}}^1$	$c_{\dot{e}}^2$	$c_{\dot{e}}^3$
Calibrated value	352	685	0.153	0.456	0.00356	0.835	0.0052	1.036	0.04

Table 8.2.: Nominal NT parameter set.

Parameter	f_0	f_c	κ	q_1	q_2	k_ω	η_1	η_2	Mesh size
Calibrated value	0.009	0.015	1.5	1.5	1.0	3.8	0.8	1.3	0.06mm

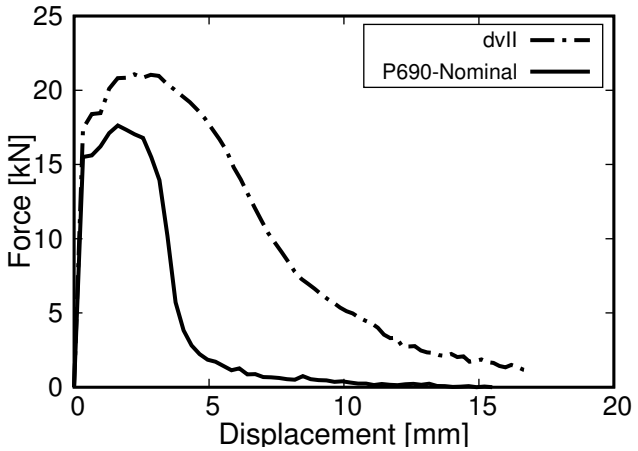

Figure 8.3.: Result of the Charpy simulation for the original parameter set of dvII and the adapted nominal parameter set.

This parameter set was then used in cell element simulations to derive the nominal LSL. The corresponding parameters are provided in Table 8.3. The locus derived is displayed in comparison to the one of dvII in Fig. 8.4. It is evident that the derived nominal limit strains are much lower than the ones calibrated from experimental parameter sets. The nominal flow curve and the nominal LSL provide a measure for a nominal limit state assumption within simulations for probabilistic safety concepts.

Table 8.3.: Fitted nominal LSL parameter set.

Parameter	D_1	D_2	D_3	D_4
Calibrated value	1.565	2.059	0.3051	0.9682

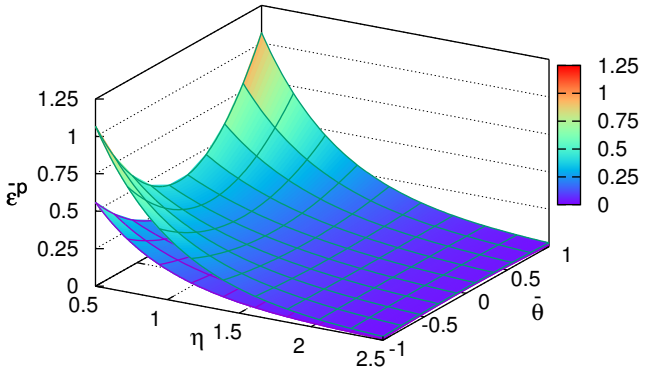

Figure 8.4.: Plotted nominal limit strain locus (lower locus) in comparison to the limit strain locus of dvII (upper locus).

8.2. Nominal pressure vessel simulation

This nominal parameter set was tested within a modelling of the demonstrator pressure vessel to determine the predicted nominal limit load. The results on full scale vessel modelling presented in the following section were created in cooperation with the Institute of Steel construction at RWTH Aachen University within the accompanying research project [117].

In contrast to the previous simulations, the nominal material properties were the only ones to be included in the nominal pressure vessel simulation. Consequently the weld seam was only considered by its geometry. This induced some changes in the load distribution because no transition of material properties was given around the weld seam. The distribution of the plastic equivalent strain around the weld seam, displayed in Fig. 8.5, shows that under these circumstances also regions at the upper boundary of the weld seam are highly loaded.

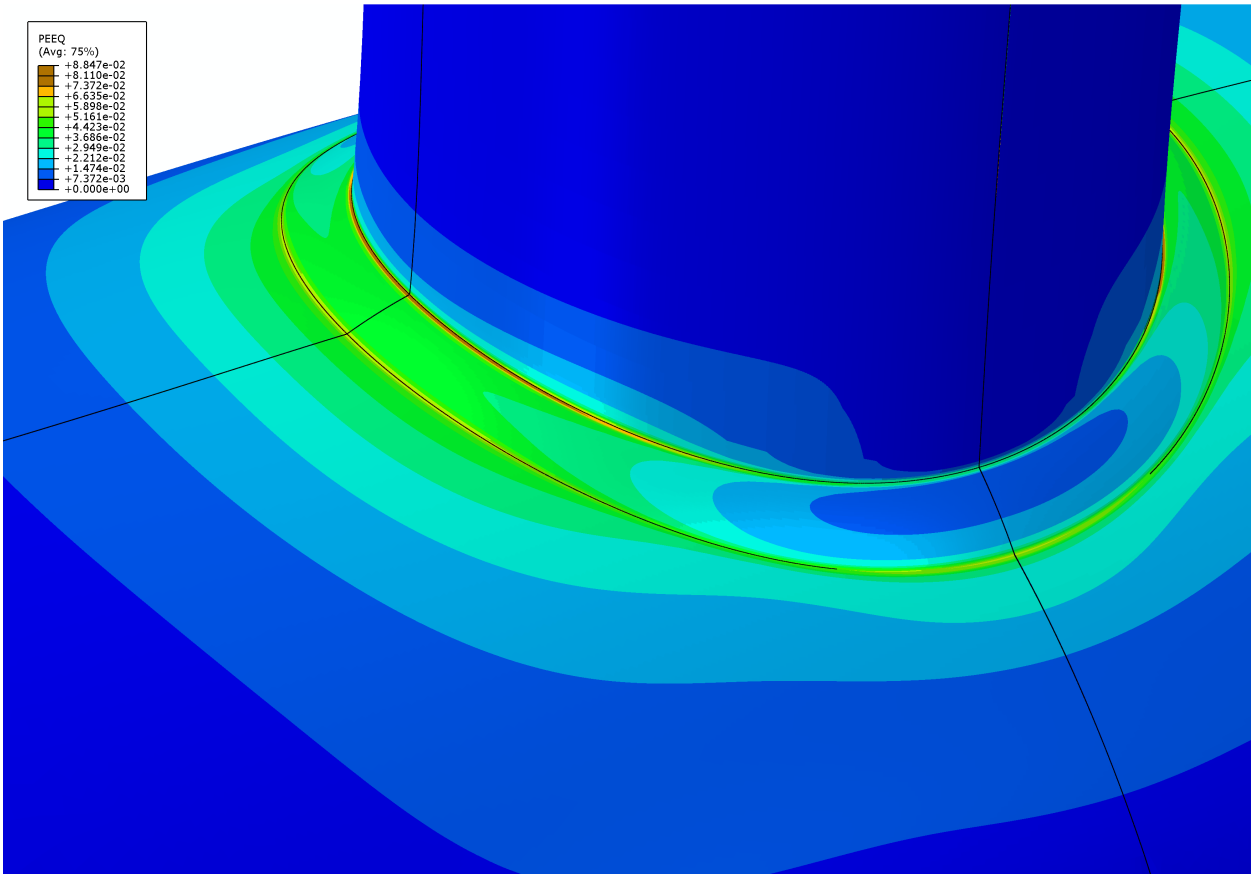

Figure 8.5.: Distribution of the plastic equivalent stress around the weld seam at a simulated pressure of 600 bar using the nominal material properties.

A strain localisation around the weld seam transition, in this case induced purely by the geometry, was also detected. Therefore, the scaling function had to be applied. In this model, the highest strains are to be found in Cut 1, yet at the upper boundary of the weld seam. However, the loading conditions at upper and lower boundary are similar. To keep the results comparable to the full scale vessel simulation with real material properties, the calibration of the scaling function was performed at the same location on the lower boundary of the weld seam as before. The calibrated

function, using the parameters $a = 0.4206$ and $b = -0.3042$ for Eq. 7.4, can very well reproduce the extracted strains (Fig. 8.6). The calibrated parameters are similar to the ones derived on the real material although the overall strain level is lower.

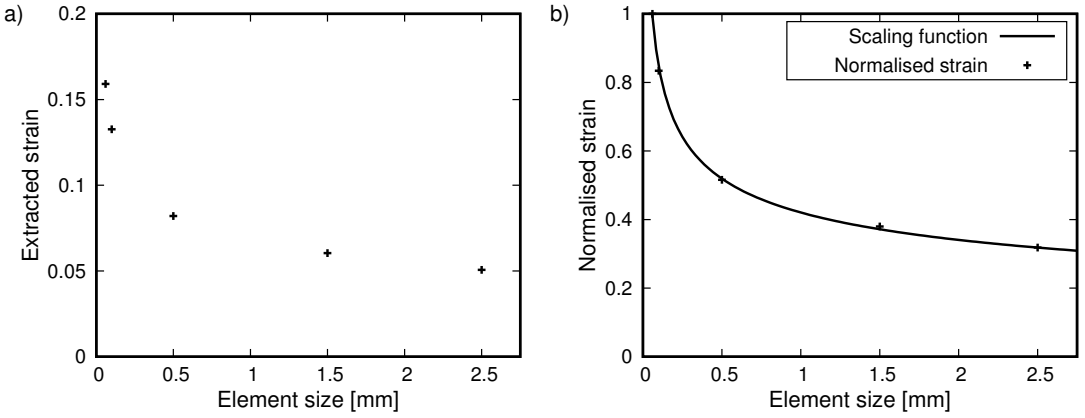

Figure 8.6.: a) Extracted strain values in the critical location of Cut 1 at a pressure of 600 bar.

Based on this function, scaled LSL were derived (Tab. 8.4 and Fig. 8.7). These were subsequently applied in the vessel simulations. Similar to the full scale vessel results, the deviations in reaching the LSL for the evaluated spot could by this be decreased to approximately 1%.

Table 8.4.: Fitted LSL parameters for the scaled LSL of dvII and dvIV.

Material	Element size [mm]	D_1	D_2	D_3	D_4
P690Q	0.06	1.565	2.059	0.3051	0.9682
P690Q	0.1	1.326	2.059	0.2585	0.9682
P690Q	0.5	0.8127	2.059	0.1584	0.9682
P690Q	1.5	0.5819	2.059	0.1134	0.9682
P690Q	2.5	0.4981	2.059	0.09711	0.9682

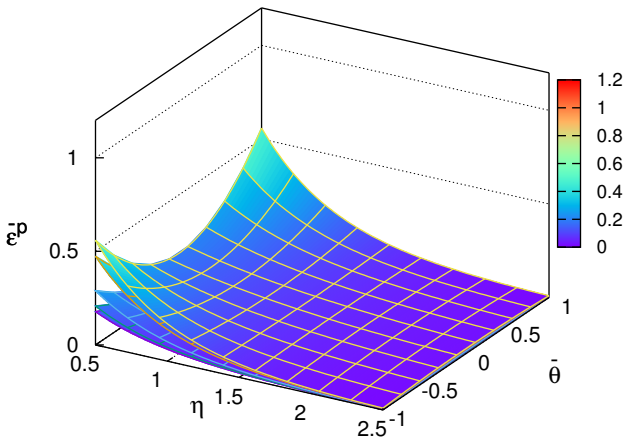

Figure 8.7.: Scaled nominal limit strain loci.

Finally, a full scale vessel simulation, using a mesh size of 2.5mm, the nominal flow curve, and the scaled nominal LSL, was performed to determine the nominally predicted limit pressure. The scaled LSL was reached first at the upper boundary of the weld seam within the longitudinal section. The predicted nominal limit pressure was 536 bar. Figure 8.8 shows the distribution of the limit indicator shortly before the predicted limit pressure. A comparison with the model with 1.5 mm mesh size proved that the scaling function is also valid for this location. In this model with smaller mesh, the scaled nominal LSL was reached in the same location at a pressure of 540 bar. This is a deviation of less than 1%. Consequently, the predicted limit pressure of 536 bar was accepted as the nominal limit pressure. It is well below the actual burst pressure. Moreover, it is also below 570 bar, the pressure at which global nonlinear behaviour was detected in the burst test. In summary, this nominal approach, including the scaling function, provides conservative, but more realistic limit states. It is thus assumed to provide suitable limit states for an application within probabilistic safety concepts.

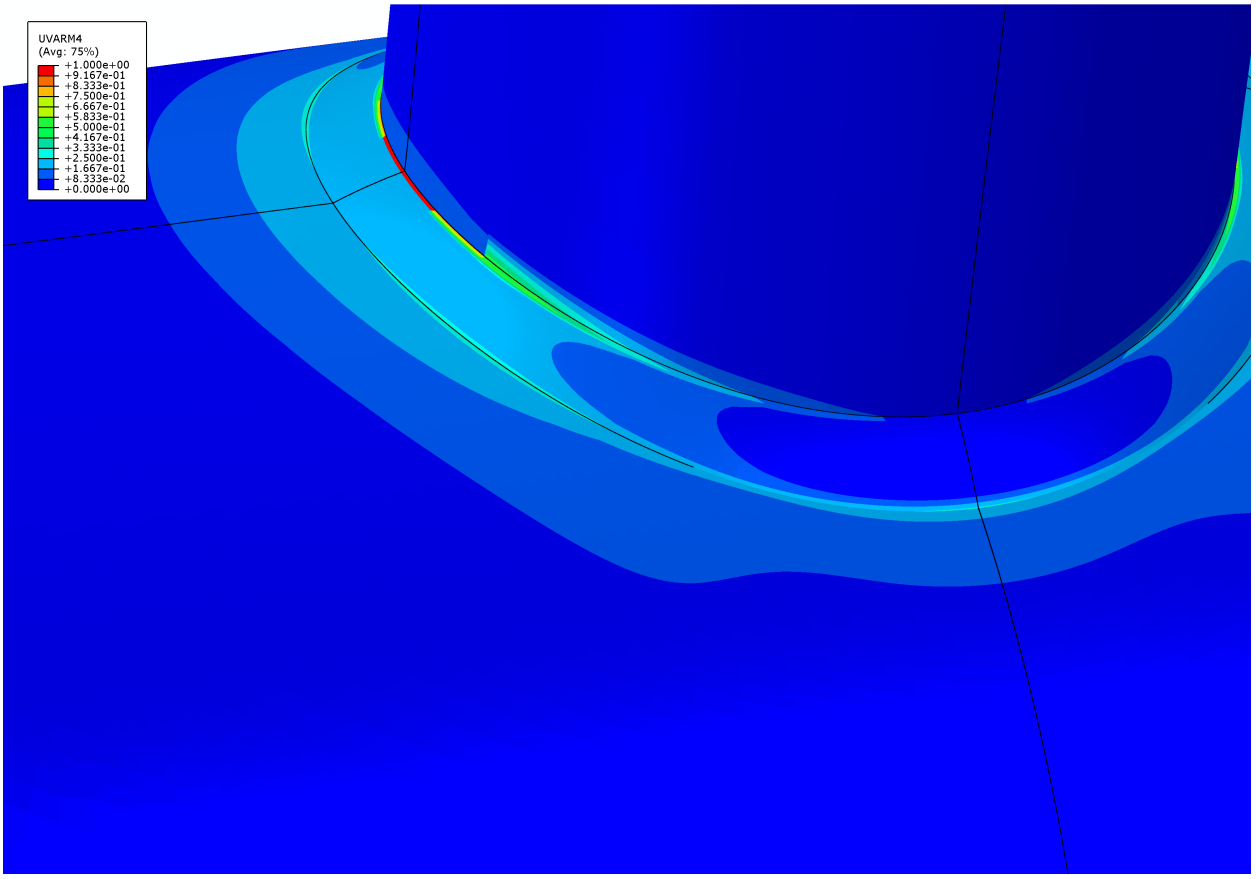

Figure 8.8.: Distribution of the limit indicator around the weld seam at a simulated pressure of 530 bar using the nominal scaled material properties.

8.3. Application in probabilistic safety concepts

The investigations on probabilistic concepts were performed by the project partner, the Institute for Steel Construction at RWTH Aachen University, in the accompanying research project. An excerpt of the results is reported here for the sake of a complete discussion of the prediction capabilities of the developed modelling concept. The full record of the procedure and the results are available in [117].

The nominal flow curve and the scaled limit strain locus were applied in over 30 full scale pressure vessel simulations. The vessel diameter, the wall thickness, the nozzle diameter and the nozzle location were varied to cover a large span of possible constructions. The limit pressures that resulted out of these simulations were used as an input for the probabilistic safety concepts. The probabilistic safety concept was applied for different levels of failure probability. The most conservative assumption was to assign the pressure vessels to the category with the highest possible failure consequences as defined in EN 1990 Annex B. Constructions assigned to this category, have to be designed according to the rules for the lowest failure probability class “RC3”. For an operation span of one year, this category aims at a technical failure probability of 10^{-7}.

The application of the semiprobabilistic procedure according to EN 1990, Annex D, rendered safety factors on yield and tensile strength that resulted in the same design stress. The design stress f_{d-PSC} for which, according to these procedures, a failure probability of 10^{-7} is given for the considered pressure vessels, would be $f_{d-PSC} = 434$ MPa. This design stress exceeds the current one of $f_d = 321$ MPa by 35%. The use of probabilistic safety concepts thereby suggests an appropriate yield strength exploitation for the high strength steel P690Q of 63% instead of the currently defined 46%. The corresponding safety factor on the yield strength is 1.59, the one on the tensile strength 1.77.

Hence, the application of probabilistic safety concepts in combination with damage mechanics suggests a significant reduction potential in the current safety factors. A discussion of this result is provided in the following chapter.

9. Discussion

The motivation of this study is to foster the application of modern high strength steels in pressure vessels and other steel constructions by providing means for an increased exploitation of their properties while maintaining suitable safety levels. Probabilistic safety concepts may be used to derive adequate safety factors which consider the improved toughness properties of modern high strength steels. Such safety factors could enable an efficient and safe application. However, such approaches need a large data basis on full-scale component failure. In the case of pressure vessels a purely experimental approach is not feasible due to the extensive efforts of burst tests.

The aim of this study was therefore to develop a comprehensive modelling concept for the prediction of ductile failure in large-scaled components so that a part of the required full scale tests can be replaced by simulations. According to the design philosophy of the common pressure vessel codes, the concept should be able to reflect varying toughness levels so that a reference to nominal properties is possible. Such a concept enables the derivation of optimised safety factors and design rules on the basis of simulations. Those optimised design rules or safety factors subsequently have to be validated only in a significantly reduced number of burst tests.

Such a complete simulation concept for full-scale ductile failure prediction with toughness reference was to the author's knowledge missing until now. During the development of the concept in this study, models and approaches that were available for individual aspects were adapted and connected to fit into the global approach. Additionally, new procedures for missing links were developed and tested. Finally, the performance of the modelling concept was successfully demonstrated on a full scale burst test.

Individual aspects of the performed investigations and the achieved results are discussed in the following according to the four basic steps defined previously (Fig. 9.1).

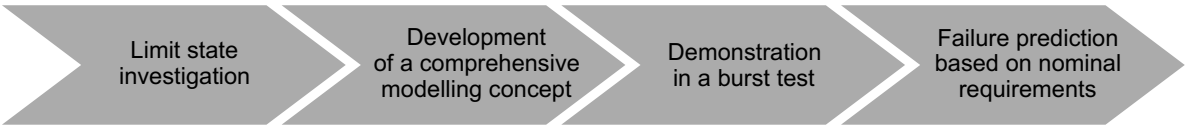

Figure 9.1.: Investigated main aspects that are discussed in this chapter.

9.1. Limit state definition

A key method applied in this study is to derive limit strain criteria, which can be effectively applied in large scale simulations, from simulations using Gurson models. Since Gurson models provide a continuous description of the damage development, it was necessary to define the state that is considered to be decisive for structural failure and use it in the derivation of the limit state.

The basis for this definition was formed by an investigation of the actual damage development in modern high strength pressure vessel steels. Stopped experiments on notched round bars were performed for this purpose. No significant void formation was detected throughout most of the deformation history. Only in the final stages of deformation, when straining had already strongly localised, an increased but still moderate number of growing and coalescing voids was found. The void area fraction was still below 1% shortly before reaching the load drop in tensile tests although a considerable amount of plastic deformation was present. Microtomography scans confirmed this for the whole notch region. The low inclusion content of modern steels seems to delay void nucleation and growth, reducing their relevance for failure. Therefore, the localisation of deformation becomes crucial. These results are in accordance with findings from the literature (e.g. [128,135]). Additionally, it could be proven that this development cannot be measured by means of the ductile current potential drop method in notched round bars.

The relevant question for developing the modelling concept was which state in this ongoing process should be considered critical with respect to ductile structural failure. Nielsen and Hutchinson argued that failure is induced by a damage localisation within existing necks in large-scaled structures [134]. This argumentation was adapted for the limit state definition as it is in accordance with the metallographic investigations. Damage localisation is characterised by the onset of local softening. This means that for a considered material volume, the void formation exceeds the hardening capacity. This instance can ideally be used for coupling Gurson simulations with limit strains by using cell element models. Hence, for this study the limit state was defined to be the local onset of softening that can be detected in cell elements using Gurson models.

This definition of the limit state could be used successfully in all subsequent steps of the developed modelling concept. It therefore represents a reasonable assumption for an application in a scale-bridging modelling concept for ductile structural failure. Nonetheless, it differs from procedures that are usually applied in strain-based failure criteria. As discussed in Chapter 2, typical definitions of such criteria rather consider the load drop point in tensile tests or the shift to uniaxial straining in voided cell models as a failure definition (e.g. [48, 60]). Previous studies on ductile failure performed at RWTH Aachen in the 1990s for example employed the first occurrence of void coalescence to derive the strains for damage curves. A comparison of limit strains derived in this study on P690Q to such damage curves of the comparable steel grade “St E 690” by stopped experiments was performed to judge the impact of this modified definition of the limit state.

Data provided by Arndt and Schlüter was used for the comparison [33, 101]. Schlüter provided a mathematical formulation for two commercial steels from this grade, designated as “D29” and “D42”. Both steels were bainitic, but steel D29 had a higher sulphur content and exhibited longitudinally rolled MnS-inclusions. Arndt provided critical strains for one bainitic steel, which was tested parallel to the rolling direction, designated as “L”, and transverse to the rolling direction, designated as “Q”. Although the data of Arndt and Schlüter seems similar there is no evidence in the references that the investigations were performed on the identical material.

This data was compared to the limit strain formulations at $\overline{\theta} = 1$ of the pressure vessel steels derived in this thesis. These formulations can be readily obtained from the limit strain locus because it reduces to $\varepsilon_c = D_1 e^{-D_2 \eta}$ for $\overline{\theta} = 1$. All results are plotted in Fig. 9.2. The comparison of the data of Schlüter and Arndt shows that inclusion content and orientation open up a typical scatter range of damage curves that becomes broader for lower triaxialities. The limit strain curves derived

in this study lie within this deviation band. Only for $\eta > 1.5$ the limit strain curves predict even lower strains which is a conservative result. The limit strain curves therefore match the damage curves, which were calibrated experimentally, very well. This indicates that the selection of local softening as limit state represents a well-justified choice for HSLA steels from a micromechanical viewpoint as well. The fact that the limit strain curves exhibit relatively low deviations from each other although they have been derived from materials of different producers and from weld seams also supports this.

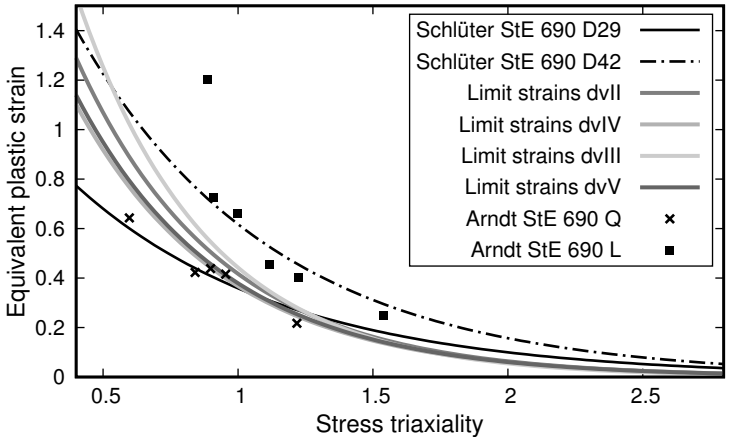

Figure 9.2.: Comparison of damage curves and data points characterising the first instance of void coalescence as provided by Arndt and Schlüter [33, 101] to the limit strains derived in this study for $\overline{\theta} = 1$.

In summary, the selection of local softening as a limit state has proven to be a reasonable and successful selection within the investigated concept. Contrary to common definitions of strain-based failure criteria it opens up the possibility of referring to nominal requirements. This enables lower-bound assumptions on ductile failure that are necessary within the design philosophy of pressure vessel codes.

9.2. Modelling concept

As outlined in Chapter 2, damage mechanics models have been under research for almost fifty years. Numerous studies on individual models, failure modes, and materials exist. The Gurson models, which were also employed in this study, form one of the most commonly applied groups of damage mechanics models. As discussed in Chapter 2, most damage mechanics studies are concerned with laboratory samples, examining the mm-scale. Fewer studies have researched the application of damage mechanics models on the m-scale or the transferability of models from the mm to the m scale. For Gurson models, this transfer was only successful if the failure spot is predefined so that a selective mesh refinement is possible. Another problem when applying damage mechanics on the m scale is the strong demand of computational resources. Consequently, only simple and efficient criteria, like the strain-based failure criteria, can successfully be applied on the m-scale.

To overcome these difficulties, in this study the procedure proposed by Schruff [8], using Gurson models to represent toughness levels and subsequently derive strain-based failure criteria from them, was adapted. The limit state definition for the numerical derivation of strain-based failure criteria was discussed in the preceding section. A remaining open question was how to deal with the non-unique GTN parameter selection that can substantially influence the results. Additionally, the previous studies did not consider temperature and strain rate dependent material properties as well as possible Lode angle influences. Moreover, it became evident during the studies that a scale-bridging concept was required because the strain computation in large-scale models may be influenced by the mesh size.

The non-uniqueness of the parameter selection in Gurson models is a well-known phenomenon that cannot be eliminated. To prevent an impact on the limit state prediction, a calibration scheme was investigated and proposed. By the application of such a calibration scheme the results become comparable and reproducible. As a basis a thorough sensitivity analysis was performed. Such sensitivity analyses were partly available in the literature (see Chapter 2); however, only limited information on the simulation of Charpy impact toughness tests was available. These are crucial for a reference to actual and nominal toughness levels. The results of the sensitivity analysis have been discussed with respect to the literature in Section 6.2.1. The initial void volume fraction f_0 was identified as the lead parameter for an adaptation of the toughness level to nominal properties because it evenly deteriorates the simulated mechanical response of all sample types. It is therefore suitable to achieve lower-bound assumptions in all aspects.

In general, it has to be noted that the use of Gurson models for deriving nominal, lower-bound assumptions provides to some extent micromechanical relations such as the dependence of void growth on hydrostatic pressure. However, the final formulations of Gurson models today, such as the GTN or NT model, contain significant phenomenological extensions that diminish this relation strongly [23, 25]. Consequently, Gurson models are rather micromechanically motivated models than actual micromechanical models. Nonetheless, the models provide a powerful description of actual material behaviour and exhibit, within certain bounds, a better transferability of model parameters than purely phenomenological models. All properties that are required for simulating artificially deteriorated, nominal toughness levels have been examined in this study and the suitability of the applied GTN and NT model for this purpose could be proven. Yet, actual micromechanical modelling has experienced great progress in the last years. Representative volume elements (RVE) are nowadays able to represent not only single voids but multiple microstructural features, including properties of individual material phases by means of crystal plasticity models. They can also be used to provide a correlation between microstructure and failure properties, for example under fatigue loading [156]. Such RVE studies could provide a significant contribution to the micromechanical relation of the procedure for future investigations on nominal toughness levels.

The used Gurson model was extended to consider strain rate and temperature, adiabatic heating, and Lode angle influences. For the latter, the formulations of Nielsen and Tvergaard were adapted [153]. All model implementations were successfully validated. The comparison of the simulation of Charpy tests with and without Lode angle considerations revealed an interesting feature. In general, Charpy tests can be successfully simulated with the common GTN model, as for example demonstrated in Fig. 6.22. The need of a consideration of adiabatic conditions hereby depends

on whether the material shows pronounced strain rate hardening and temperature softening or not. Yet, a Charpy sample usually exhibits values of $\overline{\theta} = 0$ which indicate the necessity of a Lode angle consideration. If a Lode angle dependent model, like the NT model, is applied, an adaptation of the corresponding parameters as well as the use of the strain rate parameter $c_{\dot{\varepsilon}}^3$, which accounts for dislocation damping under elevated strain rates of $\dot{\varepsilon} \geq 1000\text{s}^{-1}$, is necessary. This is reasonable because the local strain rates in a Charpy tests have values of $\dot{\varepsilon} \sim 1000\text{s}^{-1} - 3000s^{-1}$. However, it also implies that Lode angle dependent failure properties and strain rate hardening interact and partly compensate each other when using a common GTN model for simulations. This interesting aspect should be further investigated in future studies, for example by performing Charpy tests at quasi-static speed as a bending test to separate the stress state and strain rate effects. As studies on the simulation of Charpy tests are very limited in the literature for now (see Section 2.3.2), such a study could provide new insights. Nevertheless, the toughness level of the investigated materials could be reproduced accurately in the investigated materials.

The derivation procedure of limit strains could be easily adapted to the Lode angle dependence so that limit strain loci could be derived. However, these exhibited strain levels that were much higher than the ones achieved in large-scale simulation models. This was caused by the larger mesh sizes in the full-scale models that could not dissolve the local strains in localisation zones at cross section transitions. This type of mesh influence must not be confused with the mesh dependency of local formulations of damage mechanics models. Even non-local model formulations cannot predict localisations that are much smaller than the applied element.

A literature study showed that similar problems were known in the simulation of large ship structures with shell elements. Such studies correct locally obtained critical strains by scaling functions. For solid elements, as used in this study, similar investigations were not available. Consequently, based on theoretical considerations, a power law function was proposed and tested as a scaling function. The results obtained in full-scale models of the demonstrator pressure vessel showed very encouraging results, reducing the variation of the predicted limit pressure in different mesh sizes below 1%. Hereby, the calibrated parameters, which determine the final shape of the scaling function, seemed to depend rather on the local loading situation than on the material properties. In general, the calibration of the functions did not require any additional experiments, just some further simulations with a refined mesh. Further research into these functions should be performed to gain more knowledge on such functions and formulate a general approach.

In summary, this study assembled several existing and newly developed approaches to the comprehensive modelling concept that was aimed for. The development of new elements as well as the adaptation of available procedures enabled the completion of this concept. The concept fulfils all requirements that were defined in Chapter 1: It can be effectively applied in a high number of large-scale simulations, it considers the complete stress state as well as temperature and strain rate dependence and it is able to refer to nominal values.

The only comparable study known to the author is the one of Oh et al. that used strain-based failure criteria for an optimisation of the assessment procedures for corrosion defects in pipelines [115]. However, this study used only experimentally calibrated failure strains and did not refer to toughness values. Additionally, the investigated geometry was much smaller and simpler. Therefore, no scale-bridging of damage mechanics models was necessary. Hence, the developed combination of modelling procedures represents an innovative approach. The developed modelling concept was

finally tested on the demonstrator pressure vessel.

9.3. Demonstration in a burst test

Burst tests of pressure vessels are rarely reported in the literature and if so, only very simple geometries are considered [105]. Most studies that provide burst pressures refer to pipelines with pre-cracks, such as [111]. Studies that investigate the failure of pressure vessels produced from modern high strength steels are not available. Therefore, such a vessel was built within the accompanying research project [117] and tested.

The load-bearing capacities of pressure vessels made from high strength steels could be clearly demonstrated in the burst test. The vessel burst at 680 bar and thereby withstood three times its design pressure of 226 bar according to EN 13445. Moreover, the failure was good-natured as it was preceded by significant plastic deformation. The strain gauges around the nozzle measured local strains of approximately 5% at failure. Due to the high pressure, the crack propagation took place at high speed after failure initiation. The vessel was fully destroyed. A detailed investigation of the fracture surfaces enabled the reconstruction of the failure initiation site. Failure initiated most probably in the heat affected zone at the lower boundary of the weld seam joining vessel and nozzle. SEM investigations proved a ductile failure onset at this location. The crack propagated as a mixed fracture exhibiting ductile and cleavage features. In summary, this unique demonstration of the applicability of high strength pressure vessel steels proved the safe design and ductile failure initiation in the absence of defects.

The damage mechanics models were calibrated using material from the same batch as the vessel itself and from work samples of the welds. All materials were heat treated for stress relief together with the vessel to ensure that they were in the identical state. Laboratory samples were manufactured from the materials and tested to calibrate the NT model and derive the limit strains. In the presented study a very broad spectrum of loading situations needed to be covered. Therefore, in total 11 sample geometries were used in the calibration procedure defined on the basis of the sensitivity analysis. A successful calibration was achieved for all materials although for individual sample geometries no perfect matching could be realised. This concerned especially the yield point in plane strain samples which was not well met in the base materials while the agreement was better for the weld metals. Future studies could investigate whether rolling-induced anisotropy is a possible reason for this. Additionally, Lode angle dependent yielding formulations should be implemented in the future. In general, the NT model confirmed its applicability for a wide range of stress states as also reported by Dunand and Mohr [28].

Since the failure probably initiated in the HAZ, it was represented in detail in the full scale vessel model. The yield properties were successfully adapted on the basis of a hardness mapping and the limit strains were assumed to be identical to the base material. Although this is a simple approach, it led to a correct prediction of strain localisation by the simulations. This confirms the assumptions made.

The full-scale vessel simulations used the derived limit strain loci and flow curves for the material representation. Studies on submodels were used to compensate the mesh influence and test the

scaling function. The critical locations, where the limit strains were reached first, were distributed along the nozzle weld seam as they were in the experiment. First failure was predicted at 653 bar. This is a deviation of only 4% from the experimental result noting that the limit strains indicate a local onset of failure. Hence, it can be concluded that the developed modelling concept could successfully characterise the limit state for ductile failure in large-scaled pressure vessels.

A demonstration in a single burst test does not provide a validation of the method in the sense of statistics. Yet, it shows that the modelling concept fulfils all necessary requirements and is able to represent the actual failure behaviour. The proposed method itself is still too laborious and requires too much expert knowledge to be suitable for daily engineering routine. However, this method can reproduce the general response of pressure vessels with varying constructions with much less effort than it would take to perform numerous burst tests. Therefore, it can be used to investigate a large variation of constructions and derive optimised and more precise design functions and safety factors. A selective validation of such newly derived design functions can then be undertaken with reasonable effort.

9.4. Failure prediction based on nominal requirements

The design philosophy of all existing pressure vessel codes is to ignore the actual material properties and to design according to nominal properties. Consequently, this has to be regarded in the derivation of optimised design functions and safety factors. Due to this, the feasibility of a toughness correlation was implemented in the modelling concept. The NT model parameters derived on the pressure vessel material were modified according to the proposed calibration scheme in the simulation of a Charpy test. In addition, the flow curve was reduced to nominal values. A parameter set could be identified that produced a dissipated energy in the simulated Charpy test close to the nominal requirement of 60J.

The nominal limit strain locus was derived from this parameter set and tested in the simulation of the demonstrator vessel. A comparison to the experimental results and the damage curves of Arndt and Schlüter discussed above confirms that the nominal limit strains are well below all experimental results (Fig. 9.3), even for the low-quality steel investigated by Schlüter. For very low stress triaxialities, the extrapolation of Schlüter for this steel approaches the nominal formulation. However, this is an effect of the extrapolation which might also be selected differently. Furthermore all relevant failure spots in the investigated pressure vessel had triaxialities of $\eta > 0.5$. Consequently, the nominal limit strain locus provides conservative assumptions.

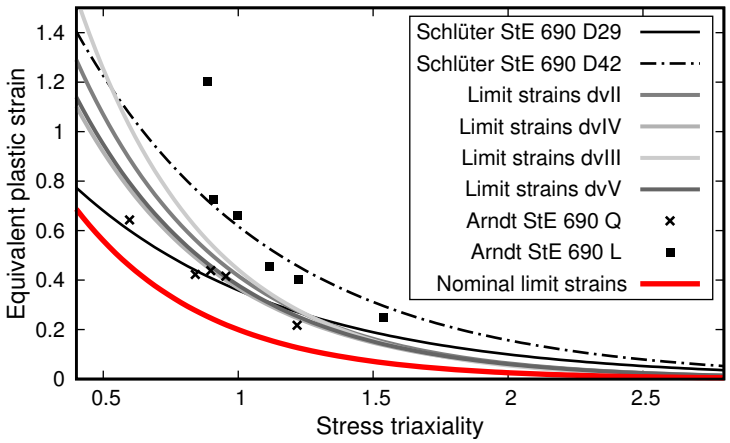

Figure 9.3.: Comparison of the nominal limit strains to experimental results and the damage curves of Arndt and Schlüter for $\overline{\theta} = 1$.

As strain localisation was present, the scaling function was successfully tested and also applied for nominal conditions. The limit pressure predicted on the basis of the scaled, nominal limit strains and a nominal flow curve was 536 bar. This nominal limit pressure prediction is illustrated in comparison to the burst pressure and simulation results in Fig.9.4. The nominal limit pressure is below the global onset of plastification but much higher than the design pressure. It therefore represents a reasonable but conservative assumption for a nominal limit state. The proposed modelling concept could therefore successfully be demonstrated in this aspect.

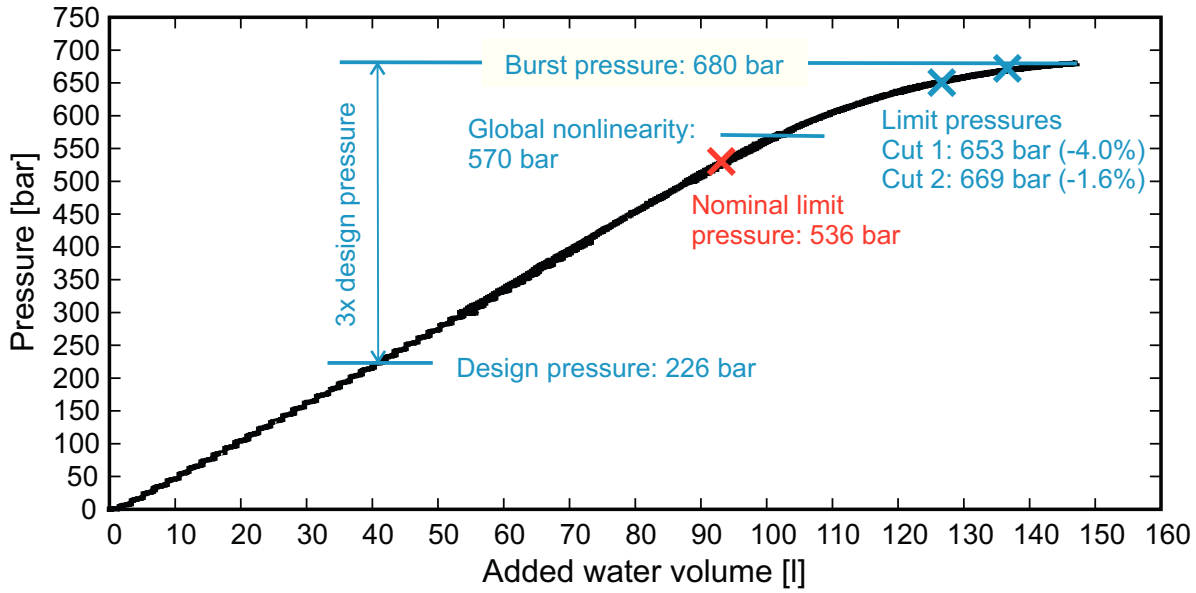

Figure 9.4.: Nominal limit pressure prediction in comparison to experimental and simulation results achieved on the demonstrator pressure vessel.

In the accompanying research project, the scaled, nominal limit strains were subsequently applied in 30 simulations of varying pressure vessel constructions by the project partner [117]. The results were used as an input for probabilistic safety concepts. This data basis should be enlarged for further studies but the results provide a good estimation about the tendency of optimised safety

factors. To achieve a failure probability of 10^{-7} per year the application of probabilistic safety concepts suggested a safety factor of 1.77 on the tensile strength. This leads to a design stress of 434 MPa. It exceeds the currently admissible one by 35%. This is illustrated in Fig. 9.5. The suggested exploitation of the nominal yield strength is 63%. This is much higher than the ones prescribed by the EN or ASME regulations. It is even higher than the one currently admissible for P275N. The application of probabilistic safety concepts on the basis of damage mechanics simulations consequently does not indicate the necessity of reduced safety factors for high strength steels.

This result is in accordance with the studies that compare DBF and DBA predictions for high strength steels [11]. Consequently, a reduction of the safety factors for high strength steels seems feasible. Thus, the benefits of damage mechanics could be made available to the engineering practice.

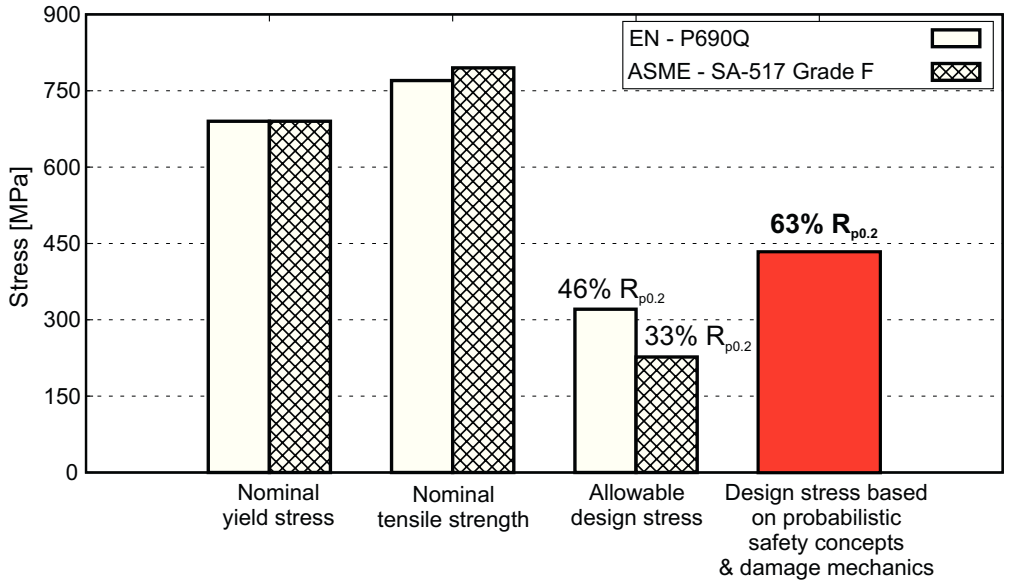

Figure 9.5.: Schematic illustration of the result of the design stress computed by using probabilistic safety concepts in combination with damage mechanics in relation to the currently defined design stresses.

10. Conclusions and Outlook

The aim of this study was to develop a comprehensive modelling concept for ductile structural failure that can be used in probabilistic safety concepts with reference to nominal toughness requirements. The background was to foster the use of high strength steels in pressure vessel design by providing means to derive more suitable design procedures for these steels. Additionally, the developed concept should be tested in a burst test demonstrating the safe applicability of high strength steels.

Within this study, such a concept could successfully be developed and demonstrated. Limit strain loci were derived from Lode angle dependent Gurson simulations that could represent varying toughness levels. The proposed calibration scheme ensures reproducible results and a reliable correlation to the toughness. Additionally, an innovative scaling function was proposed to compensate mesh size effects in large-scale simulations.

The limit strains predicted the limit pressure shortly before the actual burst pressure of the demonstrator pressure vessel. A simulation of the vessel using nominal limit strains, which were derived from nominal toughness requirements, predicted a suitable but conservative limit state shortly before the onset of global plastification. Performing probabilistic safety assessments based on findings from 30 simulations with this nominal failure criterion, suggests an increased design stress exploiting the nominal yield stress by 63% instead of currently admissible 46%. Consequently, the application of probabilistic safety concepts in combination with damage mechanics simulations provides counterarguments to the current penalisation of high strength steels in pressure vessel design.

Such an increased design stress could enable significant material savings. Using the example of the demonstrator pressure vessel, the admissible pressure could be increased by 35%. Alternatively, the wall thickness could be reduced by 10 mm or 20% resulting in weight savings of over 1t. In contrast to the currently available design procedures DBF and DBA much more realistic considerations with regard to the limit state can be achieved by the help of this method even when lower-bound, nominal failure assumptions are implemented. The developed modelling concept and its possible advantages could therefore successfully be demonstrated. Further studies with respect to the boundaries for an application of probabilistic safety concepts and the assumptions made therein should be performed. Newly derived safety factors or design functions should be validated in further tests and additional materials should be considered. An additional research question is posed by the simplified toughness assessment which is currently restricted to steels with a maximum nominal yield strength of 500 MPa. This is a further limitation to the use of high strength steels; it should be investigated whether it is justified for modern HSLA steels.

However, the most important achievement in the presented study is the successful scale-bridging of damage mechanics models from the mm to the m scale. Although under research for almost

fifty years, damage mechanics models are not part of the daily engineering routine. This is due to their complicated application that requires considerable expertise. Additionally, research studies often focused on the correct representation of laboratory investigations instead of full-scale application examples. The presented study succeeded in transferring damage mechanics models to the ductile structural failure of a flawless large-scaled pressure vessel and highlights which elements are necessary to achieve such a transfer. The developed procedure enables to fully recognise and exploit the property profile of modern high strength when investigating appropriate design rules for these materials. Using probabilistic assessments for the optimisation of the current design rules hereby brings the benefits of damage mechanics to the practical application without the need of knowledge transfer.

Of course, some of the approaches are specific to the case examined in this study, but the general roadmap is also applicable to other construction types, such as steel constructions or linepipes. Applying the proposed concept in such components could generate significant economic and ecological advantages by an increased use of modern high strength steels. Thus, further research on such application-oriented case studies should be undertaken to foster the practical application of damage mechanics in engineering processes.

A. Appendix

A.1. Metallographic characterisation of weld seams

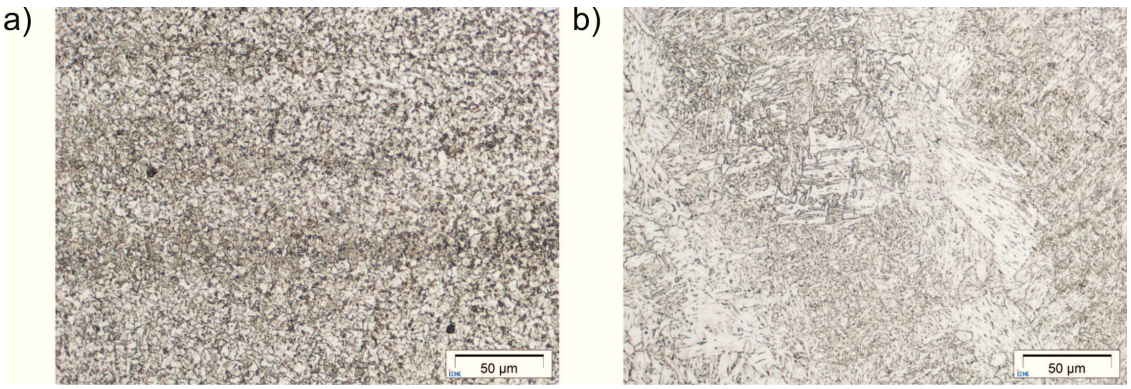

Figure A.1.: Metallographic investigations of dvIV a) fine grain zone b) coarse grain zone.

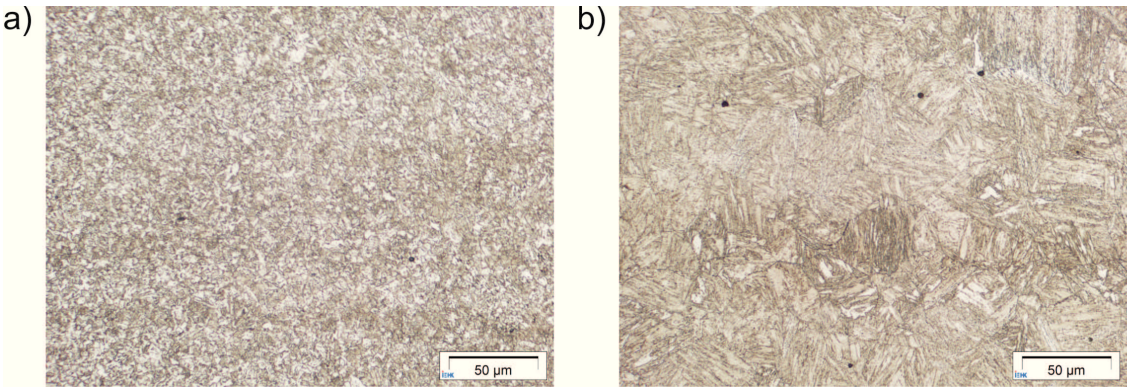

Figure A.2.: Metallographic investigations of dvV a) fine grain zone b) coarse grain zone.

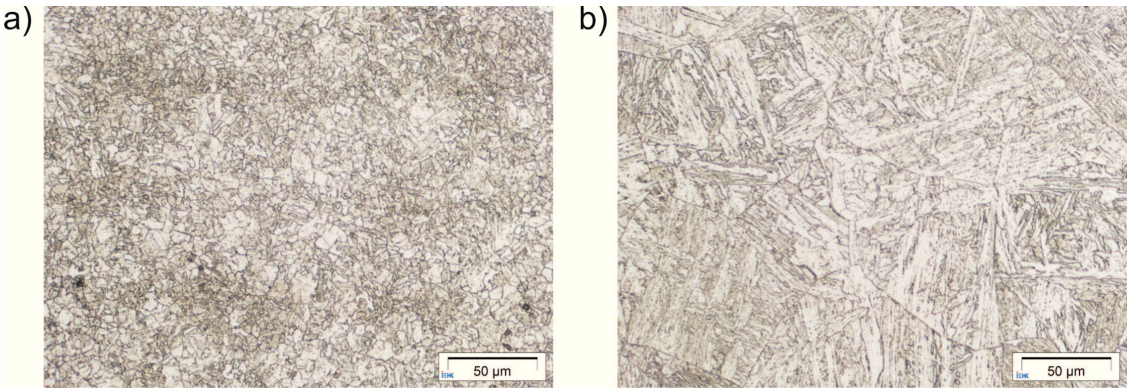

Figure A.3.: Metallographic investigations of dvVI a) fine grain zone b) coarse grain zone.

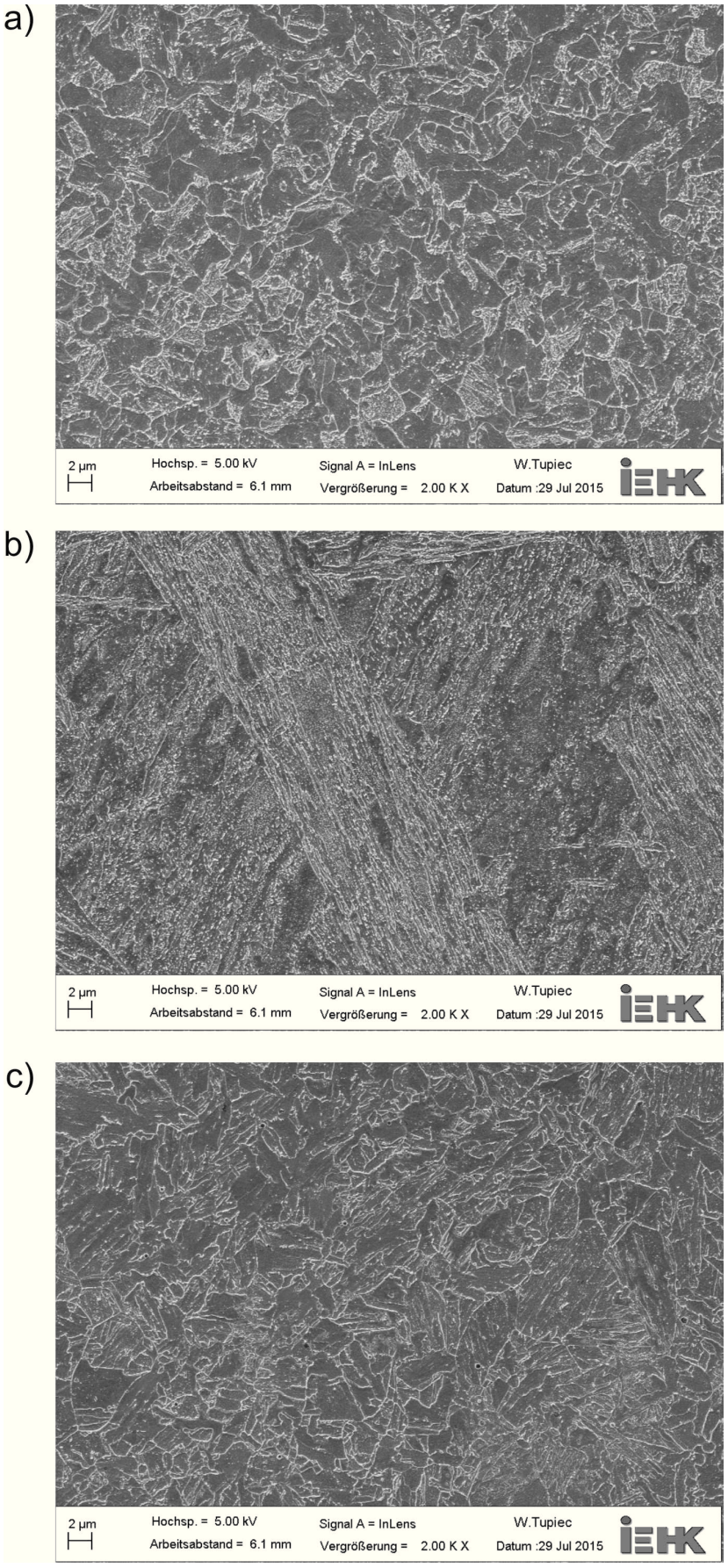

Figure A.4.: SEM investigations of dvIV a) fine grain zone b) coarse grain zone c) weld seam.

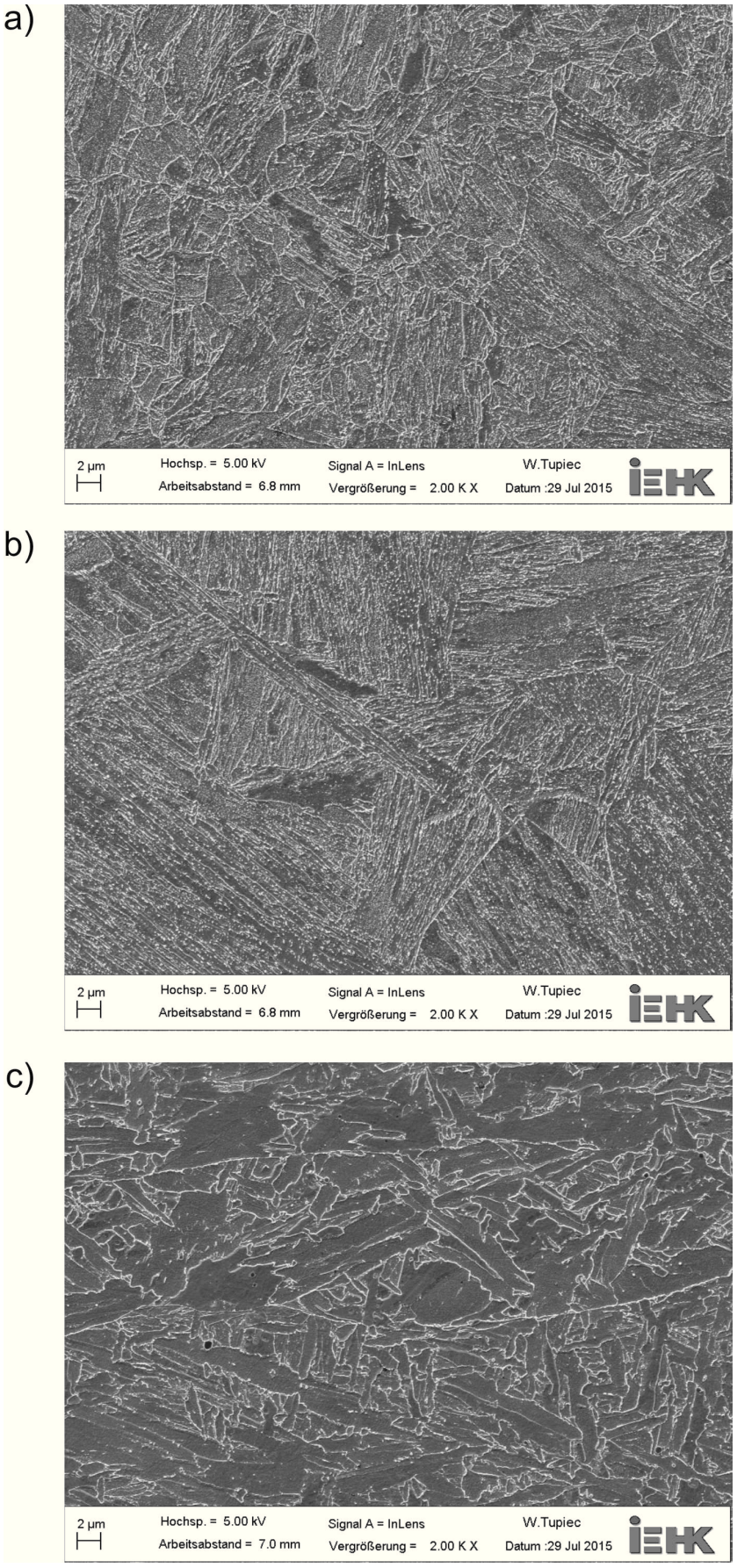

Figure A.5.: SEM investigations of dvV a) fine grain zone b) coarse grain zone c) weld seam.

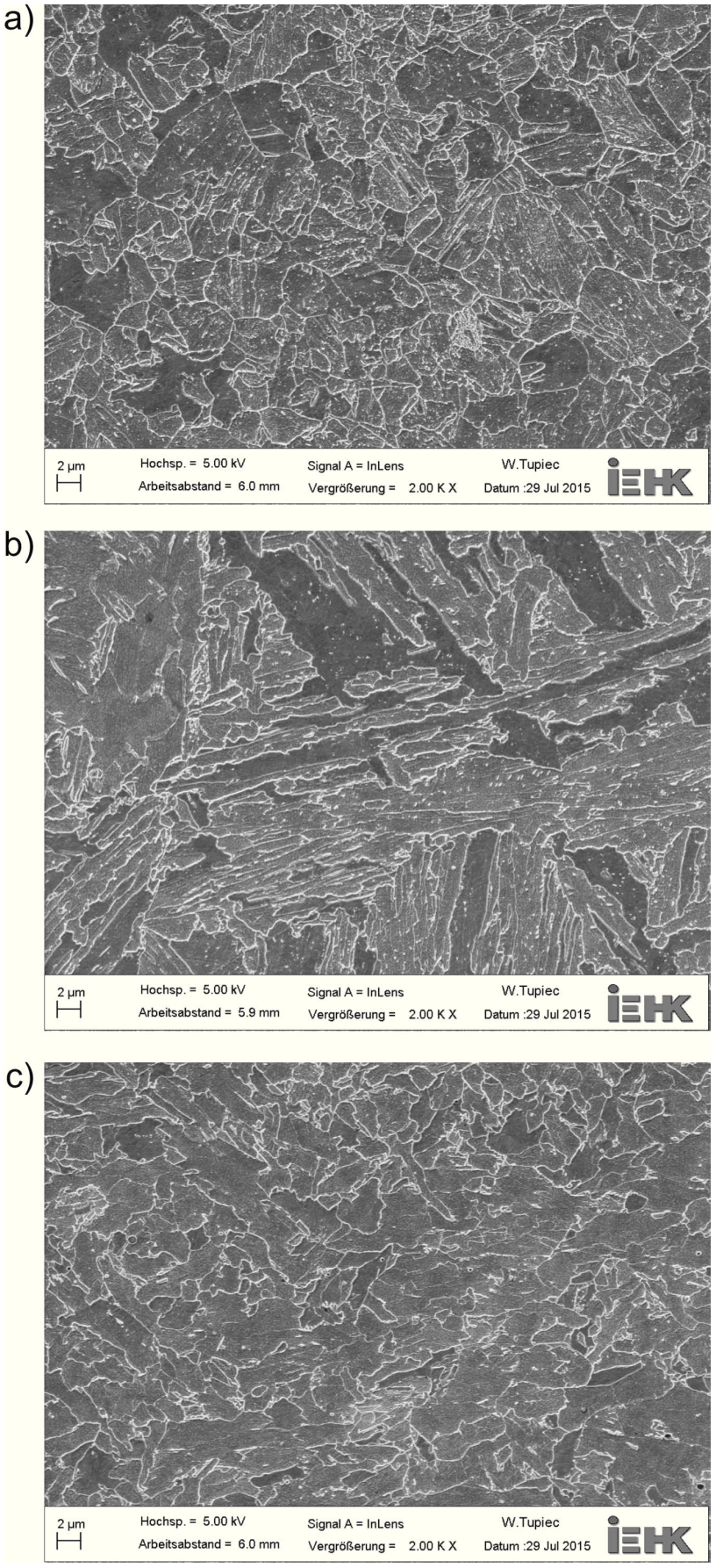

Figure A.6.: SEM investigations of dvVI a) fine grain zone b) coarse grain zone c) weld seam.

A.2. Additional information on the materials

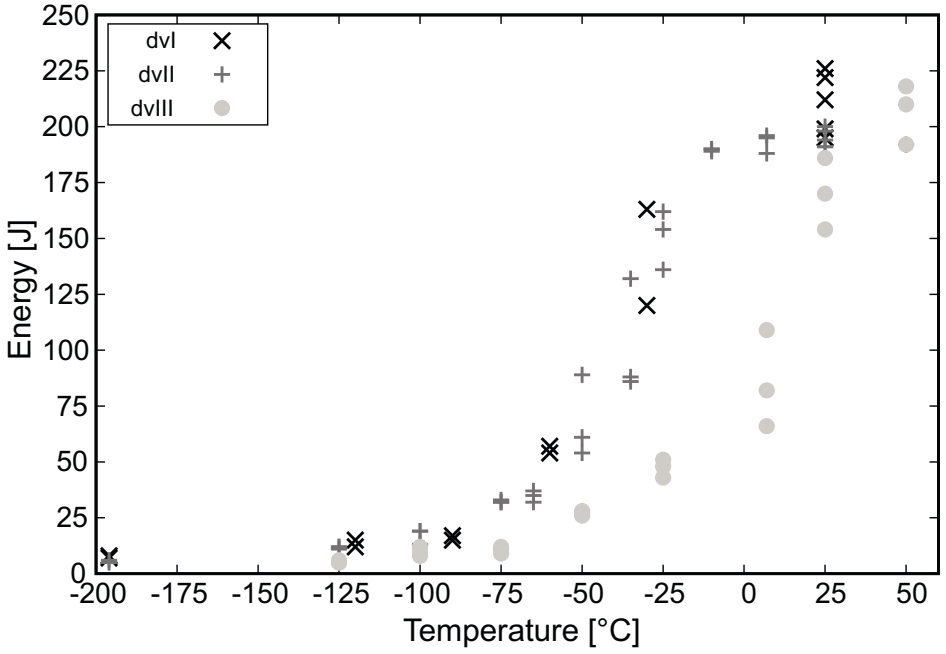

Figure A.7.: Results of Charpy impact toughness tests at different temperatures for the base materials. The decrease of toughness through the heat treatment for stress relief can be recognised comparing the results of materials dvI and dvIII.

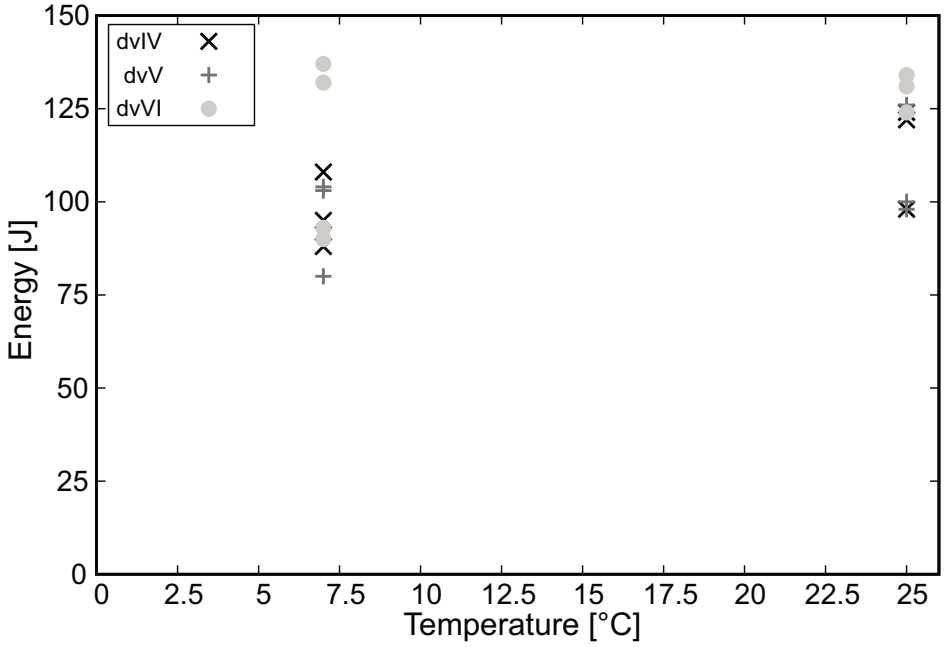

Figure A.8.: Results of Charpy impact toughness tests at room temperature and the burst test temperature (7°C) .

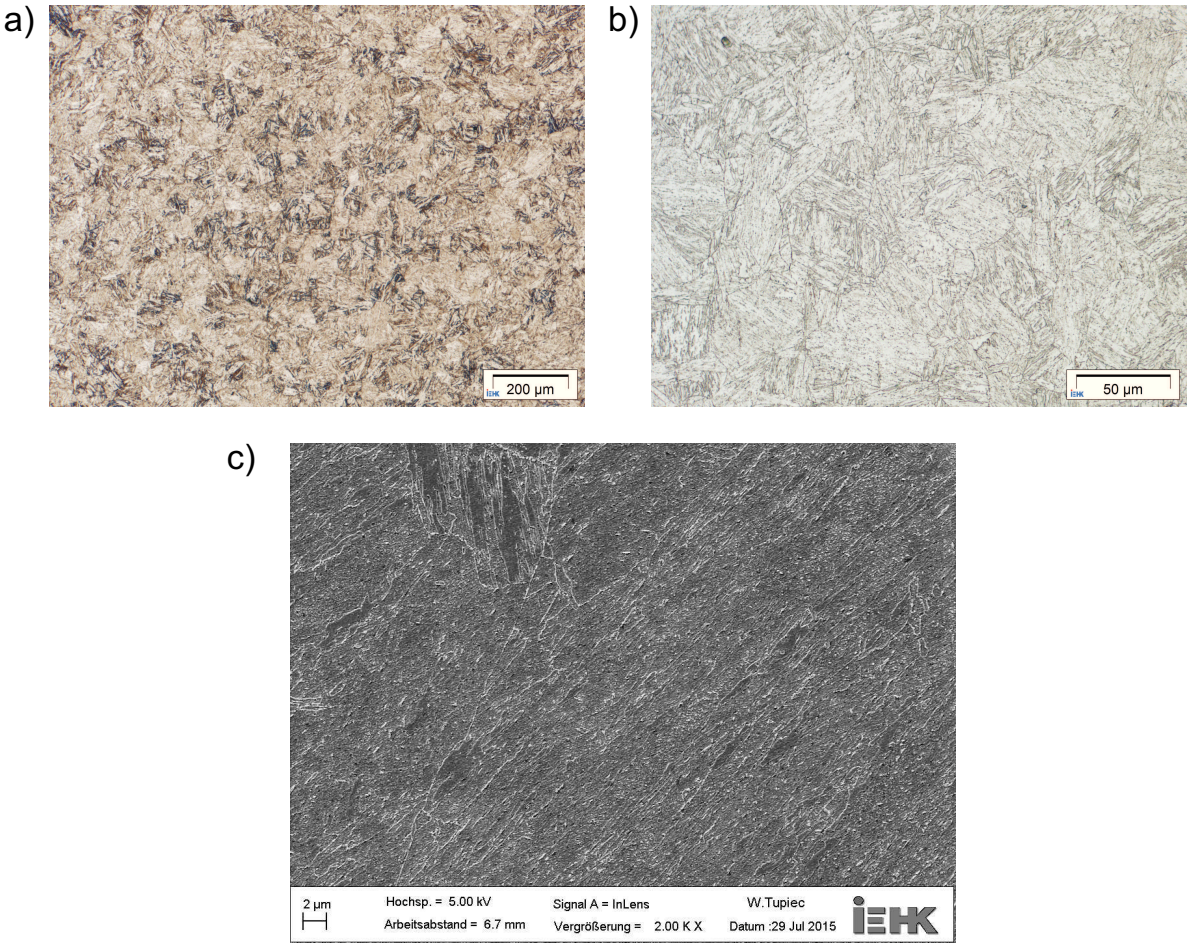

Figure A.9.: Metallographic characterisation of dvI.

A.3. Additional information on the methods

Table A.1.: Force ratios to be applied to the threedimensional unit cell modelling for achieving a certain stress state. $\overline{\theta}$ is the Lode angle factor according to Eq. 2.37, η the stress triaxiality, α, β, γ are the factors, respectively ratios of the applied forces. These can be applied for example as negative pressures.

$\overline{\theta}$	η	α	β	γ
1	0.5	0.1429	0.1429	1
1	1	0.4	0.4	1
1	1.5	0.5385	0.5385	1
1	2	0.625	0.625	1
1	2.5	0.6842	0.6842	1
-1	0.5	-0.2	1	1
-1	1	0.25	1	1
-1	1.5	0.4545	1	1
-1	2	0.5714	1	1
-1	2.5	0.6471	1	1
0	0.5	-0.0718	0.4641	1
0	1	0.2679	0.634	1
0	1.5	0.4441	0.7221	1
0	2	0.552	0.776	1
0	2.5	0.6248	0.8124	1

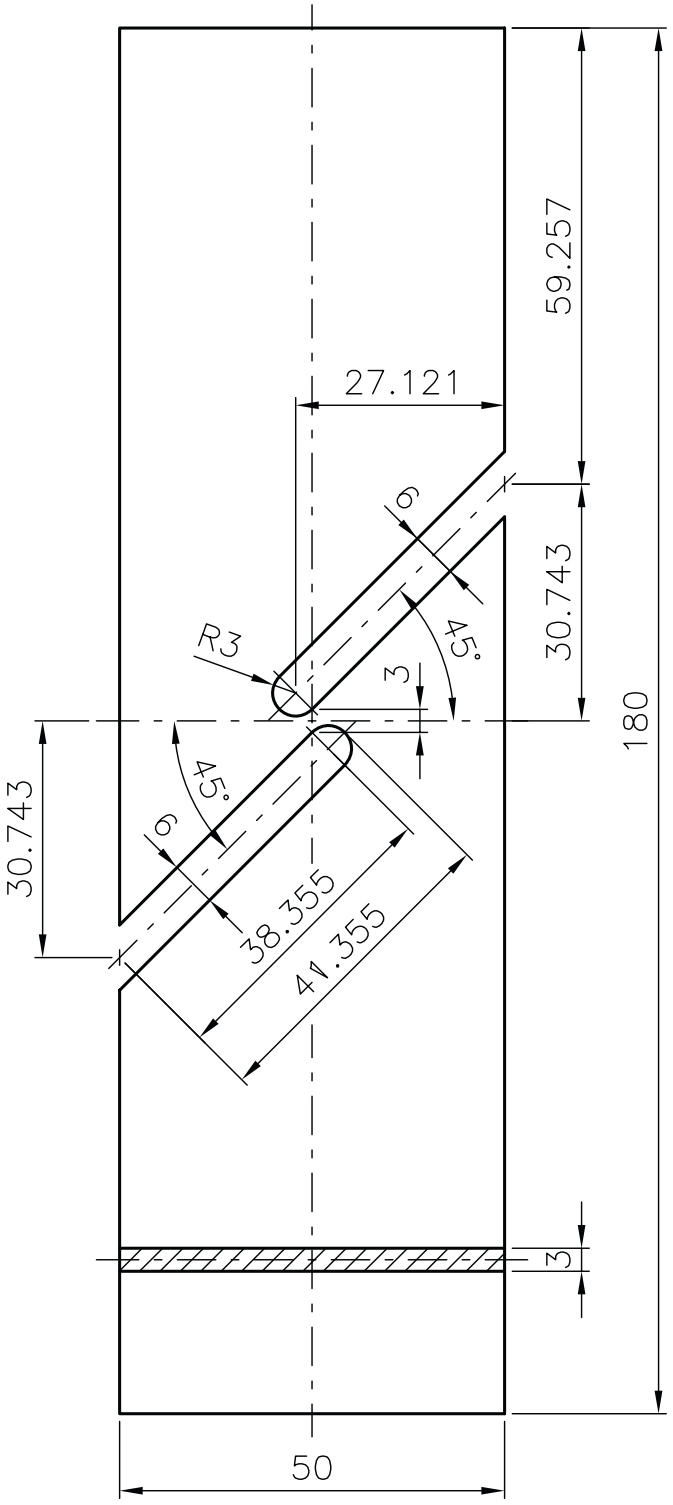

Figure A.10.: Geometry of the shear samples.

A.4. Additional material on results

A.4.1. Limit state investigation

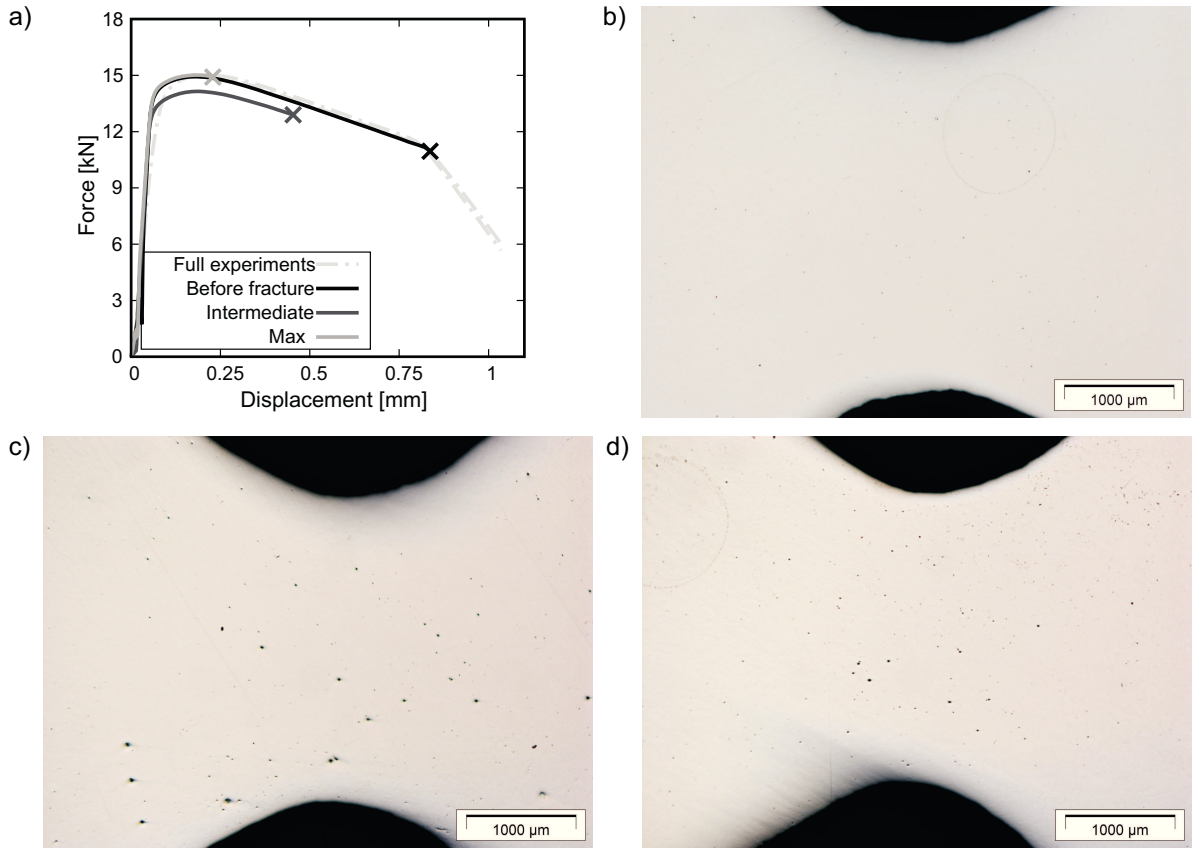

Figure A.11.: Results of stopped tensile tests on the geometry L4R2: a) Force-displacement curve as well as prepared central sections of stopped experiment at b) force maximum, c) midway between force maximum and failure, c) immediately before failure. The variation in force for the sample stopped at an intermediate displacement resulted from a slightly smaller initial cross section in the notch ground. This also explains the relatively strong void growth at intermediate deformation.

A.4.2. Sensitivity analysis

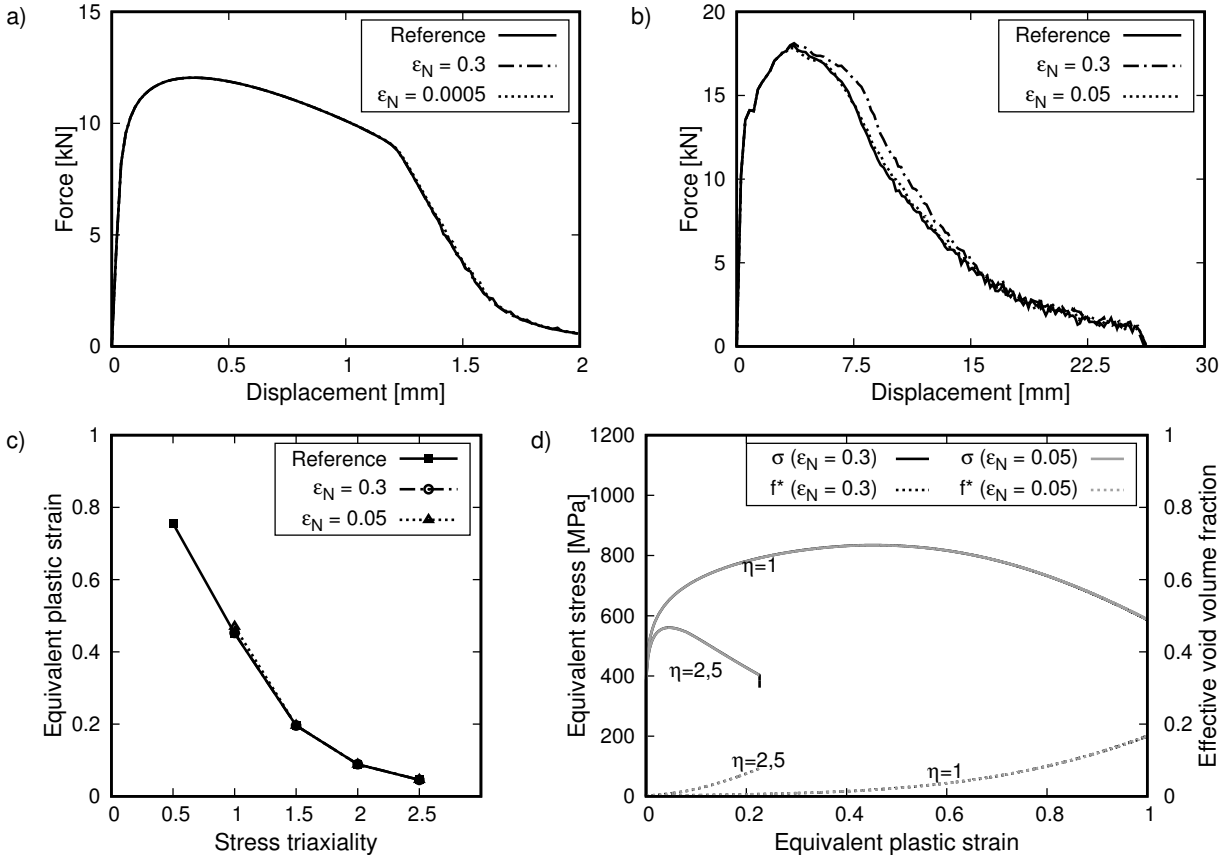

Figure A.12.: Influence of ε_N (for $f_N = 0.00215$) on a) NRB and b) Charpy simulations, c) the derived critical strains from and d) σ_e and f^* within cell element simulations for η=1.0 and $\eta = 2.5$.

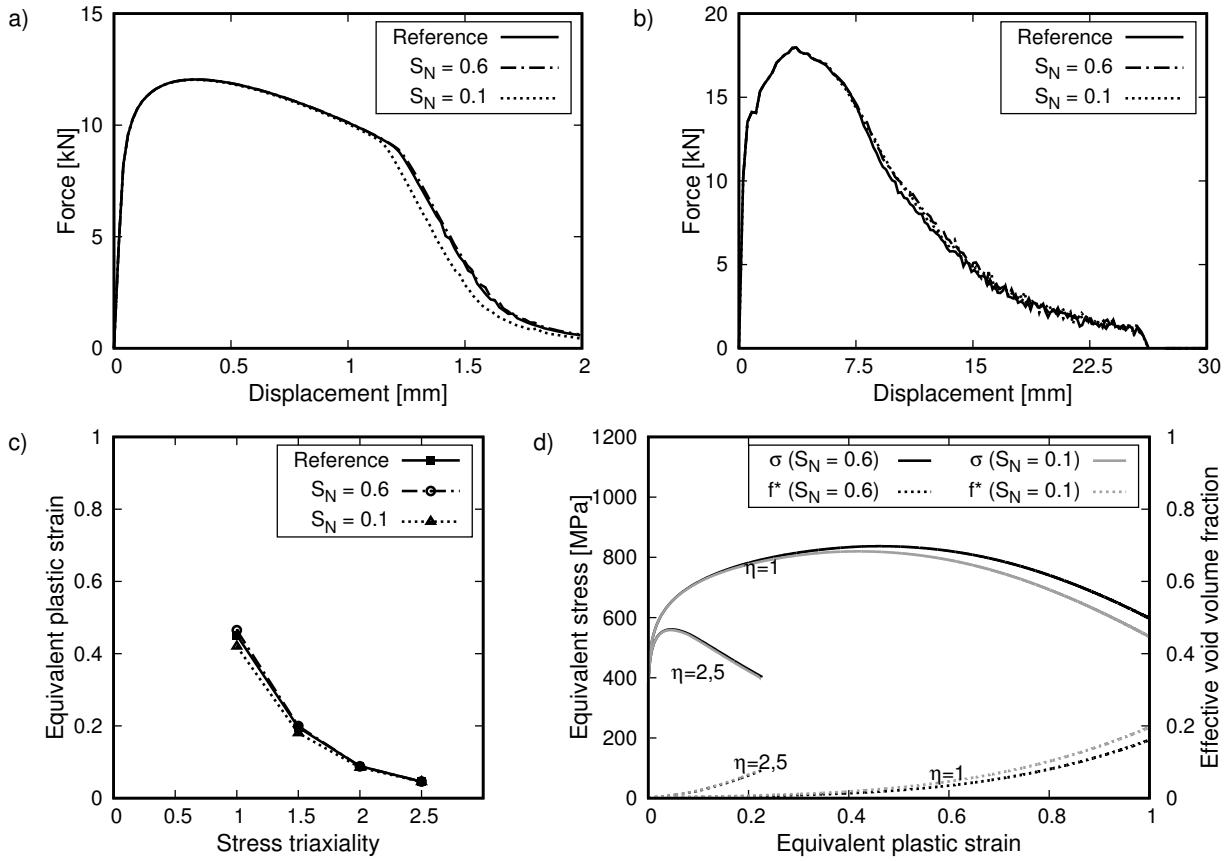

Figure A.13.: Influence of S_N (for $f_N = 0.00215$) on a) NRB and b) Charpy simulations, c) the derived critical strains from and d) σ_e and f^* within cell element simulations for η=1.0 and $\eta = 2.5$.

A.4.3. Additional material on Lode angle consideration

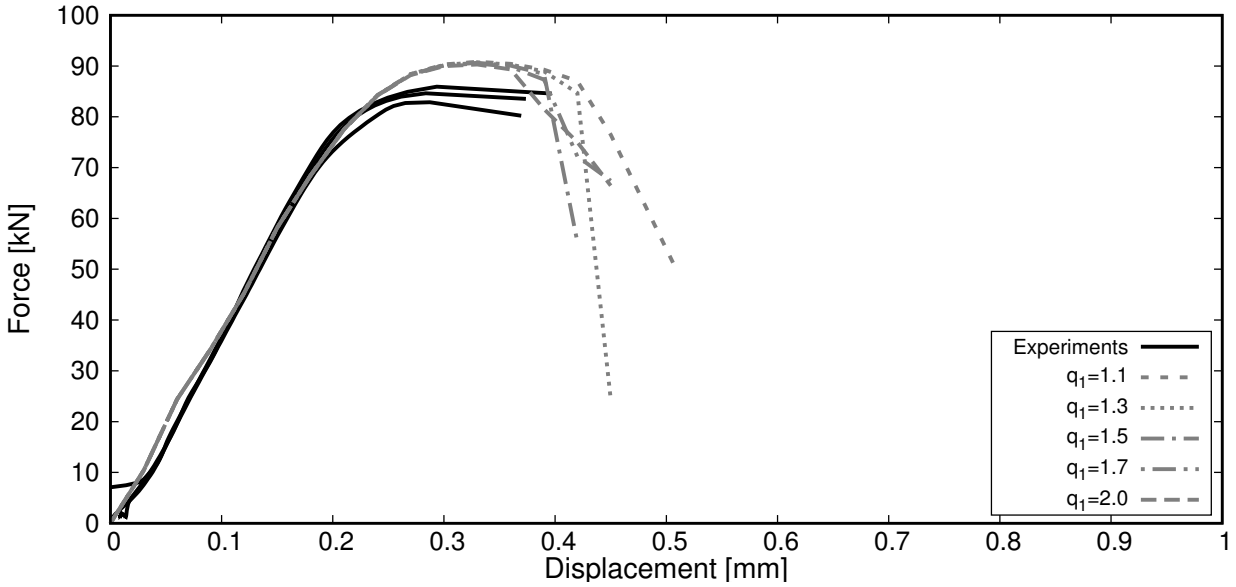

Figure A.14.: Effect of a variation of $q_1$on the simulation of plane strain samples with a radius of 1.5 mm using the NH model.

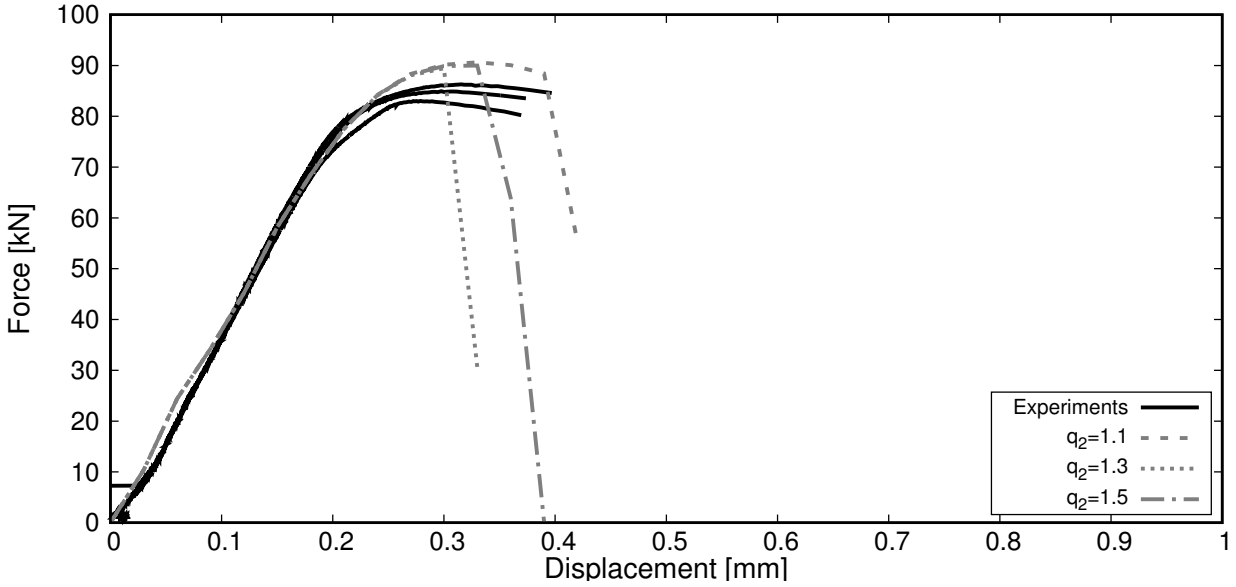

Figure A.15.: Effect of a variation of $q_2$on the simulation of plane strain samples with a radius of 1.5 mm using the NH model.

A.4.4. Results on the parameter calibration for head material and longitudinal vessel weld seam

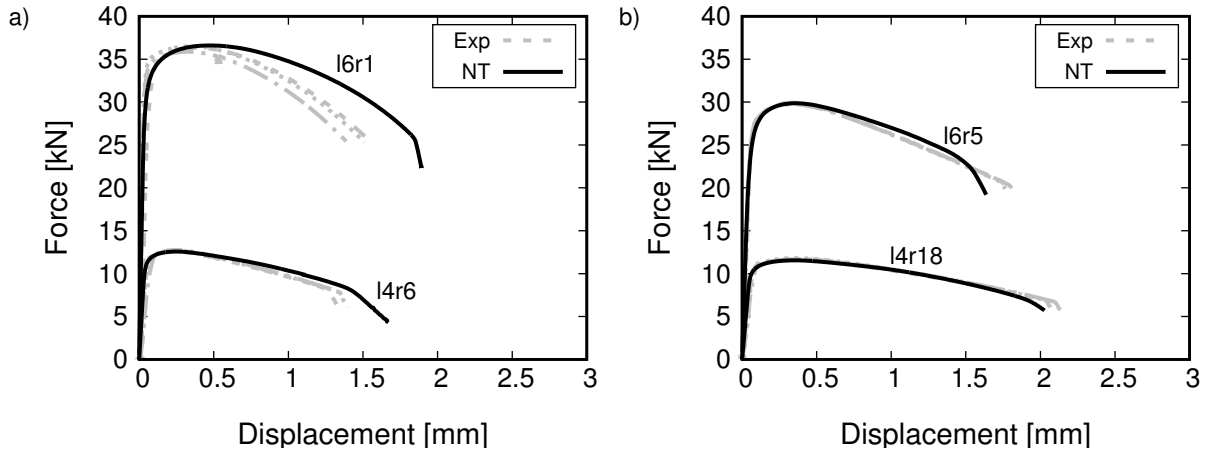

Figure A.16.: Result of NRB simulation and experiments (dashed lines) a) L6R1 and L4R6 b) L6R6 and L4R18 of dvIII.

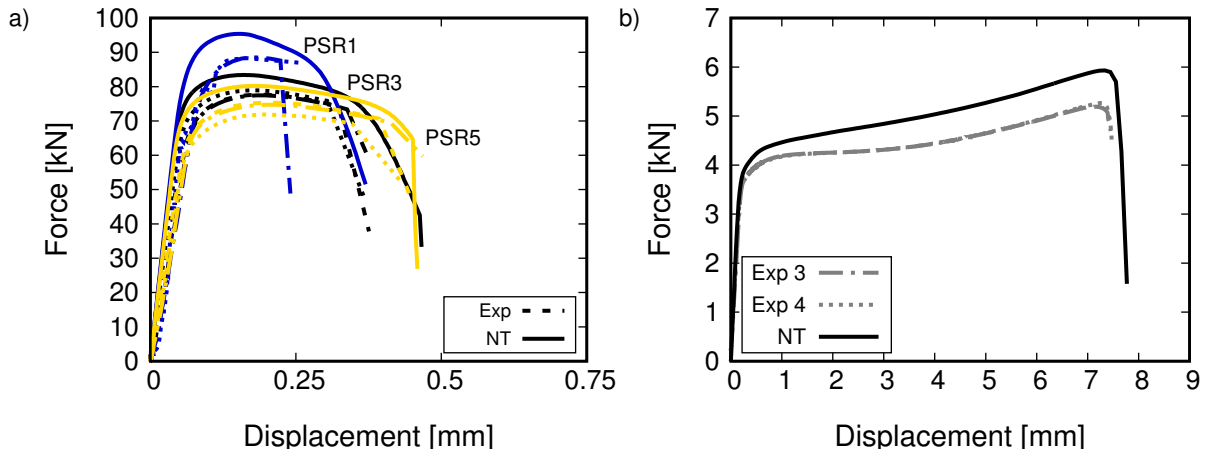

Figure A.17.: Result of NRB simulation and experiments (dashed lines) of a) shear and b) plane strain samples of dvIII.

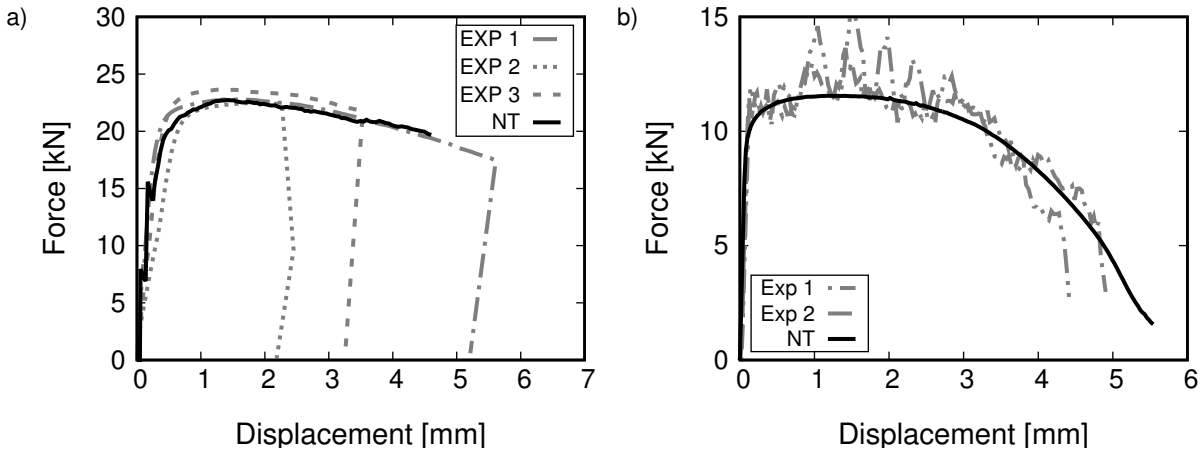

Figure A.18.: Result of simulation and experiments (dashed lines) of a) SENB tests b) high speed tensile tests at a strain rate of 150/s of dvIII.

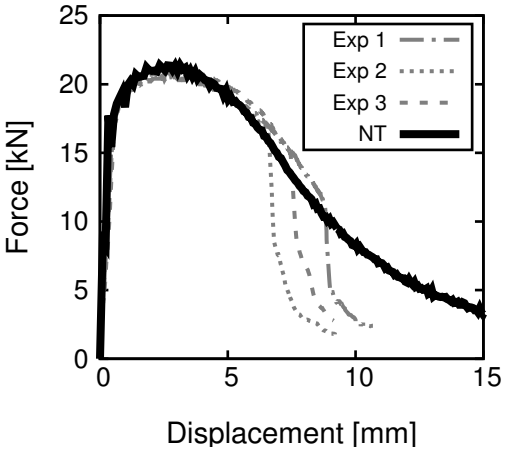

Figure A.19.: Result of simulation and experiments for Charpy tests at room temperature of dvIII.

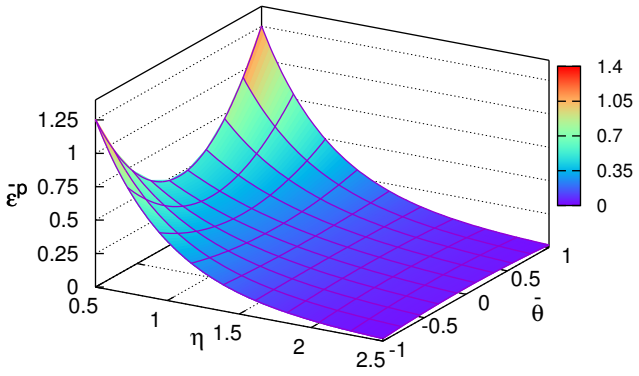

Figure A.20.: Plotted local softening locus of dvIII.

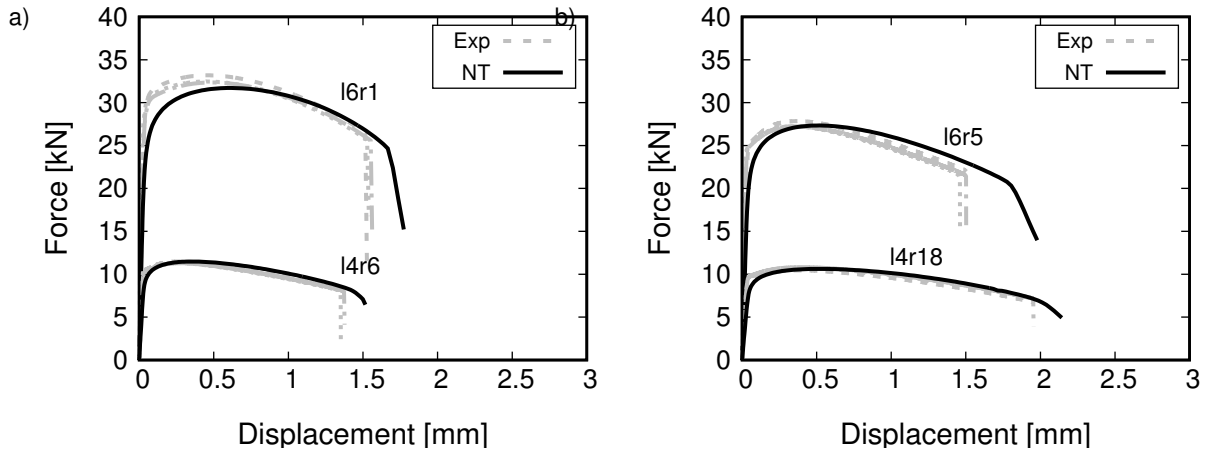

Figure A.21.: Result of NRB simulation and experiments (dashed lines) a) L6R1 and L4R6 b) L6R6 and L4R18 of dvV.

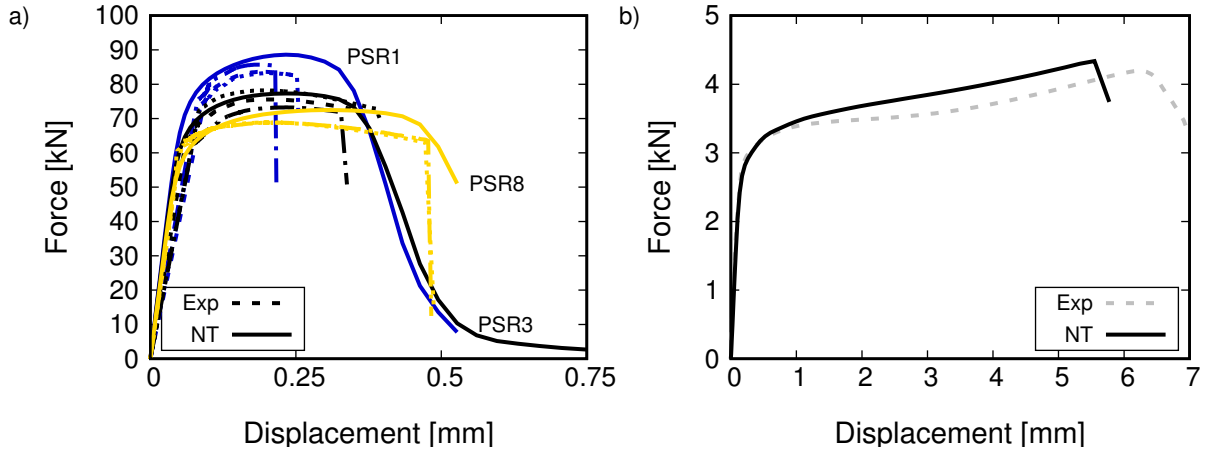

Figure A.22.: Result of NRB simulation and experiments (dashed lines) of a) shear and b) plane strain samples of dvV.

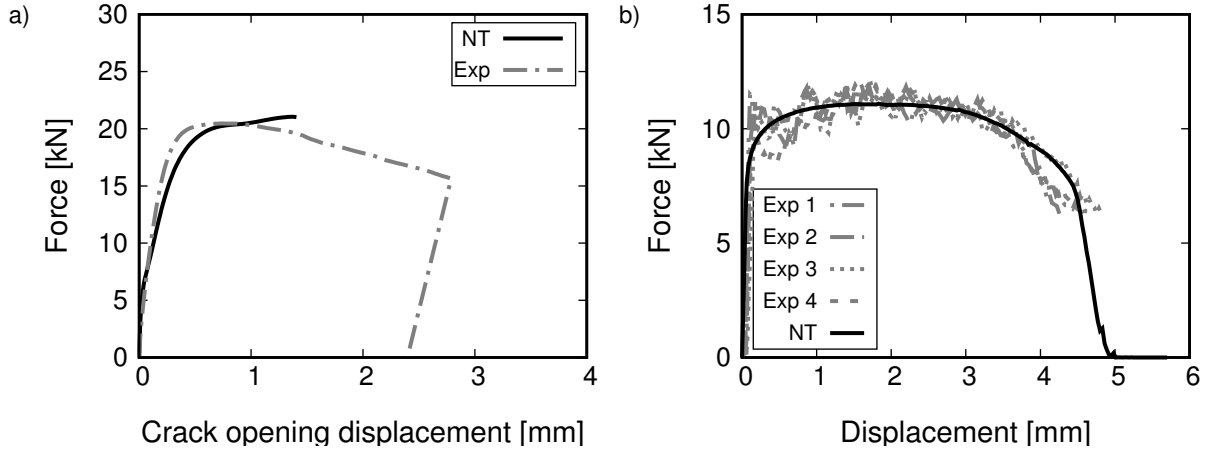

Figure A.23.: Result of simulation and experiments (dashed lines) of a) SENB tests b) high speed tensile tests at a strain rate of 150/s of dvIV.

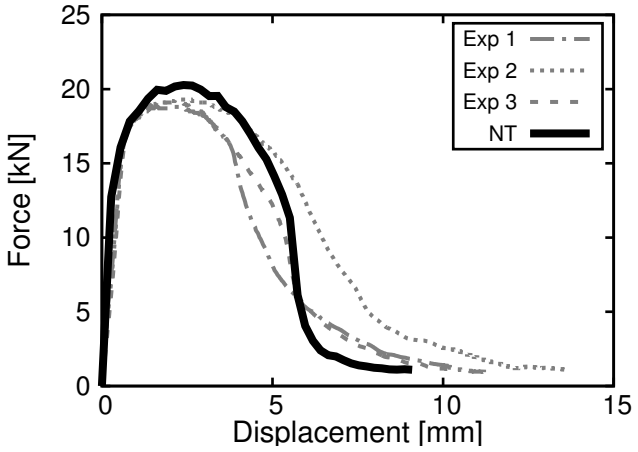

Figure A.24.: Result of simulation and experiments for Charpy tests at room temperature of dvV.

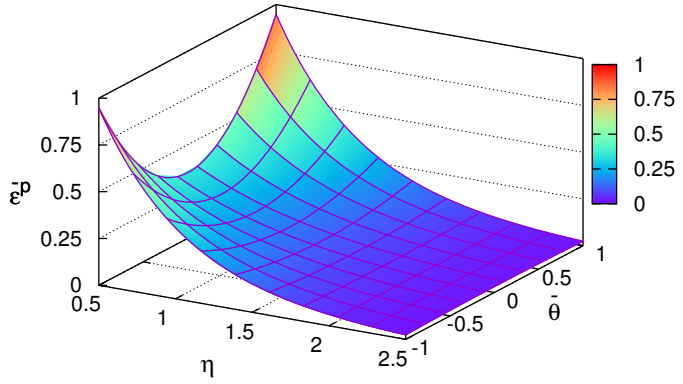

Figure A.25.: Plotted local softening locus of dvV.

Bibliography

[1] United Nations, "Paris agreement." https://treaties.un.org, 2016.

[2] Enerdata, "Energy statistics yearbook." https://yearbook.enerdata.net/, 2005.

[3] V. Brinnel, S. Münstermann, W. Bleck, M. Feldmann, and S. Reese, "Structural requirements and material solutions for sustainable buildings," *Revue de Métallurgie*, vol. 110, pp. 37–46, 2013.

[4] L. Cederfeldt, "High strength steel in Friends Arena - Savings in weight and cost," in *IABSE Symposium Report*, vol. 101, pp. 1–7, International Association for Bridge and Structural Engineering, 2013.

[5] H. Mohrbacher, *Molybdenum in Irons and Steels for Clean and Green Power Generation*. International Molybdenum Association, 2011.

[6] T. Heller, H.-J. Kaiser, A. Kern, and H.-J. Tschersich, "Moderne hochfeste Stähle im Nutzfahrzeug- und Mobilkranbau," *ATZ - Automobiltechnische Zeitschrift*, vol. 100, no. 9, pp. 664–668, 1998.

[7] T. Ummenhofer, M. Spannaus, G. Steidl, W. Hölbling, and V. Di Rosa, "Die Anwendung hochfester Feinkornbaustähle im konstruktiven Ingenieurbau," *Stahlbau*, vol. 82, no. 4, pp. 236–245, 2013.

[8] C. Schruff, *Ressourceneffizienter Einsatz hochfester Stähle durch schädigungsmechanische Bemessung unbefeuerter Druckbehälter*. PhD thesis, RWTH Aachen University, Institut für Eisenhüttenkunde, 2013.

[9] H. Berns and W. Theisen, *Eisenwerkstoffe - Stahl und Gusseisen*. Berlin, Heidelberg: Springer, 2008.

[10] P. Rohart, S. Panier, S. Hariri, Y. Simonet, and M. Afzali, "Contribution to pressure vessels design of innovative methods and comparative application with standardized rules on a realistic structure - Part I," *International Journal of Pressure Vessels and Piping*, vol. 134, pp. 25–32, 2015.

[11] A. Diamantoudis and T. Kermanidis, "Design by analysis versus design by formula of high strength steel pressure vessels: a comparative study," *International Journal of Pressure Vessels and Piping*, vol. 82, no. 1, pp. 43–50, 2005.

[12] W. Bleck, S. Münstermann, C. Schruff, M. Feldmann, D. Schäfer, and P. Langenberg, *Forschungsvorhaben P758 - Verbesserte Ausnutzung der Festigkeiten hochfester Druckbehälterstähle durch Erfassung des Grenzzustands der Tragfähigkeit mit Hilfe der Fließbruchmechanik*. Düsseldorf: Vertriebs- und Verlagsgesellschaft, 2014.

[13] W. Bleck, ed., *Material Characterisation*. Aachen: Mainz, 2011.

[14] H. Bargel and G. Schulze, eds., *Werkstoffkunde*. Berlin, Heidelberg: Springer, 2008.

[15] J. Roesler, H. Harders, and M. Baeker, *Mechanisches Verhalten der Werkstoffe*. Berlin, Heidelberg: Springer, 2008.

[16] A. Hosten, *Numerische Modellierung dynamischer Belastung von Stählen*. PhD thesis, RWTH Aachen University, Institut für Eisenhüttenkunde, 2013.

[17] D. Gross, W. Hauger, W. Schnell, and P. Wriggers, *Technische Mechanik 4*. Berlin, Heidelberg: Springer, 2007.

[18] D. Gross and T. Seelig, *Bruchmechanik*. Berlin, Heidelberg: Springer, 2007.

[19] F. A. McClintock, "Plasticity aspects of fracture," in *Fracture - An Advanced Treatise* (H. Liebowitz, ed.), ch. 2, pp. 48–225, New York, London: Academic Press, 1971.

[20] M. Merkel and A. Öchsner, *Eindimensionale Finite Elemente*. Berlin, Heidelberg: Springer, 2010.

[21] R. v. Mises, "Mechanik der festen Körper im plastisch-deformablen Zustand," *Nachrichten von der Gesellschaft der Wissenschaften zu Göttingen, Mathematisch-Physikalische Klasse*, vol. 1913, pp. 582–592, 1913.

[22] R. V. Mises, "Mechanik der plastischen Formänderung von Kristallen," *ZAMM - Journal of Applied Mathematics and Mechanics / Zeitschrift für Angewandte Mathematik und Mechanik*, vol. 8, no. 3, pp. 161–185, 1928.

[23] M. Seidenfuß, "Schädigungsmechanische Modelle zur Beschreibung des Versagensablaufs in metallischen Bauteilen," Habilitation thesis, Universität Stuttgart, 2013.

[24] F. Dunne and N. Petrinic, *Introduction to Computational Plasticity*. Oxford: Oxford University Press, 2005.

[25] A. A. Benzerga and J.-B. Leblond, "Ductile fracture by void growth to coalescence," in *Advances in Applied Mechanics* (H. Aref and E. van der Giessen, eds.), vol. 44, pp. 169–305, New York, London: Academic Press, 2010.

[26] Y. Bai and T. Wierzbicki, "A new model of metal plasticity and fracture with pressure and Lode dependence," *International Journal of Plasticity*, vol. 24, no. 6, pp. 1071–1096, 2008.

[27] K. Nahshon and J. Hutchinson, "Modification of the Gurson model for shear failure," *European Journal of Mechanics - A/Solids*, vol. 27, no. 1, pp. 1–17, 2008.

[28] M. Dunand and D. Mohr, "On the predictive capabilities of the shear modified Gurson and the modified Mohr-Coulomb fracture models over a wide range of stress triaxialities and lode angles," *Journal of the Mechanics and Physics of Solids*, vol. 59, no. 7, pp. 1374–1394, 2011.

[29] G. Golisch and S. Münstermann, "Entwicklung eines schädigungsmechanischen Spaltbruchmodells unter Berücksichtigung des Spannungszustandes und der Versagenswahrscheinlichkeit," in *DVM Bericht 248 - Bruchmechanische Werkstoff- und Bauteilbewertung: Beanspruchungsanalyse, Prüfmethoden und Anwendungen, 48. Tagung*

des Arbeitskreises Bruchmechanik und Bauteilsicherheit, 16.-17. Februar 2016, Freiburg, pp. 21–30, 2016.

[30] W. Garrison and N. Moody, "Ductile fracture," *Journal of Physics and Chemistry of Solids*, vol. 48, no. 11, pp. 1035 – 1074, 1987.

[31] I. Barsoum and J. Faleskog, "Rupture mechanisms in combined tension and shear: Experiments," *International Journal of Solids and Structures*, vol. 44, no. 6, pp. 1768–1786, 2007.

[32] M. A. M. Halim, *Einfluß der Mikrostruktur und des Spannungszustandes auf die Bruchvorgänge in technischen Stählen*. PhD thesis, RWTH Aachen University, Institut für Eisenhüttenkunde, 1989.

[33] N. Schlüter, *Einfluß der Beanspruchung und des Gefüges auf die lokale Schädigung beim Gleitbruch von Baustählen*. PhD thesis, RWTH Aachen University, Institut für Eisenhüttenkunde, 1997.

[34] R. D. Thomson and J. W. Hancock, "Ductile failure by void nucleation, growth and coalescence," *International Journal of Fracture*, vol. 26, no. 2, pp. 99–112, 1984.

[35] D. P. Clausing, "Effect of plastic strain state on ductility and toughness," *International Journal of Fracture Mechanics*, vol. 6, no. 1, pp. 71–85, 1970.

[36] Y. Bao and T. Wierzbicki, "On fracture locus in the equivalent strain and stress triaxiality space," *International Journal of Mechanical Sciences*, vol. 46, no. 1, pp. 81–98, 2004.

[37] Y. Bai, X. Teng, and T. Wierzbicki, "On the application of stress triaxiality formula for plane strain fracture testing," *Journal of Engineering Materials and Technology*, vol. 131, no. 2, pp. 021002–1–021002–10, 2009.

[38] K. Wallin, "Modified tanh fitting algorithm for charpy impact data," ECOPRESS reports, 2001.

[39] T. Anderson, *Fracture Mechanics: Fundamentals and Applications*. Boca Raton: CRC press, 2005.

[40] A. A. Griffith, "The phenomena of rupture and flow in solids," *Philosophical Transactions of the Royal Society of London A: Mathematical, Physical and Engineering Sciences*, vol. 221, no. 582-593, pp. 163–198, 1921.

[41] G. R. Irwin, "Analysis of stresses and strains near the end of a crack traversing a plate," *Journal of Applied Mechanics*, 1957.

[42] A. Wells, "Unstable crack propagation in metals: cleavage and fast fracture," in *Proceedings of the crack propagation symposium, Cranfield, UK*, vol. 1, 1961.

[43] J. R. Rice, "A path independent integral and the approximate analysis of strain concentration by notches and cracks," *Journal of Applied Mechanics*, vol. 35, no. 2, pp. 379–386, 1968.

[44] F. A. McClintock, "A criterion for ductile fracture by the growth of holes," *Journal of Applied Mechanics*, vol. 35, no. 2, pp. 363–371, 1968.

[45] J. Rice and D. Tracey, "On the ductile enlargement of voids in triaxial stress fields," *Journal of the Mechanics and Physics of Solids*, vol. 17, no. 3, pp. 201–217, 1969.

[46] J. Hancock and A. Mackenzie, "On the mechanisms of ductile failure in high-strength steels subjected to multi-axial stress-states," *Journal of the Mechanics and Physics of Solids*, vol. 24, no. 2-3, pp. 147–160, 1976.

[47] J. Lian, *A generalised hybrid damage damage mechanics model for steel sheets and heavy plates*. PhD thesis, RWTH Aachen University, Insitut für Eisenhüttenkunde, 2015.

[48] J. Koplik and A. Needleman, "Void growth and coalescence in porous plastic solids," *International Journal of Solids and Structures*, vol. 24, no. 8, pp. 835–853, 1988.

[49] M. Kuna and D. Z. Sun, "Three-dimensional cell model analyses of void growth in ductile materials," *International Journal of Fracture*, vol. 81, pp. 235–258, 1996.

[50] J. Kim, X. Gao, and T. S. Srivatsan, "Modeling of void growth in ductile solids: effects of stress triaxiality and initial porosity," *Engineering Fracture Mechanics*, vol. 71, no. 3, pp. 379–400, 2004.

[51] J. Faleskog, X. Gao, and C. Shih, "Cell model for nonlinear fracture analysis - I. Micromechanics calibration," *International Journal of Fracture*, vol. 89, pp. 355–373, 1998.

[52] X. Gao, J. Faleskog, and C. Shih, "Cell model for nonlinear fracture analysis - II. Fracture-process calibration and verification," *International Journal of Fracture*, vol. 89, pp. 375–398, 1998.

[53] O. West, J. Lian, S. Münstermann, and W. Bleck, "Numerical determination of the damage parameters of a dual-phase sheet steel," *ISIJ International*, vol. 52, no. 4, pp. 743–752, 2012.

[54] V. Tvergaard and A. Needleman, "Analysis of the cup-cone fracture in a round tensile bar," *Acta Metallurgica*, vol. 32, no. 1, pp. 157–169, 1984.

[55] V. Tvergaard and K. L. Nielsen, "Relations between a micro-mechanical model and a damage model for ductile failure in shear," *Journal of the Mechanics and Physics of Solids*, vol. 58, no. 9, pp. 1243–1252, 2010.

[56] J. Lemaitre, "A continuous damage mechanics model for ductile fracture," *Journal of Engineering Materials and Technology*, vol. 107, no. 1, pp. 83–89, 1985.

[57] J. Lemaitre and R. Desmorat, *Engineering damage mechanics: ductile, creep, fatigue and brittle failures*. Berlin, Heidelberg: Springer, 2005.

[58] J. Besson, "Continuum models of ductile fracture: A review," *International Journal of Damage Mechanics*, vol. 19, no. 1, pp. 3–52, 2010.

[59] G. Johnson and W. Cook, "A constitutive model and data for metals subjected to large strains, high strain rates and high temperatures.," in *Proceedings of the 7th International Symposium on Ballistics*, pp. 541–547, 1983.

[60] G. R. Johnson and W. H. Cook, "Fracture characteristics of three metals subjected to various strains, strain rates, temperatures and pressures," *Engineering Fracture Mechanics*, vol. 21, no. 1, pp. 31–48, 1985.

[61] J. Lian, M. Sharaf, F. Archie, and S. Münstermann, "A hybrid approach for modelling of plasticity and failure behaviour of advanced high-strength steel sheets," *International Journal of Damage Mechanics*, vol. 22, no. 2, pp. 188–218, 2013.

[62] A. Gurson, "Continuum theory of ductile rupture by void nucleation and growth: Part I - Yield criteria and flow rules for porous ductile media," *Journal of Engineering Materials and Technology*, vol. 99, no. 2, pp. 2–15, 1977.

[63] V. Tvergaard, "Influence of voids on shear band instabilities under plane strain conditions," *International Journal of Fracture*, vol. 17, pp. 389–407, 1981.

[64] N. Aravas, "On the numerical integration of a class of pressure-dependent plasticity models," *International Journal for Numerical Methods in Engineering*, vol. 24, no. 7, pp. 1395–1416, 1987.

[65] C. Chu and A. Needleman, "Void nucleation in biaxially stretched sheets," *Journal of Engineering Materials and Technology*, vol. 102, pp. 249–256, 1980.

[66] S. Münstermann, *Numerische Beschreibung des duktilen Versagensverhaltens von hochfesten Baustählen unter Berücksichtigung der Mikrostruktur*. PhD thesis, RWTH Aachen University, Institut für Eisenhüttenkunde, 2006.

[67] V. Brinnel, J. Langenberg, F. Kordtomeikel, Y. Di, and S. Münstermann, "Numerical derivation of strain-based criteria for ductile failure: Discussions on sensitivity and validity," *Engineering Fracture Mechanics*, vol. 148, pp. 421–440, 2015.

[68] F. Reusch, *Entwicklung und Anwendung eines nicht-lokalen Materialmodells zur Simulation duktiler Schädigung in metallischen Werkstoffen*. PhD thesis, Universität Dortmund, 2003.

[69] T. Linse, G. Hütter, and M. Kuna, "Simulation of crack propagation using a gradient-enriched ductile damage model based on dilatational strain," *Engineering Fracture Mechanics*, vol. 95, pp. 13–28, 2012.

[70] M. Kuna and D.-Z. Sun, "Analyses of void growth and coalescence in cast iron by cell models," *Journal de Physique IV*, vol. 6, no. C6, pp. 113–122, 1996.

[71] V. Tvergaard, "Behaviour of voids in a shear field," *International Journal of Fracture*, vol. 158, pp. 41–49, 2009.

[72] N. Bonora, "Identification and measurement of ductile damage parameters," *The Journal of Strain Analysis for Engineering Design*, vol. 34, no. 6, pp. 463–478, 1999.

[73] D. Steglich, "Structure damage simulation," in *Continuum Scale Simulation of Engineering Materials* (D. Raabe, F. Roters, F. Barlat, and L. Chen, eds.), pp. 797–808, Weinheim: WILEY-VCH, 2004.

[74] Z. L. Zhang, "A sensitivity analysis of material parameters for the Gurson constitutive model," *Fatigue & Fracture of Engineering Materials & Structures*, vol. 19, no. 5, pp. 561–570, 1996.

[75] S. Münstermann, C. Schruff, J. Lian, B. Döbereiner, V. Brinnel, and B. Wu, "Predicting lower bound damage curves for high-strength low-alloy steels," *Fatigue & Fracture of Engineering Materials & Structures*, vol. 36, no. 8, pp. 779–794, 2013.

[76] B. Tanguy, J. Besson, R. Piques, and A. Pineau, "Ductile to brittle transition of an A508 steel characterized by Charpy impact test: Part II: modeling of the charpy transition curve," *Engineering Fracture Mechanics*, vol. 72, no. 3, pp. 413–434, 2005.

[77] M. Springmann and M. Kuna, "Identification of material parameters of the Gurson-Tvergaard-Needleman model by combined experimental and numerical techniques," *Computational Materials Science*, vol. 32, no. 3-4, pp. 544–552, 2005.

[78] G. Bernauer and W. Brocks, "Micro-mechanical modelling of ductile damage and tearing - results of a European numerical round robin," *Fatigue & Fracture of Engineering Materials & Structures*, vol. 25, no. 4, pp. 363–384, 2002.

[79] Z. Xue, M. Pontin, F. Zok, and J. Hutchinson, "Calibration procedures for a computational model of ductile fracture," *Engineering Fracture Mechanics*, vol. 77, no. 3, pp. 492–509, 2010.

[80] H. Tu, S. Schmauder, and U. Weber, "Numerical study of electron beam welded butt joints with the gtn model," *Computational Mechanics*, vol. 50, no. 2, pp. 245–255, 2012.

[81] G. Hütter, T. Linse, U. Mühlich, and M. Kuna, "Simulation of ductile crack initiation and propagation by means of a non-local Gurson-model," *International Journal of Solids and Structures*, vol. 50, no. 5, pp. 662–671, 2013.

[82] V. Tvergaard and A. Needleman, "Analysis of the Charpy V-notch test for welds," *Engineering Fracture Mechanics*, vol. 65, no. 6, pp. 627–643, 2000.

[83] V. Tvergaard and A. Needleman, "3D analyses of the effect of weld orientation in Charpy specimens," *Engineering Fracture Mechanics*, vol. 71, no. 15, pp. 2179–2195, 2004.

[84] A. Rossoll, C. Berdin, P. Forget, C. Prioul, and B. Marini, "Mechanical aspects of the Charpy impact test," *Nuclear Engineering and Design*, vol. 188, no. 2, pp. 217–229, 1999.

[85] A. Rossoll, C. Berdin, and C. Prioul, "Determination of the fracture toughness of a low alloy steel by the instrumented Charpy impact test," *International Journal of Fracture*, vol. 115, no. 3, pp. 205–226, 2002.

[86] D.-Z. Sun, W. Brocks, and W. Schmitt, "Fracture toughness evaluation by tensile and Charpy-type tests based on micromechanical models of materials," *Materials Science*, vol. 30, no. 2, pp. 223–229, 1995.

[87] K. K. Mathur, A. Needleman, and V. Tvergaard, "Dynamic 3D analysis of the Charpy V-notch test," *Modelling and Simulation in Materials Science and Engineering*, vol. 1, no. 4, pp. 467–484, 1993.

[88] K. K. Mathur, A. Needleman, and V. Tvergaard, "3D analysis of failure modes in the Charpy impact test," *Modelling and Simulation in Materials Science and Engineering*, vol. 2, no. 3A, pp. 617–635, 1994.

[89] A. Nonn and H. Brauer, "Establishing the correlation between Charpy impact energies for different sized specimens of modern pipeline steels," in *Proceedings of the 2014 10th International Pipeline Conference*, American Society of Mechanical Engineers, 2014.

[90] O. Zienkiwicz and R. Taylor, *The Finite Element Method Volume 1: The Basis*. Oxford: Butterworth Heinemann, 2005.

[91] P. Wriggers, *Nonlinear Finite Element Methods*. Berlin, Heidelberg: Springer, 2008.

[92] O. Zienkiwicz and R. Taylor, *The Finite Element Method Volume 2: Solid Mechanics*. Oxford: Butterworth Heinemann, 2005.

[93] K. Müsch, *Untersuchungen zum Einfluß örtlicher Festigkeitsunterschiede (Mismatch) auf das Versagensverhalten von Schweißverbindungen aus höherfesten Feinkornbaustählen*. PhD thesis, RWTH Aachen University, Institut für Eisenhüttenkunde, 1999.

[94] J. T. Buchholz, *Sicherheitskonzepte zur Vermeidung von Sprödbruch hochfester Stähle im Stahl- und Druckbehälterbau*. PhD thesis, RWTH Aachen University, Institut für Eisenhüttenkunde, 2006.

[95] R. Hubo, *Bruchmechanische Untersuchungen zum Einsatz von Stählen unterschiedlicher Festigkeit und Zähigkeit*. PhD thesis, RWTH Aachen University, Institut für Eisenhüttenkunde, 1990.

[96] A. Liessem, *Bruchmechanische Sicherheitsanalysen von Stahlbauten aus hochfesten, niedriglegierten Stählen*. PhD thesis, RWTH Aachen University, Institut für Eisenhüttenkunde, 1996.

[97] C. Beltrami, *Numerische Analyse der lokalen und globalen Beanspruchung in Bauteilen mit Rissen und Quantifizierung der Zähigkeitsanforderungen*. PhD thesis, RWTH Aachen University, Institut für Eisenhüttenkunde, 1995.

[98] P. Langenberg, *Bruchmechanische Sicherheitsanalyse anrißgefährdeter Bauteile im Stahlbau*. PhD thesis, RWTH Aachen University, Institut für Eisenhüttenkunde, 1995.

[99] T. Nießen, *Auswirkungen von lokalen Werkstoffeigenschaften auf das Bruchverhalten bauteilähnlicher Großzugproben aus hochfesten Feinkornbaustählen*. PhD thesis, RWTH Aachen University, Institut für Eisenhüttenkunde, 2000.

[100] D. Holland, *Einfluß des Spannungszustandes auf die Vorgänge beim Gleitbruch von Baustählen*. PhD thesis, RWTH Aachen University, Institut für Eisenhüttenkunde, 1993.

[101] J. Arndt, *Experimentelle und rechnerische Untersuchungen zur Schädigung von Baustählen bei duktilem Versagen*. PhD thesis, RWTH Aachen University, Institut für Eisenhüttenkunde, 1997.

[102] U.-J. Achenbach, *Einfluß des Gefüges auf die Schädigung von Stählen*. PhD thesis, RWTH Aachen University, Institut für Eisenhüttenkunde, 1999.

[103] F. Thönnessen, *Mikrostrukturbasierte Zähigkeitsvorhersagen am Beispiel von Pipelinestählen*. PhD thesis, RWTH Aachen University, Institut für Eisenhüttenkunde, 2009.

[104] A. Nonn, *Experimentelle und numerische Analyse des Schädigungsverhaltens von Hybridlaserschweißverbindungen*. PhD thesis, RWTH Aachen University, Institut für Eisenhüttenkunde, 2009.

[105] T. Christopher, B. R. Sarma, P. G. Potti, B. N. Rao, and K. Sankarnarayanasamy, "A comparative study on failure pressure estimations of unflawed cylindrical vessels," *International Journal of Pressure Vessels and Piping*, vol. 79, no. 1, pp. 53–66, 2002.

[106] M. Law and G. Bowie, "Prediction of failure strain and burst pressure in high yield-to-tensile strength ratio linepipe," *International Journal of Pressure Vessels and Piping*, vol. 84, no. 8, pp. 487–492, 2007.

[107] W. Zhou and G. T. Huang, "Model error assessment of burst capacity models for defect-free pipes," in *Proceedings of the 2012 9th International Pipeline Conference*, pp. 601–607, American Society of Mechanical Engineers, 2012.

[108] X.-K. Zhu and B. N. Leis, "Evaluation of burst pressure prediction models for line pipes," *International Journal of Pressure Vessels and Piping*, vol. 89, pp. 85–97, 2012.

[109] J. Mackerle, "Finite elements in the analysis of pressure vessels and piping, an addendum: A bibliography (2001-2004)," *International Journal of Pressure Vessels and Piping*, vol. 82, no. 7, pp. 571–592, 2005.

[110] M. Guerrero, C. Betegón, and J. Belzunce, "Fracture analysis of a pressure vessel made of high strength steel (HSS)," *Engineering Failure Analysis*, vol. 15, no. 3, pp. 208–219, 2008.

[111] A. Sandvik, E. Østby, and C. Thaulow, "Fracture control - Offshore pipelines JIP Use of Abaqus/Explicit to simulate ductile tearing in pipes with defects loaded beyond yielding," in *Proceedings of the Eighteenth (2008) International Offshore and Polar Engineering Conference*, International Society of Offshore and Polar Engineers, 2008.

[112] J. Dybwad, R. Tornqvist, E. Østby, and C. Thaulow, "Simulations of ductile tearing at large strains of biaxially loaded pipes," in *ASME 2009 28th International Conference on Ocean, Offshore and Arctic Engineering*, pp. 115–122, American Society of Mechanical Engineers, 2009.

[113] F. Dotta and C. Ruggieri, "Structural integrity assessments of high pressure pipelines with axial flaws using a micromechanics model," *International Journal of Pressure Vessels and Piping*, vol. 81, no. 9, pp. 761–770, 2004.

[114] T. Pavankumar, M. Samal, J. Chattopadhyay, B. Dutta, H. Kushwaha, E. Roos, and M. Seidenfuß, "Transferability of fracture parameters from specimens to component level," *International Journal of Pressure Vessels and Piping*, vol. 82, no. 5, pp. 386–399, 2005.

[115] C.-K. Oh, Y.-J. Kim, J.-H. Baek, Y.-P. Kim, and W.-S. Kim, "Ductile failure analysis of API X65 pipes with notch-type defects using a local fracture criterion," *International Journal of Pressure Vessels and Piping*, vol. 84, no. 8, pp. 512–525, 2007.

[116] T. Coppola, F. Iob, L. Cortese, and F. Campanelli, "Prediction of ductile fracture in anisotropic steels for pipeline applications," *Procedia Structural Integrity*, vol. 2, pp. 2936–2943, 2016.

[117] W. Bleck, S. Münstermann, V. Brinnel, M. Feldmann, and S. Schaffrath, "Forschungsvorhaben P950 - Dehnungsbasierte Bemessungskriterien für unbefeuerte Druckbehälter: Demonstration eines erweiterten DBF-Verfahrens," - in press -, Forschungsvereinigung Stahlanwendung e.V., Düsseldorf, 2017.

[118] F. Hanus and J. Schütz, "Kleine Ursache große Wirkung - Mögliche Beeinträchtigung der Schweißeignung durch Mikrolegierungs- und Begleitelemente in Bau- und Druckbehälterstählen," technical report, AG der Dillinger Hüttenwerke, Dillingen an der Saar, 2002.

[119] E. Maire, O. Bouaziz, M. D. Michiel, and C. Verdu, "Initiation and growth of damage in a dual-phase steel observed by X-ray microtomography," *Acta Materialia*, vol. 56, no. 18, pp. 4954–4964, 2008.

[120] T. Morgeneyer, L. Helfen, I. Sinclair, H. Proudhon, F. Xu, and T. Baumbach, "Ductile crack initiation and propagation assessed via in situ synchrotron radiation-computed laminography," *Scripta Materialia*, vol. 65, no. 11, pp. 1010–1013, 2011.

[121] C. Landron, E. Maire, J. Adrien, and O. Bouaziz, "Damage characterization in dual-phase steels using X-ray tomography," in *Optical Measurements, Modeling, and Metrology, Volume 5* (T. Proulx, ed.), pp. 11–18, New York: Springer, 2011.

[122] E. Maire and P. J. Withers, "Quantitative X-ray tomography," *International Materials Reviews*, vol. 59, no. 1, pp. 1–43, 2014.

[123] J. Lemaitre and J. Dufailly, "Damage measurements," *Engineering Fracture Mechanics*, vol. 28, no. 5-6, pp. 643–661, 1987.

[124] M. Alves, "Measurement of ductile material damage," *Mechanics of Structures and Machines*, vol. 29, no. 4, pp. 451–476, 2001.

[125] N. Bonora, A. Ruggiero, D. Gentile, and S. De Meo, "Practical applicability and limitations of the elastic modulus degradation technique for damage measurements in ductile metals," *Strain*, vol. 47, no. 3, pp. 241–254, 2011.

[126] C. Tasan, J. Hoefnagels, and M. Geers, "A critical assessment of indentation-based ductile damage quantification," *Acta Materialia*, vol. 57, no. 17, pp. 4957–4966, 2009.

[127] C. Tasan, J. Hoefnagels, and M. Geers, "Indentation-based damage quantification revisited," *Scripta Materialia*, vol. 63, no. 3, pp. 316–319, 2010.

[128] C. Tasan, J. Hoefnagels, and M. Geers, "Identification of the continuum damage parameter: An experimental challenge in modeling damage evolution," *Acta Materialia*, vol. 60, no. 8, pp. 3581–3589, 2012.

[129] P. Ljustell, "The effect of large scale plastic deformation on fatigue crack length measurement with the potential drop method," *Journal of Testing and Evaluation*, vol. 39, no. 6, pp. 985–1002, 2011.

[130] S. Zhang, Q. Xia, W. Li, and X. Zhou, "Ductile damage measurement and necking analysis of metal sheets based on digital image correlation and direct current potential drop methods," *International Journal of Damage Mechanics*, vol. 23, no. 8, pp. 1133–1149, 2014.

[131] J. S. Zhang, C. Zhou, X. Q. Xia, and M. S. Chen, "Quantification and characterization of full field ductile damage evolution for sheet metals using an improved direct current potential drop method," *Experimental Mechanics*, vol. 55, no. 3, pp. 611–621, 2015.

[132] V. Brinnel, B. Döbereiner, and S. Münstermann, "Ductile damage and failure: Application of the direct current potential drop method to uncracked tensile specimens," *Procedia Materials Science*, vol. 3, pp. 1161–1166, 2014.

[133] I. Wolff, *Grundlagen der Elektrotechnik Band 1: Das elektrische und das magnetische Feld*. Aachen: Verlagsbuchhandlung Dr. Wolff, 2003.

[134] K. Nielsen and J. Hutchinson, "Cohesive traction-separation laws for tearing of ductile metal plates," *International Journal of Impact Engineering*, vol. 48, pp. 15–23, 2012.

[135] M. Daly, F. Leonard, J. Sharples, and A. H. Sherry, "Advanced assessment of ductile tearing in nuclear reactor pressure vessel steel using X-ray tomography," in *Proceedings of the 13th International Conference on Fracture, Beijing, China*, 2013.

[136] N. Tada, Y. Hayashi, T. Kitamura, and R. Ohtani, "Analysis on the applicability of direct current electrical potential method to the detection of damage by multiple small internal cracks," *International Journal of Fracture*, vol. 85, no. 1, pp. 1–9, 1997.

[137] W. Brocks, S. Hao, and D. Steglich, "Micromechanical modelling of the damage and toughness behaviour of nodular cast iron materials," *Journal de Physique IV*, vol. 6, no. C6, pp. 43–52, 1996.

[138] L. Xue, "Constitutive modeling of void shearing effect in ductile fracture of porous materials," *Engineering Fracture Mechanics*, vol. 75, no. 11, pp. 3343–3366, 2008.

[139] X. Gao, T. Zhang, J. Zhou, S. M. Graham, M. Hayden, and C. Roe, "On stress-state dependent plasticity modeling: Significance of the hydrostatic stress, the third invariant of stress deviator and the non-associated flow rule," *International Journal of Plasticity*, vol. 27, no. 2, pp. 217–231, 2011.

[140] J. Jackiewicz, "Use of a modified Gurson model approach for the simulation of ductile fracture by growth and coalescence of microvoids under low, medium and high stress triaxiality loadings," *Engineering Fracture Mechanics*, vol. 78, no. 3, pp. 487–502, 2011.

[141] Z. Xue, J. Faleskog, and J. W. Hutchinson, "Tension-torsion fracture experiments - Part II: Simulations with the extended Gurson model and a ductile fracture criterion based on plastic strain," *International Journal of Solids and Structures*, vol. 50, no. 25-26, pp. 4258–4269, 2013.

[142] K. L. Nielsen and V. Tvergaard, "Effect of a shear modified Gurson model on damage development in a FSW tensile specimen," *International Journal of Solids and Structures*, vol. 46, no. 3-4, pp. 587–601, 2009.

[143] M. Achouri, G. Germain, P. D. Santo, and D. Saidane, "Numerical integration of an advanced Gurson model for shear loading: Application to the blanking process," *Computational Materials Science*, vol. 72, pp. 62–67, 2013.

[144] Z. Zhang, "Explicit consistent tangent moduli with a return mapping algorithm for pressure-dependent elastoplasticity models," *Computer Methods in Applied Mechanics and Engineering*, vol. 121, no. 1, pp. 29–44, 1995.

[145] K. Nahshon and Z. Xue, "A modified Gurson model and its application to punch-out experiments," *Engineering Fracture Mechanics*, vol. 76, no. 8, pp. 997–1009, 2009.

[146] X. Gao and J. Kim, "Modeling of ductile fracture: Significance of void coalescence," *International Journal of Solids and Structures*, vol. 43, no. 20, pp. 6277–6293, 2006.

[147] P. B. Woelke, M. D. Shields, N. N. Abboud, and J. W. Hutchinson, "Simulations of ductile fracture in an idealized ship grounding scenario using phenomenological damage and cohesive zone models," *Computational Materials Science*, vol. 80, pp. 79–95, 2013.

[148] M. Storheim, H. S. Alsos, O. S. Hopperstad, and J. Amdahl, "A damage-based failure model for coarsely meshed shell structures," *International Journal of Impact Engineering*, vol. 83, pp. 59–75, 2015.

[149] C. L. Walters, "Framework for adjusting for both stress triaxiality and mesh size effect for failure of metals in shell structures," *International Journal of Crashworthiness*, vol. 19, no. 1, pp. 1–12, 2014.

[150] M. Kõrgesaar and J. Romanoff, "Influence of mesh size, stress triaxiality and damage induced softening on ductile fracture of large-scale shell structures," *Marine Structures*, vol. 38, pp. 1–17, 2014.

[151] D. Raabe, F. Roters, F. Barlat, and L.-Q. Chen, eds., *Continuum Scale Simulation of Engineering Materials*. Weinheim: WILEY-VCH, 2004.

[152] G. Bernauer, W. Brocks, U. Mühlich, D. Steglich, and M. Werwer, "Hinweise zur Anwendung des Gurson-Tvergaard-Needleman-Modells," technical report, Institut für Werkstoffforschung, GKSS-Forschungszentrum Geesthacht, 1999.

[153] K. L. Nielsen and V. Tvergaard, "Ductile shear failure or plug failure of spot welds modelled by modified Gurson model," *Engineering Fracture Mechanics*, vol. 77, no. 7, pp. 1031–1047, 2010.

[154] S. Sommer, D. Steffes-lai, and T. Clees, "Entwicklung einer numerischen Methode zur Berücksichtigung stochastischer Effekte für die Crashsimulation von Punktschweißverbindungen," *FAT-Schriftenreihe*, vol. 266, 2014.

[155] Institut für Eisenhüttenkunde, RWTH Aachen University, "Burst test pressure vessel P690Q." https://www.youtube.com/watch?v=L41A-OirYGE, 2016.

[156] M. Sharaf and S. Münstermann, "Fatigue modeling: From microstructure to component scale," in *Handbook of Software Solutions for ICME* (G. J. Schmitz and U. Prahl, eds.), pp. 209–225, Weinheim: WILEY-VCH, 2016.